Chen, M., et al., 2023, Boninitic melt percolation makes depleted mantle wedges rich in silica: Geology, https://doi.org/10.1130/G51050.1

Supplemental Material

Supplemental Text.

Figures S1–S11.

Tables S1–S7.

Spot Locations for Electron Microprobe Analyses.

Supplementary Material

Boninitic melt percolation makes depleted mantle wedges rich in silica

Ming Chen [1,*], Jianping Zheng [1,*], Hong-Kun Dai [1], Qing Xiong [1], Min Sun [2], Mikhail M. Buslov [3], Xiang Zhou [1] and Jingao Liu [4]

[1] State Key Laboratory of Geological Processes and Mineral Resources, School of Earth Sciences, China University of Geosciences, Wuhan 430074, China

[2] Department of Earth Sciences, The University of Hong Kong, Hong Kong, China

[3] V.S. Sobolev Institute of Geology and Mineralogy, Siberian Branch, Russian Academy of Sciences, Novosibirsk 630090, Russia

[4] State Key Laboratory of Geological Processes and Mineral Resources, China University of Geosciences, Beijing 100083, China

** Corresponding authors: Ming Chen (chenming@cug.edu.cn), Jianping Zheng (jpzheng@cug.edu.cn)*

This file includes:

Supplemental Text

Supplementary Figures S1-S11

Supplementary Reference List

Supplemental Text

1. Samples and petrography

Seventeen peridotites were collected from the Chagan-Uzun ophiolite (Fig. S2 & S3A; Table S1). They underwent weak to moderate serpentinization and are exclusively porphyroblastic in texture (Fig. S3B-C). The porphyroblasts, being mainly about 2-5 mm in diameter, are comprised predominantly of orthopyroxenes (Opx) and, to a much lesser extent, olivines (Ol). These coarse-grained minerals always show kink banding, undulatory extinction and other signs of deformation. Ol and spinel (Sp) inclusions are common within Opx porphyroblasts (Fig. S3B-C) and, occasionally, needle-like Sp exsolutions can be observed along cleavages of these coarse-grained minerals. The matrix consists mainly of finer-grained Ol, Opx, clinopyroxene (Cpx), amphibole (Amp) and Sp (Fig. S3D-F). Some of these Ol form embayments along the lobate grain boundaries of Opx porphyroblasts. In contrast to the porphyroblasts, nearly none Sp exsolutions are identified in matrix Opx. When present, Cpx always show irregular morphology with variable sizes (Fig. S3D, F) and, less commonly, they are found as relicts within Amp (Fig. S3E). Amp mostly show euhedral to subhedral morphology and, in some samples (e.g., C17-18), reaction rims of this type of mineral after primary Cpx (Fig. S3E) are well preserved, suggesting hydrous metamorphism or metasomatism. Sp are generally < 150 μm in diameter with variable crystal shapes. They occur as discrete grains along boundaries of, or inclusions (as isolated grains or crystal clusters) within, other silicate minerals (Fig. S3D-F, S4). Point counting shows that the original mineral assemblages of the Chagan-Uzun peridotites are comprised of variable Ol (63.4-78.1 vol%), Opx (10.8-26.0 vol%), Cpx (0-4.2 vol%) and Amp (< 1.0 to 7.8 vol%)

(Table S1). Sp in most of these samples are less than 1.0 vol% but can reach up to ~ 1.5 vol% in a few samples. As such, most of the Chagan-Uzun peridotites can be classified as harzburgites (Streckeisen, 1976). For a few samples with relatively high Amp contents, this classification scheme is not applicated because the contents of primary Cpx are uncertain.

2. Analytical procedures

Whole-rock major elements were measured on fused glass disks through wavelength dispersive X-ray fluorescence (XRF) spectrometry using a Shimadzu XRF-1800 instrument in the State Key Laboratory of Geological Processes and Mineral Resources, China University of Geosciences, Wuhan (GPRM-CUGW). The loss-on-ignition values were calculated by measuring the percentage of weight loss after heating dried rock powders in a pre-heated corundum crucible to 1000 °C for 90 minutes. During the analysis, both the two Chinese national standards of ultramafic rocks (i.e., GBW07101 and GBW07102) and two duplicates of our own samples were inserted to monitor the data quality. Overall, the results show well reproductivity and, except for those elements with extremely low concentrations (e.g., TiO_2, Na_2O, K_2O and P_2O_5, which can be actually treated as minor or trace elements in the ultramafic standards), others mostly show accuracies better than 4%. The major-element data are presented in Table S2.

Whole-rock trace elements, except for the element Ti, were determined via high-resolution inductively coupled plasma mass spectrometry (HR-ICP-MS) on a Thermo® ELEMENT XR instrument in the Radiogenic Isotope Geochemistry-RIG lab of the State Key Laboratory of Geological Processes and Mineral Resources, China University of Geosciences, Beijing (GPRM-CUGB). About 50 mg powders (200 mesh) for each sample were digested in a mixture of 1 mL HNO_3 and 1 mL HF within the Teflon bombs, which were placed in a stainless-steel pressure jacket and heated to 190 °C in an oven for more than 48 hours. After cooling, the Teflon bombs were opened and placed on a hotplate at 140 °C till they dried. 1 mL HNO_3 was then added to each bomb. After drying by the same hotplate, 1 mL HNO_3, 1mL MQ water and 1mL internal standard solution containing 1 ppm In were added into the bombs. They were then resealed and placed in the oven at 190 °C for more than 24 hours. The final solutions were transferred to polyethylene bottles and diluted to 100 g by addition of 2% HNO_3 for further analyses by HR-ICP-MS. Three international standards (diabase W-2, basalt BHVO-2 and peridotite JP-1; the recommended values are from GERM database) were used to monitor the analytical quality, showing that the accuracies for most trace elements are better than 5%. The element Ti of our samples was analyzed on a quadrupole inductively coupled plasma mass spectrometer (ICP-MS; Agilent 770e) in Wuhan Sample Solution Analytical Technology Co., LTD using similar procedures. Four international standards, including AGV-2, BHVO-2, BCR-2 and RGM-2, were used to monitor the analytical quality and the data show good accuracies. The trace-element data are presented in Table S3.

Thin sections (ca. 120 μm in thickness) of our samples were carefully examined using a Zeiss Sigma 300 field emission scanning electron microprobe in the GPRM-CUGW, during which backscattered electron images and compositional mapping of representative mineral phases were captured or made by a high-definition backscattered electron detector and a X-MaxN energy-dispersive X-ray spectrometer connected to this instrument, respectively. The detailed operation conditions can be referred to Dai et al. (2019) and Zhou et al. (2021).

With referring to the petrographic examinations, in-situ mineral major-element compositions of twelve representative samples (the locations are marked in a file named as "Spot locations for electron microprobe analyses" in the Supplementary Material) were analyzed on thin sections through a four-spectrometer JEOL JXA-8100 electron microprobe in the Key Laboratory of Submarine Geosciences, Second Institute of Oceanography, Ministry of Natural Administration and Wuhan Sample Solution Analytical Technology Co., LTD. The accelerating voltage, current and beam diameter are 15 kV, 20 nA and 1-5 μm, respectively, with a counting time of 20 s (10 s for peaks and 5 s for both prior- and post-peak backgrounds) for each spectrometer. Data were corrected using a modified ZAF (atomic number, absorption, fluorescence) correction procedure. The in-situ mineral major-element data are presented in Table S4.

In-situ mineral trace-element analyses of nine representative samples on thin sections by laser ablation inductively coupled plasma mass spectrometry (LA-ICP-MS; GeoLas 2005 + Agilent 7500a) were further conducted in GPMR-CUGW and Wuhan Sample Solution Analytical Technology Co., LTD following the method from Liu et al. (2008). The diameters of ablation spots vary in the interval 90-130 μm on the basis of the mineral sizes with frequencies of 8-10 Hz and energy densities of 4.8-5.9 J/cm^2 during multiple rounds of experiments. In each round, the same spot size, frequency and energy density were used to analyze samples and standards. Helium was used as carrier gas and nitrogen was added into the central gas flow (He + Ar) of the Ar plasma to increase the sensitivity (Hu et al., 2008). Each analysis consists of 20-30 s background acquisition and 50 s data acquisition from the sample. NIST SRM 612 was applied in GPMR-CUGW and NIST SRM 610 in Wuhan Sample

Solution Analytical Technology Co., LTD to correct the time-dependent drift of sensitivity. Before this correction, all count rates were firstly normalized by Si. The trace-element concentrations of our samples were calibrated using multiple external standards (i.e., USGS reference glasses BCR-2G, BIR-1G and BHVO-2G) without applying internal standard (Liu et al., 2008). All oxides are normalized to 100 wt% for nominal anhydrous minerals (i.e., clinopyroxenes and orthopyroxenes). Off-line signal selection, quantitative calibration, and time-drift correction were processed by software ICPMSDataCal (Liu et al., 2008). During data reduction, the ablation yield correction factor (AYCF = $100/\sum_{j=1}^{N}\left(cps_{sam}^{j} \times l^{j}\right)$, $l^{j} = C_{rm}^{j} \,/\, cps_{rm}^{j}$) was applied to correct the matrix-dependent absolute amount of materials ablated in each run. In this formula, cps_{sam}^{j} and cps_{rm}^{j} represent net count rates of analyte element j of the sample and reference material for calibration, and C_{rm}^{j} represents concentrations of element j in the reference material. N denotes the number of elements that analyzed and they include Li^{7}, B^{11}, Na^{23}, Mg^{25}, Al^{27}, Si^{29}, K^{39}, Ca^{42}, Sc^{45}, Ti^{47}, V^{51}, Cr^{53}, Mn^{55}, Fe^{57}, Co^{59}, Ni^{60}, Rb^{85}, Sr^{88}, Y^{89}, Zr^{90}, Nb^{93}, Ba^{137}, La^{139}, Ce^{140}, Pr^{141}, Nd^{146}, Sm^{147}, Eu^{153}, Gd^{157}, Tb^{159}, Dy^{163}, Ho^{165}, Er^{166}, Tm^{169}, Yb^{173}, Lu^{175}, Hf^{178}, Ta^{181}, Pb^{208}, Th^{232} and U^{238} in this study. l value can be calculated using regression statistics on the basis of the used multiple reference materials. The in-situ mineral trace-element data are presented in Tables S5.

3. Major-element compositions of silicate minerals

Ol within peridotites from the Chagan-Uzun ophiolite show $Mg^{\#}$, NiO and MnO in the ranges of 90.2-91.8, 0.29-0.52 wt% and 0.03-0.21 wt% (Fig. S5A-B), respectively. Opx from these peridotites all belong to clinoenstatites, and they yield quite low Al_2O_3 (0.37-2.43 wt%)

and CaO (0.14-0.44 wt%), with $Mg^{\#}$ varying from 90.6 to 92.1 (Fig. S5C-D). Cpx from the peridotite samples are exclusively diopsides. They show elevated $Mg^{\#}$ (93.6-95.7) and CaO (23.6-25.0 wt%) but low Al_2O_3 (0.68-1.79 wt%; Fig. S5E-F) and TiO_2 (< 0.08 wt%). All Amp grains belong to the calcic species. They are dominated by magnesiohornblendes and only a small proportion belongs to tremolites (Leake et al., 1997; Fig. S6). Two types of Amp were identified in sample C17-68. The first type yields un-zoned internal structures and these Amp belong to magnesiohornblendes (Fig. S6). The second type is characterized by core-rim structures with sharp compositional boundaries. While the cores yield nearly identical compositions to those of the first type, the rims are all tremolites as envisaged by their elevated Si in formula.

4. Trace-element modeling procedures on partial melting

Melting curves of a depleted mid-ocean-ridge basalt (MORB) mantle source (Salters and Stracke, 2004) are constructed for both bulk residues and residual clinopyroxene applying incongruent dynamic melting (Zou and Reid, 2001), a common process in the mantle (Walter, 1998). The mineral mode in the Sp-facies mantle is assumed to be 0.53 Ol + 0.27 Opx + 0.17 Cpx + 0.03 Sp (Kinzler, 1997) and the anhydrous and hydrous Sp-facies melt modes are further assumed to be 0.28 Opx + 0.67 Cpx + 0.11 Sp = 0.06 Ol + 1.00 melt (Kinzler, 1997) and 0.51 Opx + 0.62 Cpx + 0.12 Sp = 0.25 Ol + 1.00 melt (Gaetani and Grove, 1998), respectively. Hydrous partitioning coefficients of Cpx and Opx from McDade et al. (2003a) and anhydrous ones of these two minerals from the same research group (McDade et al., 2003b) are applied in the modeling to make comparison between anhydrous and hydrous melting as meaningful as possible. Only anhydrous partitioning coefficients are available for Ol and these values are referenced from McDade et al. (2003b). As to Sp, the partitioning coefficient of Yb is assumed to be zero and a value of 0.176 is used for Ti (McDade et al., 2003a) in both hydrous and anhydrous conditions. Furthermore, the porosity is assumed to be 0.001, which is regarded as the threshold to allow melt migration (Faul, 2001). The modeled Yb and Ti concentrations in Cpx and bulk rocks of residual peridotites after Sp-facies hydrous and anhydrous melting are shown in Figure S9.

5. Procedures in modeling hydrous fluxing melting and peridotite-melt interaction

These processes are modelled using Adiabat_1ph, a text-based front-end of the (pH)MELTS family of algorithms (Smith and Asimow, 2005) that are solved for thermodynamic equilibrium between solid phases and silicate liquid.

Following the common thermal structures of mantle wedges of intra-oceanic arcs (Syracuse et al., 2010), the mantle peridotites are set to keep at 1250 ºC and 1.25 GPa during hydrous fluxing melting with initial major-element compositions of depleted MORB mantle (Salters and Stracke, 2004; Table S6) and an initial oxygen fugacity of QFM-1.0. The melting degrees increase through incremental addition of slab-derived hydrous fluid (Bénard et al., 2021) produced during the transition from amphibolite- to eclogite-facies metamorphism (ca. 550 ºC at 1.75 GPa; Manning, 2004; Table S6). The initial mantle peridotite is set to be 100 gram in mass and 0.1 gram of the fluxing agent is added at each step to get equilibrium with the peridotite. The modeling runs in a near-fractional mode with melt extraction threshold of 0.5%, the melt fraction beyond which will be extracted. The residual system after the extraction, normally consisting of peridotite and < 0.5% instantaneous melt, will undergo another round of fluid invasion, equilibration/melting and possible melt extraction. The bulk-rock major-element compositions of the melting residues are presented in Table S7 and Figure S11.

Melting residua after ~20% and 25% fluxing melting are then used as initial solid reactants to react with two kinds of percolating boninitic melts, a high-Si one from Cape Vogel of Papua New Guinea (Kamenetsky et al., 2002) and a low-Si one from Northern Tonga (Sobolev and Danyushevsky, 1994; Table S6). The former has an estimated liquidus temperature of 1440 ºC (Kamenetsky et al., 2002), while the latter is assumed to be at 1400 ºC. The melt-rock interactions run at an isenthalpic mode and the threshold for instantaneous melt extraction remains at 0.5%. The initial solid mass is 100 gram and melt parcel of 1 gram is added interactively to react with the solid. The net melt consumption is the mass increase of the solid or the remains between the total melt addition and the sum of the melt mass extracted at each step. The mineral abundances and bulk-rock major-element compositions of the percolated peridotites are shown in Table S7 and Figure 4.

6. Compiled data sources

The data of abyssal peridotites in figures 1 and 3 of this manuscript are compiled from Niu (2004) and Warren (2016) and references therein. The data of modern forearc peridotites are sourced from Ishii (1992), Ohara and Ishii (1998), Parkinson and Pearce (1998), Pearce et al. (2000), Okamura et al. (2006), Birner et al. (2017), Bénard et al. (2021) and Day and Brown (2021), and those of arc peridotite xenoliths are from McInnes et al. (2001), Ishimaru et al. (2007), Ionov (2010), Bénard et al. (2017) and Tollan et al. (2017). The data of peridotites of supra-subduction zone ophiolites are collected from Uysal et al. (2007, 2012, 2014), Choi et al. (2008), Pagé et al. (2008, 2009), Shi et al. (2008), Aldanmaz et al. (2009, 2020), Song et al. (2009), Jean et al. (2010), Ulrich et al. (2010), Batanova et al. (2011), Dai et al. (2011), Liu et al. (2012, 2016a, b, 2018), Pirard et al. (2013), Huang et al. et al. (2015), Kaczmarek et al. (2015), Niu et al. (2015), Xiong et al. (2015, 2016, 2017), Chen et al. (2020), Secchiari et al. (2020), Zhang et al. (2020), Zhou et al. (2021) and Barrett et al. (2022). The data of spinels within boninites from the Izu-Bonin-Mariana arc are collected from Umino (1986), Bloomer and Hawkins (1987), van der Laan et al. (1992), Yajima and Fujimaki (2001), Maehara and Maeda (2004), Dobson et al. (2006), Whattam et al. (2020) and Scholpp et al. (2022).

Supplementary Figures

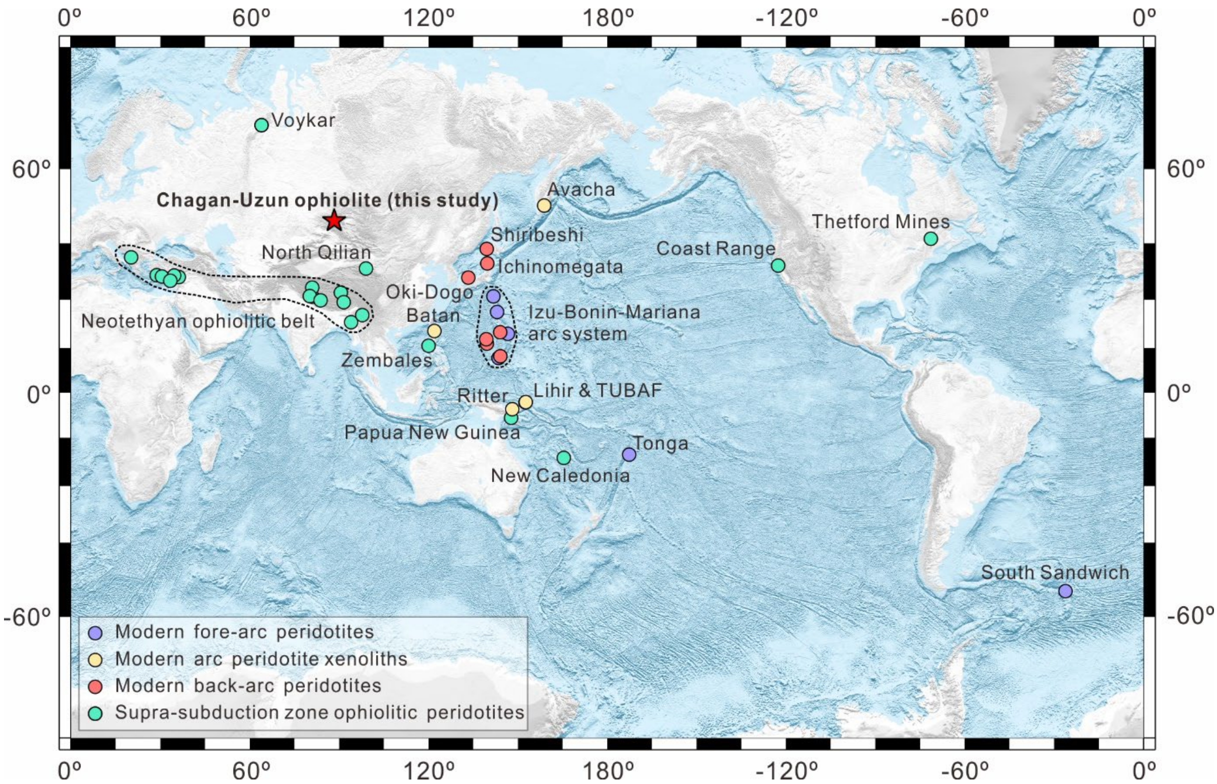

Figure S1 Global distribution of modern fore-arc, sub-arc and back-arc peridotites and typical supra-subduction zone ophiolitic peridotites. The data sources are summarized in the supplemental text. Also shown includes the late Neoproterozoic Chagan-Uzun ophiolite in this study.

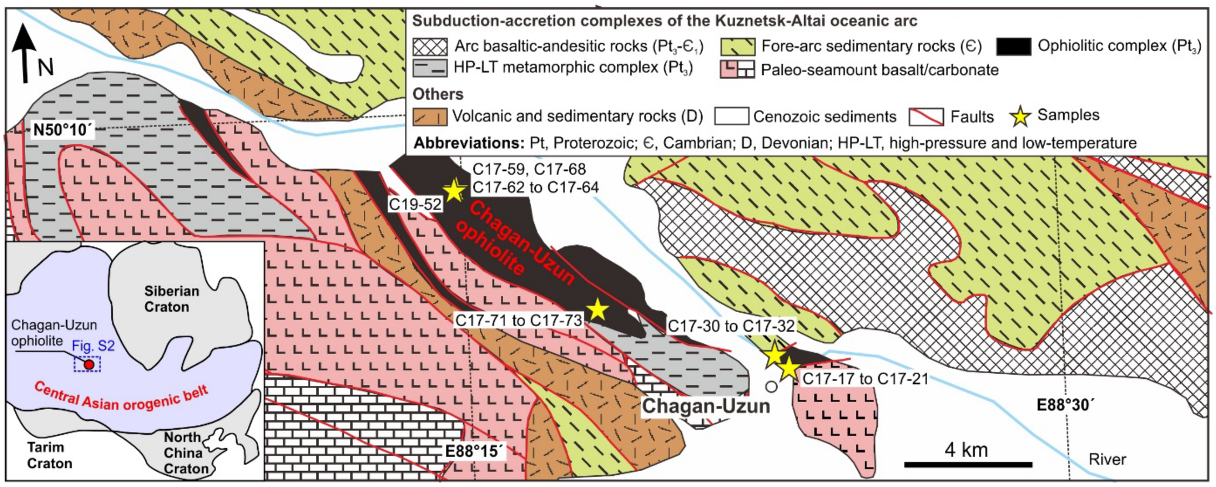

Figure S2 Geological units surrounding the Chagan-Uzun ophiolite (modified after Ota et al. (2007)). Inset shows the location of this ophiolite within the Central Asian orogenic belt.

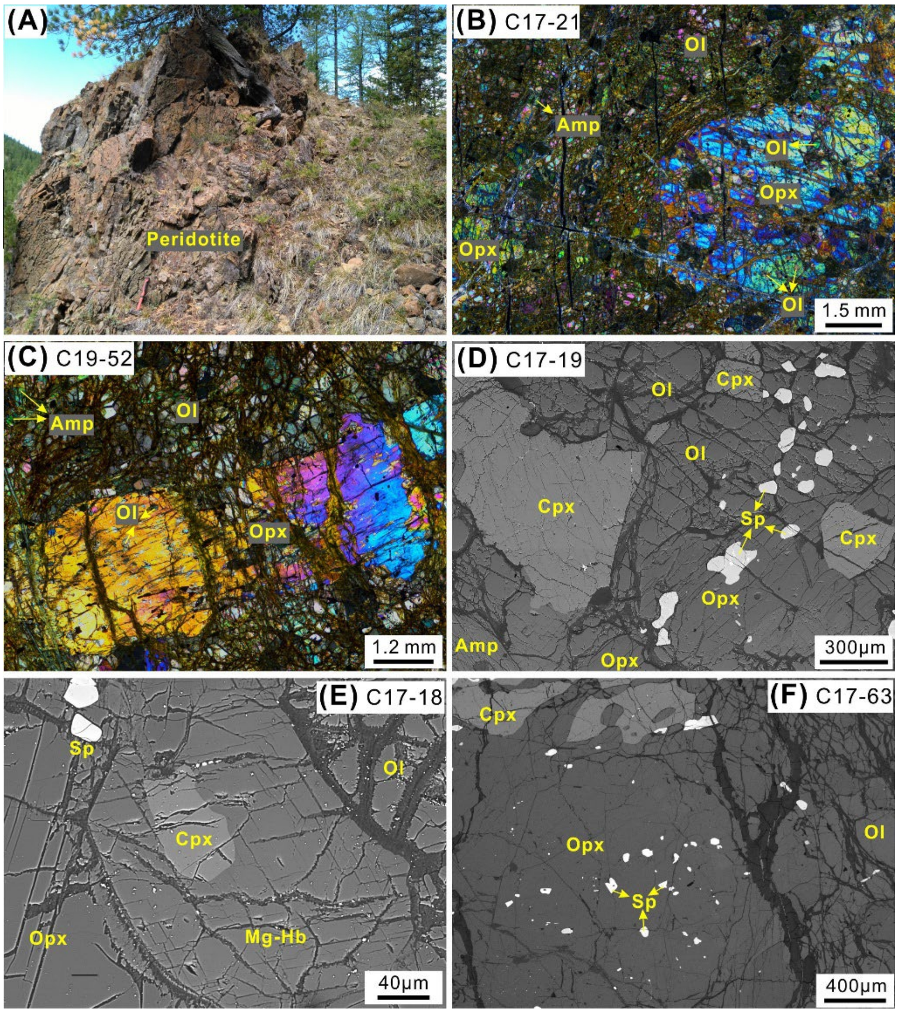

Figure S3 The field occurrence (A) and petrography (B-F) of representative peridotites from the Chagan-Uzun ophiolite. (A) The outcrop showing relatively fresh peridotites. (B-C) Samples C17-21 and C19-52 exhibiting porphyroblastic textures, in which abundant olivine (Ol) inclusions are preserved in association with tiny spinel (Sp) grains within orthopyroxene (Opx) porphyroblasts. (D) Backscattered electron image revealing the mineral assemblage mainly of Ol, Opx, clinopyroxene (Cpx), amphiboles (Amp) and Sp in sample C17-19. (E) Backscattered electron image showing that a Cpx grain is partially transformed into Amp. (F) Backscattered electron image exhibiting that the Opx porphyroblast in sample C17-63 contains abundant Sp inclusions with variable crystal morphologies. Some Ol inclusions are also identified within this porphyroblast (see compositional mapping in figure 2A).

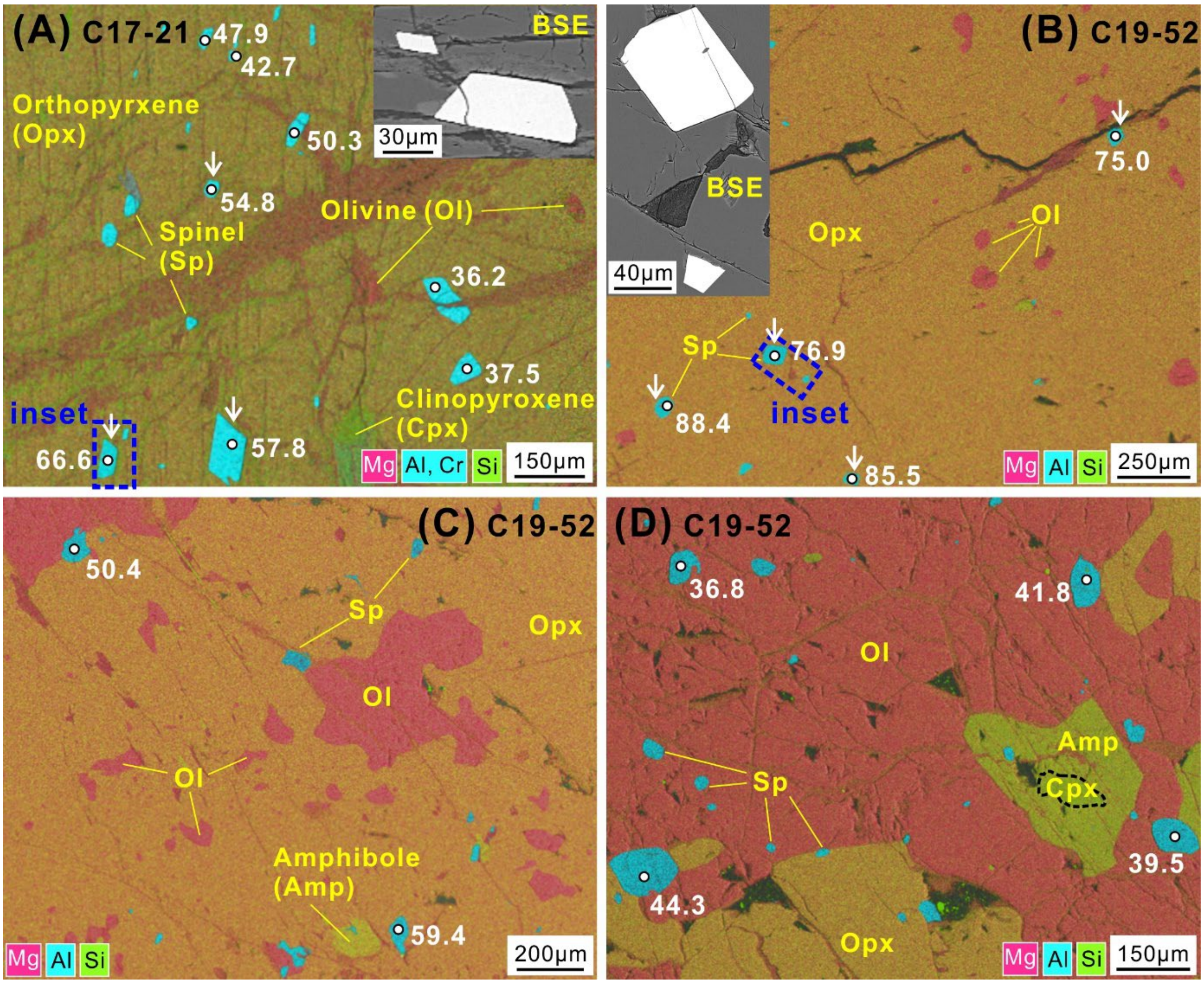

Figure S4 (A-C) Compositional maps showing resorbed olivines and variable-shaped spinels (Sp) within orthopyroxene porphyroblasts from peridotite samples C17-21 and C19-52. Insets in (A) and (B) show close-up views of representative euhedral Sp inclusions in backscattered electron (BSE) images. White arrows indicate euhedral Sp inclusions. (D) Interstitial Sp in sample C19-52. Numbers labeling Sp are Cr# (100 × Cr/[Cr + Al], atomic ratios).

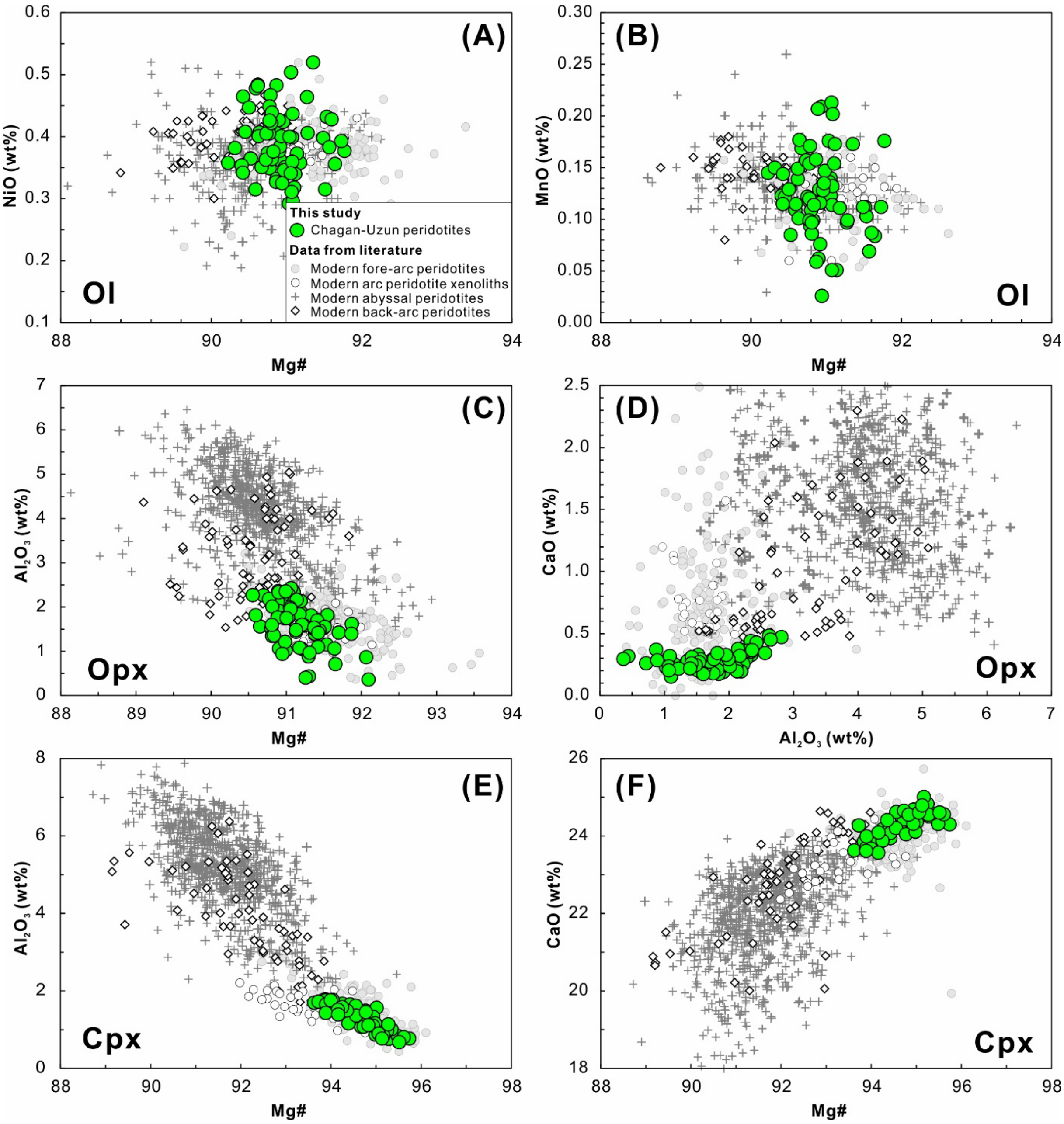

Figure S5 Major-element compositions of olivines (Ol), orthopyroxenes (Opx) and clinopyroxenes (Cpx) in peridotites from the Chagan-Uzun ophiolite. Mg# = 100 × MgO/(MgO + FeO^{total}), molar ratios. Reference data for those minerals in abyssal, fore-arc, arc and back-arc peridotites (see data sources in the supplemental text) are shown for comparison.

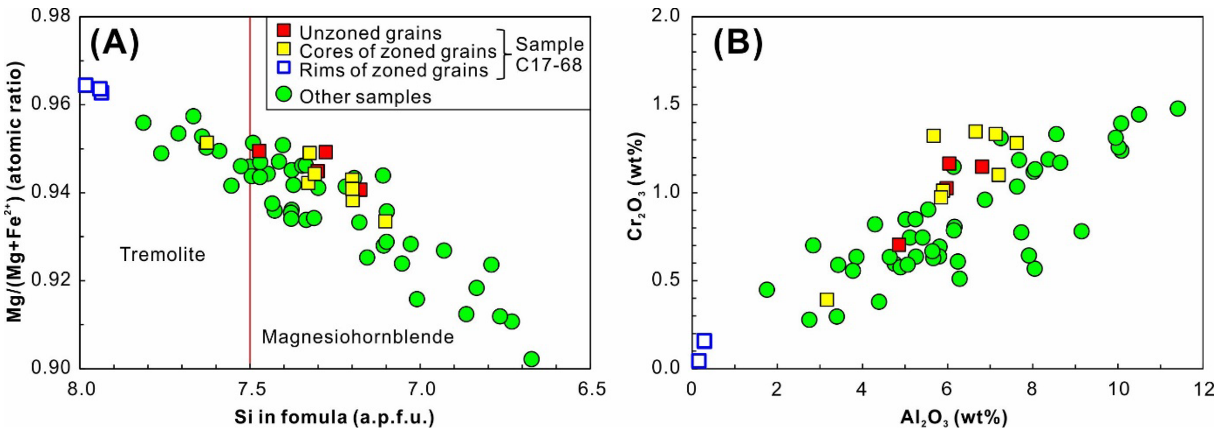

Figure S6 Compositional variations of amphiboles in peridotites from the Chagan-Uzun ophiolite. The formula was calculated using a machine learning method on the basis of principle components regression (Li et al., 2020).

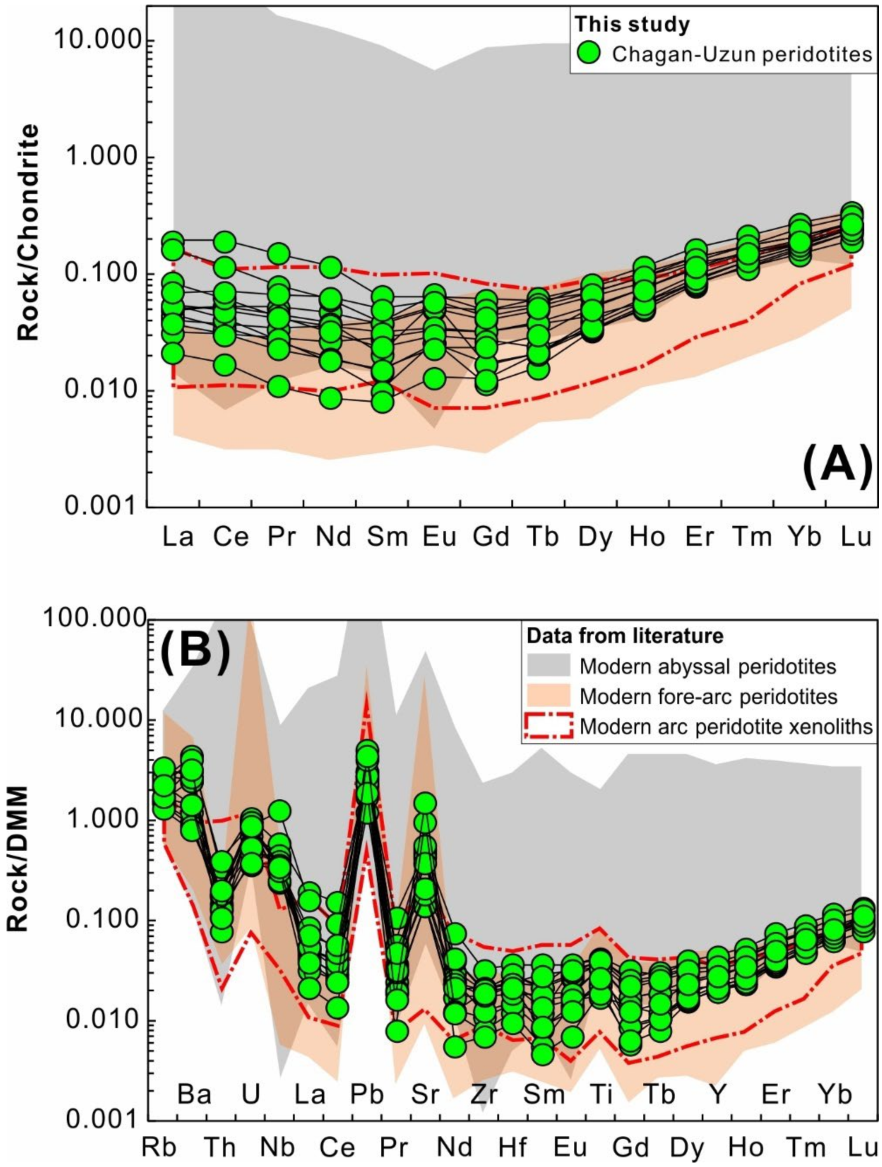

Figure S7 Whole-rock trace-element compositions of peridotites from the Chagan-Uzun ophiolite that are normalized to chondrite (Sun and Mcdonough, 1989) and depleted mid-ocean-ridge basalt (MORB) mantle (DMM; Salters and Stracke, 2004). Reference data for abyssal peridotites (Niu, 2004), fore-arc peridotites (Parkinson and Pearce, 1998) and arc peridotites (Ionov, 2010; Ishimaru et al., 2007) are shown for comparison.

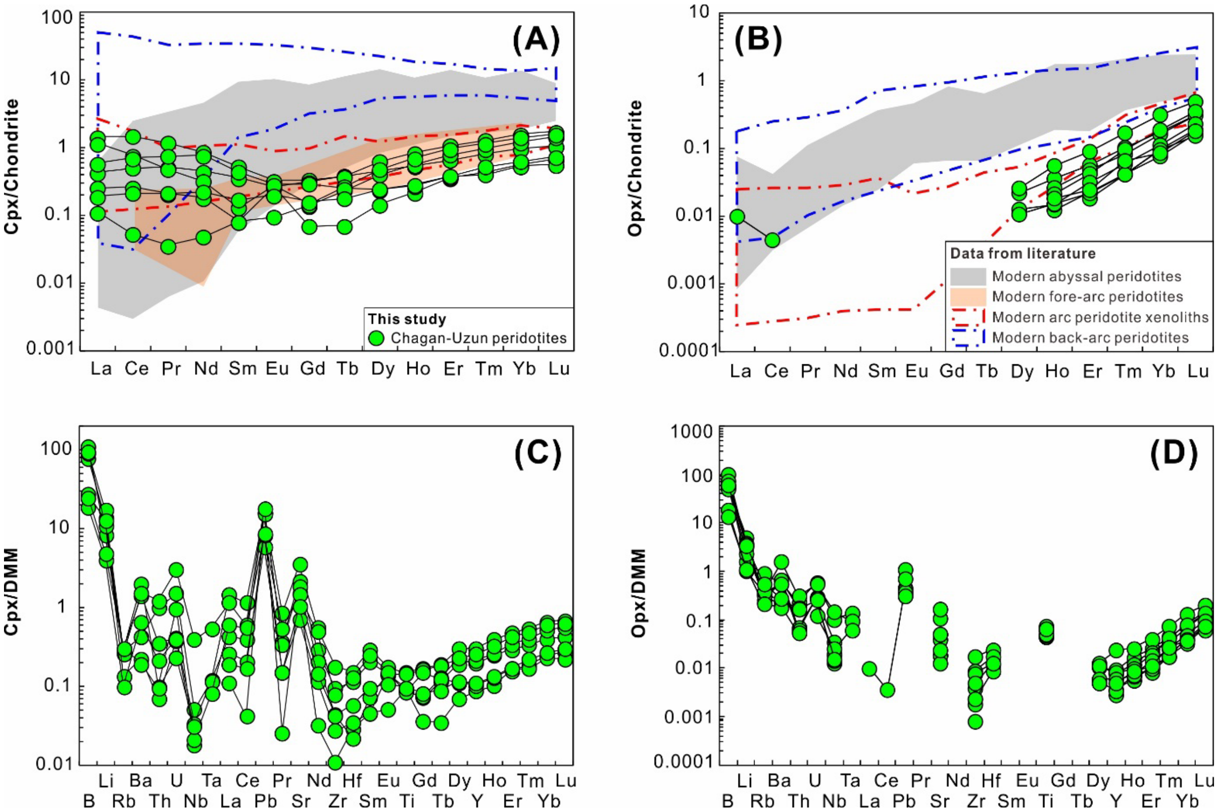

Figure S8 Chondrite-normalized rare earth element patterns and depleted mid-ocean-ridge basalt (MORB) mantle (DMM)-normalized trace-element patterns of clinopyroxenes (Cpx) and orthopyroxenes (Opx) within peridotites from the Chagan-Uzun ophiolite. Reference data for the same types of minerals from abyssal, fore-arc, arc and back-arc peridotites (see data sources in the supplemental text) are shown for comparison. The normalizing values of chondrite and DMM are from Sun and McDonough (1989) and Salters and Stracke (2004), respectively.

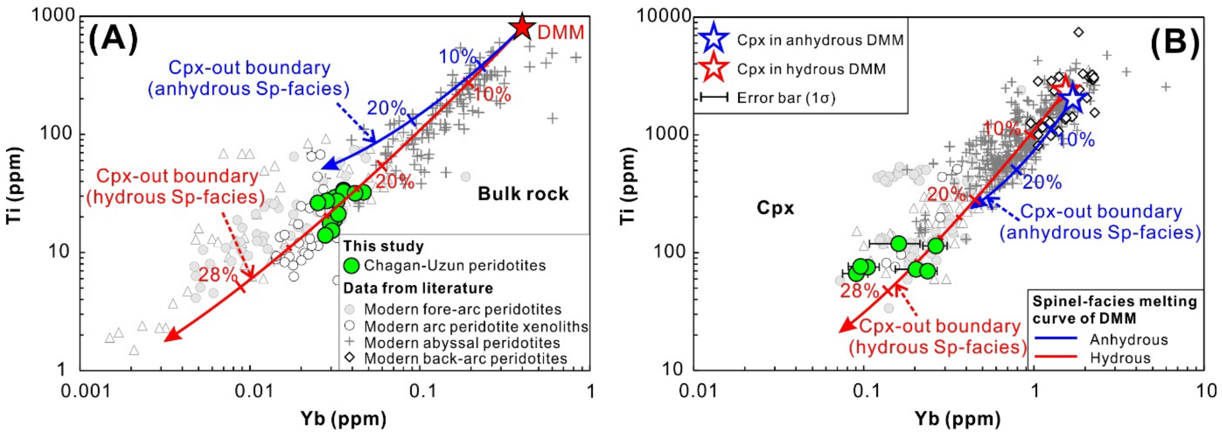

Figure S9 Bulk-rock/clinopyroxene (Cpx) Yb-Ti variations of the Chagan-Uzun peridotites in comparison with spinel (Sp)-facies melting curves of depleted mid-ocean-ridge basalt (MORB) mantle (DMM; Salters and Stracke, 2004). The data sources of fore-arc, arc, back-arc, abyssal and supra-subduction zone ophiolitic peridotites and detailed modeling procedures can be referred to the supplemental text.

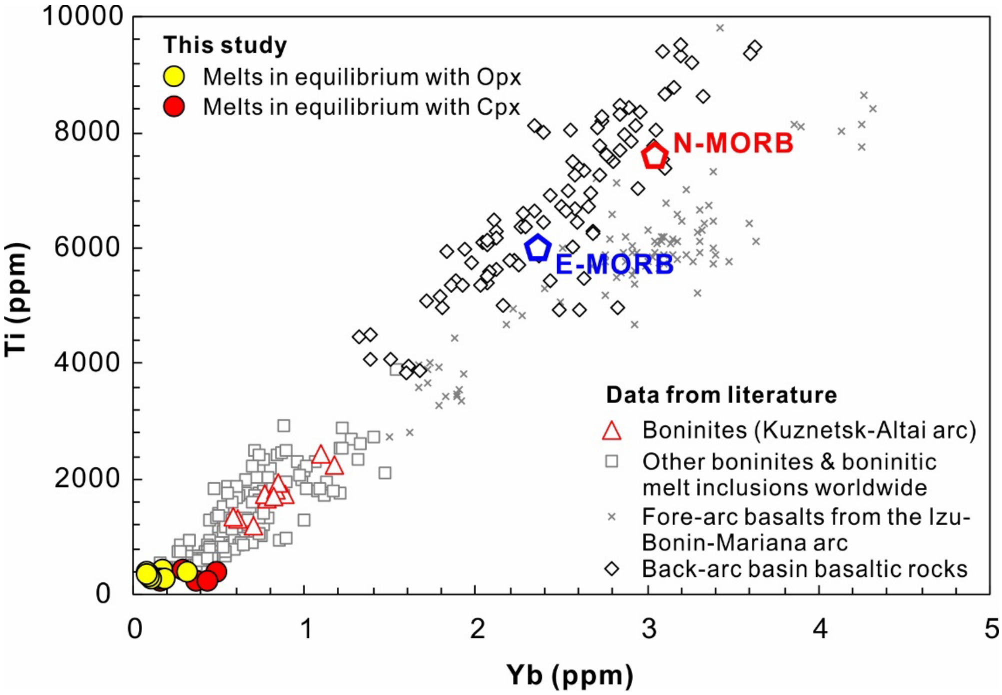

Figure S10 Estimated melts in equilibrium with Chagan-Uzun peridotitic clinopyroxenes (Cpx) and orthopyroxenes (Opx) using partition coefficients from McDade et al. (2003a, b). Boninites from the Kuznetsk-Altai oceanic arc (Chen et al., 2018), other boninites and boninitic melt inclusions worldwide (Bénard et al., 2016; Kamenetsky et al., 2002; König et al., 2008, 2010; Li et al., 2013, 2019; Osozawa et al., 2012; Reagan et al., 2010; Shervais et al., 2021; Taylor et al., 1994; Woodland et al., 2002), fore-arc basalts from the Izu-Bonin-Mariana arc (Li et al., 2019; Reagan et al., 2010; Shervais et al., 2019), and back-arc basin basaltic rocks (Fretzdorff et al., 2006; Gribble et al., 1996, 1998; Pearce et al., 2005) are show for comparison. The data of average normal and enriched mid-ocean-ridge basalt (N-MORB and E-MORB) are from Sun and McDonough (1989).

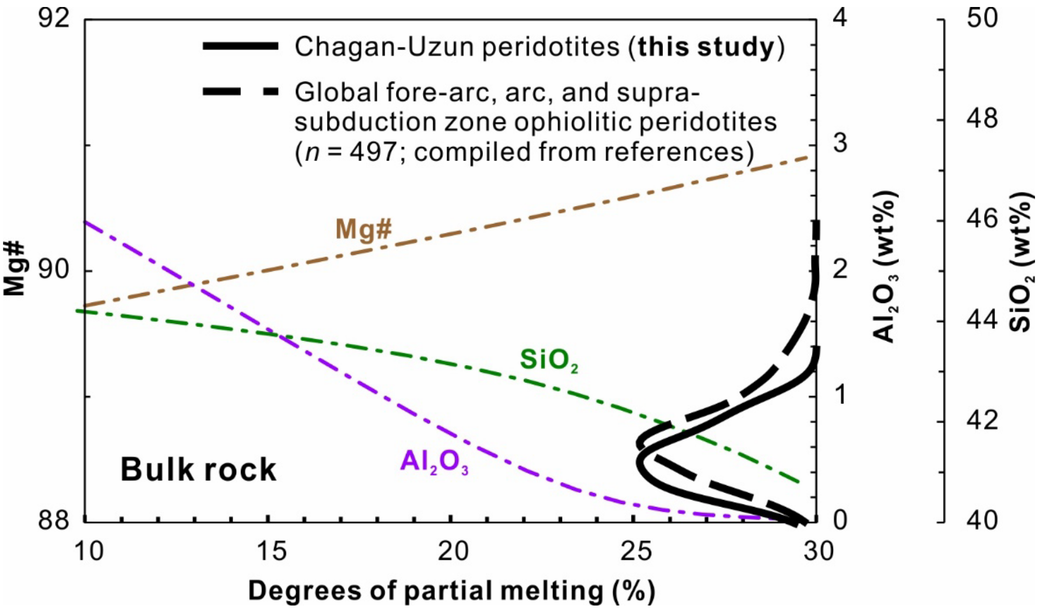

Figure S11 Bulk-rock major elements of residues after isothermal fluxing melting of depleted MORB mantle (Salters and Stracke, 2004) at 1.25 GPa and 1250 °C. Mg# = 100 × MgO/(MgO + FeO^{total}), molar ratios. Kernel density plots of Al_2O_3 for the Chagan-Uzun peridotites and global fore-arc, arc and supra-subduction zone (SSZ) ophiolitic counterparts are shown for comparison. The detailed modeling procedures and conditions can be referred to the supplemental text.

Supplementary Reference List

Aldanmaz, E., Schmidt, M. W., Gourgaud, A., and Meisel, T., 2009, Mid-ocean ridge and supra-subduction geochemical signatures in spinel–peridotites from the Neotethyan ophiolites in SW Turkey: Implications for upper mantle melting processes: Lithos, v. 113, no. 3, p. 691-708.

Aldanmaz, E., van Hinsbergen, D. J. J., Yıldız-Yüksekol, Ö., Schmidt, M. W., McPhee, P. J., Meisel, T., Güçtekin, A., and Mason, P. R. D., 2020, Effects of reactive dissolution of orthopyroxene in producing incompatible element depleted melts and refractory mantle residues during early fore-arc spreading: constraints from ophiolites in eastern Mediterranean: Lithos, v. 360-361, p. 105438.

Barrett, N., Jaques, A. L., González-Álvarez, I., Walter, M. J., and Pearson, D. G., 2022, Ultra-Refractory Peridotites of Phanerozoic Mantle Origin: the Papua New Guinea Ophiolite Mantle Tectonites: Journal of Petrology, v. 63, no. 3, p. egac014.

Batanova, V. G., Belousov, I. A., Savelieva, G. N., and Sobolev, A. V., 2011, Consequences of Channelized and Diffuse Melt Transport in Supra-subduction Zone Mantle: Evidence from the Voykar Ophiolite (Polar Urals): Journal of Petrology, v. 52, no. 12, p. 2483-2521.

Bénard, A., Arculus, R. J., Nebel, O., Ionov, D. A., and McAlpine, S. R. B., 2017, Silica-enriched mantle sources of subalkaline picrite-boninite-andesite island arc magmas: Geochimica et Cosmochimica Acta, v. 199, p. 287-303.

Bénard, A., Müntener, O., Pilet, S., Arculus, R. J., and Nebel, O., 2021, Silica-rich spinel harzburgite residues formed by fractional hybridization-melting of the intra-oceanic supra-subduction zone mantle: New evidence from TUBAF seamount peridotites: Geochimica et Cosmochimica Acta, v. 293, p. 477-506.

Bénard, A., Nebel, O., Ionov, D. A., Arculus, R. J., Shimizu, N., and Métrich, N., 2016, Primary Silica-rich Picrite and High-Ca Boninite Melt Inclusions in Pyroxenite Veins from the Kamchatka Sub-arc Mantle: Journal of Petrology, v. 57, no. 10, p. 1955-1982.

Birner, S. K., Warren, J. M., Cottrell, E., Davis, F. A., Kelley, K. A., and Falloon, T. J., 2017, Forearc Peridotites from Tonga Record Heterogeneous Oxidation of the Mantle following Subduction Initiation: Journal of Petrology, v. 58, no. 9, p. 1755-1780.

Bloomer, S. H., and Hawkins, J. W., 1987, Petrology and geochemistry of boninite series volcanic rocks from the Mariana trench: Contributions to Mineralogy and Petrology, v. 97, no. 3, p. 361-377.

Chen, C., Su, B.-X., Xiao, Y., Uysal, İ., Lin, W., Chu, Y., Jing, J.-J., and Sakyi, P. A., 2020, Highly siderophile elements and Os isotope constraints on the genesis of peridotites from the Kızıldağ ophiolite, southern Turkey: Lithos, v. 368-369, p. 105583.

Choi, S. H., Shervais, J. W., and Mukasa, S. B., 2008, Supra-subduction and abyssal mantle peridotites of the Coast Range ophiolite, California: Contributions to Mineralogy and Petrology, v. 156, no. 5, p. 551.

Dai, H.-K., Zheng, J.-P., Xiong, Q., Su, Y.-P., Pan, S.-K., Ping, X.-Q., and Zhou, X., 2019, Fertile lithospheric mantle underlying ancient continental crust beneath the northwestern North China craton: Significant effect from the southward subduction of the Paleo–Asian Ocean: GSA Bulletin, v. 131, no. 1-2, p. 3-20.

Dai, J.-G., Wang, C.-S., Hébert, R., Santosh, M., Li, Y.-L., and Xu, J.-Y., 2011, Petrology and geochemistry of peridotites in the Zhongba ophiolite, Yarlung Zangbo Suture Zone: Implications for the Early Cretaceous intra-oceanic subduction zone within the Neo-Tethys: Chemical Geology, v. 288, no. 3, p. 133-148.

Day, J. M. D., and Brown, D. B., 2021, Ancient Melt-Depletion in Fresh to Strongly Serpentinized Tonga Trench Peridotites: Journal of Petrology, v. 62, no. 12, p. egab088.

Dobson, P. F., Blank, J. G., Maruyama, S., and Liou, J. G., 2006, Petrology and Geochemistry of Boninite-Series Volcanic Rocks, Chichi-Jima, Bonin Islands, Japan: International Geology Review, v. 48, no. 8, p. 669-701.

Faul, U. H., 2001, Melt retention and segregation beneath mid-ocean ridges: Nature, v. 410, no. 6831, p. 920-923.

Fretzdorff, S., Schwarz-Schampera, U., Gibson, H. L., Garbe-Schönberg, C. D., Hauff, F., and Stoffers, P., 2006, Hydrothermal activity and magma genesis along a propagating back-arc basin: Valu Fa Ridge (southern Lau Basin): Journal of Geophysical Research: Solid Earth, v. 111, no. B8.

Gaetani, G. A., and Grove, T. L., 1998, The influence of water on melting of mantle peridotite: Contributions to Mineralogy and Petrology, v. 131, no. 4, p. 323-346.

Gribble, R. F., Stern, R. J., Bloomer, S. H., Stüben, D., O'Hearn, T., and Newman, S., 1996, MORB mantle and subduction components interact to generate basalts in the southern Mariana Trough back-arc basin: Geochimica et Cosmochimica Acta, v. 60, no. 12, p. 2153-2166.

Gribble, R. F., Stern, R. J., Newman, S., Bloomer, S. H., and O'Hearn, T., 1998, Chemical and

Isotopic Composition of Lavas from the Northern Mariana Trough: Implications for Magmagenesis in Back-arc Basins: Journal of Petrology, v. 39, no. 1, p. 125-154.

Hu, Z., Gao, S., Liu, Y., Hu, S., Chen, H., and Yuan, H., 2008, Signal enhancement in laser ablation ICP-MS by addition of nitrogen in the central channel gas: Journal of Analytical Atomic Spectrometry, v. 23, no. 8, p. 1093-1101.

Huang, Q.-S., Shi, R.-D., O'Reilly, S. Y., Griffin, W. L., Zhang, M., Liu, D.-L., and Zhang, X.-R., 2015, Re-Os isotopic constraints on the evolution of the Bangong-Nujiang Tethyan oceanic mantle, Central Tibet: Lithos, v. 224-225, p. 32-45.

Ionov, D. A., 2010, Petrology of Mantle Wedge Lithosphere: New Data on Supra-Subduction Zone Peridotite Xenoliths from the Andesitic Avacha Volcano, Kamchatka: Journal of Petrology, v. 51, no. 1-2, p. 327-361.

Ishii, T., Petrological studies of peridotites from diapiric serpentinite seamounts in the Izu-Ogasawara-Mariana forearc, Leg 125, in Proceedings Proceedings of the ocean drilling program, scientific results1992, Volume 125, Ocean Drilling Program, p. 401-414.

Ishimaru, S., Arai, S., Ishida, Y., Shirasaka, M., and Okrugin, V. M., 2007, Melting and Multi-stage Metasomatism in the Mantle Wedge beneath a Frontal Arc Inferred from Highly Depleted Peridotite Xenoliths from the Avacha Volcano, Southern Kamchatka: Journal of Petrology, v. 48, no. 2, p. 395-433.

Jean, M. M., Shervais, J. W., Choi, S.-H., and Mukasa, S. B., 2010, Melt extraction and melt refertilization in mantle peridotite of the Coast Range ophiolite: an LA–ICP–MS study: Contributions to Mineralogy and Petrology, v. 159, no. 1, p. 113-116.

Kaczmarek, M.-A., Jonda, L., and Davies, H. L., 2015, Evidence of melting, melt percolation and deformation in a supra-subduction zone (Marum ophiolite complex, Papua New Guinea): Contributions to Mineralogy and Petrology, v. 170, no. 2, p. 19.

Kamenetsky, V. S., Sobolev, A. V., Eggins, S. M., Crawford, A. J., and Arculus, R. J., 2002, Olivine-enriched melt inclusions in chromites from low-Ca boninites, Cape Vogel, Papua New Guinea: evidence for ultramafic primary magma, refractory mantle source and enriched components: Chemical Geology, v. 183, no. 1, p. 287-303.

Kinzler, R. J., 1997, Melting of mantle peridotite at pressures approaching the spinel to garnet transition: Application to mid-ocean ridge basalt petrogenesis: Journal of Geophysical Research: Solid Earth, v. 102, no. B1, p. 853-874.

König, S., Münker, C., Schuth, S., and Garbe-Schönberg, D., 2008, Mobility of tungsten in subduction zones: Earth and Planetary Science Letters, v. 274, no. 1, p. 82-92.

König, S., Münker, C., Schuth, S., Luguet, A., Hoffmann, J. E., and Kuduon, J., 2010, Boninites as windows into trace element mobility in subduction zones: Geochimica et Cosmochimica Acta, v. 74, no. 2, p. 684-704.

Leake, B. E., Woolley, A. R., Arps, C. E. S., Birch, W. D., Gilbert, M. C., Grice, J. D., Hawthorne, F. C., Kato, A., Kisch, H. J., Krivovichev, V. G., Linthout, K., Laird, J., Mandarino, J. A., Maresch, W. V., Nickel, E. H., Rock, N. M. S., Schumacher, J. C., Smith, D. C., Stephenson, N. C. N., Ungaretti, L., Whittaker, E. J. W., and Youzhi, G., 1997, Nomenclature of amphiboles: report of the subcommittee on amphiboles of the International Mineralogical Association, Commission on New Minerals and Mineral Names: The Canadian Mineralogist, v. 35, no. 1, p. 219-246.

Li, H.-Y., Taylor, R. N., Prytulak, J., Kirchenbaur, M., Shervais, J. W., Ryan, J. G., Godard, M., Reagan, M. K., and Pearce, J. A., 2019, Radiogenic isotopes document the start of subduction in the Western Pacific: Earth and Planetary Science Letters, v. 518, p. 197-210.

Li, X., Zhang, C., Behrens, H., and Holtz, F., 2020, Calculating amphibole formula from electron microprobe analysis data using a machine learning method based on principal components regression: Lithos, v. 362-363, p. 105469.

Li, Y.-B., Kimura, J.-I., Machida, S., Ishii, T., Ishiwatari, A., Maruyama, S., Qiu, H.-N., Ishikawa, T., Kato, Y., Haraguchi, S., Takahata, N., Hirahara, Y., and Miyazaki, T., 2013, High-Mg Adakite and Low-Ca Boninite from a Bonin Fore-arc Seamount: Implications for the Reaction between Slab Melts and Depleted Mantle: Journal of Petrology, v. 54, no. 6, p. 1149-1175.

Liu, C.-Z., Wu, F.-Y., Chu, Z.-Y., Ji, W.-Q., Yu, L.-J., and Li, J.-L., 2012, Preservation of ancient Os isotope signatures in the Yungbwa ophiolite (southwestern Tibet) after subduction modification: Journal of Asian Earth Sciences, v. 53, p. 38-50.

Liu, C.-Z., Xu, Y., and Wu, F.-Y., 2018, Limited recycling of crustal osmium in forearc mantle during slab dehydration: Geology, v. 46, no. 3, p. 239-242.

Liu, C.-Z., Zhang, C., Xu, Y., Wang, J.-G., Chen, Y., Guo, S., Wu, F.-Y., and Sein, K., 2016a, Petrology and geochemistry of mantle peridotites from the Kalaymyo and Myitkyina ophiolites (Myanmar): Implications for tectonic settings: Lithos, v. 264, p. 495-508.

Liu, T., Zhai, Q.-g., Wang, J., Bao, P.-s., Qiangba, Z., Tang, S.-h., and Tang, Y., 2016b, Tectonic significance of the Dongqiao ophiolite in the north-central Tibetan plateau:

Evidence from zircon dating, petrological, geochemical and Sr–Nd–Hf isotopic characterization: Journal of Asian Earth Sciences, v. 116, p. 139-154.

Liu, Y., Hu, Z., Gao, S., Günther, D., Xu, J., Gao, C., and Chen, H., 2008, In situ analysis of major and trace elements of anhydrous minerals by LA-ICP-MS without applying an internal standard: Chemical Geology, v. 257, no. 1, p. 34-43.

Maehara, K., and Maeda, J., 2004, Evidence for high-Ca boninite magmatism from Paleogene primitive low-K tholeiite, Mukoojima, Hahajima Island group, southern Bonin (Ogasawara) forearc, Japan: Island Arc, v. 13, no. 3, p. 452-465.

Manning, C. E., 2004, The chemistry of subduction-zone fluids: Earth and Planetary Science Letters, v. 223, no. 1, p. 1-16.

McDade, P., Blundy, J. D., and Wood, B. J., 2003a, Trace element partitioning between mantle wedge peridotite and hydrous MgO-rich melt: American Mineralogist, v. 88, no. 11-12, p. 1825-1831.

McDade, P., Blundy, J. D., and Wood, B. J., 2003b, Trace element partitioning on the Tinaquillo Lherzolite solidus at 1.5GPa: Physics of the Earth and Planetary Interiors, v. 139, no. 1, p. 129-147.

McInnes, B. I. A., Gregoire, M., Binns, R. A., Herzig, P. M., and Hannington, M. D., 2001, Hydrous metasomatism of oceanic sub-arc mantle, Lihir, Papua New Guinea: petrology and geochemistry of fluid-metasomatised mantle wedge xenoliths: Earth and Planetary Science Letters, v. 188, no. 1, p. 169-183.

Niu, X., Yang, J., Dilek, Y., Xu, J., Li, J., Chen, S., Feng, G., Liu, F., Xiong, F., and Liu, Z., 2015, Petrological and Os isotopic constraints on the origin of the Dongbo peridotite massif, Yarlung Zangbo Suture Zone, Western Tibet: Journal of Asian Earth Sciences, v. 110, p. 72-84.

Niu, Y., 2004, Bulk-rock major and trace element compositions of abyssal peridotites: implications for mantle melting, melt extraction and post-melting processes beneath mid-ocean ridges: Journal of Petrology, v. 45, no. 12, p. 2423-2458.

Ohara, Y., and Ishii, T., 1998, Peridotites from the southern Mariana forearc: Heterogeneous fluid supply in mantle wedge: Island Arc, v. 7, no. 3, p. 541-558.

Okamura, H., Arai, S., and Kim, Y.-U., 2006, Petrology of forearc peridotite from the Hahajima Seamount, the Izu-Bonin arc, with special reference to chemical characteristics of chromian spinel: Mineralogical Magazine, v. 70, no. 1, p. 15-26.

Osozawa, S., Shinjo, R., Lo, C.-H., Jahn, B.-m., Hoang, N., Sasaki, M., Ishikawa, K. i., Kano, H., Hoshi, H., Xenophontos, C., and Wakabayashi, J., 2012, Geochemistry and geochronology of the Troodos ophiolite: An SSZ ophiolite generated by subduction initiation and an extended episode of ridge subduction?: Lithosphere, v. 4, no. 6, p. 497-510.

Ota, T., Utsunomiya, A., Uchio, Y., Isozaki, Y., Buslov, M. M., Ishikawa, A., Maruyama, S., Kitajima, K., Kaneko, Y., Yamamoto, H., and Katayama, I., 2007, Geology of the Gorny Altai subduction–accretion complex, southern Siberia: Tectonic evolution of an Ediacaran–Cambrian intra-oceanic arc-trench system: Journal of Asian Earth Sciences, v. 30, no. 5, p. 666-695.

Pagé, P., Bédard, J. H., Schroetter, J.-M., and Tremblay, A., 2008, Mantle petrology and mineralogy of the Thetford Mines Ophiolite Complex: Lithos, v. 100, no. 1, p. 255-292.

Pagé, P., Bédard, J. H., and Tremblay, A., 2009, Geochemical variations in a depleted fore-arc mantle: The Ordovician Thetford Mines Ophiolite: Lithos, v. 113, no. 1, p. 21-47.

Parkinson, I. J., and Pearce, J. A., 1998, Peridotites from the Izu–Bonin–Mariana Forearc (ODP Leg 125): Evidence for Mantle Melting and Melt–Mantle Interaction in a Supra-Subduction Zone Setting: Journal of Petrology, v. 39, no. 9, p. 1577-1618.

Pearce, J. A., Barker, P., Edwards, S., Parkinson, I. J., and Leat, P., 2000, Geochemistry and tectonic significance of peridotites from the South Sandwich arc–basin system, South Atlantic: Contributions to Mineralogy and Petrology, v. 139, no. 1, p. 36-53.

Pearce, J. A., Stern, R. J., Bloomer, S. H., and Fryer, P., 2005, Geochemical mapping of the Mariana arc-basin system: Implications for the nature and distribution of subduction components: Geochemistry, Geophysics, Geosystems, v. 6, no. 7.

Pirard, C., Hermann, J., and O'Neill, H. S. T. C., 2013, Petrology and Geochemistry of the Crust–Mantle Boundary in a Nascent Arc, Massif du Sud Ophiolite, New Caledonia, SW Pacific: Journal of Petrology, v. 54, no. 9, p. 1759-1792.

Reagan, M. K., Ishizuka, O., Stern, R. J., Kelley, K. A., Ohara, Y., Blichert-Toft, J., Bloomer, S. H., Cash, J., Fryer, P., Hanan, B. B., Hickey-Vargas, R., Ishii, T., Kimura, J.-I., Peate, D. W., Rowe, M. C., and Woods, M., 2010, Fore-arc basalts and subduction initiation in the Izu-Bonin-Mariana system: Geochemistry, Geophysics, Geosystems, v. 11, no. 3.

Salters, V. J. M., and Stracke, A., 2004, Composition of the depleted mantle: Geochemistry, Geophysics, Geosystems, v. 5, no. 5.

Scholpp, J. L., Ryan, J. G., Shervais, J. W., Stremtan, C., Rittner, M., Luna, A., Hill, S. A., Atlas, Z. D., and Mack, B. C., 2022, Petrologic evolution of boninite lavas from the IBM

Fore-arc, IODP Expedition 352: Evidence for open-system processes during early subduction zone magmatism: American Mineralogist, v. 107, no. 4, p. 572-586.

Secchiari, A., Montanini, A., Bosch, D., Macera, P., and Cluzel, D., 2020, Sr, Nd, Pb and trace element systematics of the New Caledonia harzburgites: Tracking source depletion and contamination processes in a SSZ setting: Geoscience Frontiers, v. 11, no. 1, p. 37-55.

Shervais, J. W., Reagan, M. K., Godard, M., Prytulak, J., Ryan, J. G., Pearce, J. A., Almeev, R. R., Li, H., Haugen, E., Chapman, T., Kurz, W., Nelson, W. R., Heaton, D. E., Kirchenbaur, M., Shimizu, K., Sakuyama, T., Vetter, S. K., Li, Y., and Whattam, S., 2021, Magmatic Response to Subduction Initiation, Part II: Boninites and Related Rocks of the Izu-Bonin Arc From IODP Expedition 352: Geochemistry, Geophysics, Geosystems, v. 22, no. 1, p. e2020GC009093.

Shervais, J. W., Reagan, M., Haugen, E., Almeev, R. R., Pearce, J. A., Prytulak, J., Ryan, J. G., Whattam, S. A., Godard, M., Chapman, T., Li, H., Kurz, W., Nelson, W. R., Heaton, D., Kirchenbaur, M., Shimizu, K., Sakuyama, T., Li, Y., and Vetter, S. K., 2019, Magmatic Response to Subduction Initiation: Part 1. Fore-arc Basalts of the Izu-Bonin Arc From IODP Expedition 352: Geochemistry, Geophysics, Geosystems, v. 20, no. 1, p. 314-338.

Shi, R., Yang, J., Xu, Z., and Qi, X., 2008, The Bangong Lake ophiolite (NW Tibet) and its bearing on the tectonic evolution of the Bangong–Nujiang suture zone: Journal of Asian Earth Sciences, v. 32, no. 5, p. 438-457.

Smith, P. M., and Asimow, P. D., 2005, Adiabat_1ph: A new public front-end to the MELTS, pMELTS, and pHMELTS models: Geochemistry, Geophysics, Geosystems, v. 6, no. 2.

Sobolev, A. V., and Danyushevsky, L. V., 1994, Petrology and Geochemistry of Boninites from the North Termination of the Tonga Trench: Constraints on the Generation Conditions of Primary High-Ca Boninite Magmas: Journal of Petrology, v. 35, no. 5, p. 1183-1211.

Song, S., Su, L., Niu, Y., Lai, Y., and Zhang, L., 2009, CH4 inclusions in orogenic harzburgite: Evidence for reduced slab fluids and implication for redox melting in mantle wedge: Geochimica et Cosmochimica Acta, v. 73, no. 6, p. 1737-1754.

Streckeisen, A., 1976, To each plutonic rock its proper name: Earth-Science Reviews, v. 12, no. 1, p. 1-33.

Sun, S. S., and Mcdonough, W. F., 1989, Chemical and isotopic systematics of oceanic basalts: Implications for mantle composition and source processes: Geological Society of London, Special Publication, v. 42, no. 1, p. 313-345.

Syracuse, E. M., van Keken, P. E., and Abers, G. A., 2010, The global range of subduction zone thermal models: Physics of the Earth and Planetary Interiors, v. 183, no. 1, p. 73-90.

Taylor, R. N., Nesbitt, R. W., Vidal, P., Harmon, R. S., Auvray, B., and Croudace, I. W., 1994, Mineralogy, Chemistry, and Genesis of the Boninite Series Volcanics, Chichijima, Bonin Islands, Japan: Journal of Petrology, v. 35, no. 3, p. 577-617.

Tollan, P. M. E., Dale, C., Hermann, J., Davidson, J., and Arculus, R., 2017, Generation and modification of the mantle wedge and lithosphere beneath the West Bismarck island arc: melting, metasomatism and thermal history of peridotite xenoliths from Ritter island: Journal of petrology, v. 58, no. 8, p. 1475-1510.

Ulrich, M., Picard, C., Guillot, S., Chauvel, C., Cluzel, D., and Meffre, S., 2010, Multiple melting stages and refertilization as indicators for ridge to subduction formation: The

New Caledonia ophiolite: Lithos, v. 115, no. 1-4, p. 223-236.

Umino, S., 1986, Magma mixing in boninite sequence of Chichijima, Bonin Islands: Journal of Volcanology and Geothermal Research, v. 29, no. 1, p. 125-157.

Uysal, İ., Ersoy, E. Y., Karslı, O., Dilek, Y., Sadıklar, M. B., Ottley, C. J., Tiepolo, M., and Meisel, T., 2012, Coexistence of abyssal and ultra-depleted SSZ type mantle peridotites in a Neo-Tethyan Ophiolite in SW Turkey: Constraints from mineral composition, whole-rock geochemistry (major–trace–REE–PGE), and Re–Os isotope systematics: Lithos, v. 132-133, p. 50-69.

Uysal, İ., Şen, A. D., Ersoy, E. Y., Dilek, Y., Saka, S., Zaccarini, F., Escayola, M., and Karslı, O., 2014, Geochemical make-up of oceanic peridotites from NW Turkey and the multi-stage melting history of the Tethyan upper mantle: Mineralogy and Petrology, v. 108, no. 1, p. 49-69.

Uysal, I. b. m., Kaliwoda, M., Karsli, O., Tarkian, M., Sadiklar, M. B., and Ottley, C. J., 2007, Compositional variations as a result of partial melting and melt-peridotite interaction in an upper mantle section from the Ortaca area, southwestern Turkey: The Canadian Mineralogist, v. 45, no. 6, p. 1471-1493.

Van der Laan, S. R., Arculus, R., Pearce, J., Murton, B., and Fryer, P., Petrography, mineral chemistry, and phase relations of the basement boninite series of Site 786, Izu-Bonin forearc, in Proceedings Proceedings of the ocean drilling program, scientific results1992, Volume 125, College Station: Texas, p. 171-201.

Walter, M. J., 1998, Melting of Garnet Peridotite and the Origin of Komatiite and Depleted Lithosphere: Journal of Petrology, v. 39, no. 1, p. 29-60.

Warren, J. M., 2016, Global variations in abyssal peridotite compositions: Lithos, v. 248-251, p. 193-219.

Whattam, S. A., Shervais, J. W., Reagan, M. K., Coulthard, D. A., Pearce, J. A., Jones, P., Seo, J., Putirka, K., Chapman, T., Heaton, D., Li, H., Nelson, W. R., Shimizu, K., and Stern, R. J., 2020, Mineral compositions and thermobarometry of basalts and boninites recovered during IODP Expedition 352 to the Bonin forearc, v. 105, no. 10, p. 1490-1507.

Woodland, S. J., Pearson, D. G., and Thirlwall, M. F., 2002, A Platinum Group Element and Re–Os Isotope Investigation of Siderophile Element Recycling in Subduction Zones: Comparison of Grenada, Lesser Antilles Arc, and the Izu–Bonin Arc: Journal of Petrology, v. 43, no. 1, p. 171-198.

Xiong, F., Yang, J., Robinson, P. T., Dilek, Y., Milushi, I., Xu, X., Chen, Y., Zhou, W., Zhang, Z., Lai, S., Tian, Y., and Huang, Z., 2015, Petrology and geochemistry of high Cr# podiform chromitites of Bulqiza, Eastern Mirdita Ophiolite (EMO), Albania: Ore Geology Reviews, v. 70, p. 188-207.

Xiong, F., Yang, J., Robinson, P. T., Xu, X., Liu, Z., Zhou, W., Feng, G., Xu, J., Li, J., and Niu, X., 2017, High-Al and high-Cr podiform chromitites from the western Yarlung-Zangbo suture zone, Tibet: Implications from mineralogy and geochemistry of chromian spinel, and platinum-group elements: Ore Geology Reviews, v. 80, p. 1020-1041.

Xiong, Q., Griffin, W. L., Zheng, J.-P., O'Reilly, S. Y., Pearson, N. J., Xu, B., and Belousova, E. A., 2016, Southward trench migration at ~130–120 Ma caused accretion of the Neo-Tethyan forearc lithosphere in Tibetan ophiolites: Earth and Planetary Science Letters, v. 438, p. 57-65.

Yajima, K., and Fujimaki, H., 2008, High-Ca and low-Ca boninites from Chichijima, Bonin (Ogasawara) archipelago: Japanese Magazine of Mineralogical and Petrological Sciences, v. 30, p. 217-236.

Zhang, P.-F., Zhou, M.-F., and Yumul, G. P., 2020, Coexistence of high-Al and high-Cr chromite orebodies in the Acoje block of the Zambales ophiolite, Philippines: Evidence for subduction initiation: Ore Geology Reviews, v. 126, p. 103739.

Zhou, X., Zheng, J., Li, Y., Zhu, H., Griffin, W. L., and O'Reilly, S. Y., 2021, Melt Migration and Interaction in a Dunite Channel System within Oceanic Forearc Mantle: the Yushigou Harzburgite–Dunite Associations, North Qilian Ophiolite (NW China): Journal of Petrology, v. 62, no. 7, p. egaa115.

Zou, H., and Reid, M. R., 2001, Quantitative modeling of trace element fractionation during incongruent dynamic melting: Geochimica et Cosmochimica Acta, v. 65, no. 1, p. 153-162.

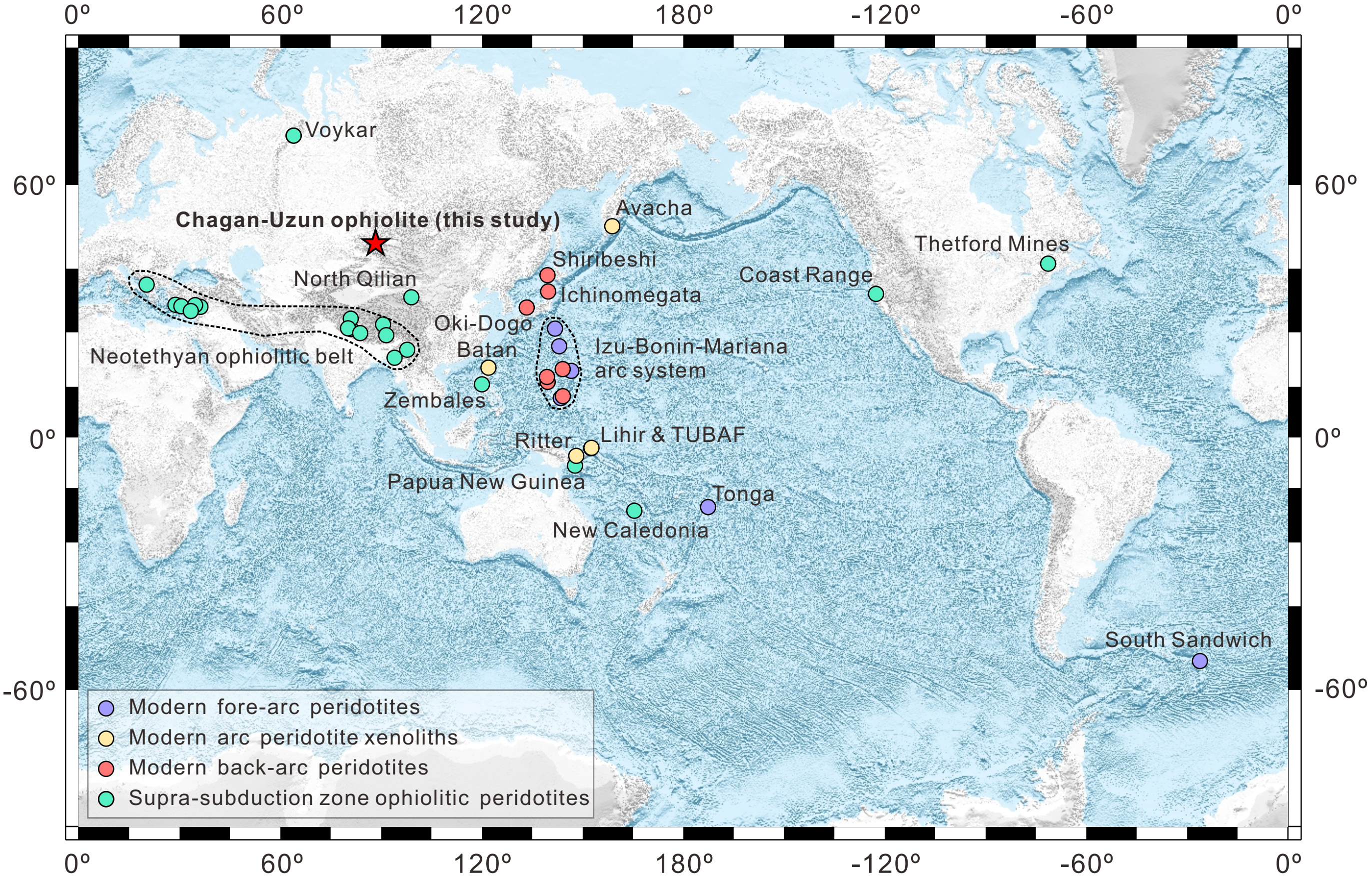
0º
60º
120º
180º
-120º
-60º
0º
60º
0º
-60º
Voykar
Chagan-Uzun ophiolite (this study)
Avacha
Thetford Mines
Shiribeshi
Coast Range
North Qilian
Ichinomegata
Oki-Dogo
Batan
Izu-Bonin-Mariana
arc system
Neotethyan ophiolitic belt
Zembales
Ritter
Lihir & TUBAF
Papua New Guinea
Tonga
New Caledonia
South Sandwich
Modern fore-arc peridotites
Modern arc peridotite xenoliths
Modern back-arc peridotites
Supra-subduction zone ophiolitic peridotites

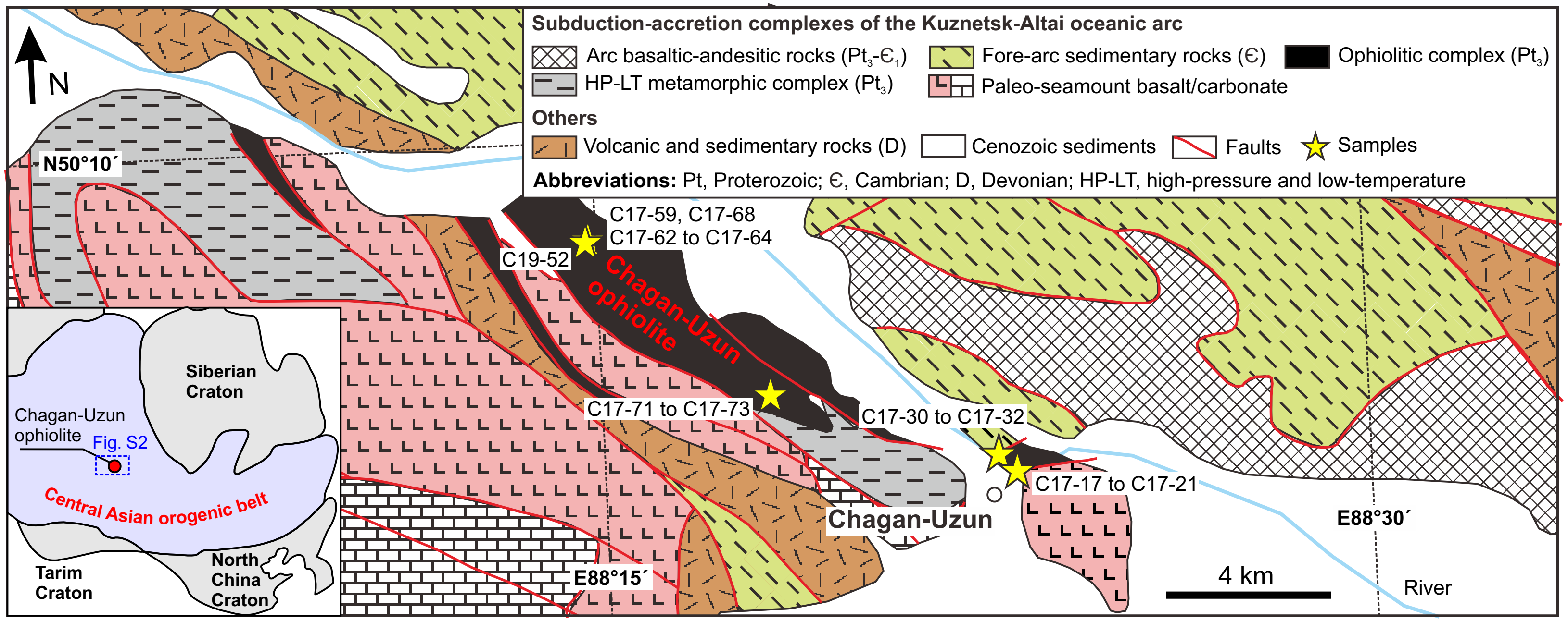

N
N50°10´
Subduction-accretion complexes of the Kuznetsk-Altai oceanic arc
Arc basaltic-andesitic rocks (Pt3-Є1)
Fore-arc sedimentary rocks (Є)
Ophiolitic complex (Pt3)
HP-LT metamorphic complex (Pt3)
Paleo-seamount basalt/carbonate
Others
Volcanic and sedimentary rocks (D)
Cenozoic sediments
Faults
Samples
Abbreviations: Pt, Proterozoic; Є, Cambrian; D, Devonian; HP-LT, high-pressure and low-temperature
C17-59, C17-68
C17-62 to C17-64
C19-52
Chagan-Uzun ophiolite
C17-71 to C17-73
C17-30 to C17-32
C17-17 to C17-21
Chagan-Uzun
E88°15´
E88°30´
4 km
River
Siberian Craton
Chagan-Uzun ophiolite
Fig. S2
Central Asian orogenic belt
Tarim Craton
North China Craton

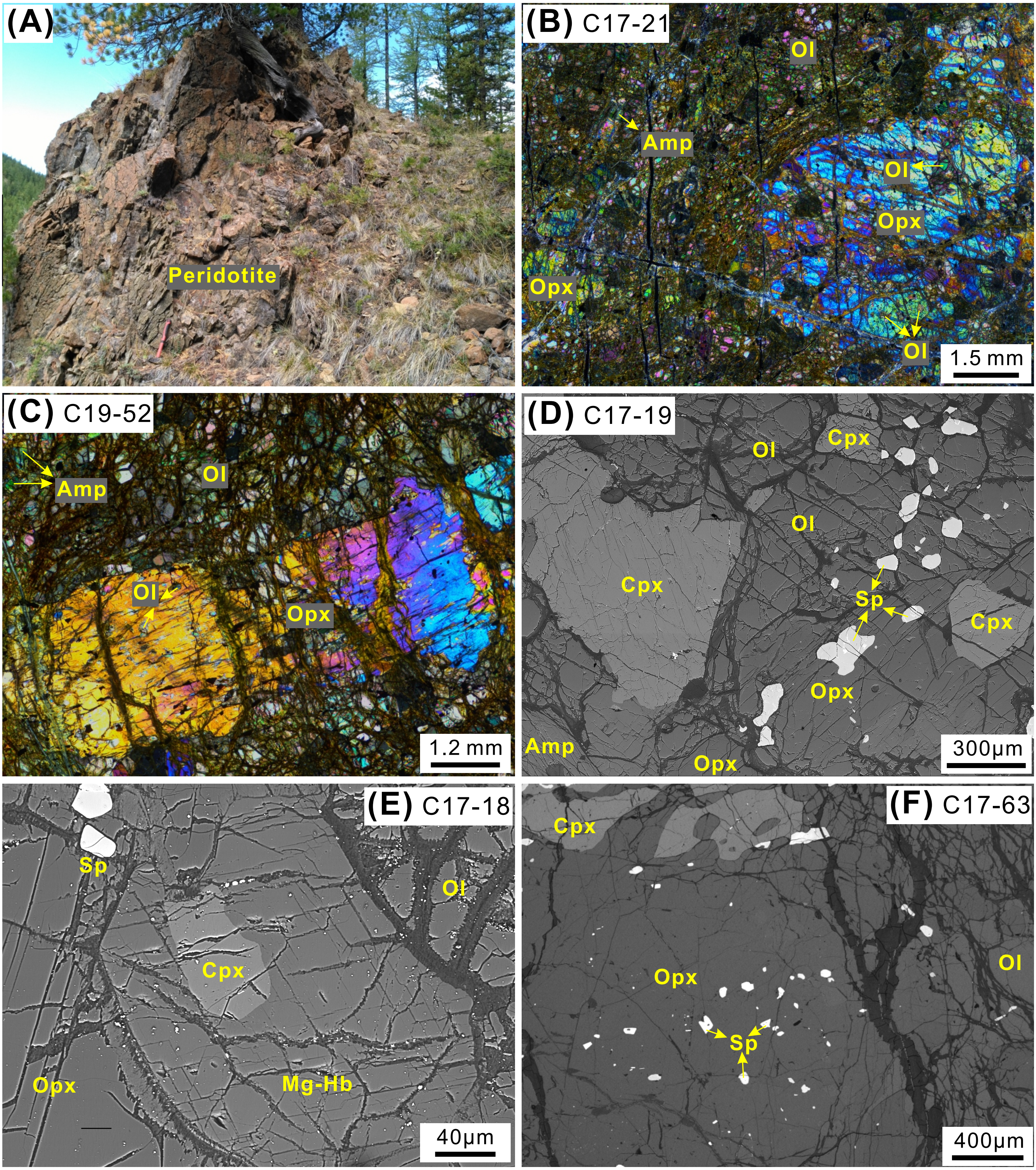

(A)
Peridotite
(B) C17-21
Ol
Amp
Ol
Opx
Opx
Ol
1.5 mm
(C) C19-52
Amp
Ol
Ol
Opx
1.2 mm
(D) C17-19
Ol
Cpx
Ol
Cpx
Sp
Cpx
Opx
Amp
Opx
300μm
(E) C17-18
Sp
Ol
Cpx
Opx
Mg-Hb
40μm
(F) C17-63
Cpx
Ol
Opx
Sp
400μm

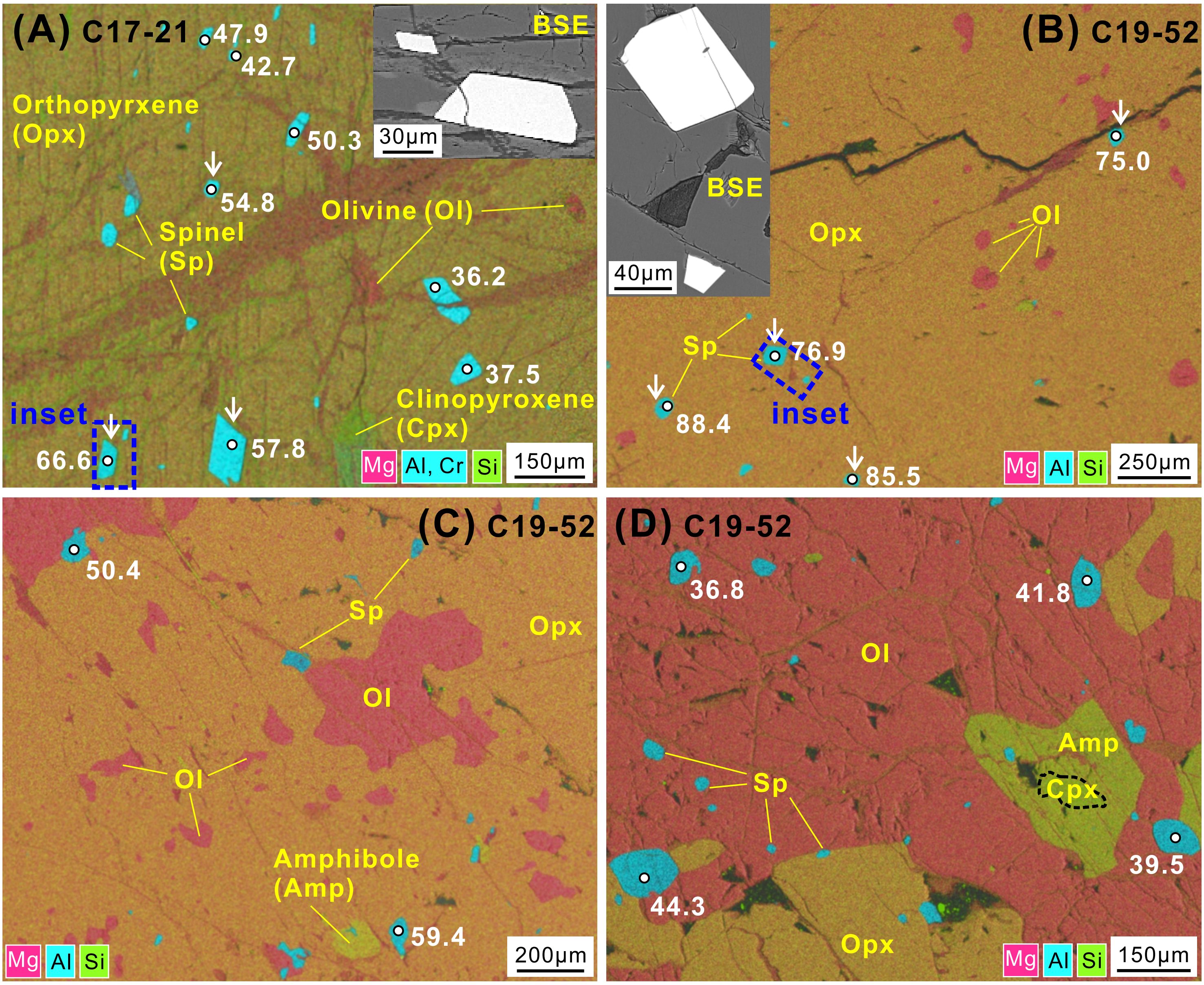

(A) C17-21
47.9
42.7
50.3
54.8
36.2
37.5
57.8
66.6
Orthopyrxene (Opx)
Spinel (Sp)
Olivine (Ol)
Clinopyroxene (Cpx)
inset
BSE
30μm
Mg
Al, Cr
Si
150μm
(B) C19-52
BSE
40μm
75.0
Opx
Ol
Sp
76.9
88.4
85.5
inset
Mg
Al
Si
250μm
(C) C19-52
50.4
Sp
Opx
Ol
Ol
Amphibole (Amp)
59.4
Mg
Al
Si
200μm
(D) C19-52
36.8
41.8
Ol
Amp
Cpx
Sp
39.5
44.3
Opx
Mg
Al
Si
150μm

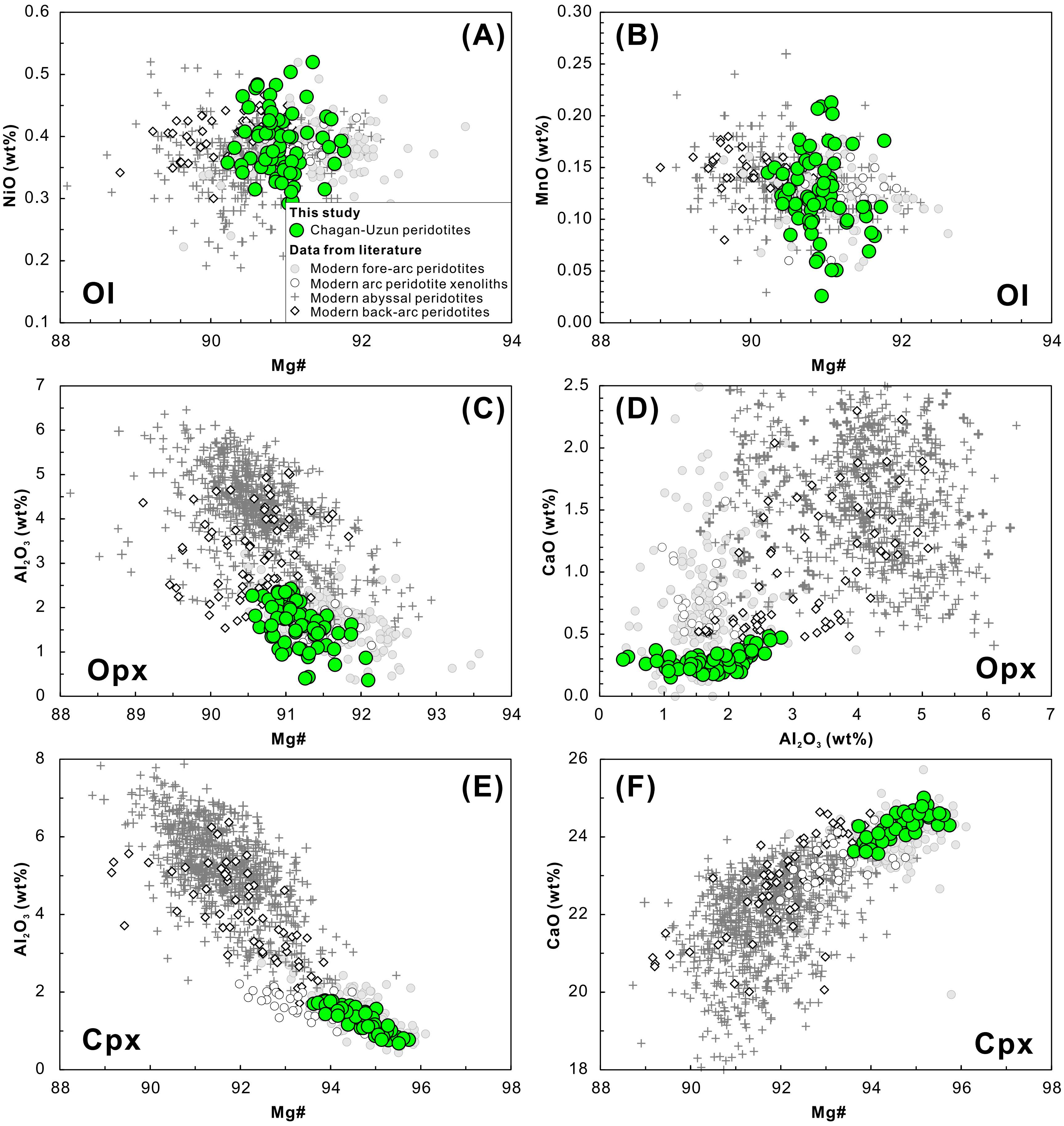

(A)
Ol
NiO (wt%)
Mg#
This study
Chagan-Uzun peridotites
Data from literature
Modern fore-arc peridotites
Modern arc peridotite xenoliths
Modern abyssal peridotites
Modern back-arc peridotites
(B)
Ol
MnO (wt%)
Mg#
(C)
Opx
Al_2O_3 (wt%)
Mg#
(D)
Opx
CaO (wt%)
Al_2O_3 (wt%)
(E)
Cpx
Al_2O_3 (wt%)
Mg#
(F)
Cpx
CaO (wt%)
Mg#

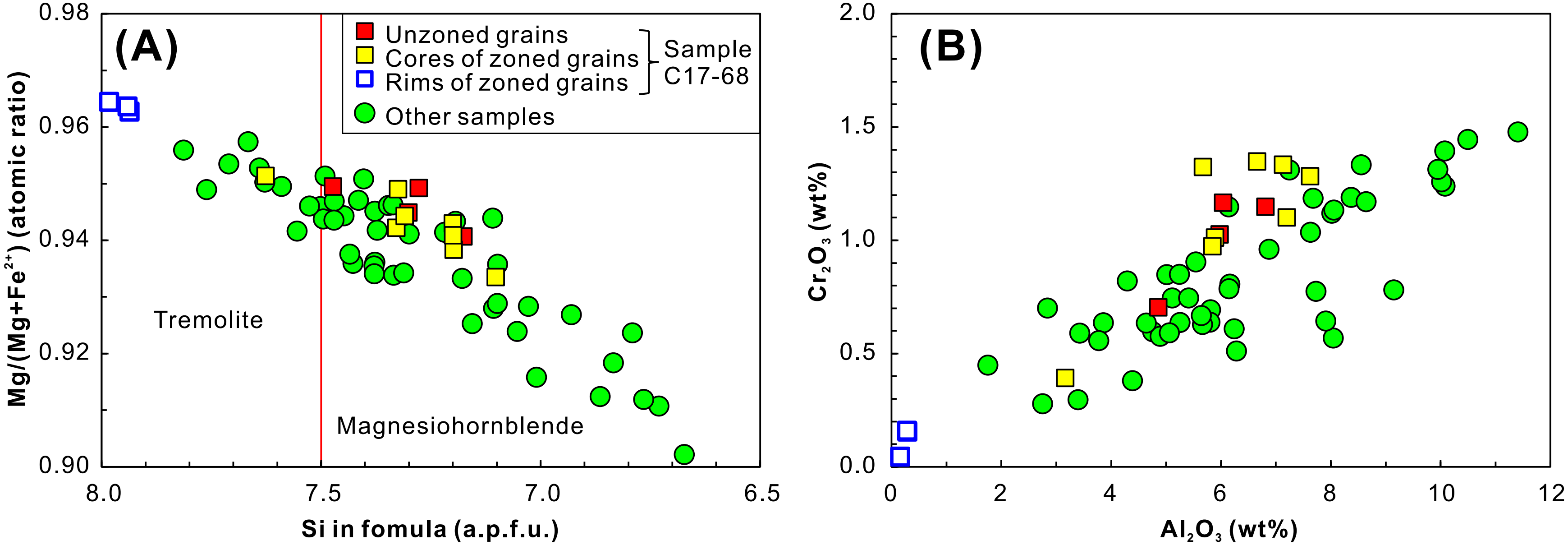
(A)
Unzoned grains
Cores of zoned grains
Rims of zoned grains
Sample C17-68
Other samples
Tremolite
Magnesiohornblende
Mg/(Mg+Fe2+) (atomic ratio)
Si in fomula (a.p.f.u.)
0.98
0.96
0.94
0.92
0.90
8.0
7.5
7.0
6.5
(B)
Cr2O3 (wt%)
Al2O3 (wt%)
2.0
1.5
1.0
0.5
0.0
0
2
4
6
8
10
12

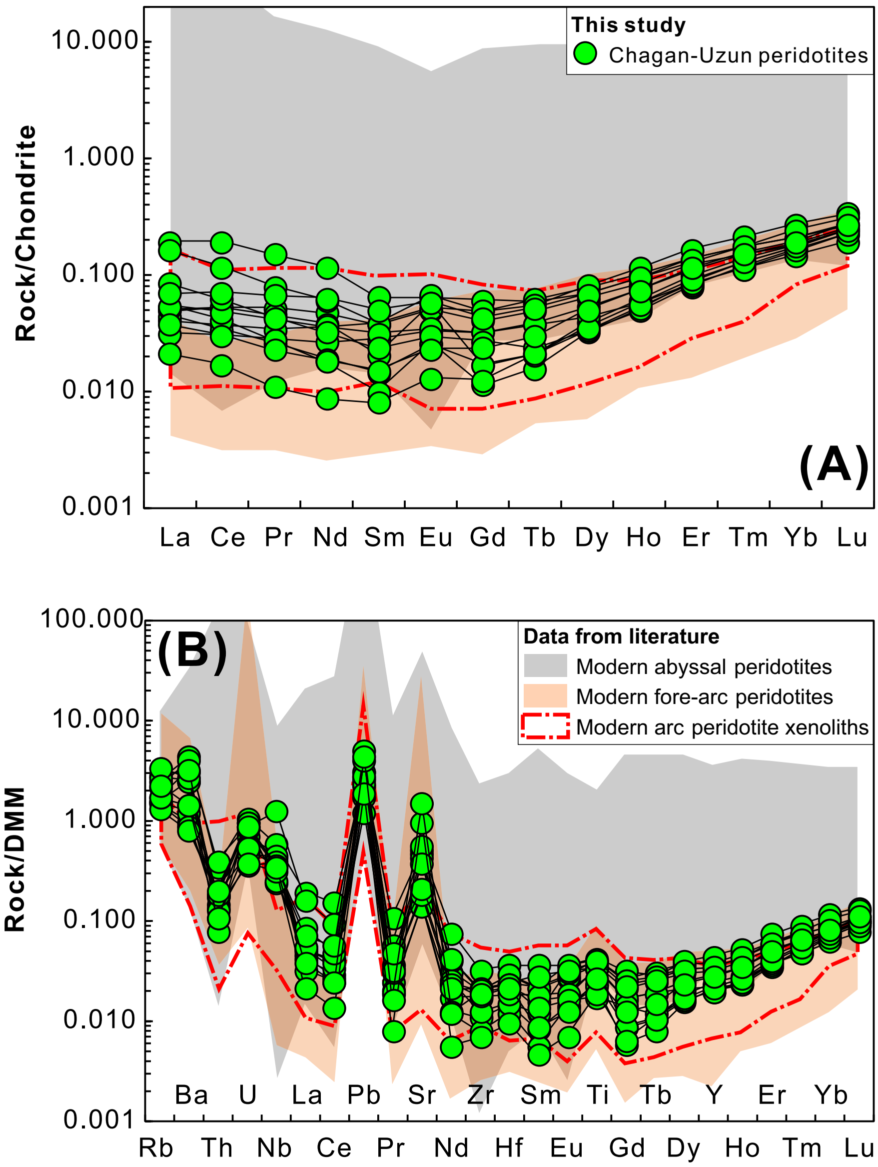

This study
Chagan-Uzun peridotites
Rock/Chondrite
10.000
1.000
0.100
0.010
0.001
(A)
La Ce Pr Nd Sm Eu Gd Tb Dy Ho Er Tm Yb Lu
(B)
100.000
10.000
1.000
0.100
0.010
0.001
Rock/DMM
Data from literature
Modern abyssal peridotites
Modern fore-arc peridotites
Modern arc peridotite xenoliths
Ba U La Pb Sr Zr Sm Ti Tb Y Er Yb
Rb Th Nb Ce Pr Nd Hf Eu Gd Dy Ho Tm Lu

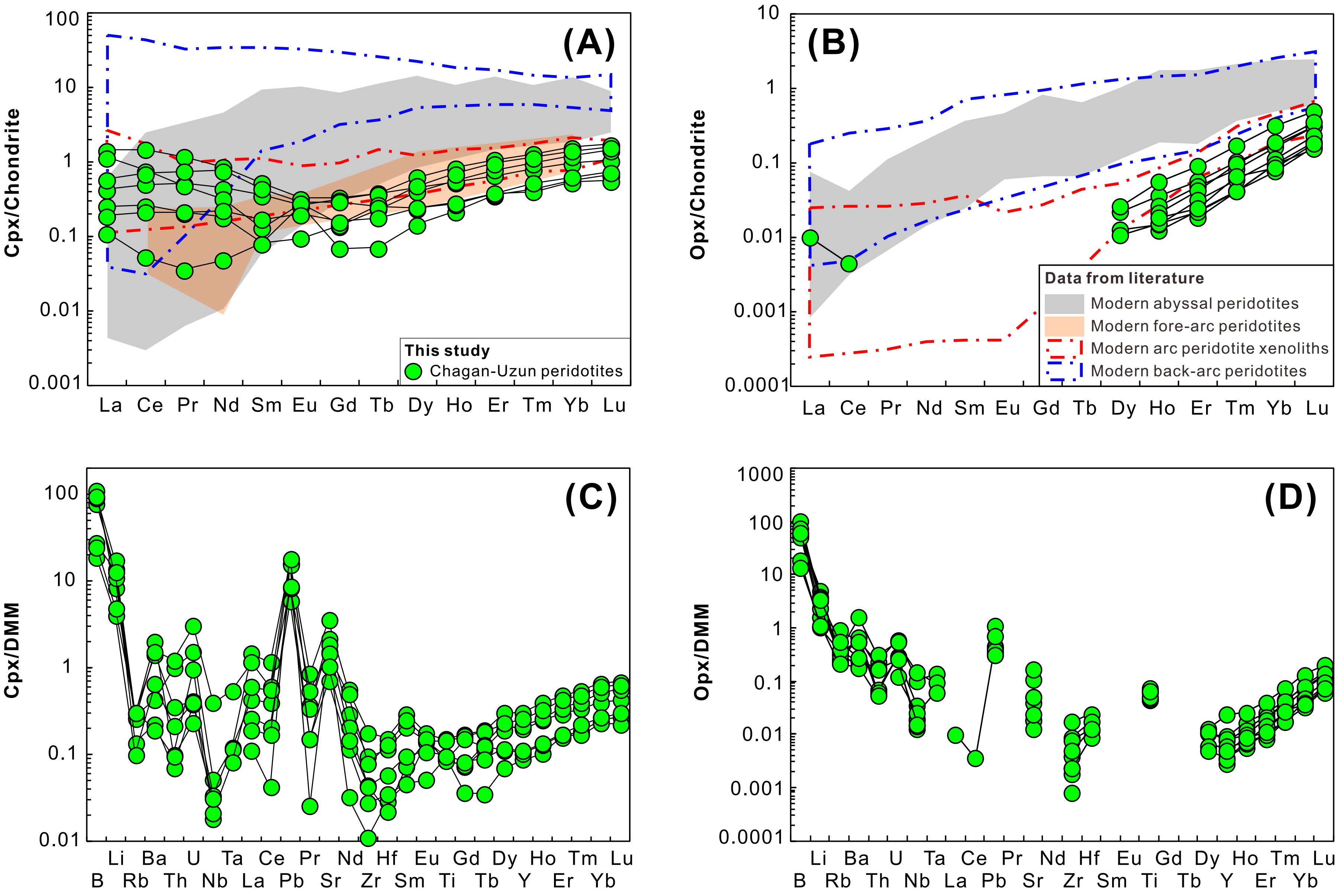
(A)
Cpx/Chondrite
100
10
1
0.1
0.01
0.001
La Ce Pr Nd Sm Eu Gd Tb Dy Ho Er Tm Yb Lu
This study
Chagan-Uzun peridotites
(B)
Opx/Chondrite
10
1
0.1
0.01
0.001
0.0001
La Ce Pr Nd Sm Eu Gd Tb Dy Ho Er Tm Yb Lu
Data from literature
Modern abyssal peridotites
Modern fore-arc peridotites
Modern arc peridotite xenoliths
Modern back-arc peridotites
(C)
Cpx/DMM
100
10
1
0.1
0.01
Li Ba U Ta Ce Pr Nd Hf Eu Gd Dy Ho Tm Lu
B Rb Th Nb La Pb Sr Zr Sm Ti Tb Y Er Yb
(D)
Opx/DMM
1000
100
10
1
0.1
0.01
0.001
0.0001
Li Ba U Ta Ce Pr Nd Hf Eu Gd Dy Ho Tm Lu
B Rb Th Nb La Pb Sr Zr Sm Ti Tb Y Er Yb

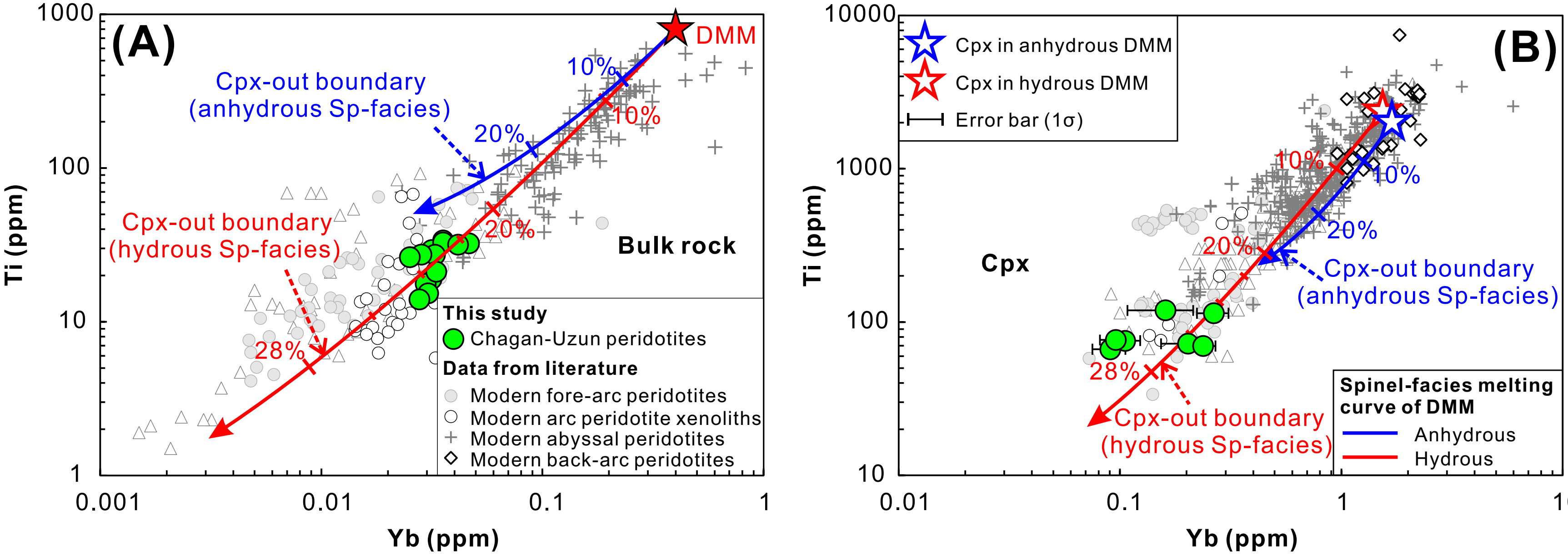

(A)
DMM
Cpx-out boundary
(anhydrous Sp-facies)
10%
20%
10%
20%
Cpx-out boundary
(hydrous Sp-facies)
28%
Bulk rock
This study
Chagan-Uzun peridotites
Data from literature
Modern fore-arc peridotites
Modern arc peridotite xenoliths
Modern abyssal peridotites
Modern back-arc peridotites
Ti (ppm)
Yb (ppm)
1000
100
10
1
0.001
0.01
0.1
1
(B)
Cpx in anhydrous DMM
Cpx in hydrous DMM
Error bar (1σ)
Cpx
10%
10%
20%
20%
Cpx-out boundary
(anhydrous Sp-facies)
28%
Cpx-out boundary
(hydrous Sp-facies)
Spinel-facies melting curve of DMM
Anhydrous
Hydrous
Ti (ppm)
Yb (ppm)
10000
1000
100
10
0.01
0.1
1
10

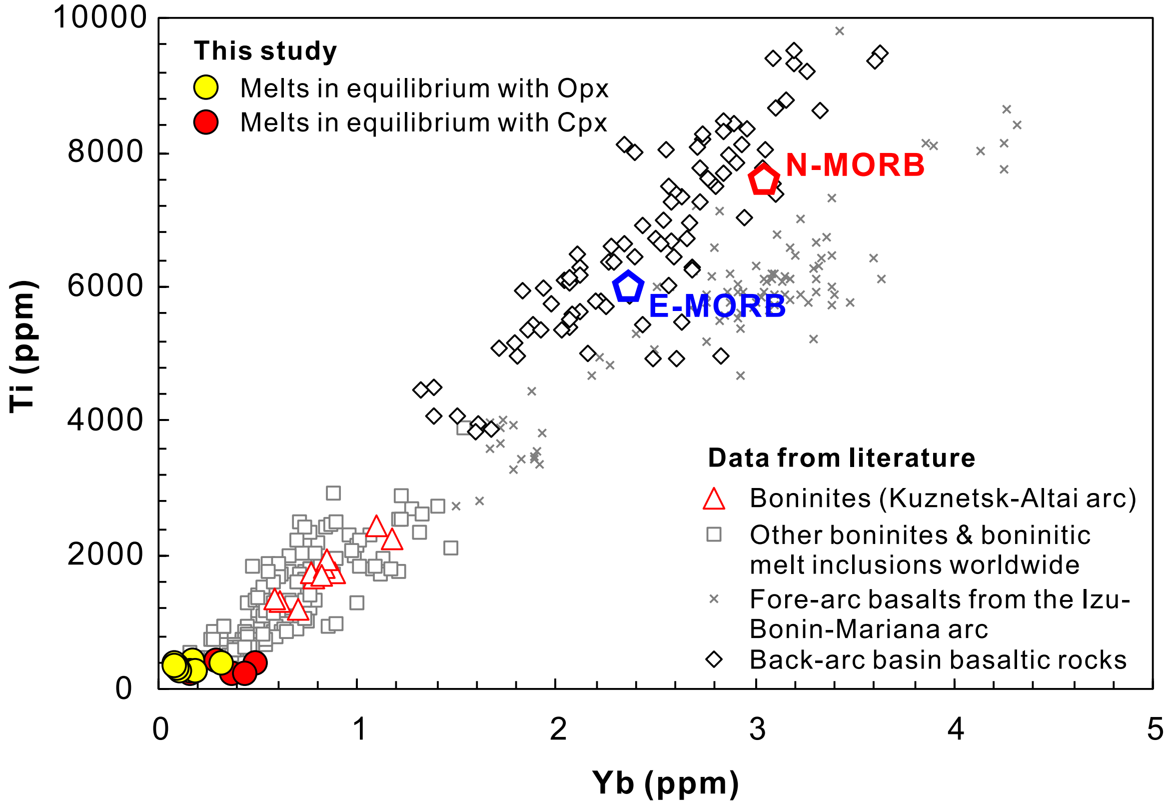

This study
Melts in equilibrium with Opx
Melts in equilibrium with Cpx
N-MORB
E-MORB
Data from literature
Boninites (Kuznetsk-Altai arc)
Other boninites & boninitic melt inclusions worldwide
Fore-arc basalts from the Izu-Bonin-Mariana arc
Back-arc basin basaltic rocks
Ti (ppm)
Yb (ppm)
0
2000
4000
6000
8000
10000
0
1
2
3
4
5

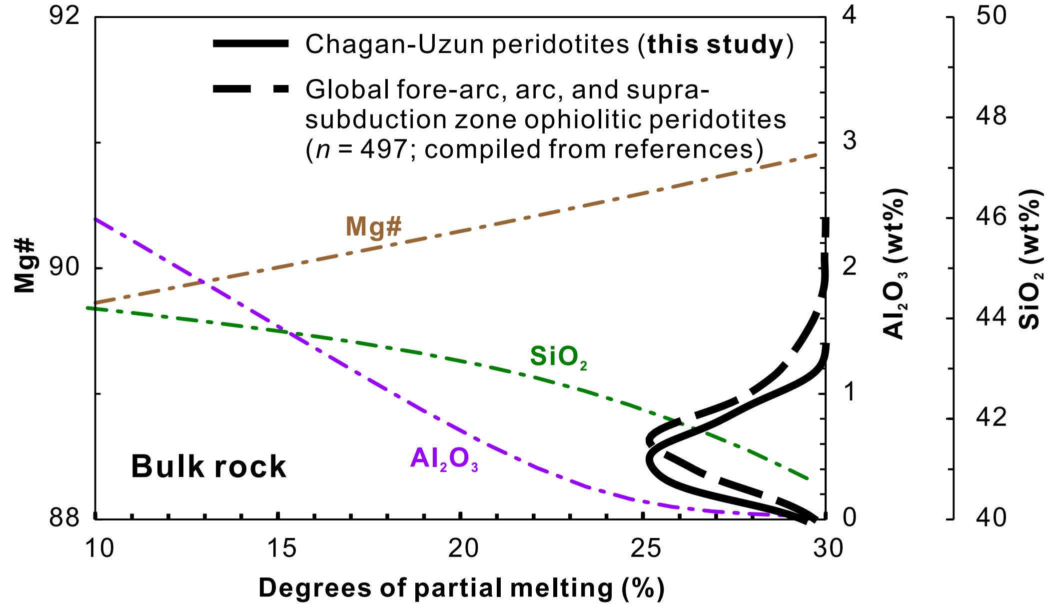

Chagan-Uzun peridotites (**this study**)
Global fore-arc, arc, and supra-subduction zone ophiolitic peridotites (*n* = 497; compiled from references)
Mg#
SiO_2
Al_2O_3
Bulk rock
Degrees of partial melting (%)
Al_2O_3 (wt%)
SiO_2 (wt%)

Description of Additional Supplementary Files:

Supplementary Table S1: Summary of locations and petrological data of peridotites from the Chagan-Uzun ophiolite

Supplementary Table S2: Bulk-rock major-element compositions (wt%) of peridotites from the Chagan-Uzun ophiolite

Supplementary Table S3: Trace-element compositions (ppm) of peridotites from the Chagan-Uzun ophiolite

Supplementary Table S4: Mineral major-element compositions (wt%) of peridotites from the Chagan-Uzun ophiolite

Supplementary Table S5: Clinopyroxene and orthopyroxene trace-element compositions (ppm) of peridotites from the Chagan-Uzun ophiolite

Supplementary Table S6: The pressure-temperature conditions and compositions of starting materials used in the modeling of hydrous fluxing melting and peridotite-melt interaction

Supplementary Table S7: Modeling results of isothermal fluxing melting and isenthalpic boninitic melt percolation

Sample C17-17

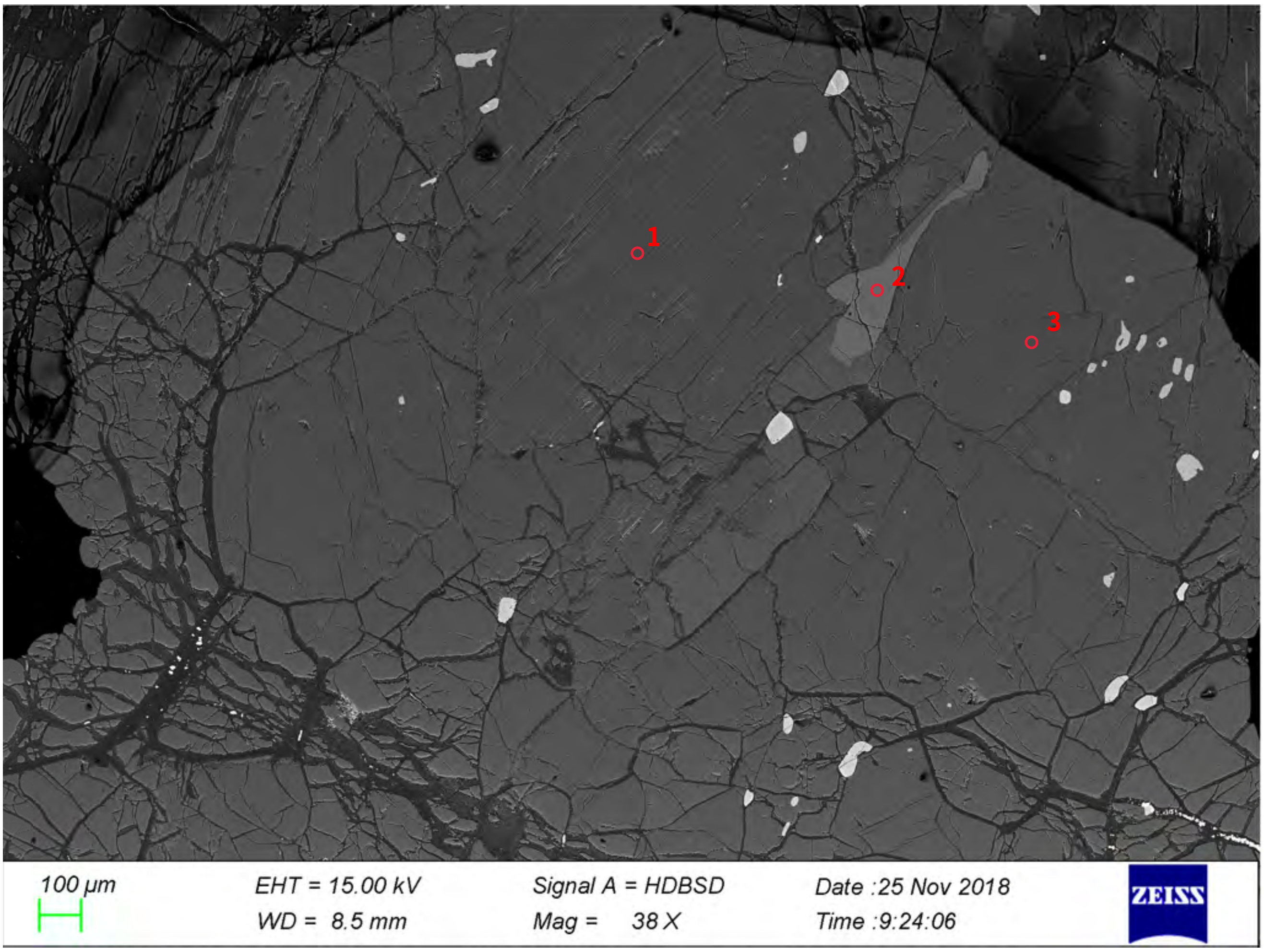

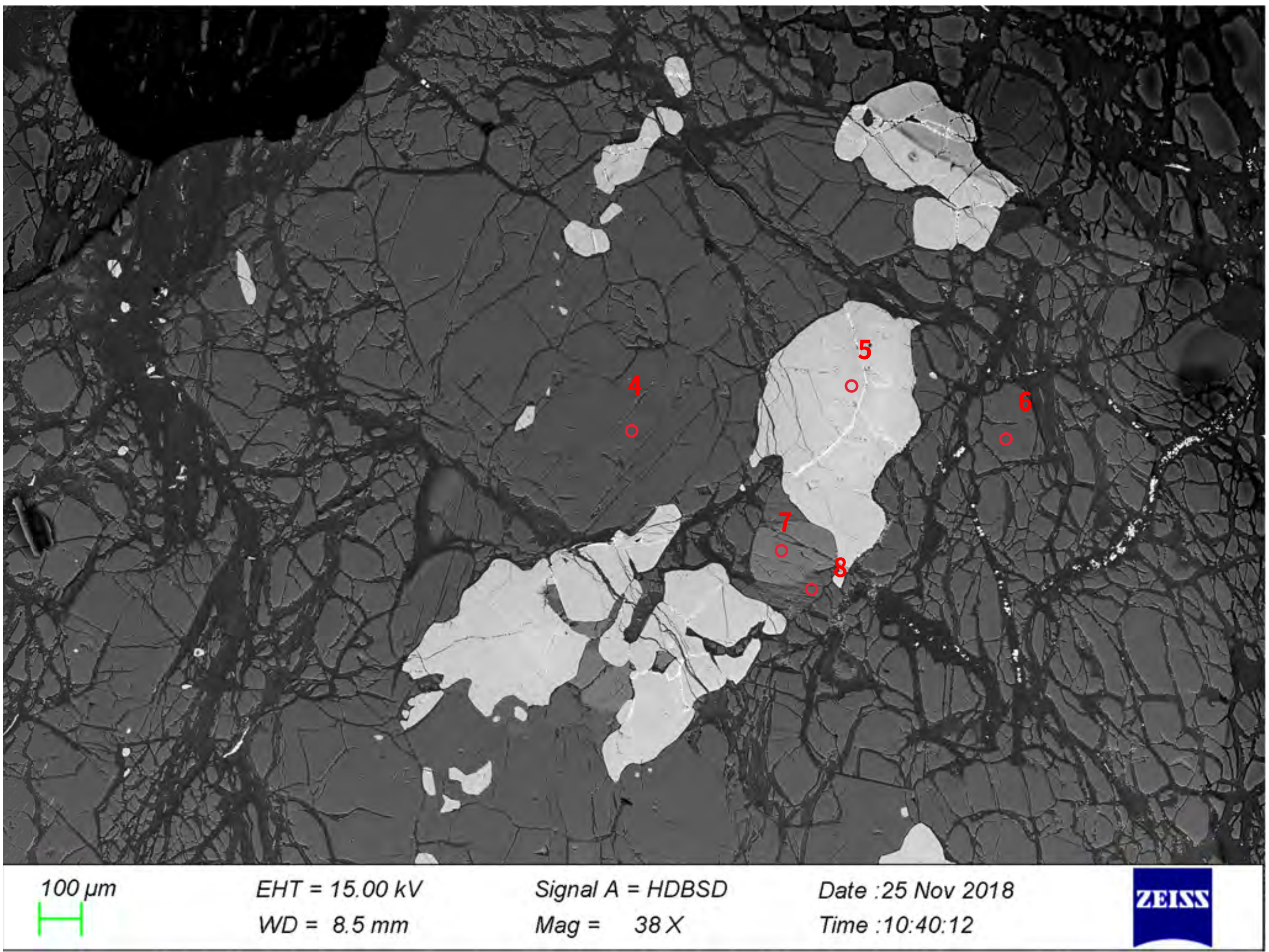

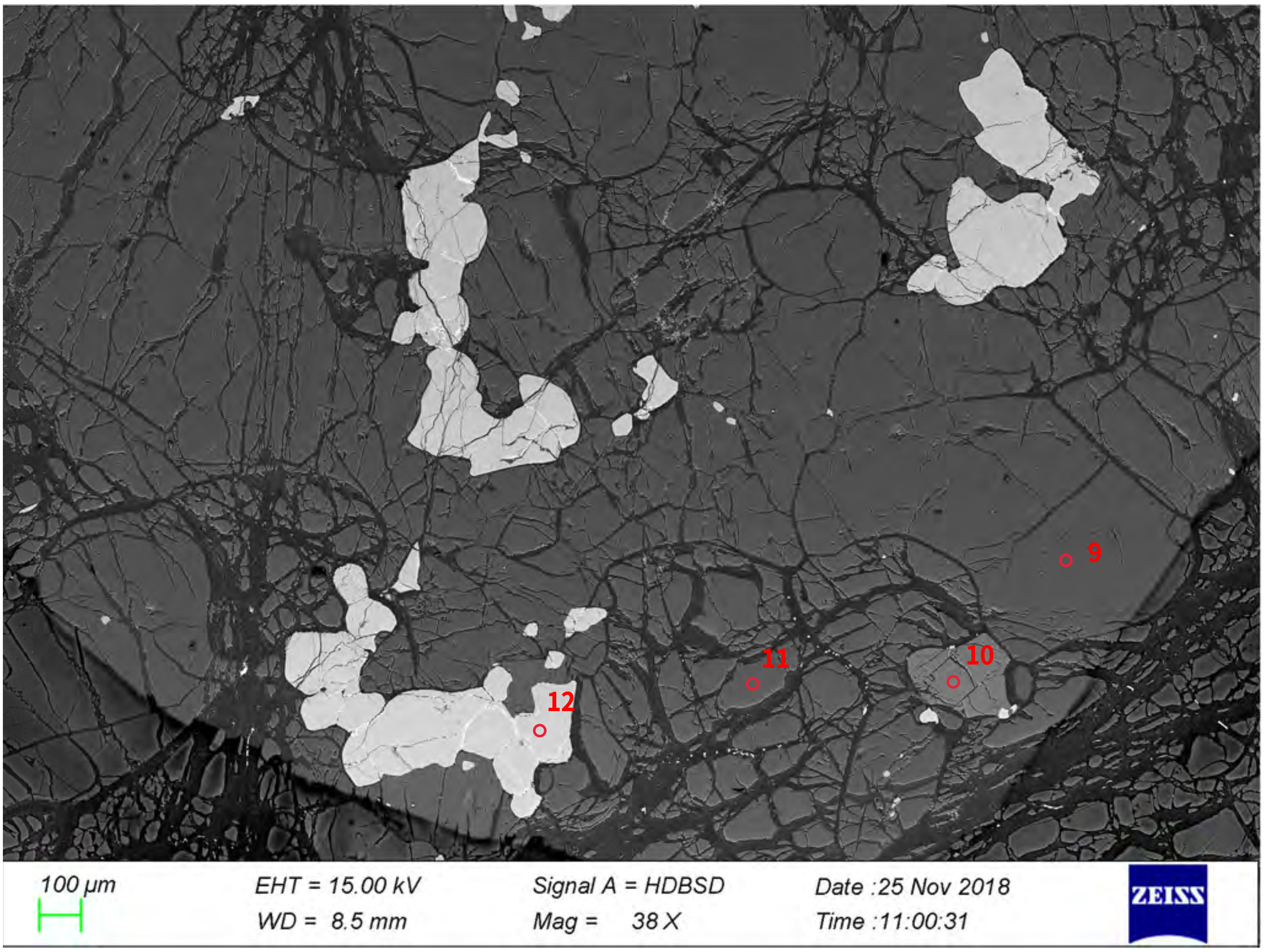
9
10
11
12
100 µm
EHT = 15.00 kV
WD = 8.5 mm
Signal A = HDBSD
Mag = 38 X
Date :25 Nov 2018
Time :11:00:31
ZEISS

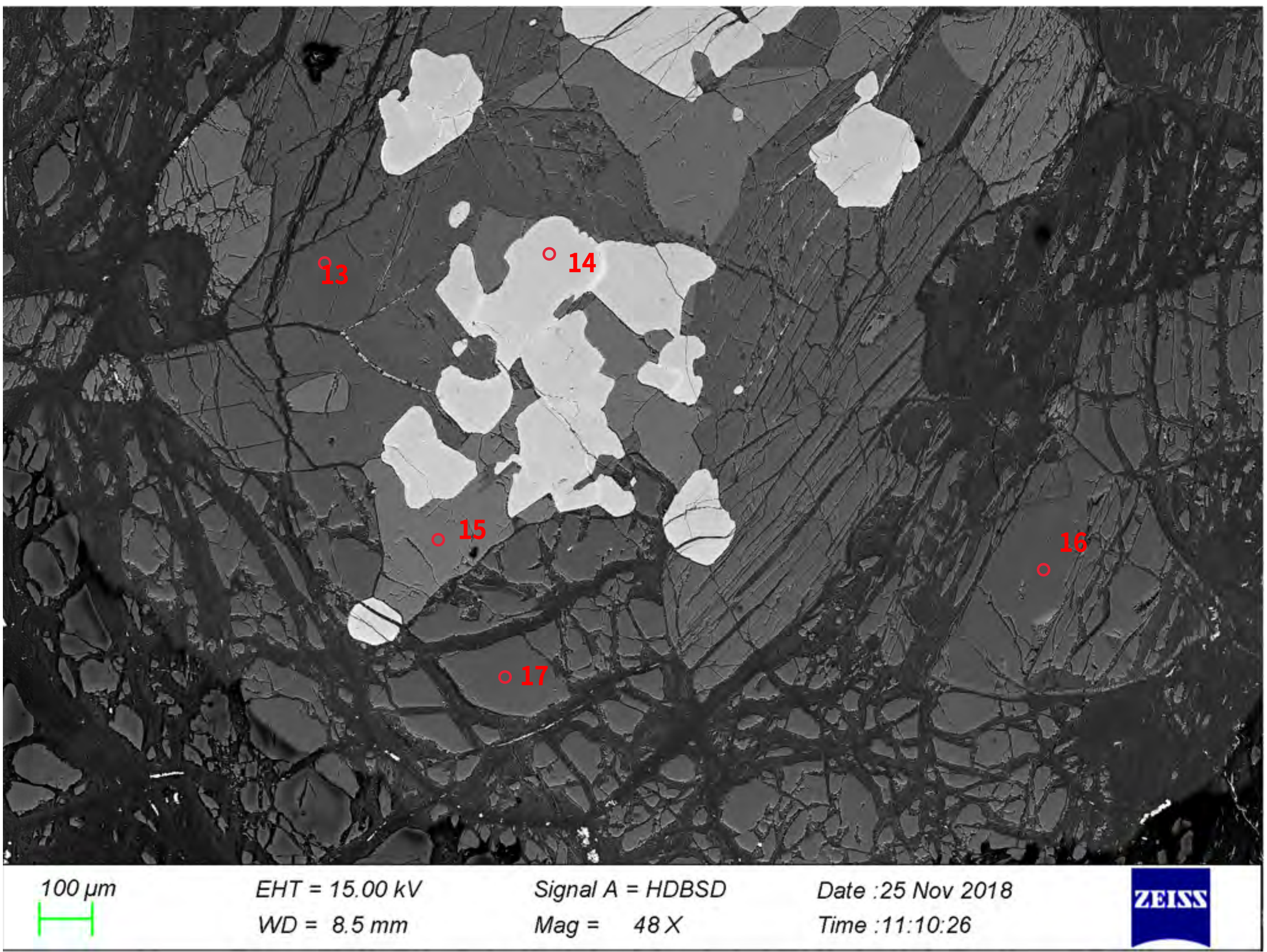
13
14
15
16
17
100 µm
EHT = 15.00 kV
WD = 8.5 mm
Signal A = HDBSD
Mag = 48 X
Date :25 Nov 2018
Time :11:10:26
ZEISS

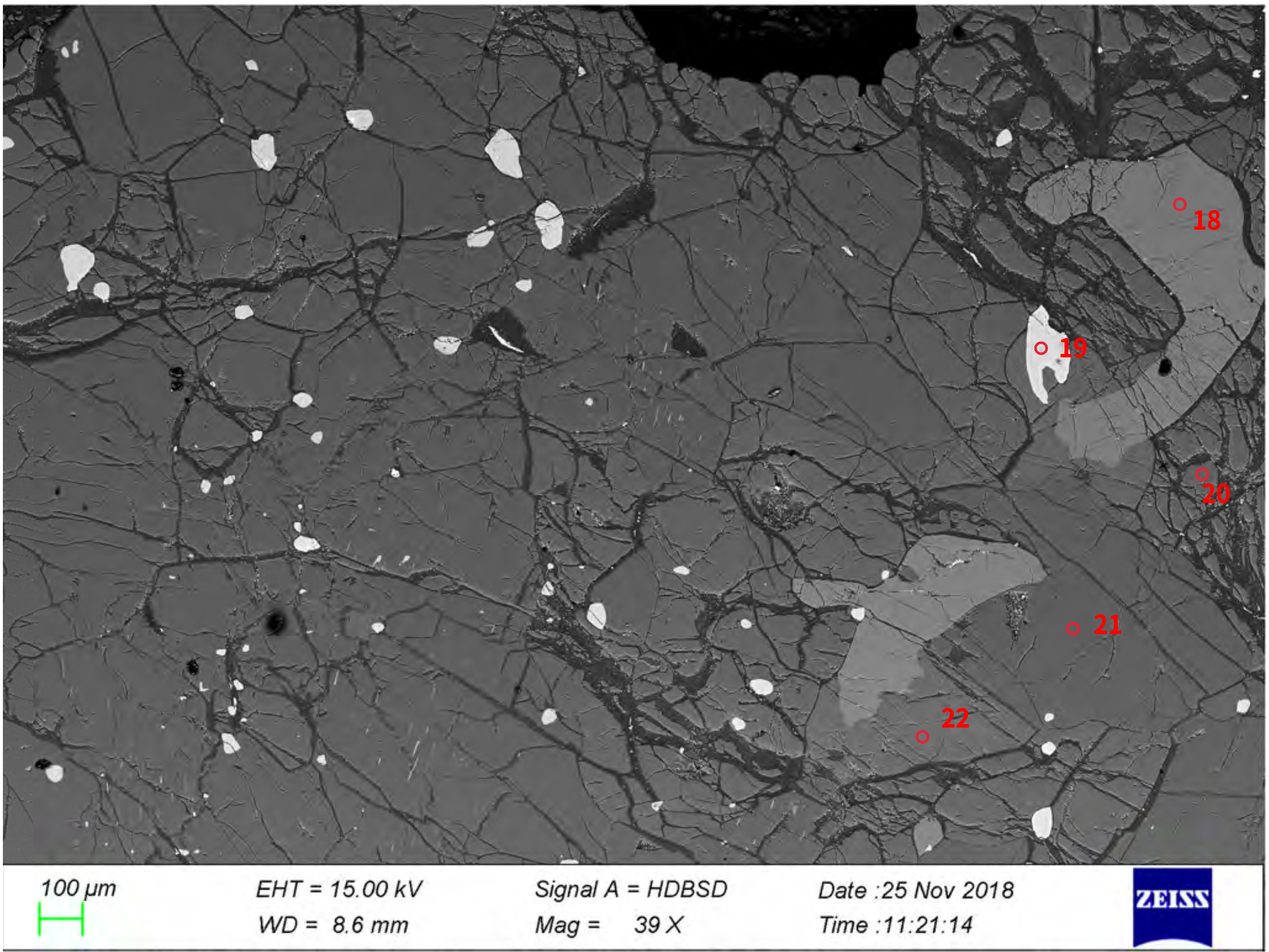
18
19
20
21
22
100 µm
EHT = 15.00 kV
WD = 8.6 mm
Signal A = HDBSD
Mag = 39 X
Date :25 Nov 2018
Time :11:21:14
ZEISS

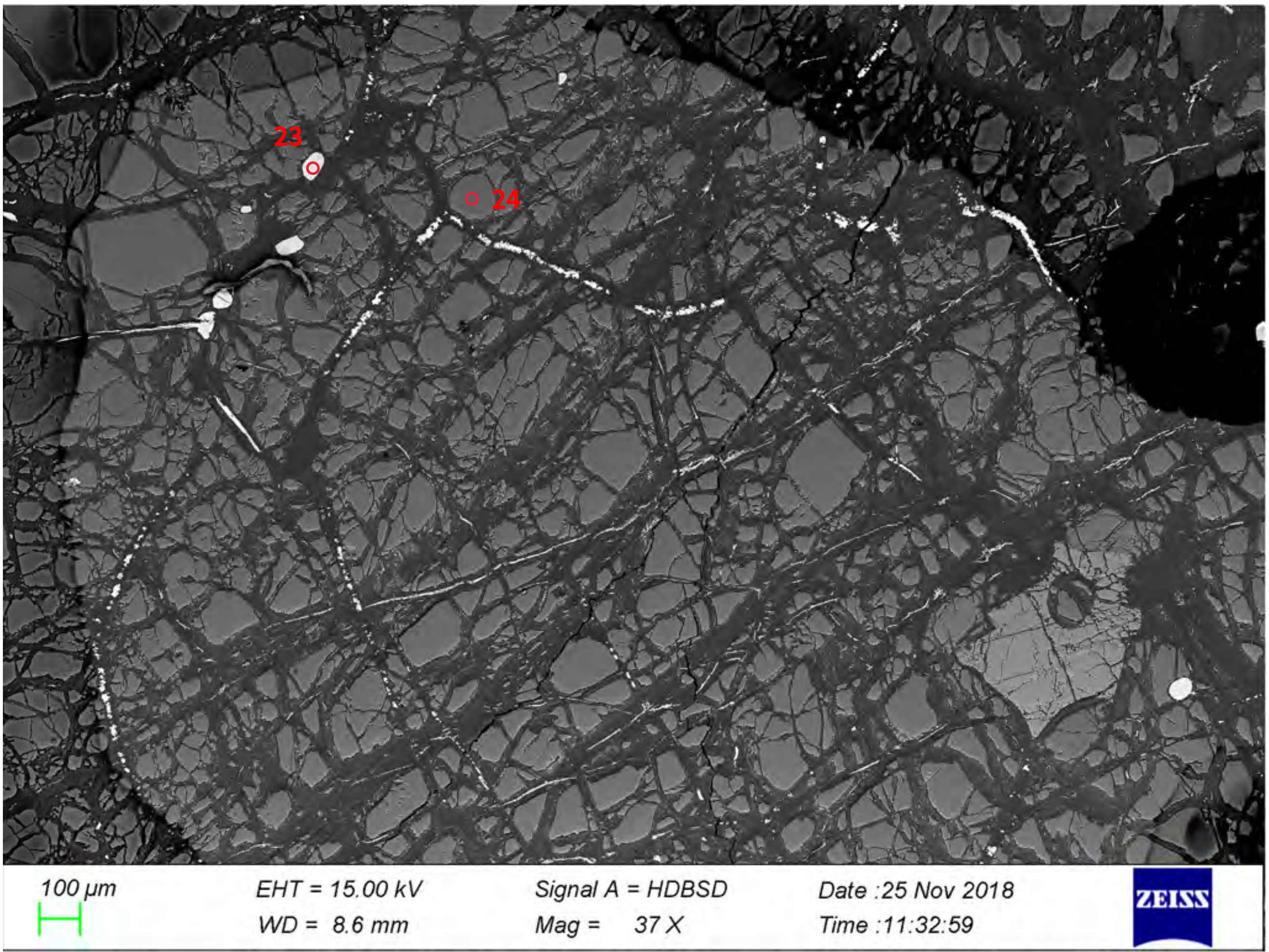
23
24
100 µm
EHT = 15.00 kV
WD = 8.6 mm
Signal A = HDBSD
Mag = 37 X
Date :25 Nov 2018
Time :11:32:59
ZEISS

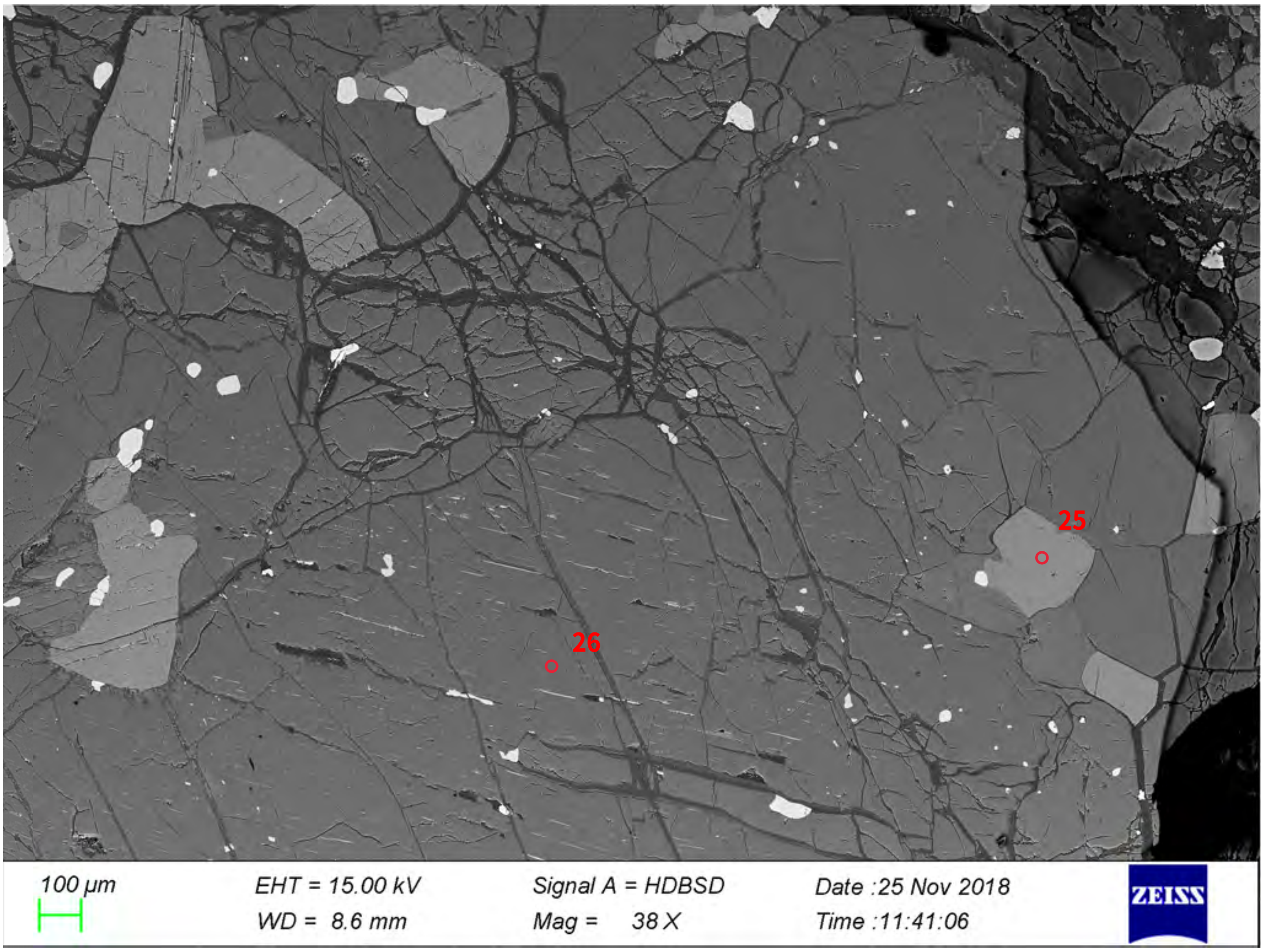
25
26
100 µm
EHT = 15.00 kV
WD = 8.6 mm
Signal A = HDBSD
Mag = 38 X
Date :25 Nov 2018
Time :11:41:06
ZEISS

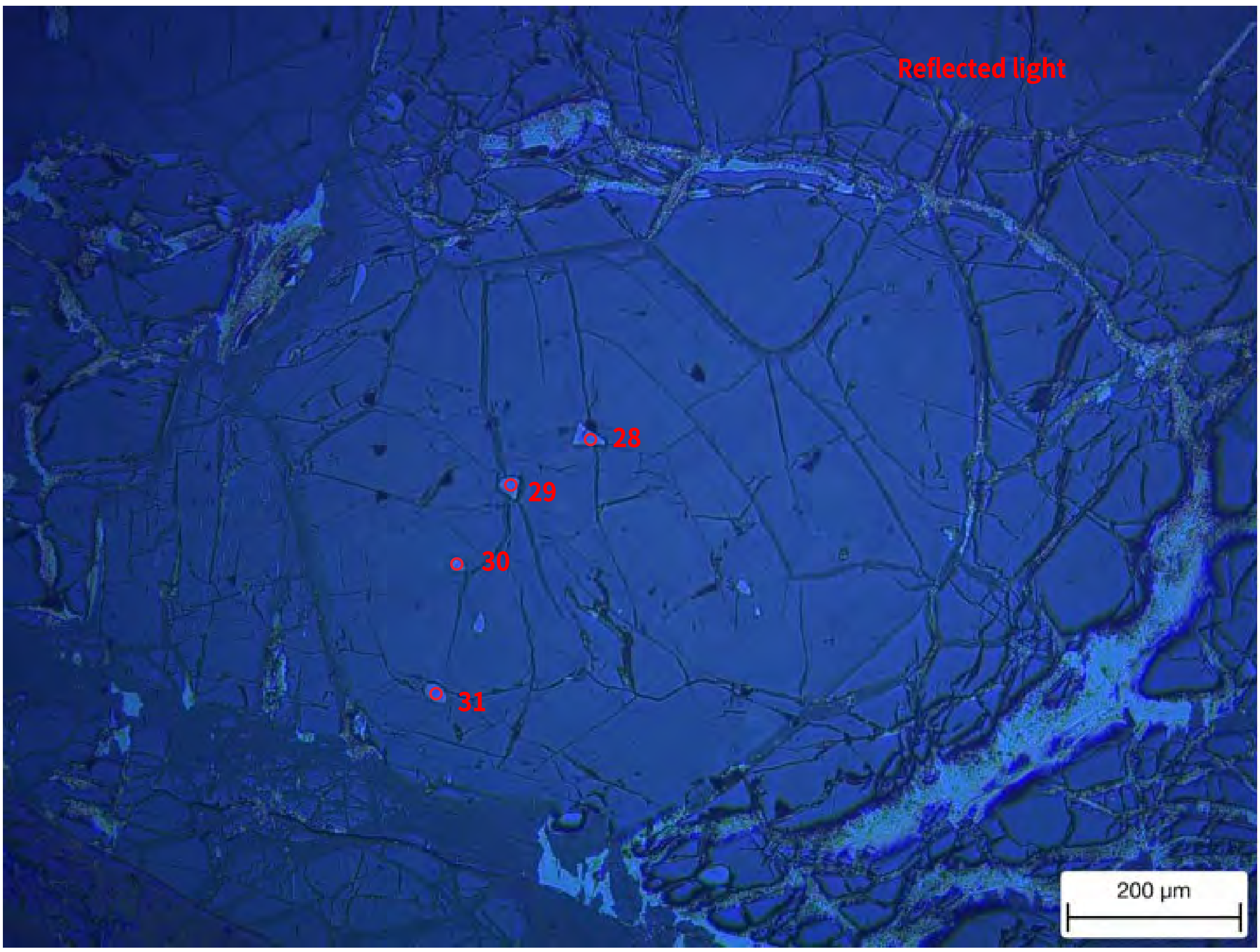
Reflected light
28
29
30
31
200 µm

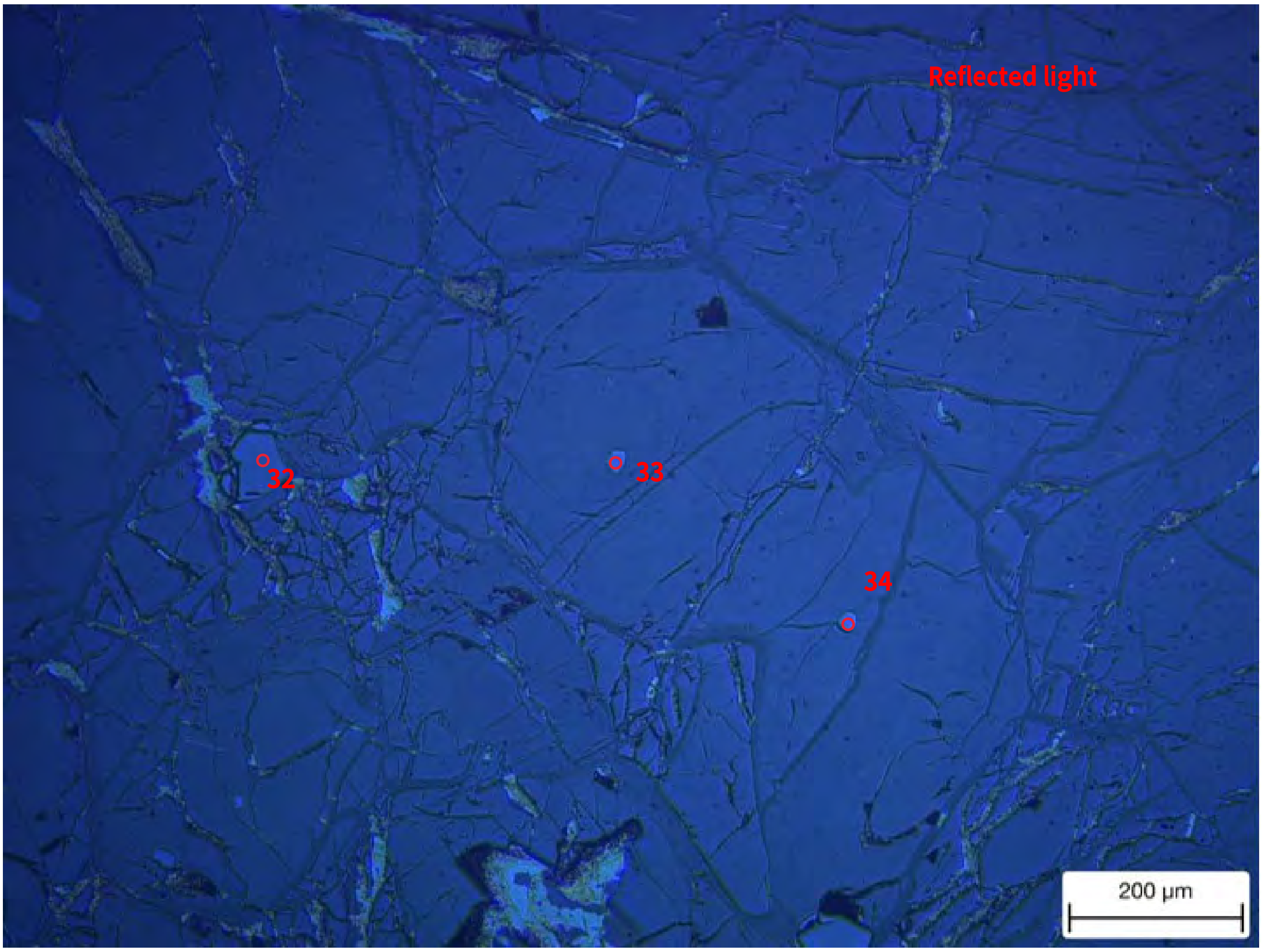
Reflected light
32
33
34
200 µm

Sample C17-18

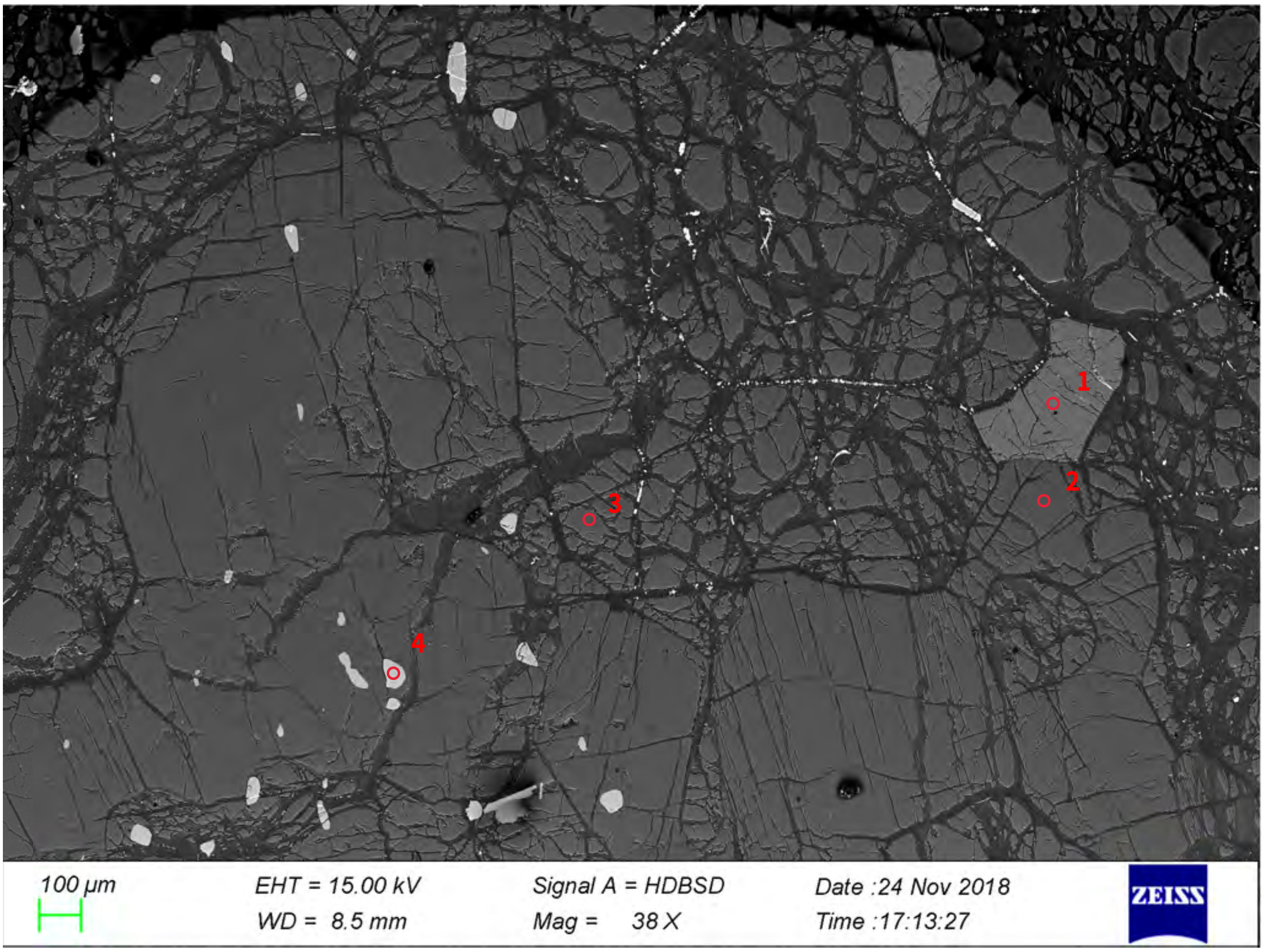

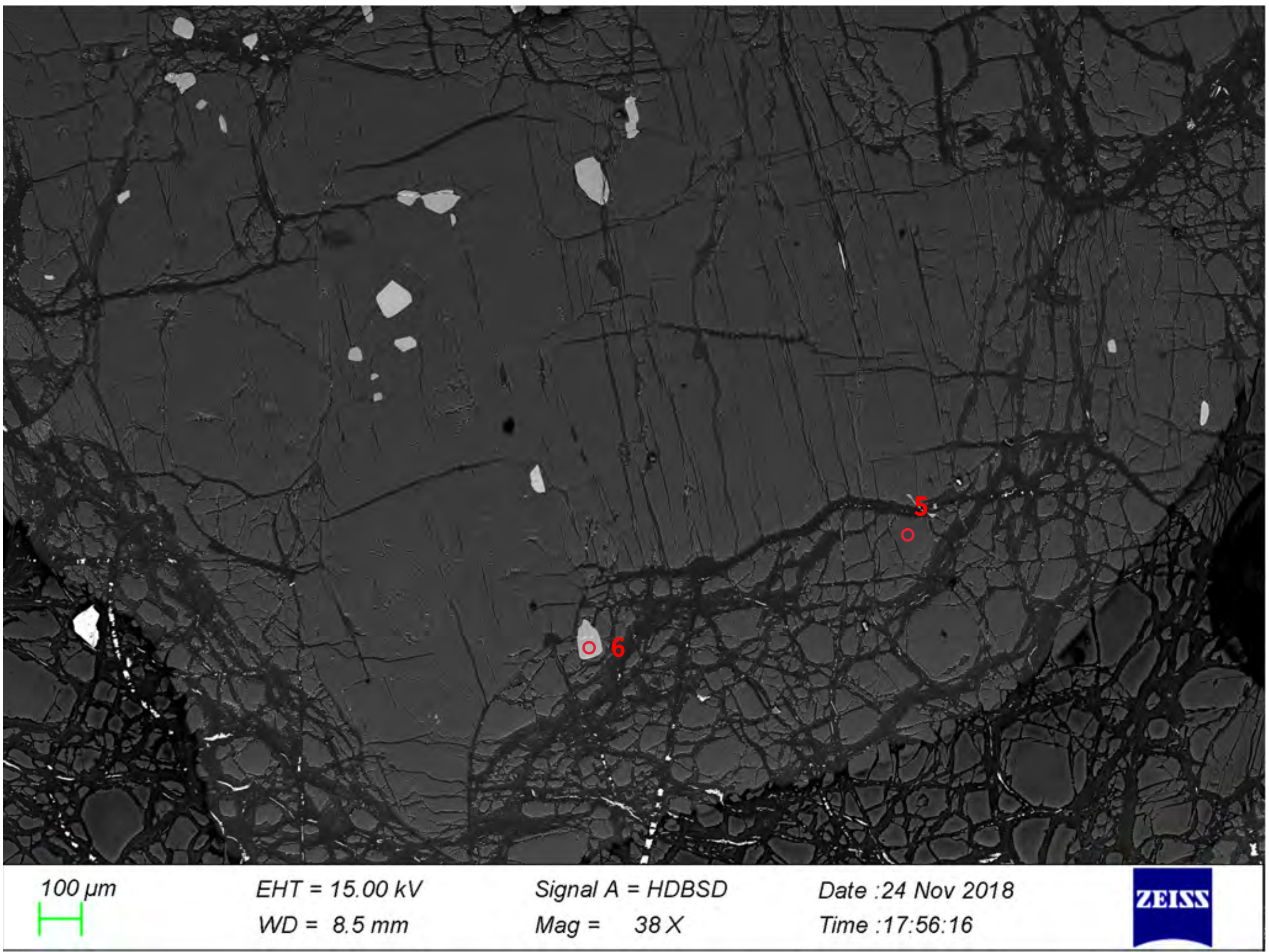

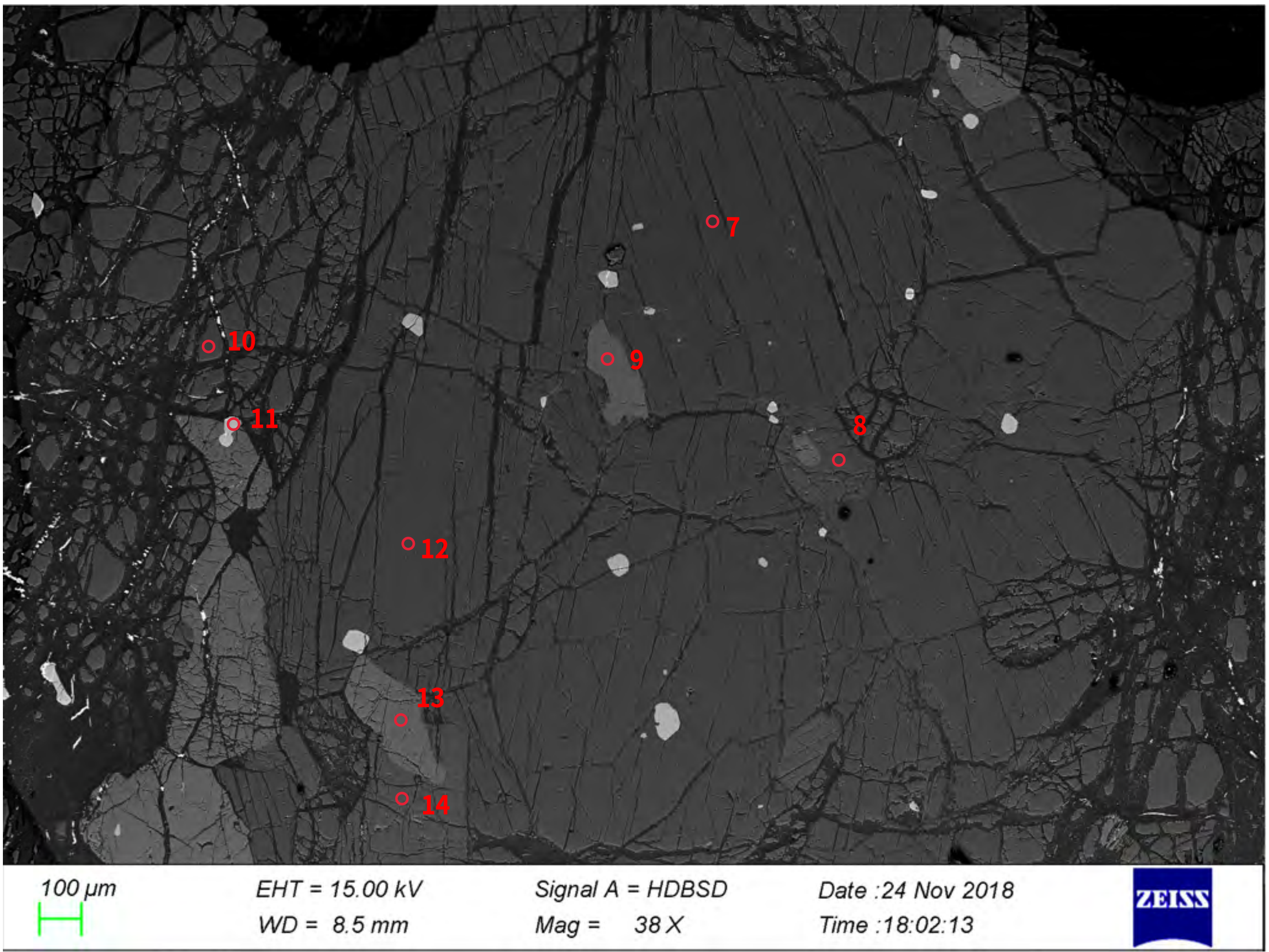
7
8
9
10
11
12
13
14
100 µm
EHT = 15.00 kV
WD = 8.5 mm
Signal A = HDBSD
Mag = 38 X
Date :24 Nov 2018
Time :18:02:13

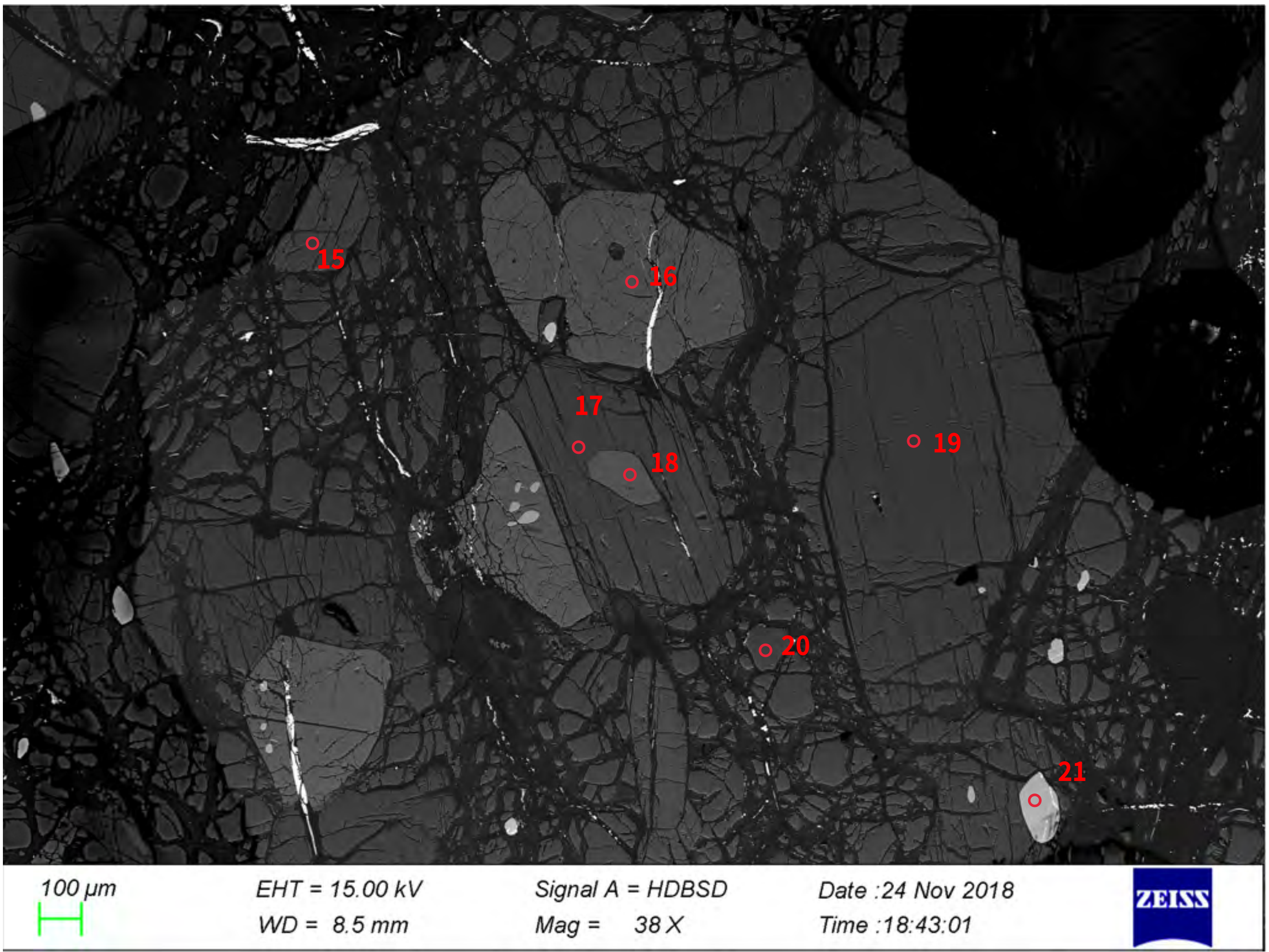
15
16
17
18
19
20
21
100 µm
EHT = 15.00 kV
WD = 8.5 mm
Signal A = HDBSD
Mag = 38 X
Date :24 Nov 2018
Time :18:43:01

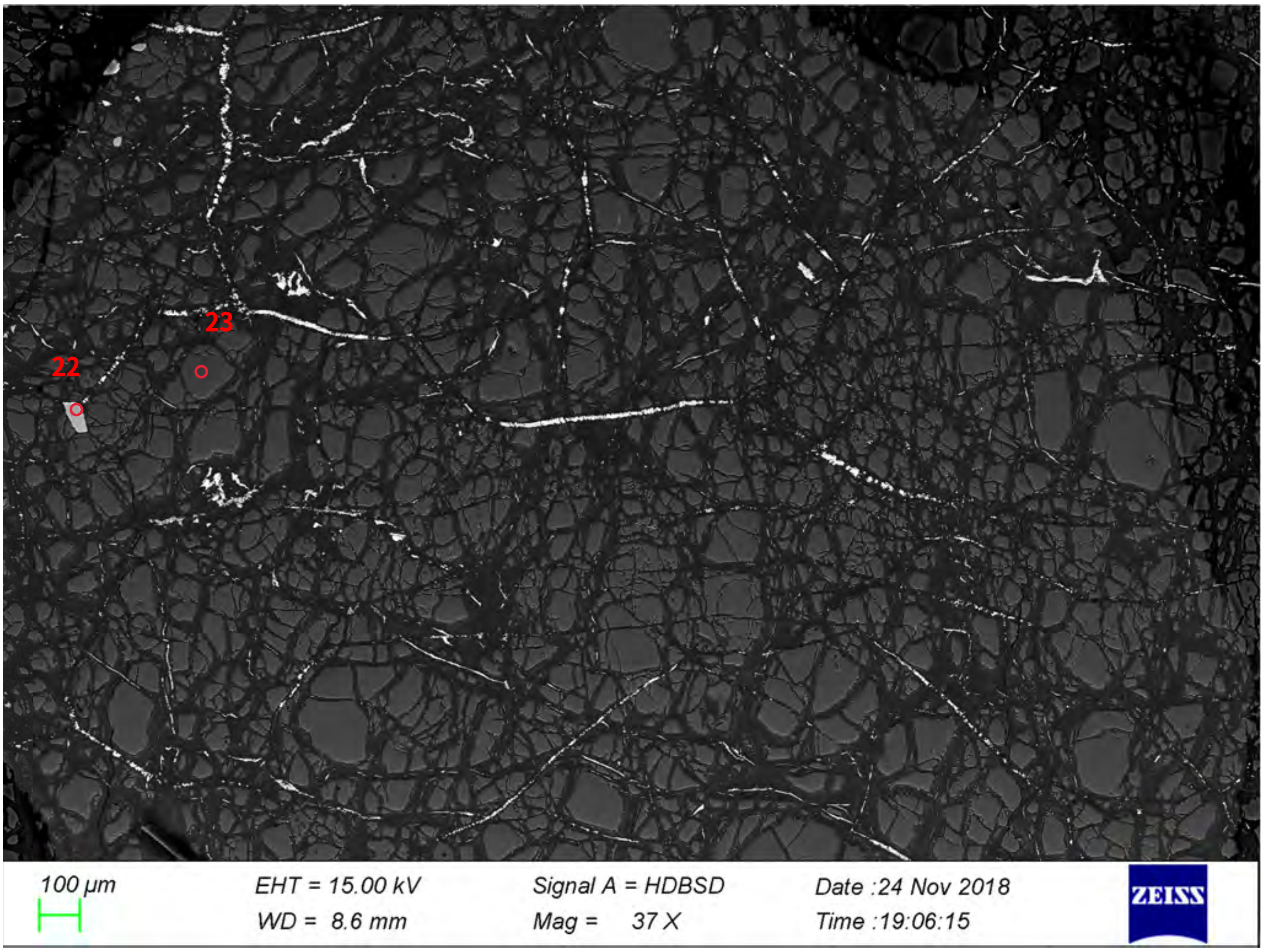
22
23
100 µm
EHT = 15.00 kV
WD = 8.6 mm
Signal A = HDBSD
Mag = 37 X
Date :24 Nov 2018
Time :19:06:15

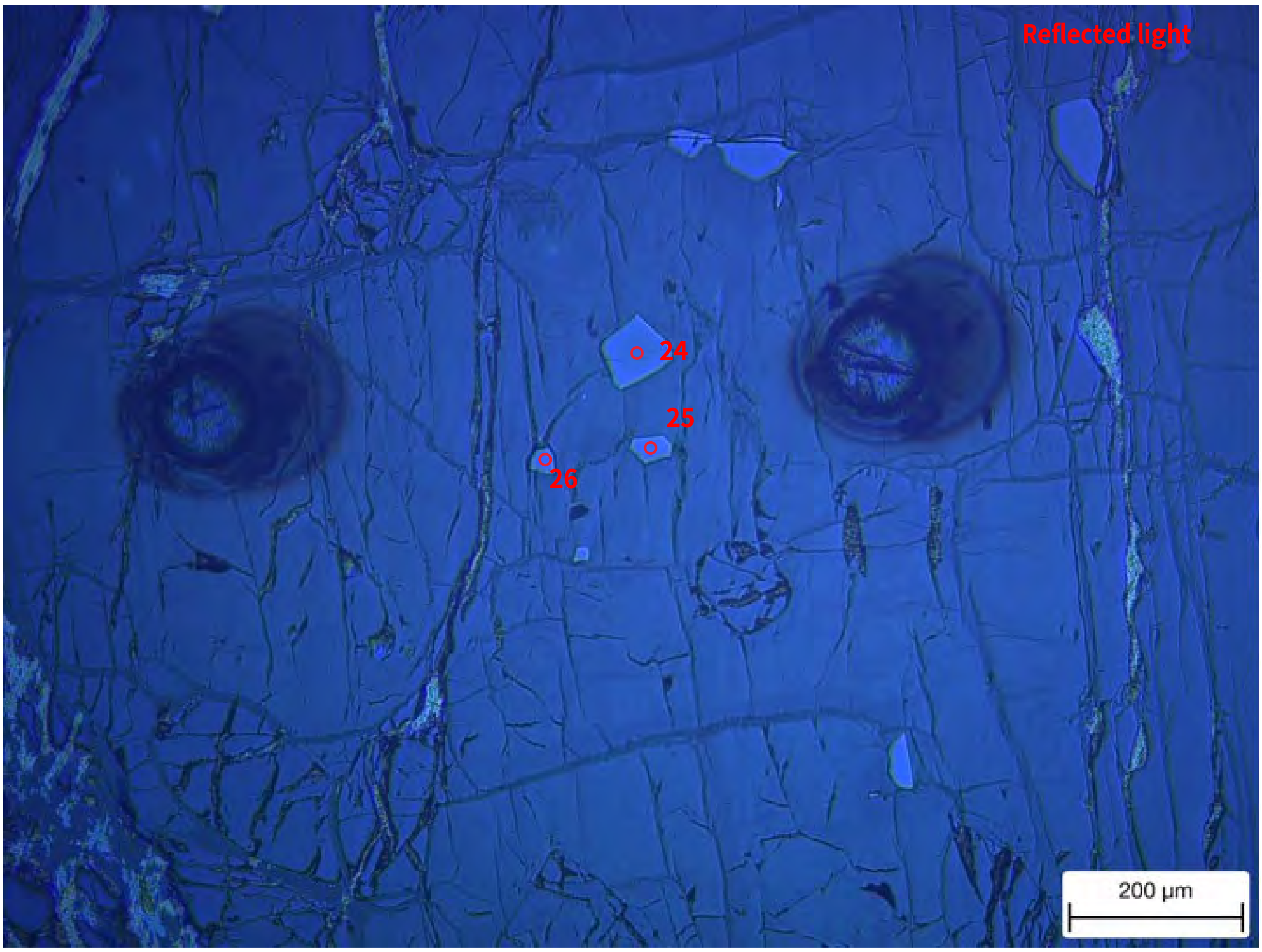
Reflected light
24
25
26
200 µm

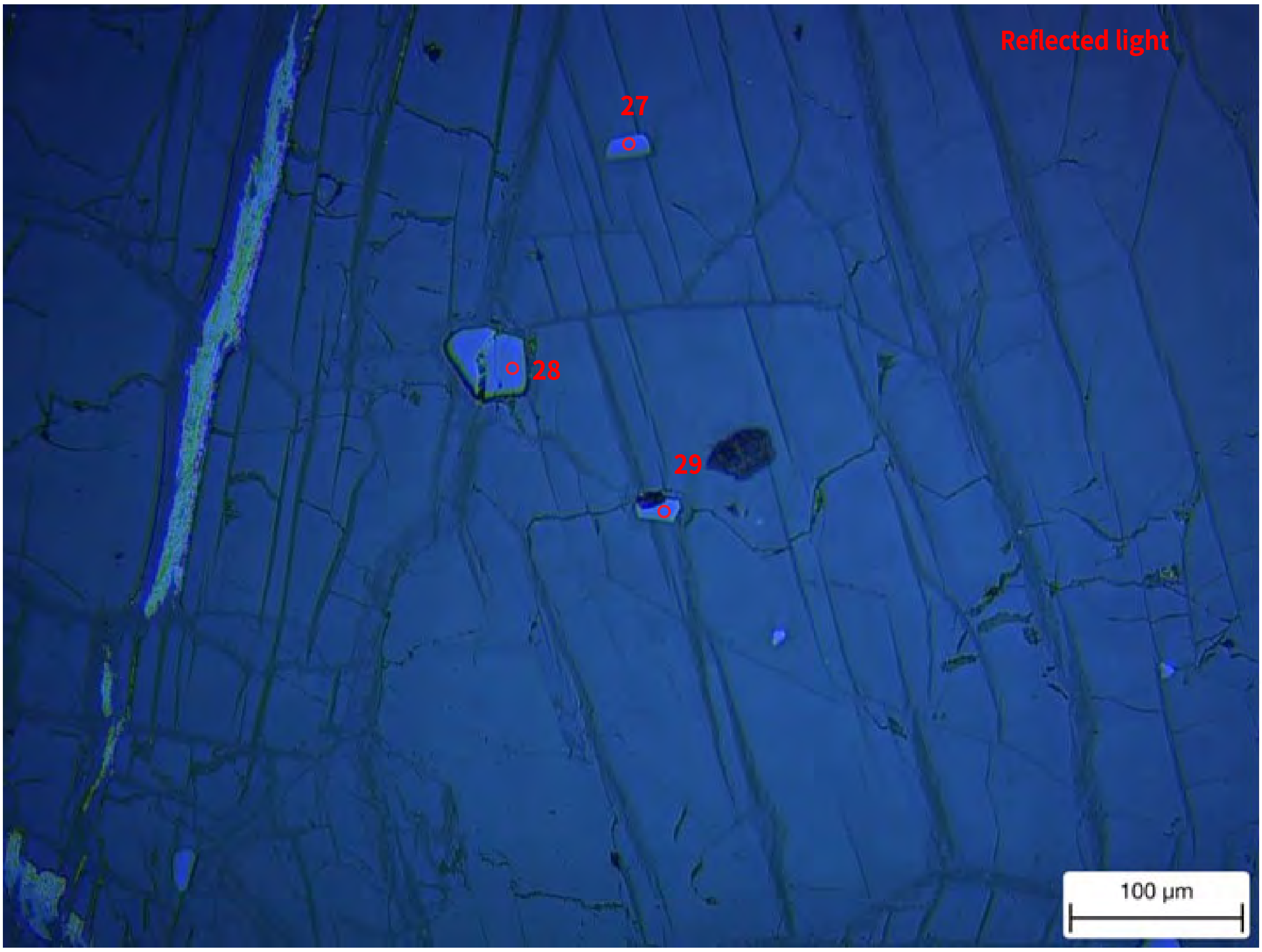
Reflected light
27
28
29
100 µm

Sample C17-19

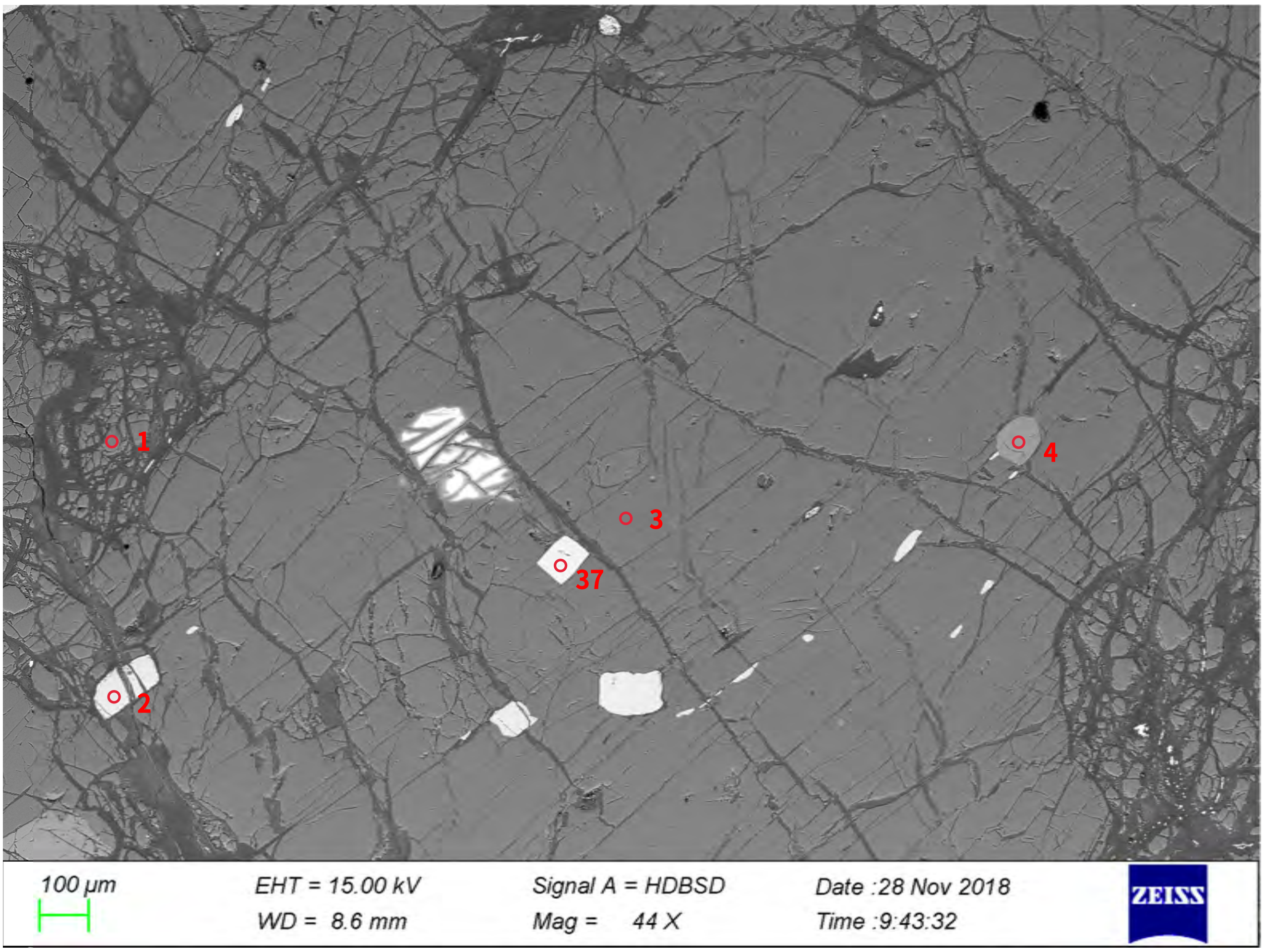

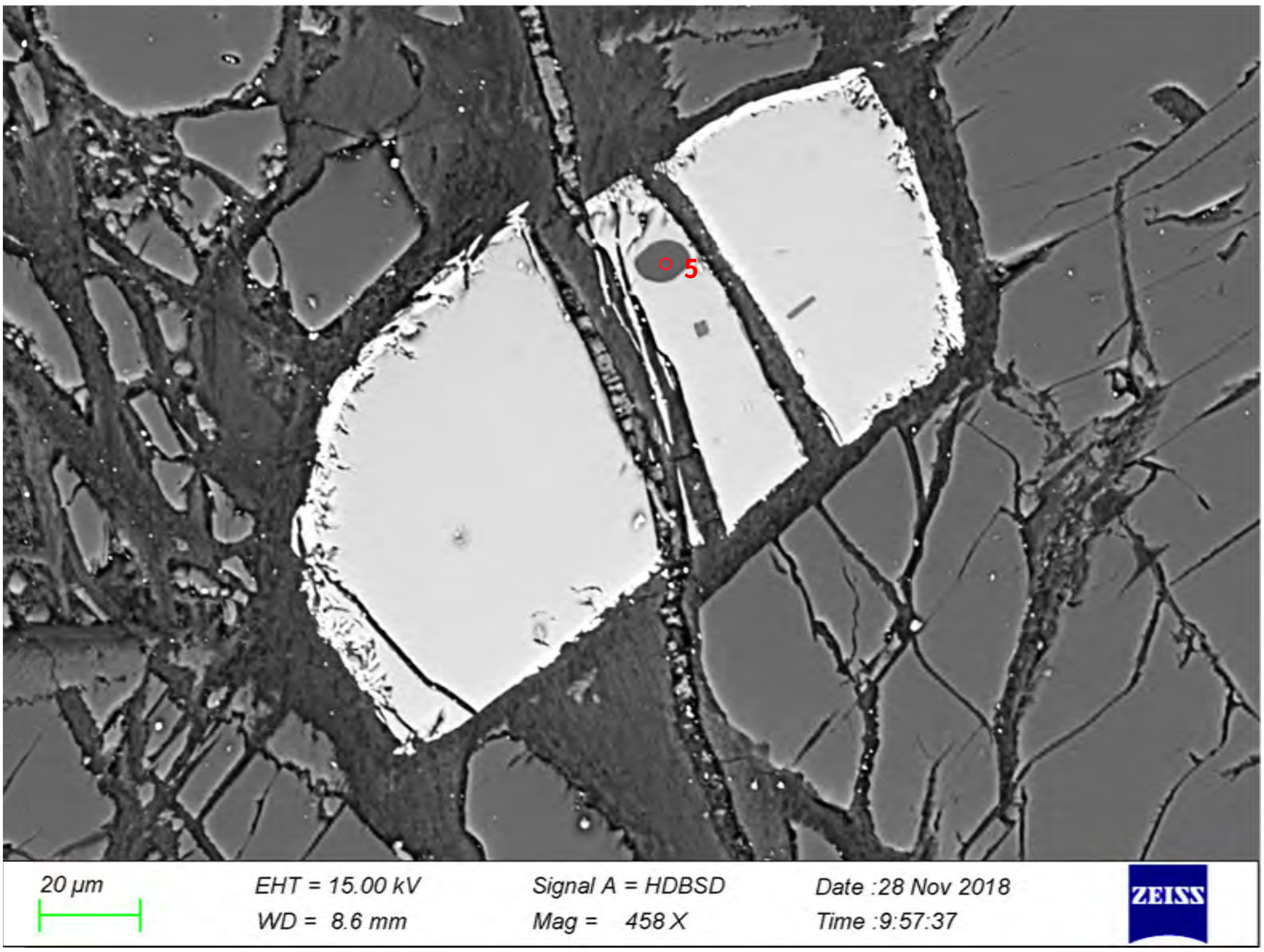

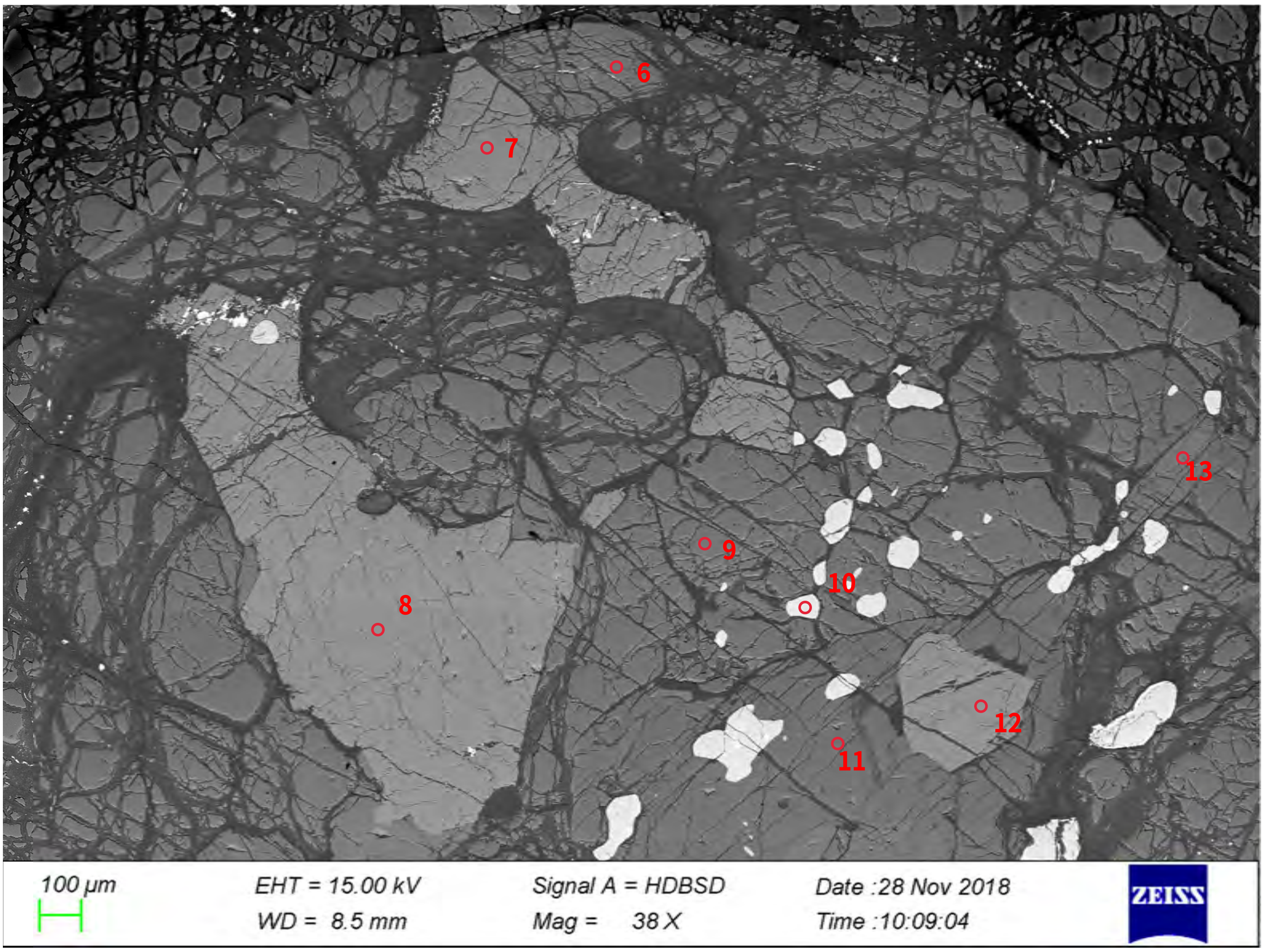
6
7
8
9
10
11
12
13
100 µm
EHT = 15.00 kV
WD = 8.5 mm
Signal A = HDBSD
Mag = 38 X
Date :28 Nov 2018
Time :10:09:04
ZEISS

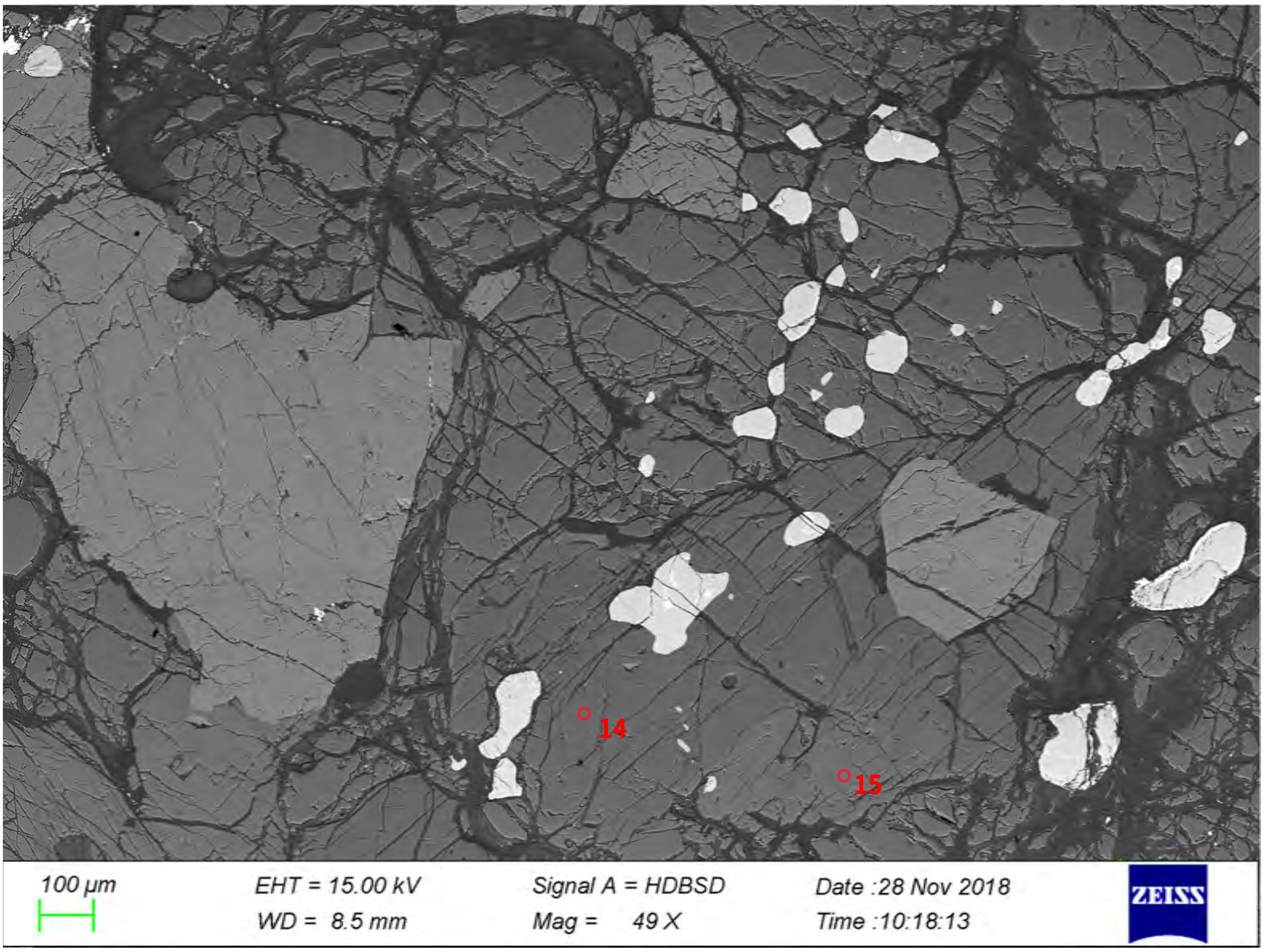
14
15
100 µm
EHT = 15.00 kV
WD = 8.5 mm
Signal A = HDBSD
Mag = 49 X
Date :28 Nov 2018
Time :10:18:13
ZEISS

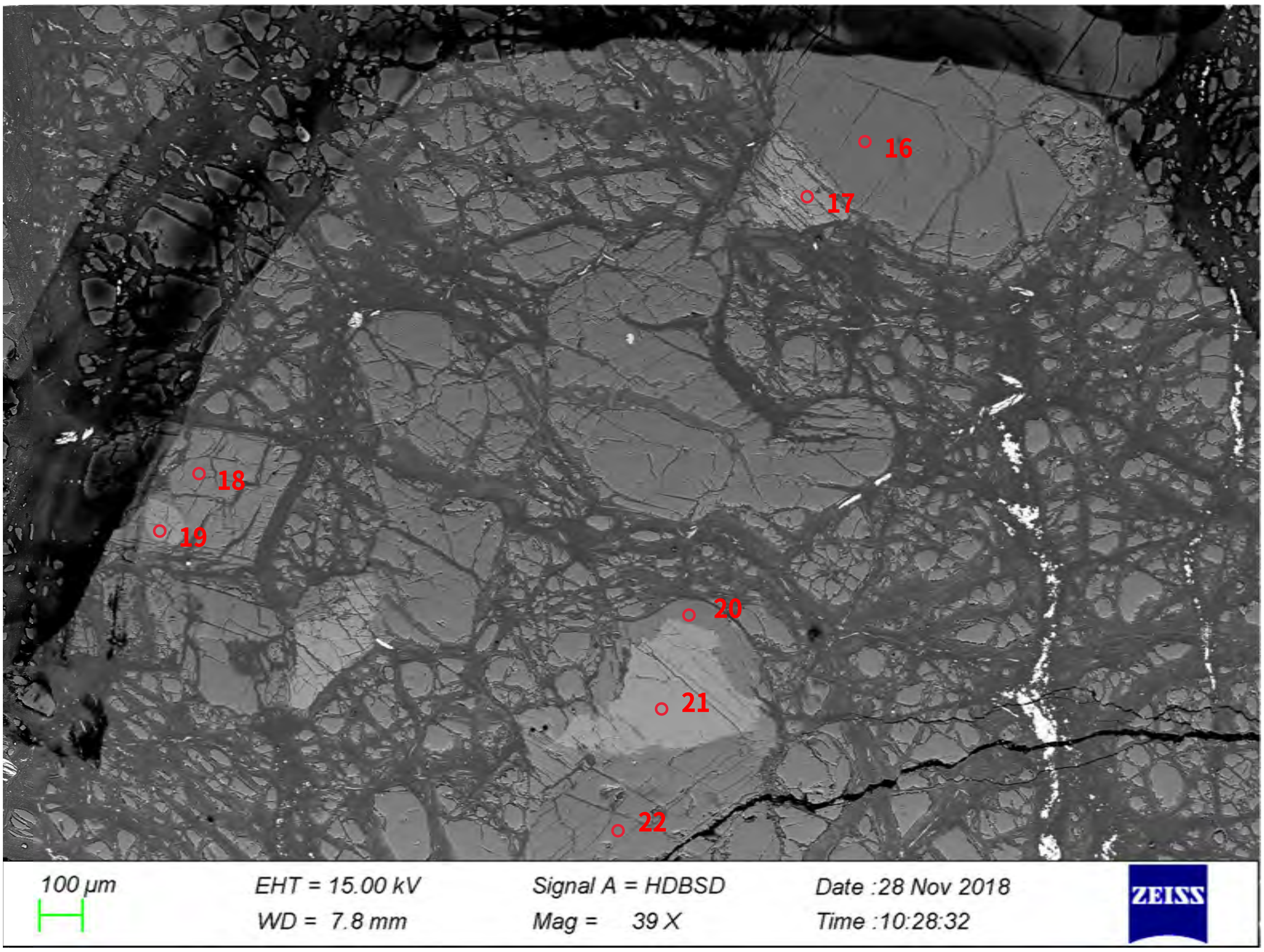
16
17
18
19
20
21
22
100 µm
EHT = 15.00 kV
WD = 7.8 mm
Signal A = HDBSD
Mag = 39 X
Date :28 Nov 2018
Time :10:28:32

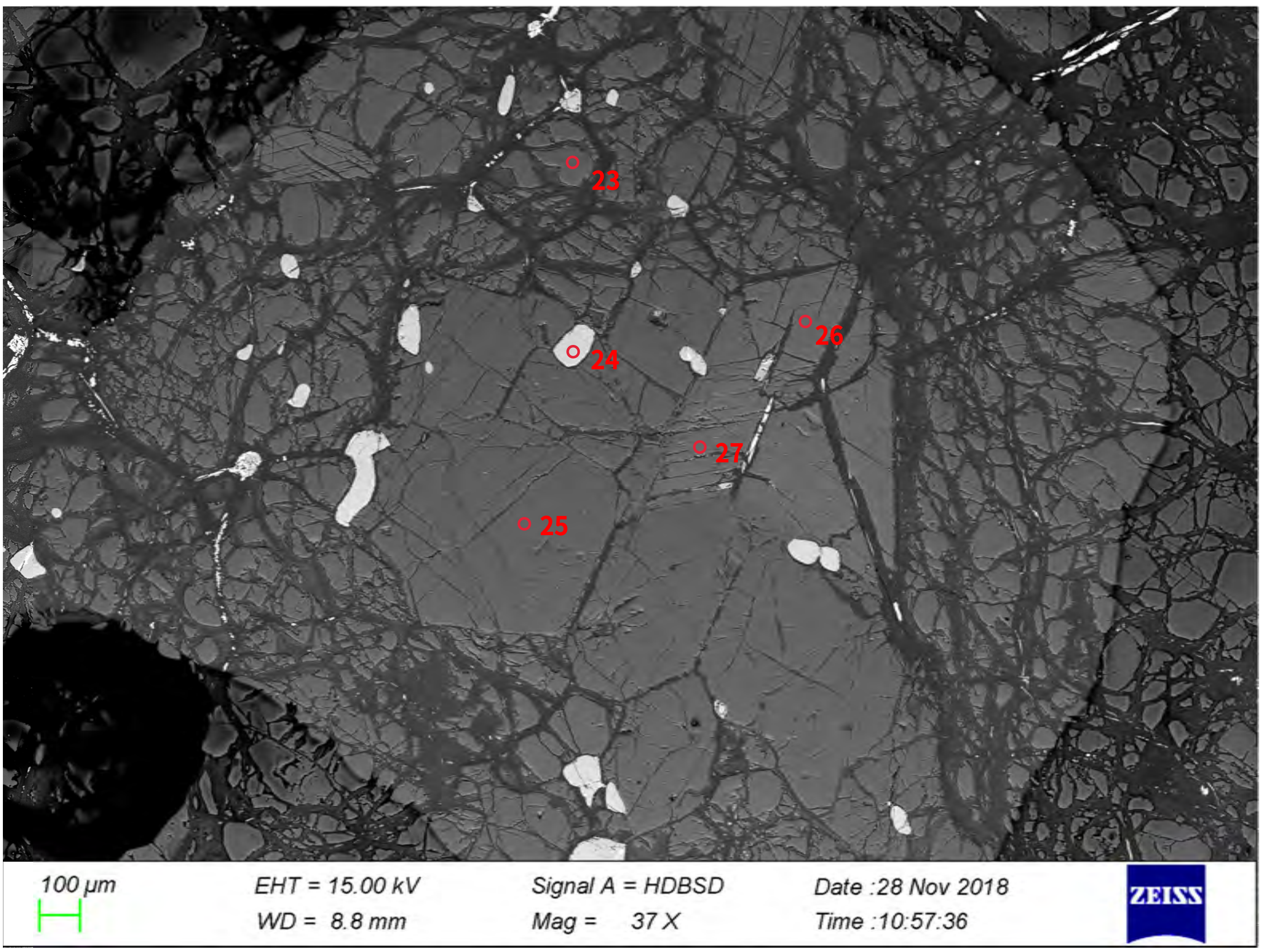
23
24
25
26
27
100 µm
EHT = 15.00 kV
WD = 8.8 mm
Signal A = HDBSD
Mag = 37 X
Date :28 Nov 2018
Time :10:57:36

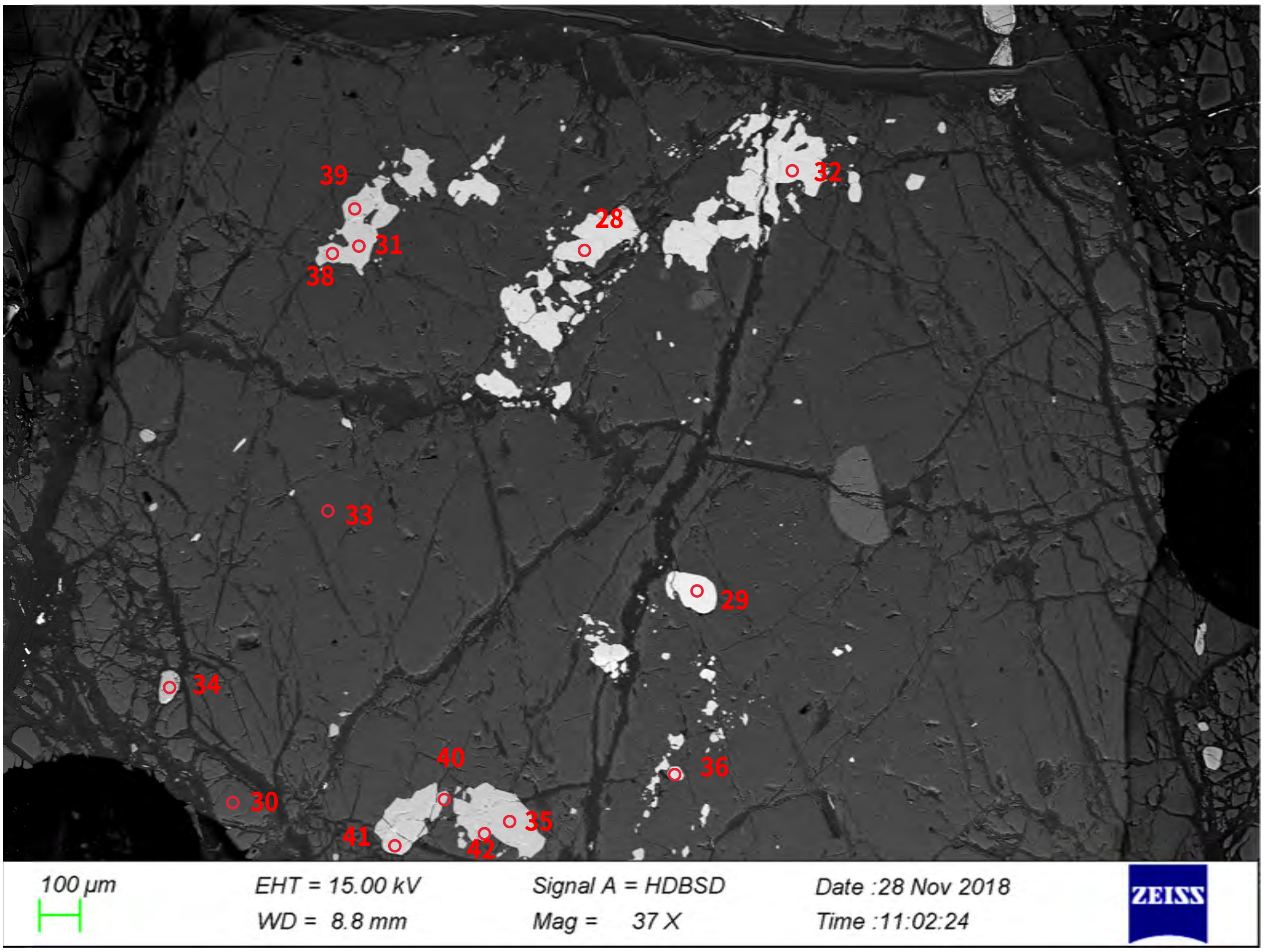
39
31
38
28
32
33
29
34
36
40
30
35
41
42
100 µm
EHT = 15.00 kV
WD = 8.8 mm
Signal A = HDBSD
Mag = 37 X
Date :28 Nov 2018
Time :11:02:24
ZEISS

Sample C17-20

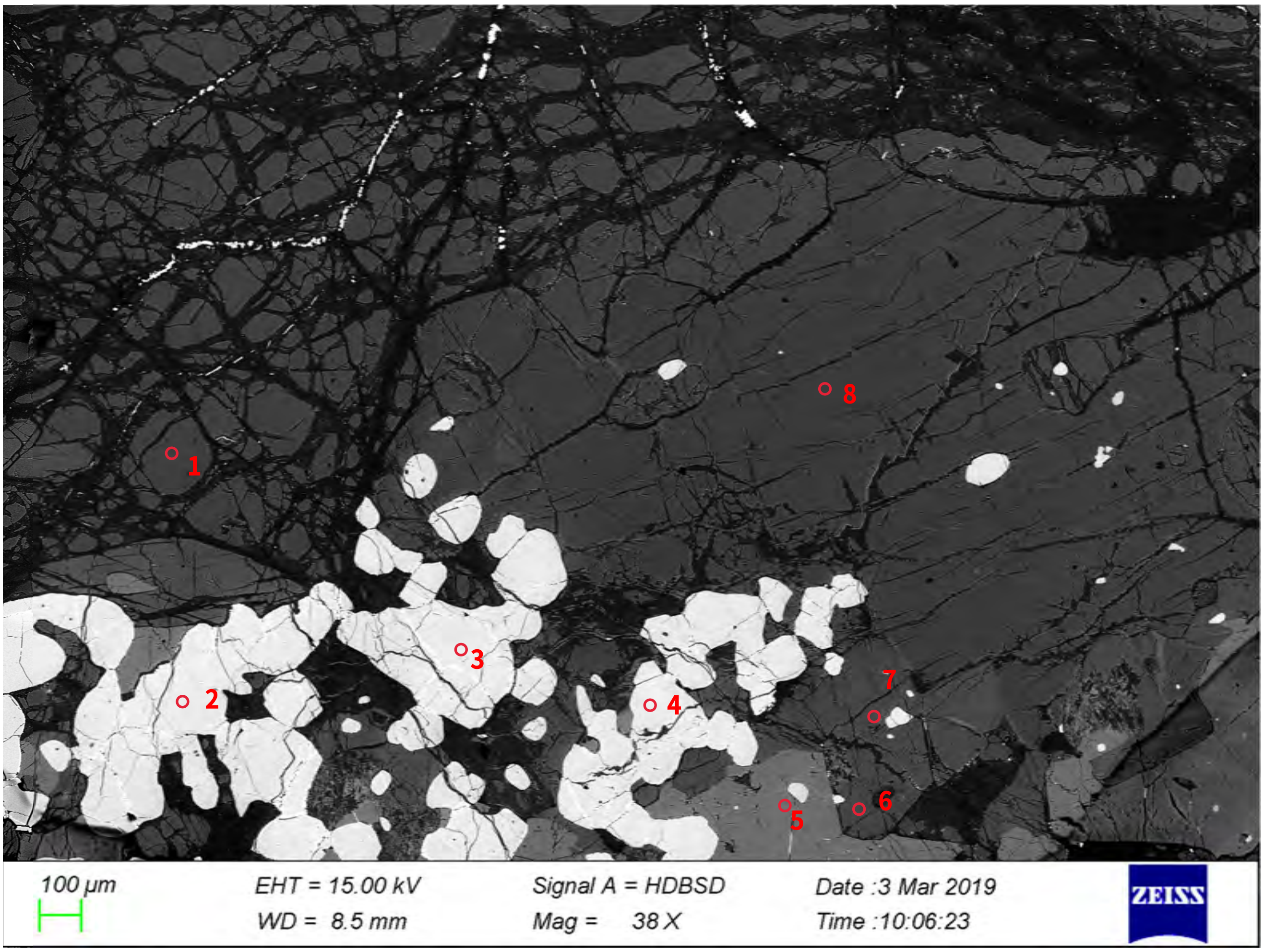

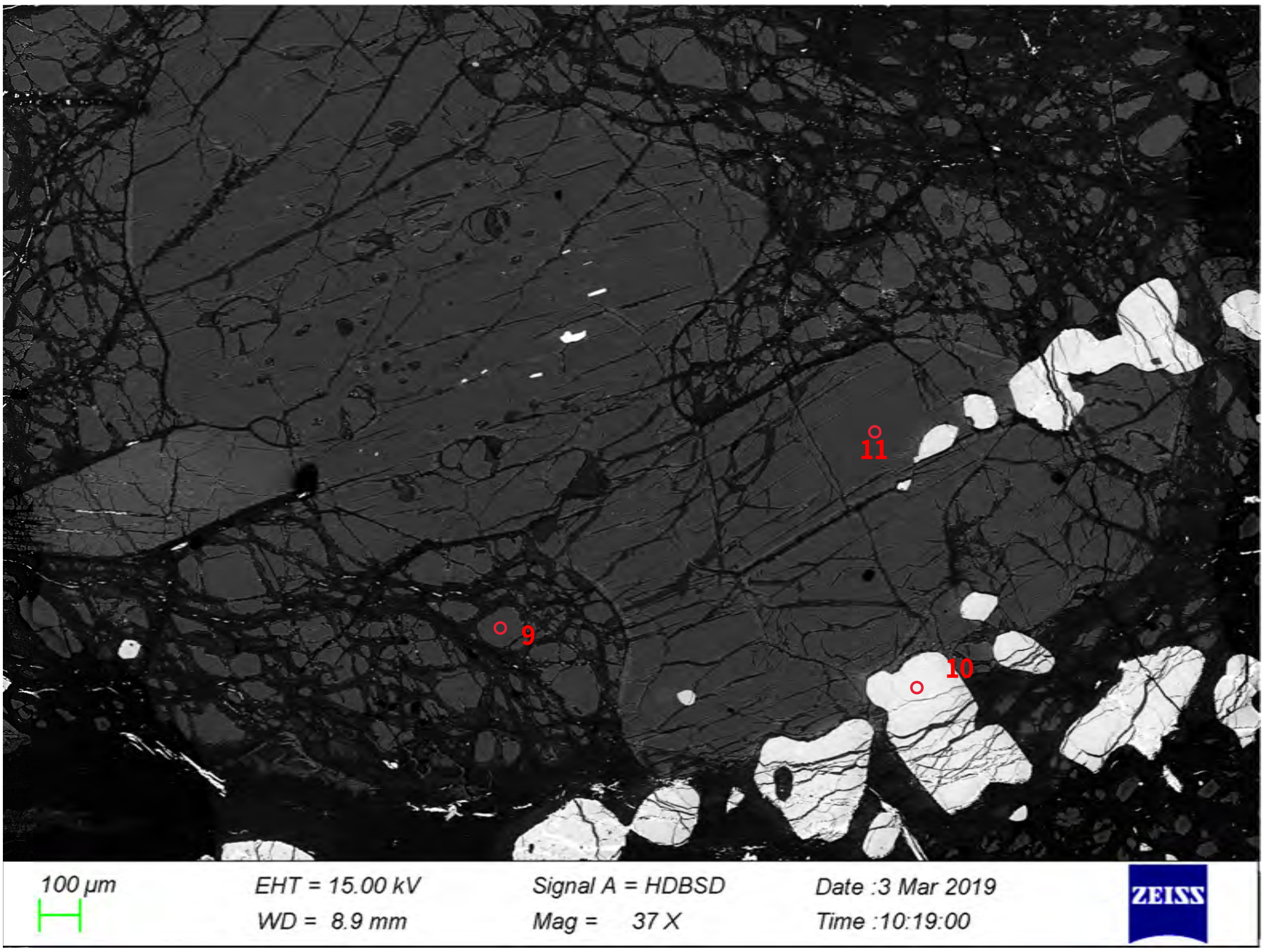

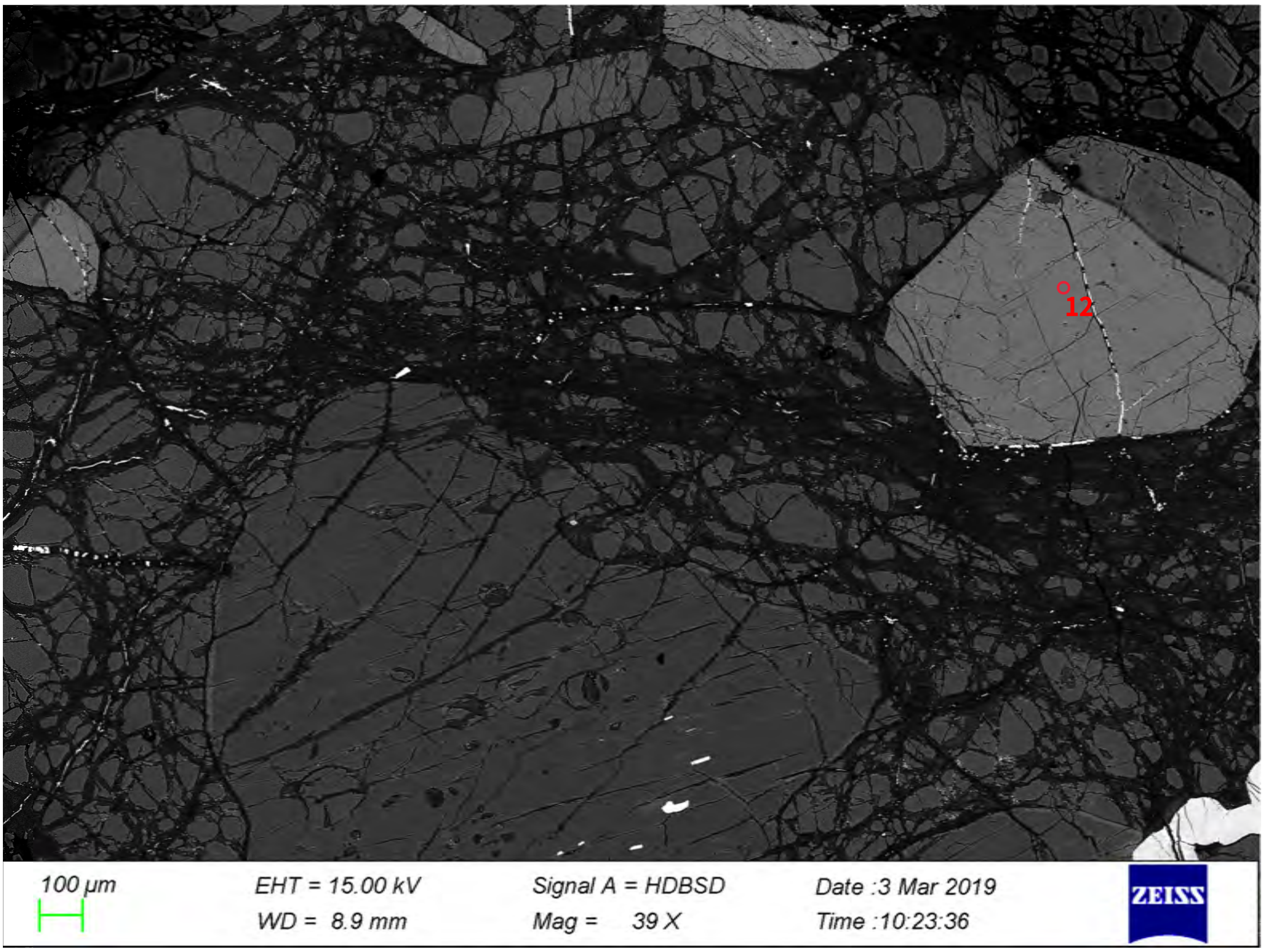
12
100 µm
EHT = 15.00 kV
WD = 8.9 mm
Signal A = HDBSD
Mag = 39 X
Date :3 Mar 2019
Time :10:23:36
ZEISS

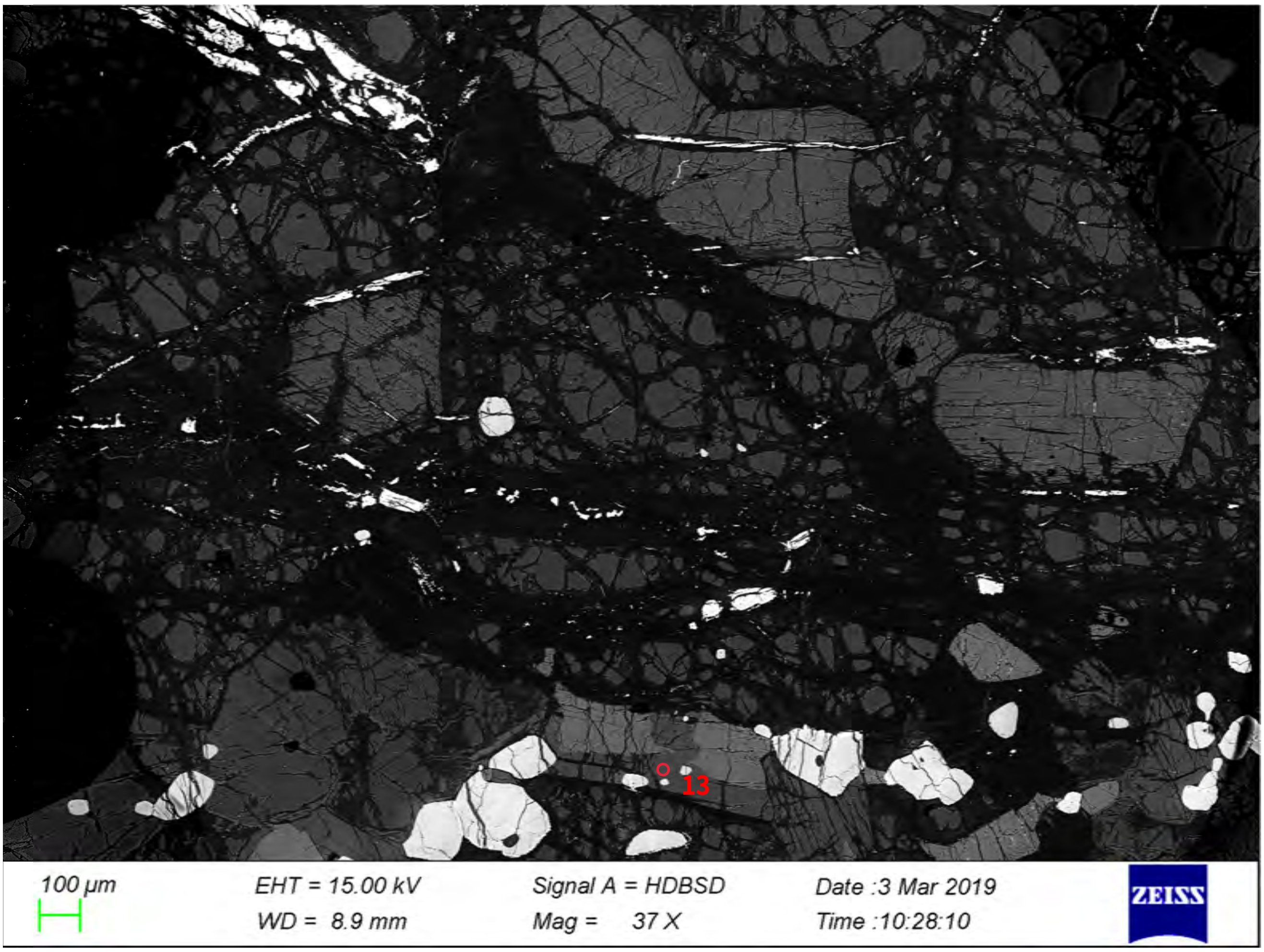
13
100 µm
EHT = 15.00 kV
WD = 8.9 mm
Signal A = HDBSD
Mag = 37 X
Date :3 Mar 2019
Time :10:28:10
ZEISS

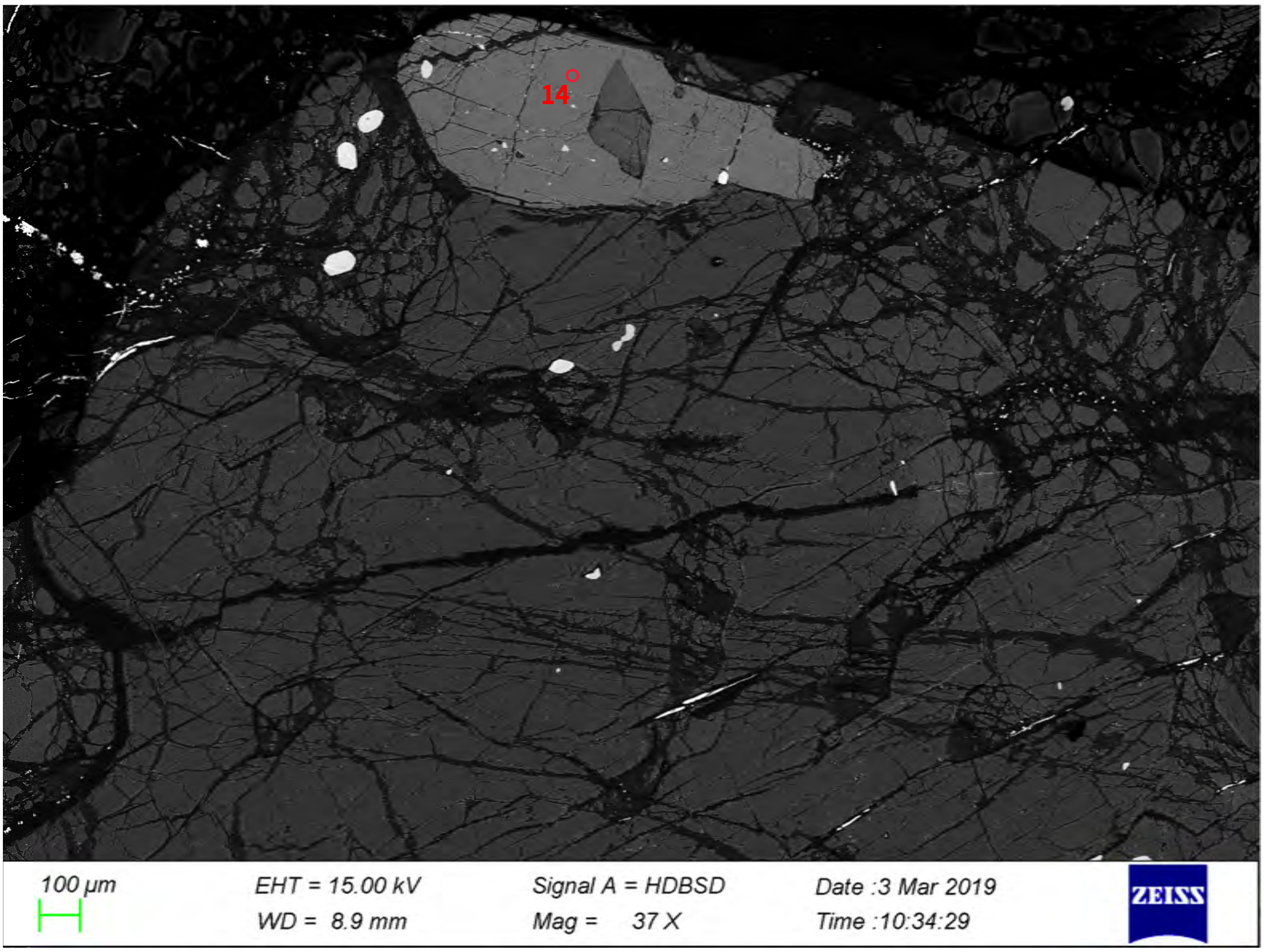
14
100 µm
EHT = 15.00 kV
WD = 8.9 mm
Signal A = HDBSD
Mag = 37 X
Date :3 Mar 2019
Time :10:34:29
ZEISS

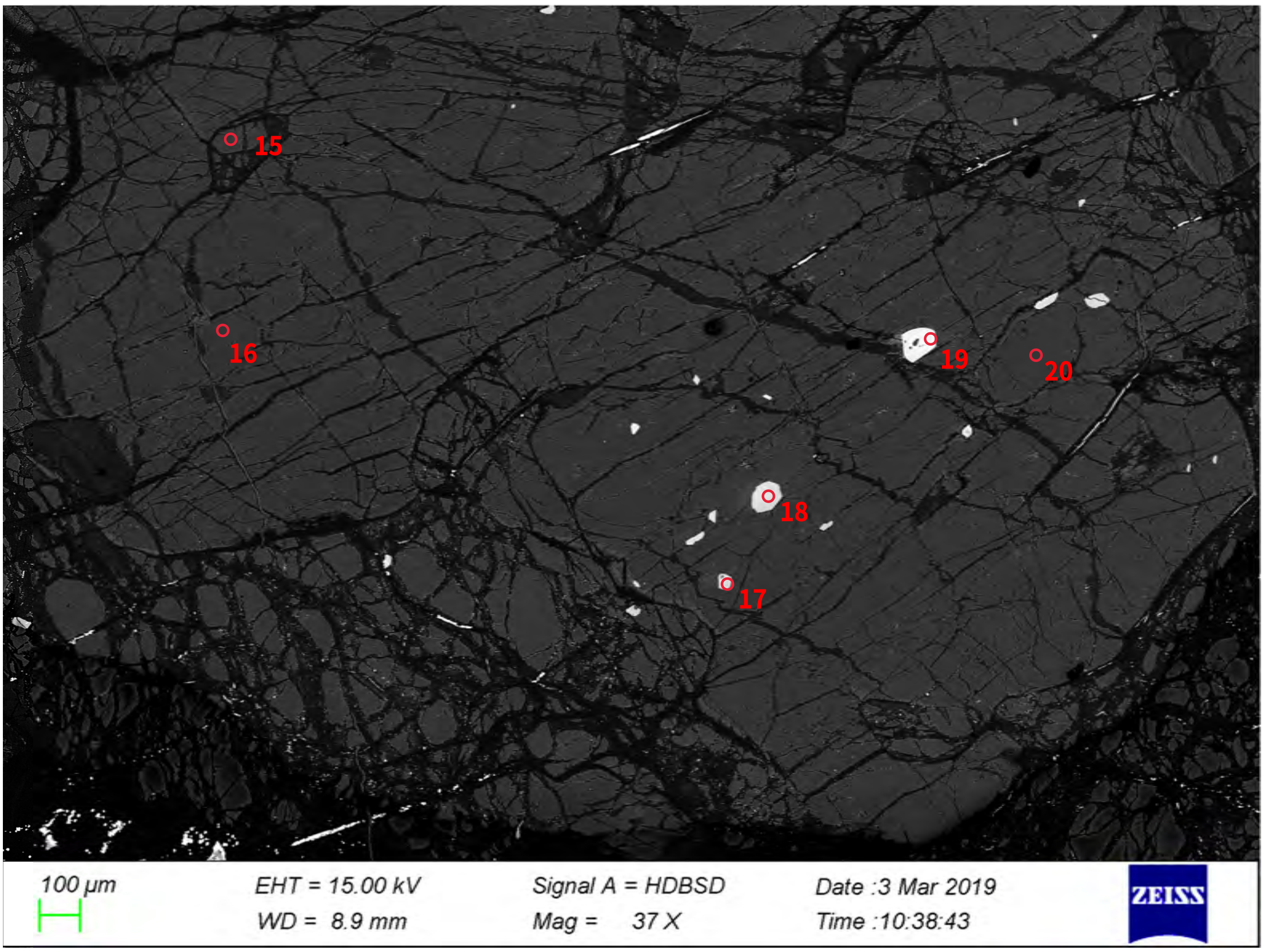
15
16
17
18
19
20
100 µm
EHT = 15.00 kV
WD = 8.9 mm
Signal A = HDBSD
Mag = 37 X
Date :3 Mar 2019
Time :10:38:43
ZEISS

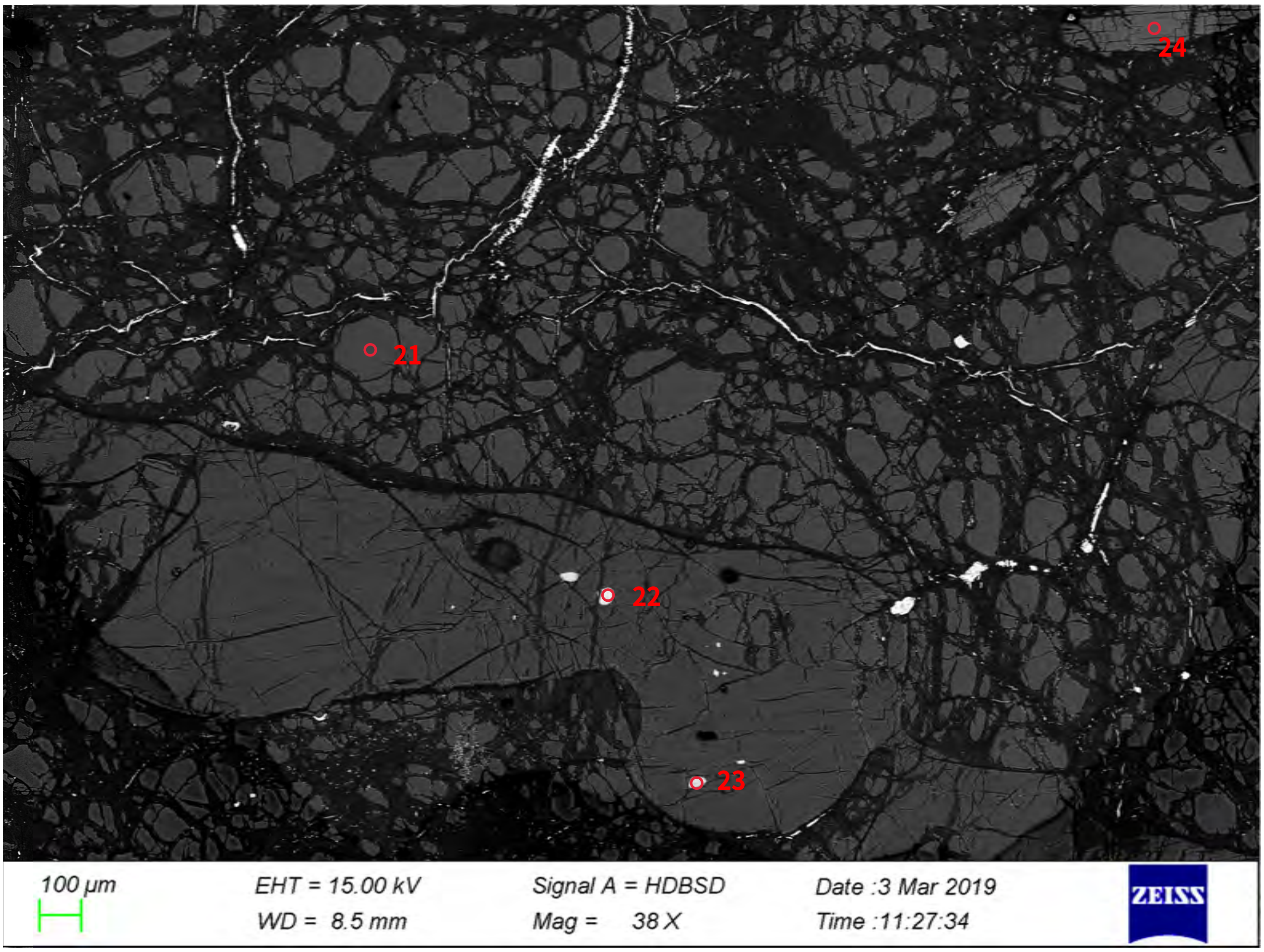
21
22
23
24
100 µm
EHT = 15.00 kV
WD = 8.5 mm
Signal A = HDBSD
Mag = 38 X
Date :3 Mar 2019
Time :11:27:34

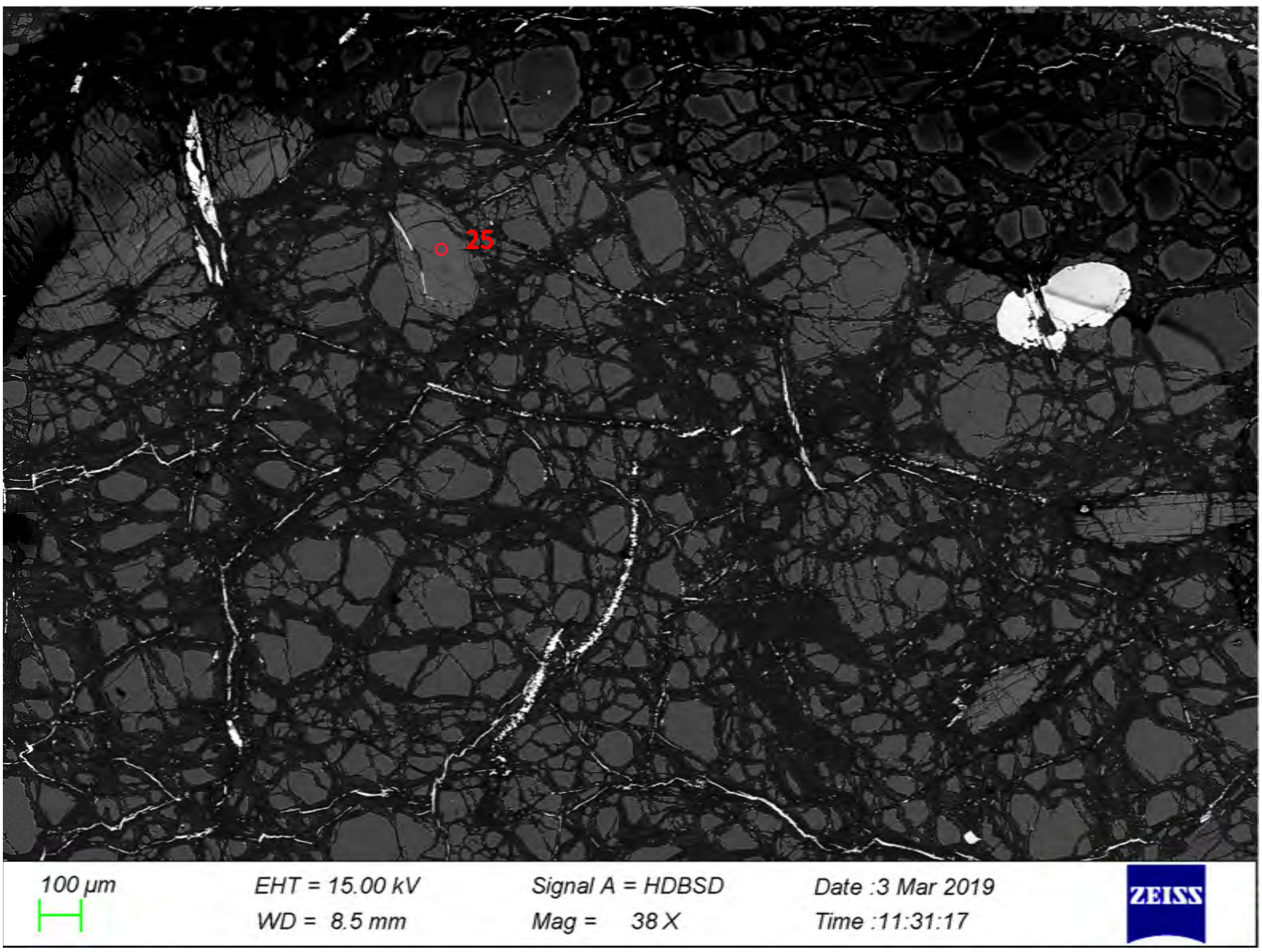
25
100 µm
EHT = 15.00 kV
WD = 8.5 mm
Signal A = HDBSD
Mag = 38 X
Date :3 Mar 2019
Time :11:31:17

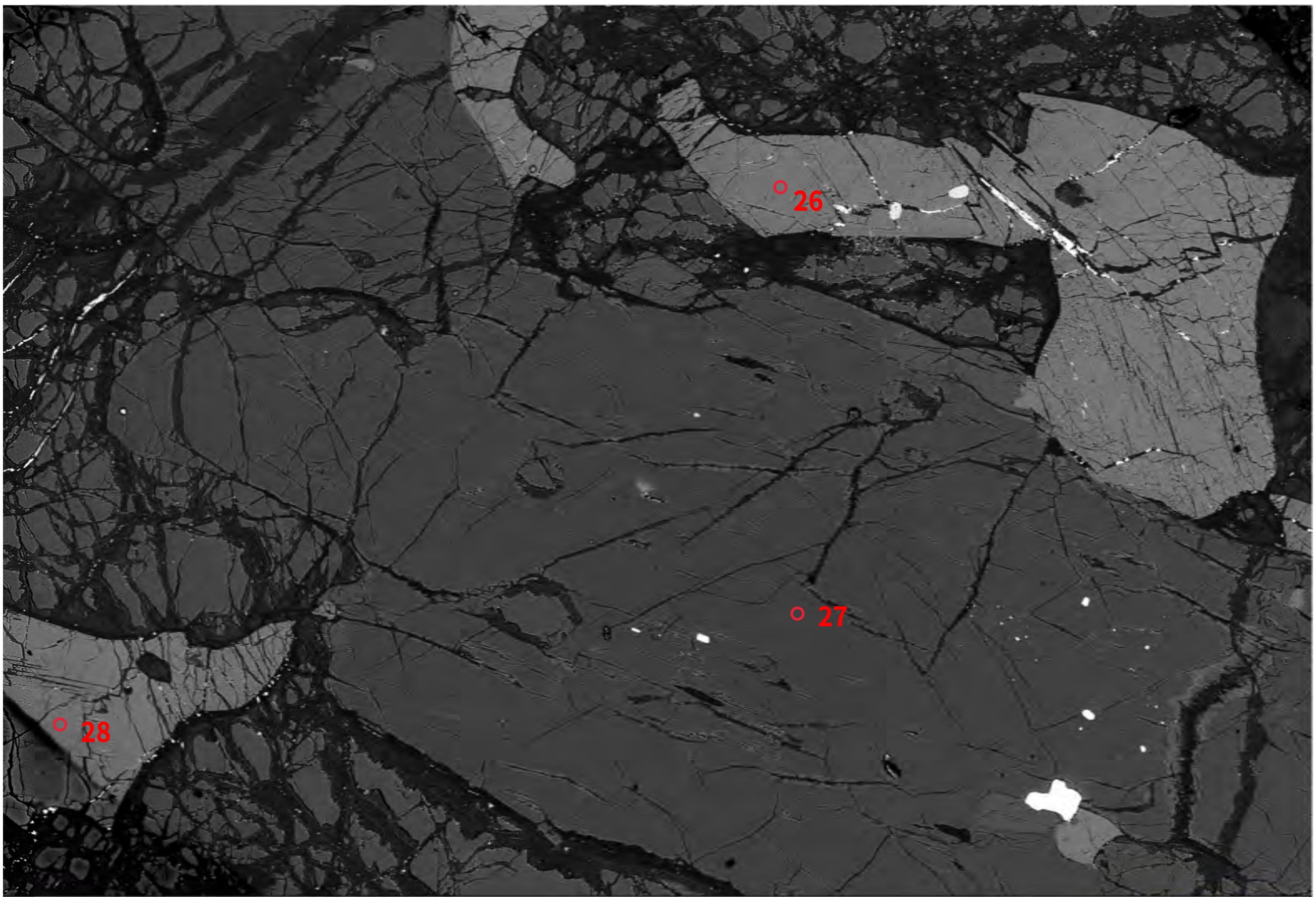

100 µm | EHT = 15.00 kV | WD = 8.5 mm | Signal A = HDBSD | Mag = 38 X | Date :3 Mar 2019 | Time :11:35:23 | ZEISS

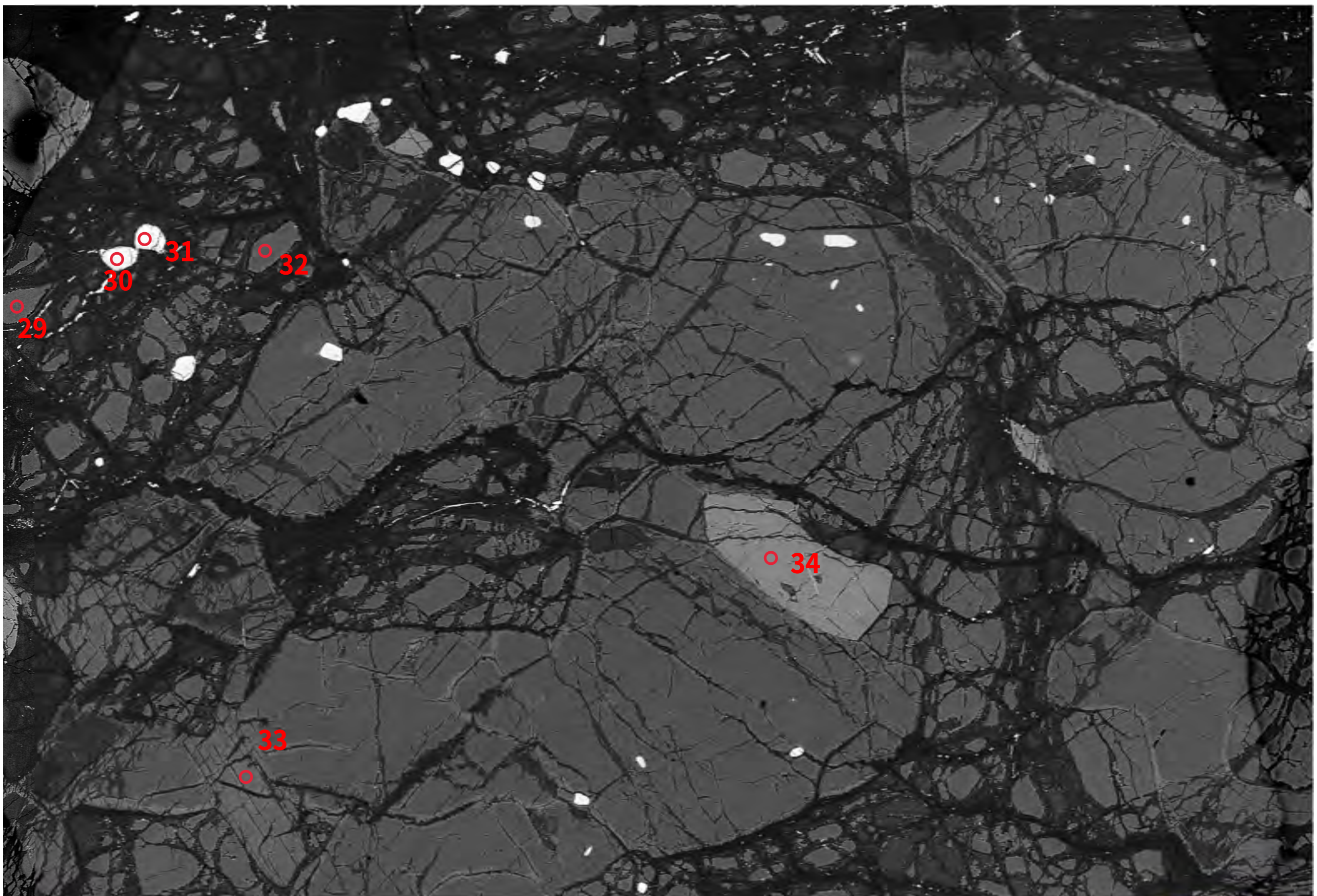

100 µm | EHT = 15.00 kV | WD = 8.5 mm | Signal A = HDBSD | Mag = 38 X | Date :3 Mar 2019 | Time :11:39:50 | ZEISS

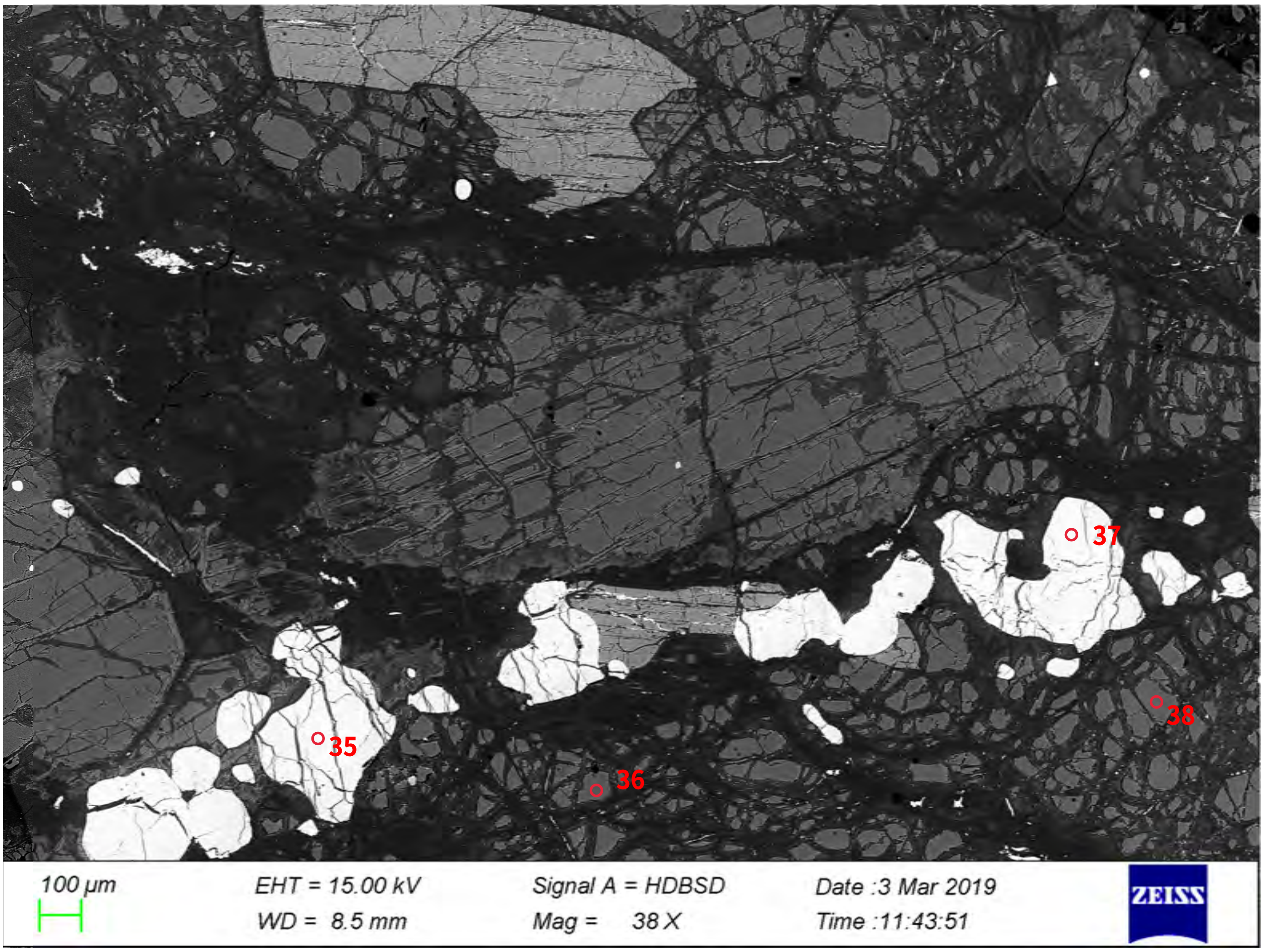
35
36
37
38
100 µm
EHT = 15.00 kV
WD = 8.5 mm
Signal A = HDBSD
Mag = 38 X
Date :3 Mar 2019
Time :11:43:51
ZEISS

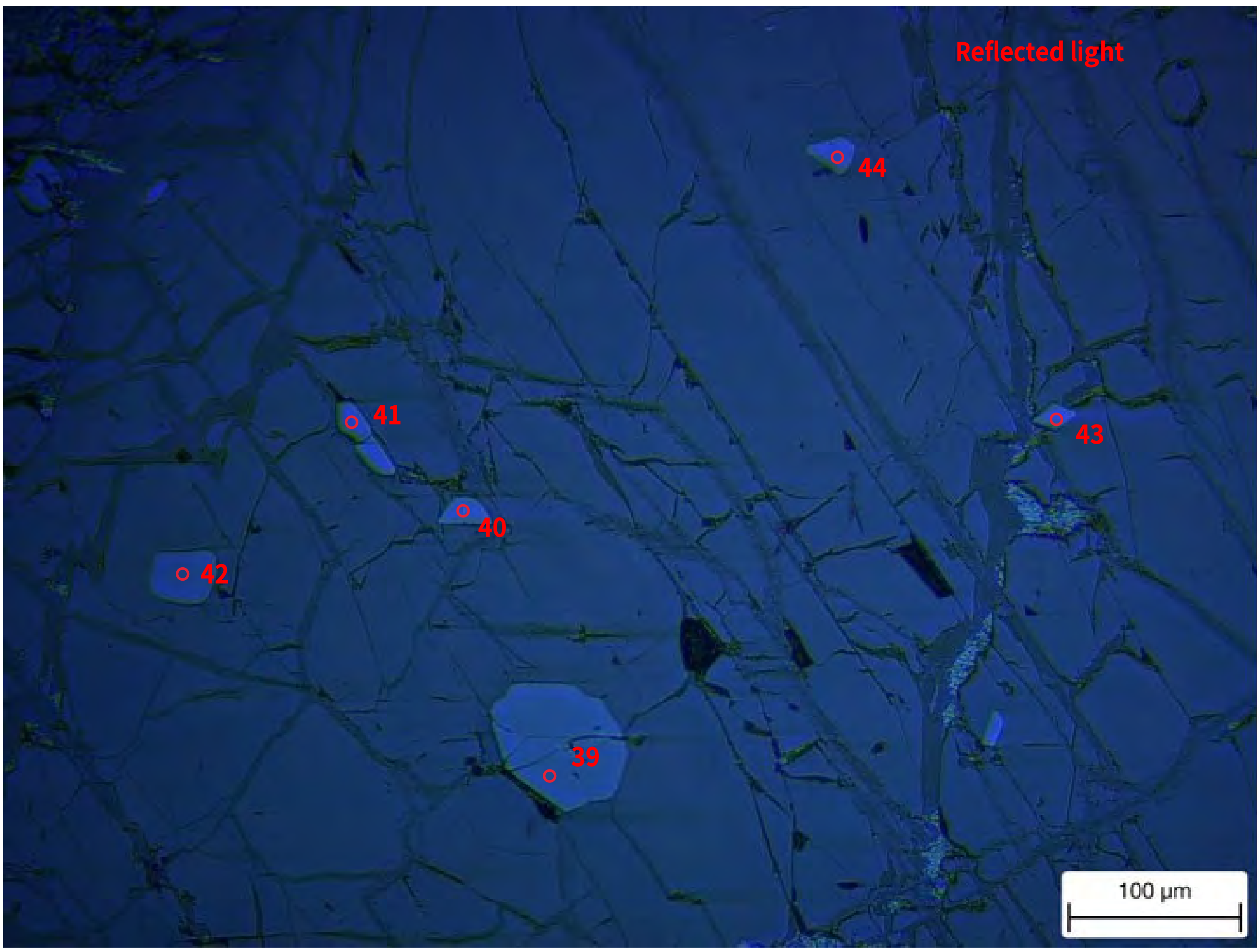
Reflected light
44
41
43
40
42
39
100 µm

Sample C17-21

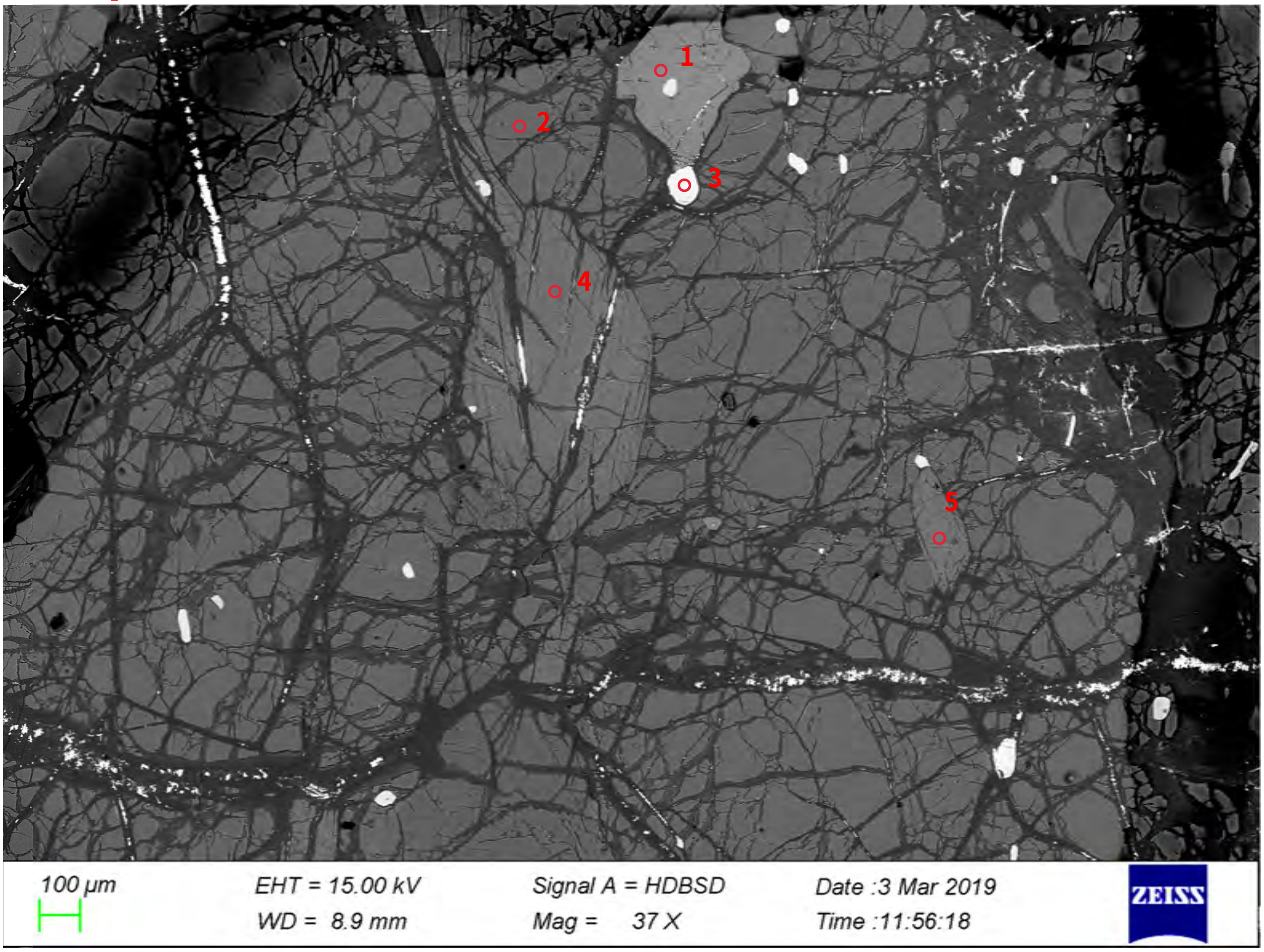

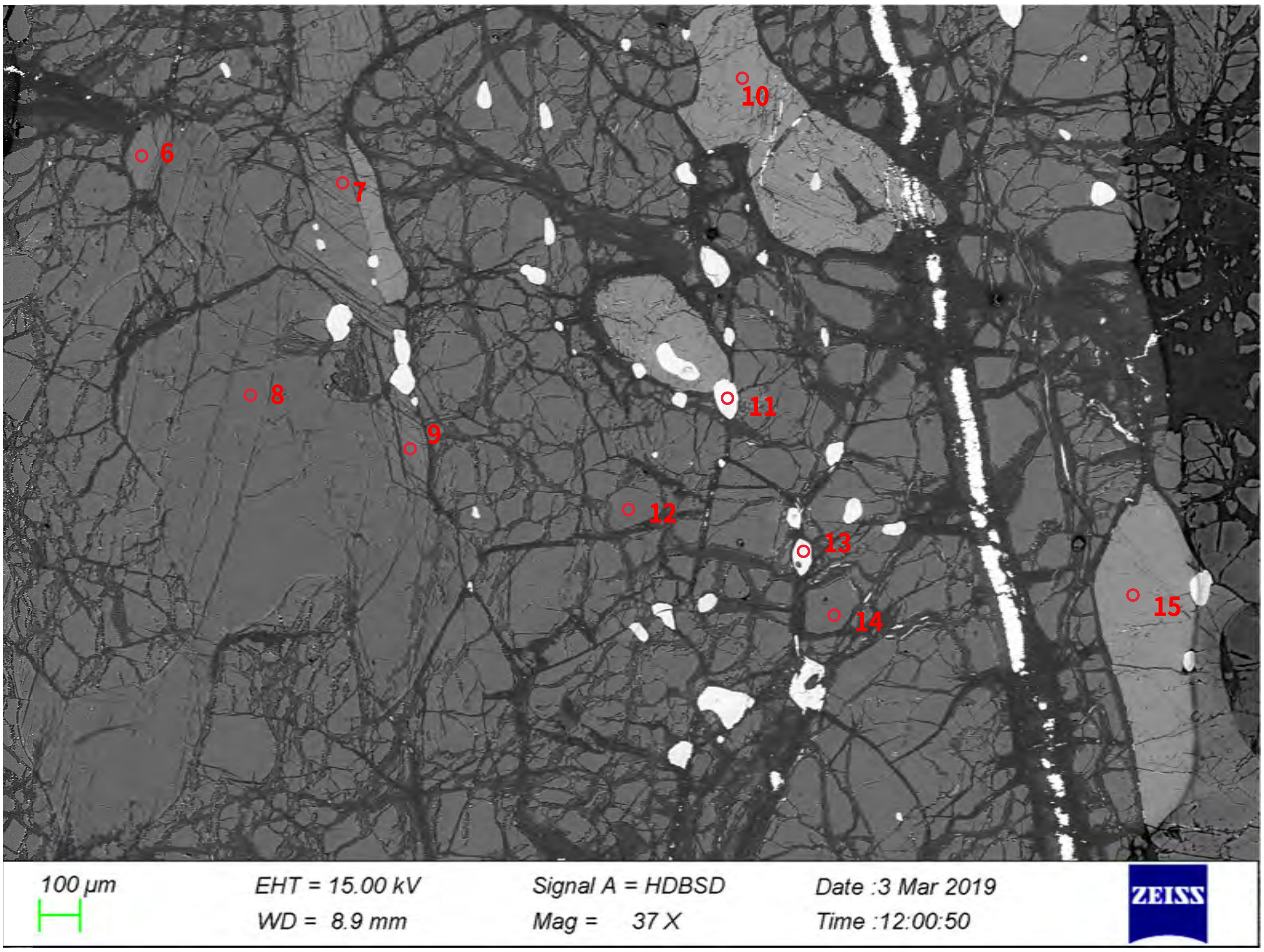

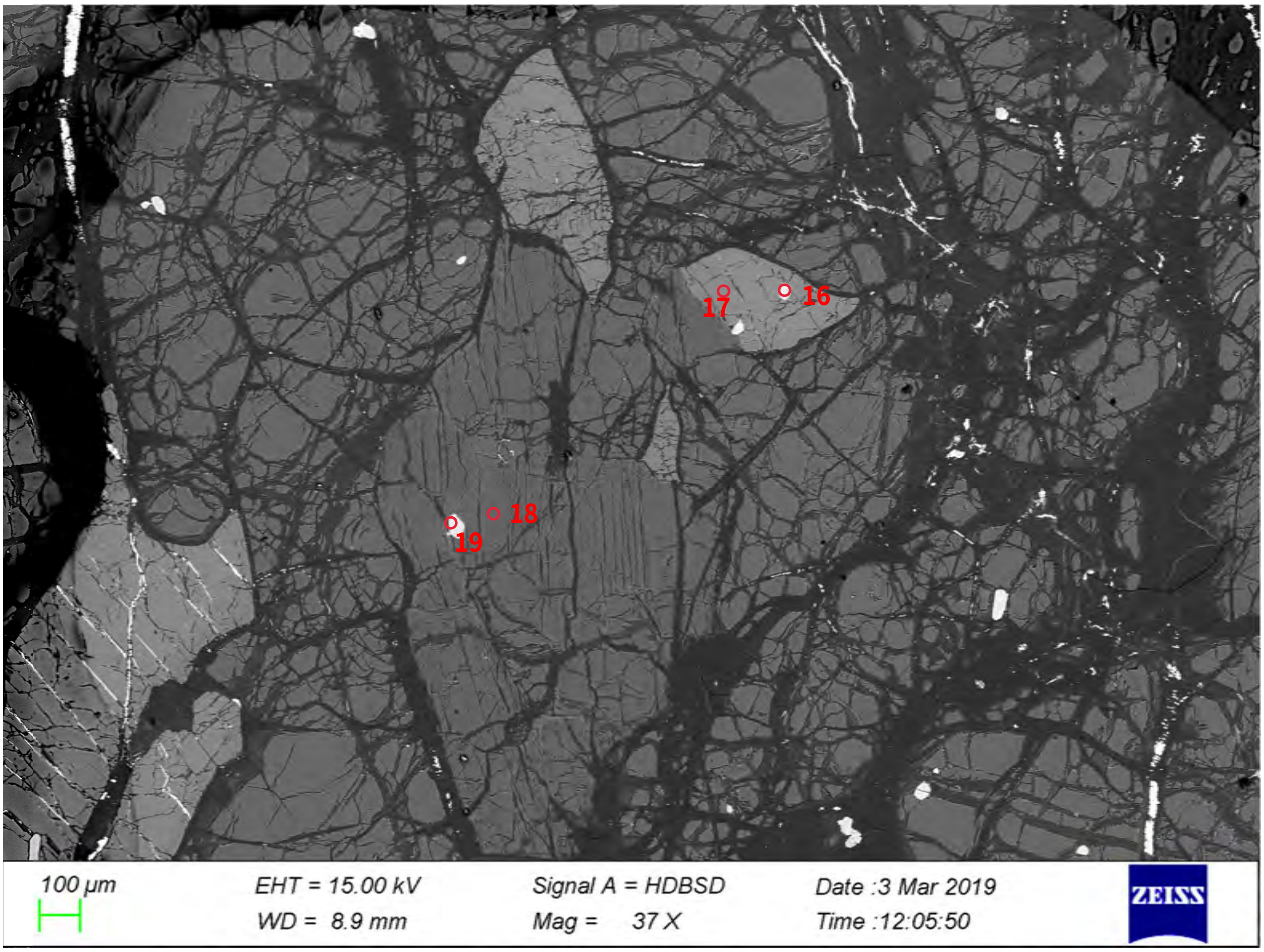
17
16
18
19
100 µm
EHT = 15.00 kV
WD = 8.9 mm
Signal A = HDBSD
Mag = 37 X
Date :3 Mar 2019
Time :12:05:50
ZEISS

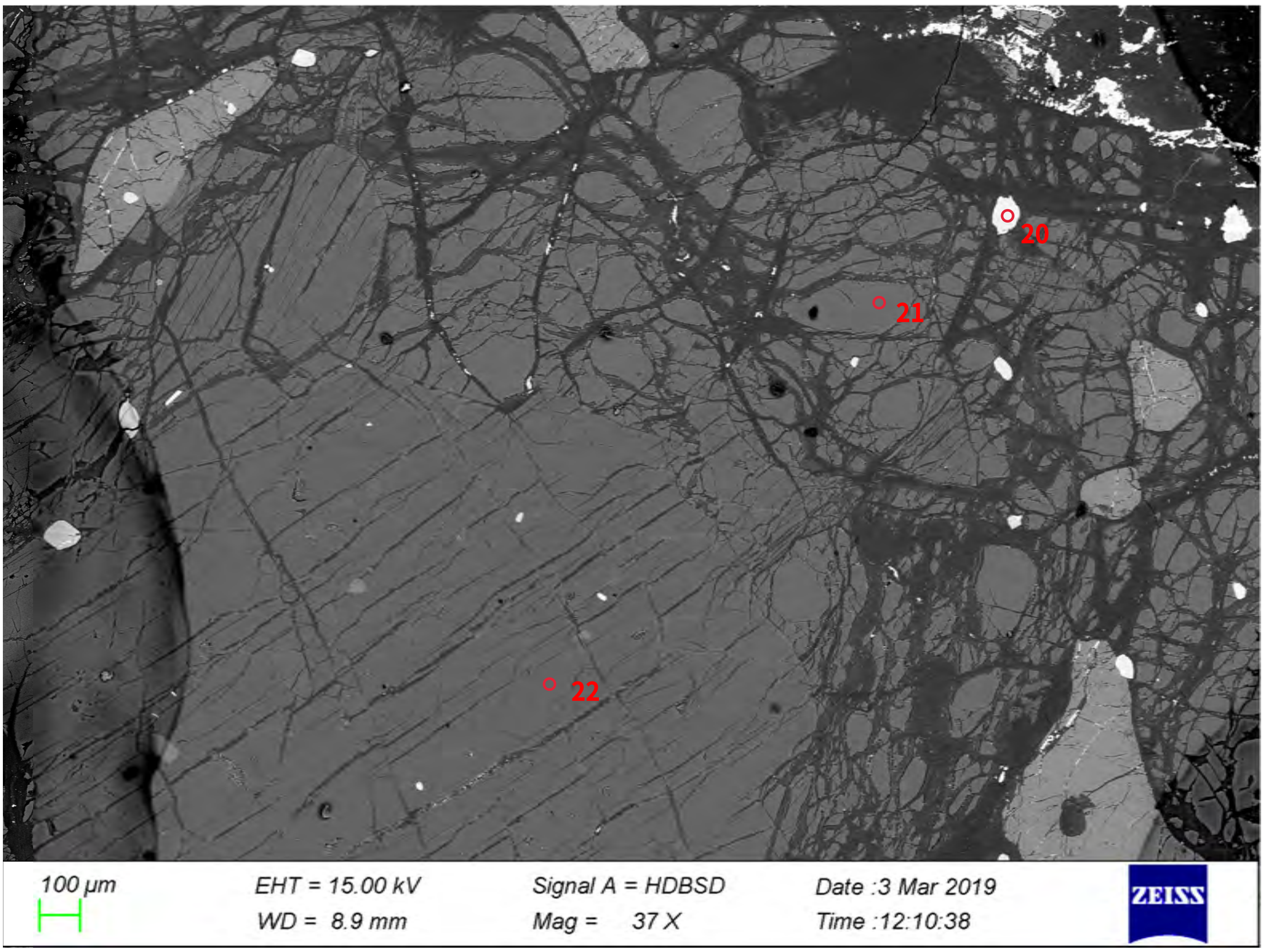
20
21
22
100 µm
EHT = 15.00 kV
WD = 8.9 mm
Signal A = HDBSD
Mag = 37 X
Date :3 Mar 2019
Time :12:10:38
ZEISS

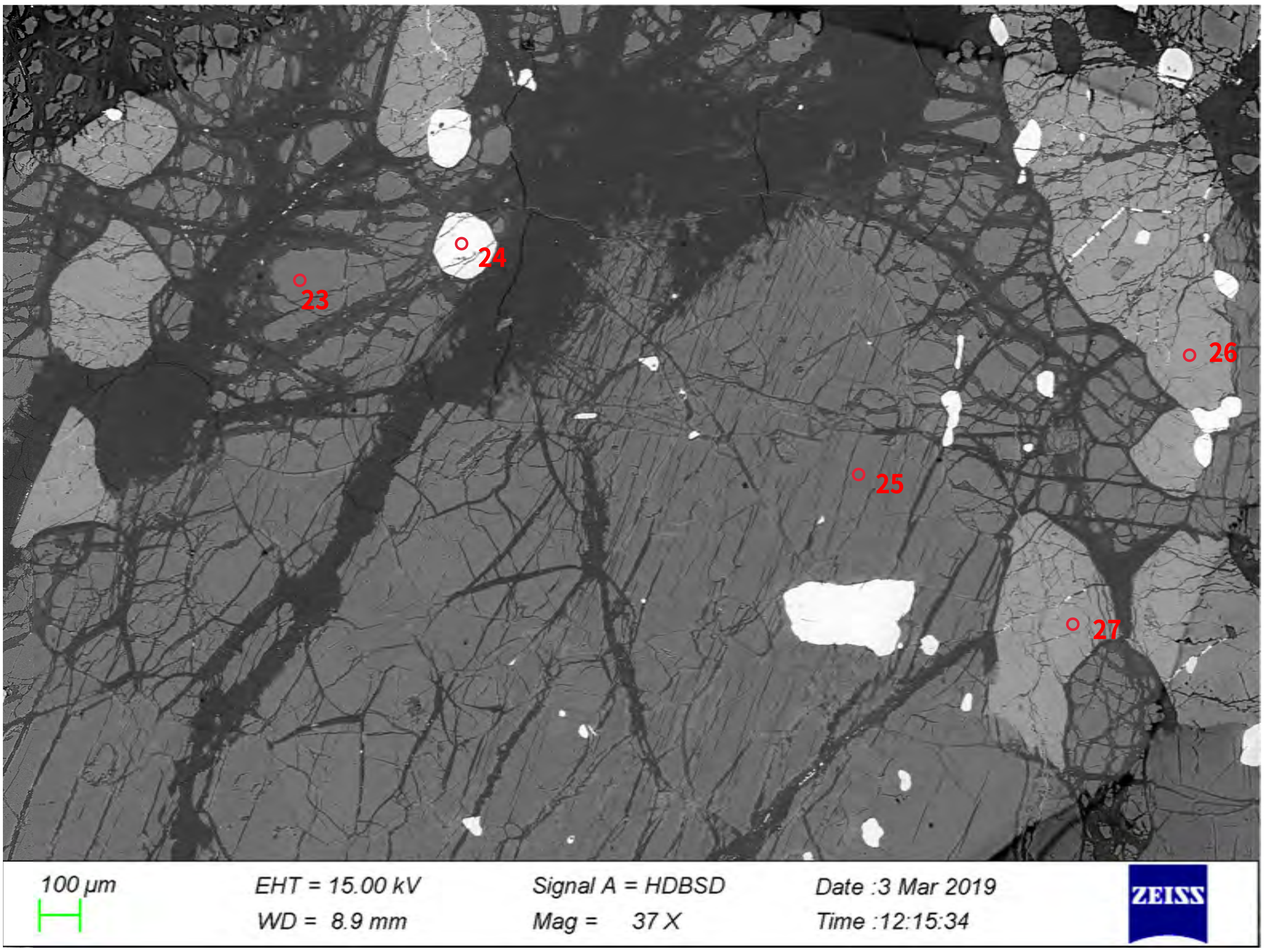
23
24
25
26
27
100 µm
EHT = 15.00 kV
WD = 8.9 mm
Signal A = HDBSD
Mag = 37 X
Date :3 Mar 2019
Time :12:15:34
ZEISS

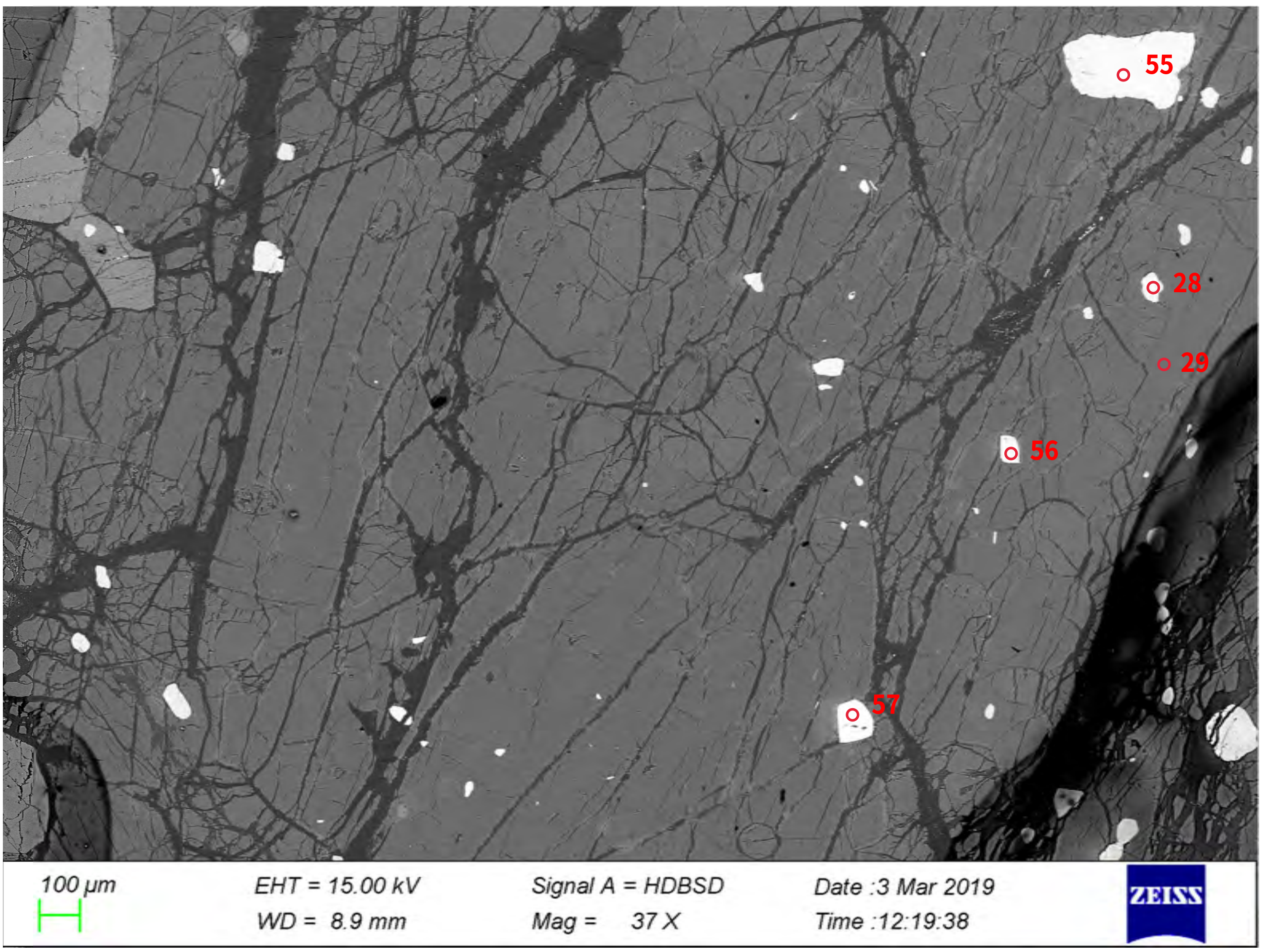
55
28
29
56
57
100 µm
EHT = 15.00 kV
WD = 8.9 mm
Signal A = HDBSD
Mag = 37 X
Date :3 Mar 2019
Time :12:19:38
ZEISS

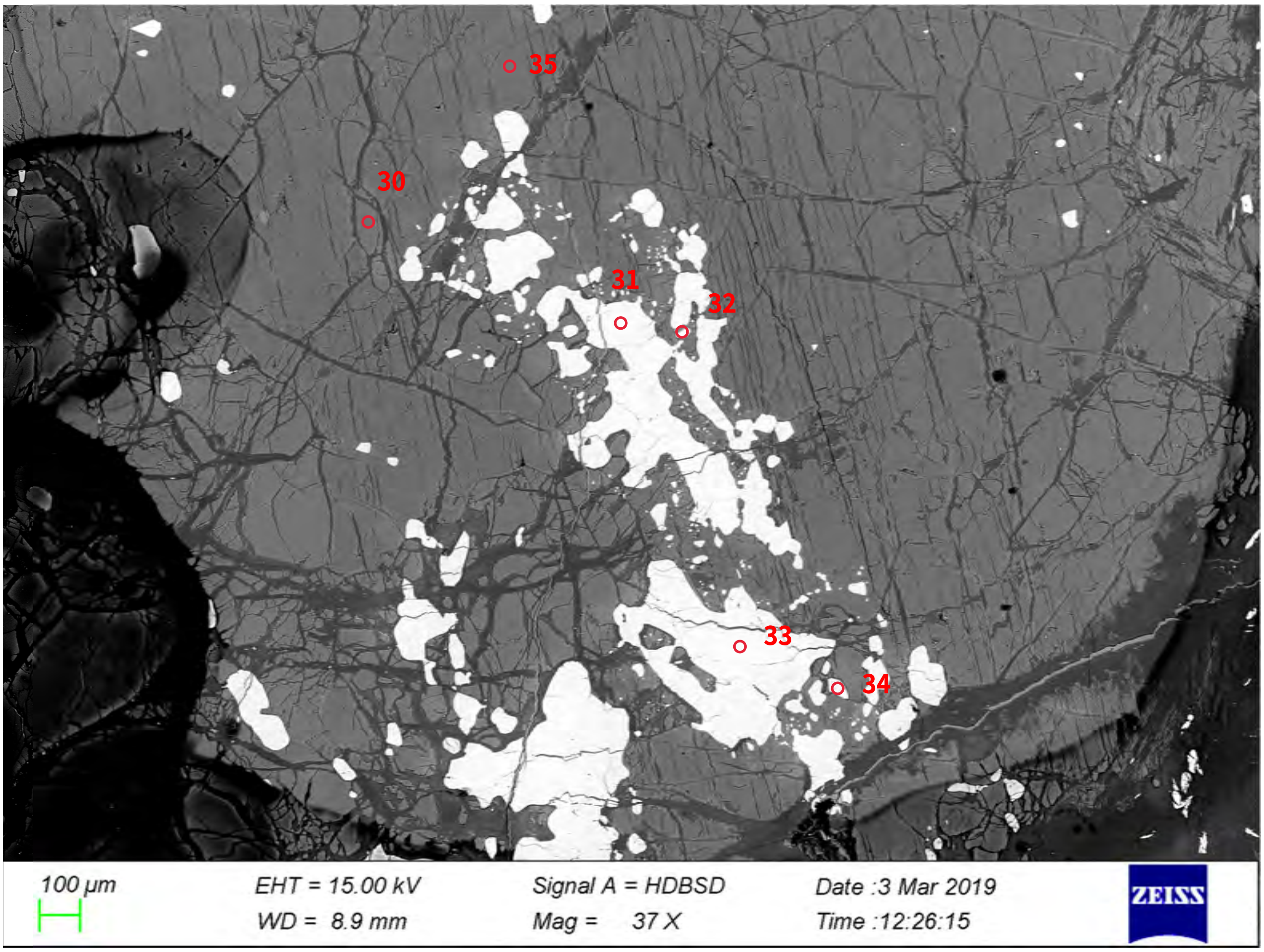
35
30
31
32
33
34
100 µm
EHT = 15.00 kV
WD = 8.9 mm
Signal A = HDBSD
Mag = 37 X
Date :3 Mar 2019
Time :12:26:15
ZEISS

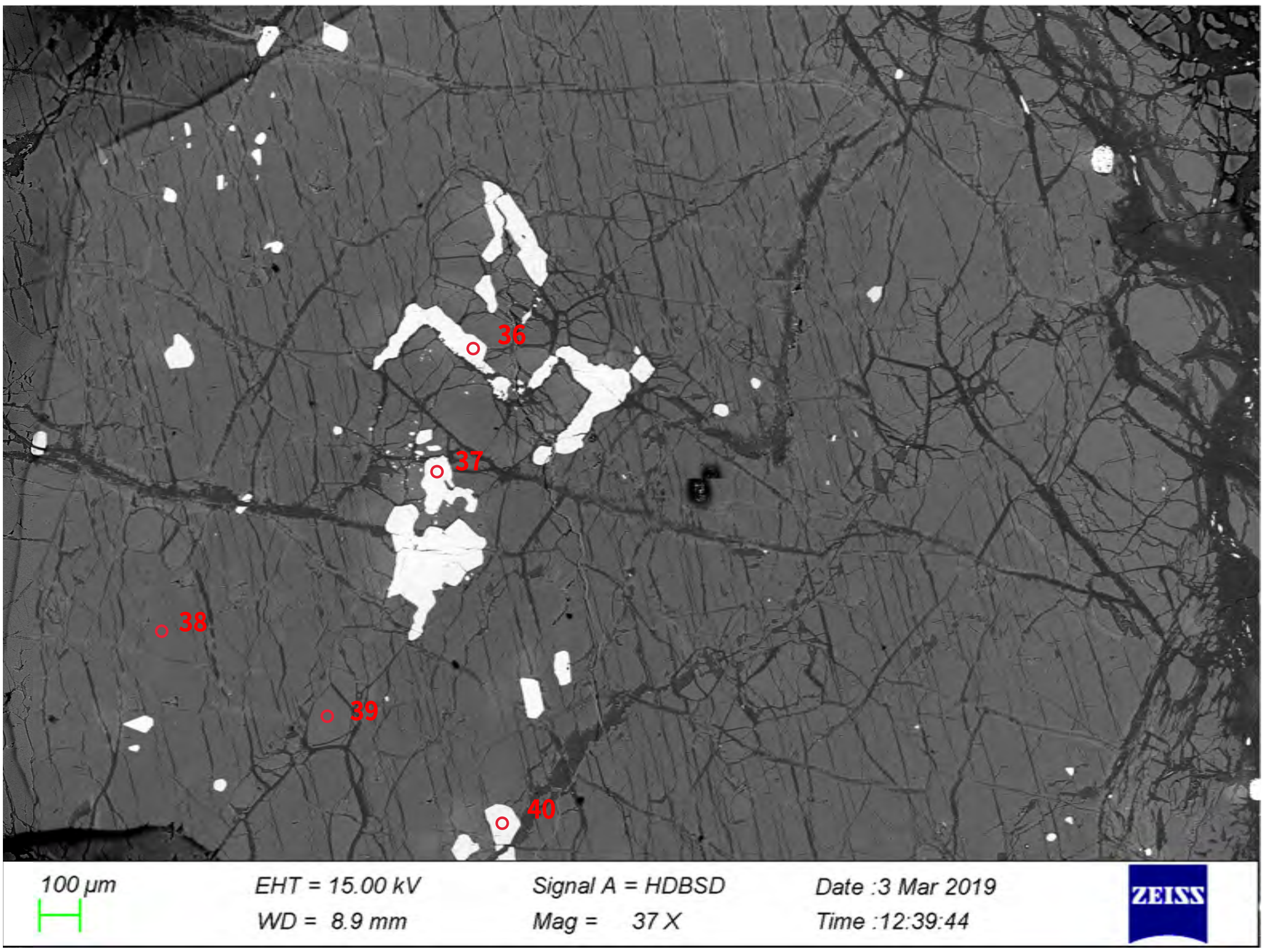
36
37
38
39
40
100 µm
EHT = 15.00 kV
WD = 8.9 mm
Signal A = HDBSD
Mag = 37 X
Date :3 Mar 2019
Time :12:39:44
ZEISS

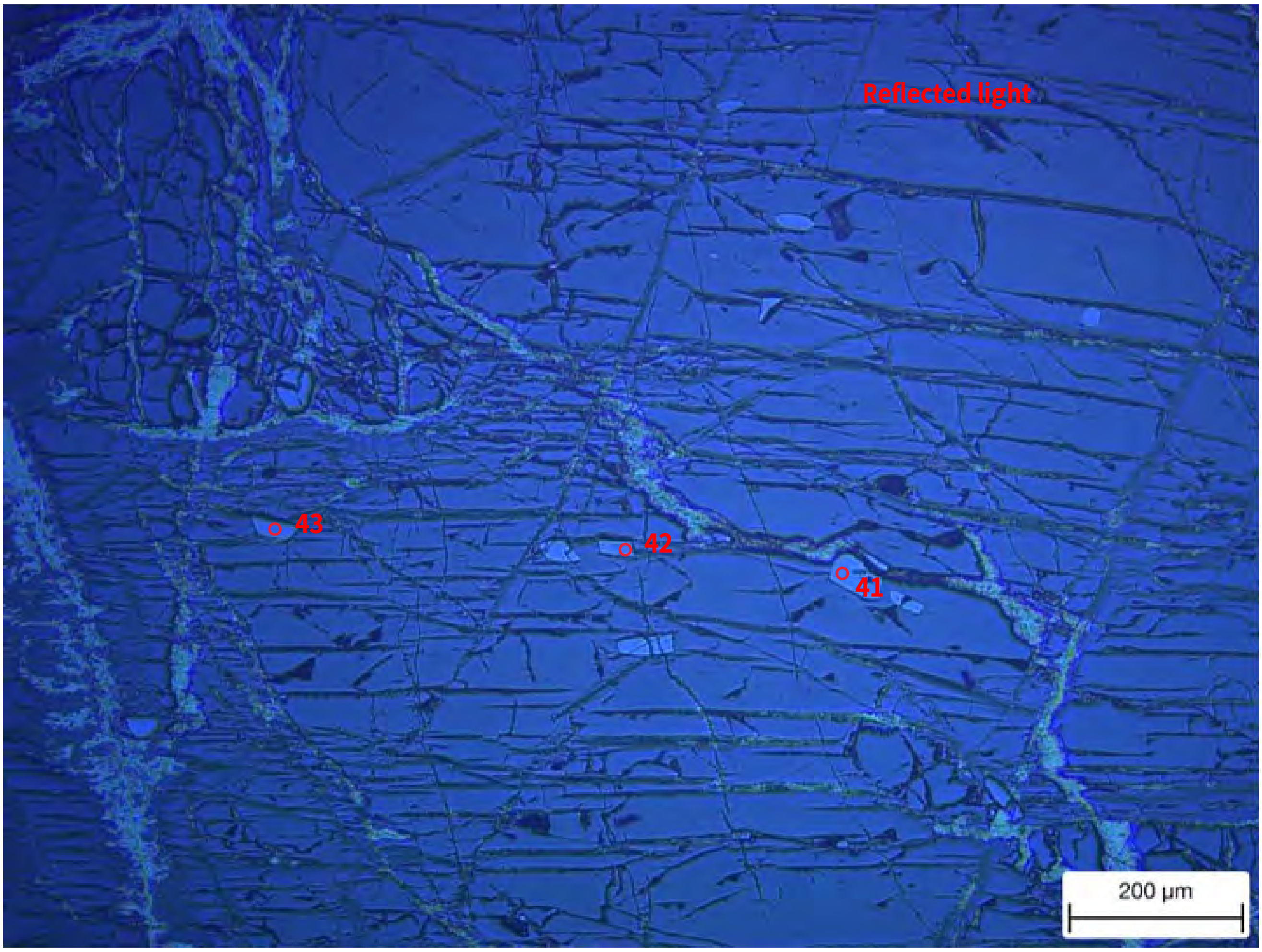
Reflected light
43
42
41
200 µm

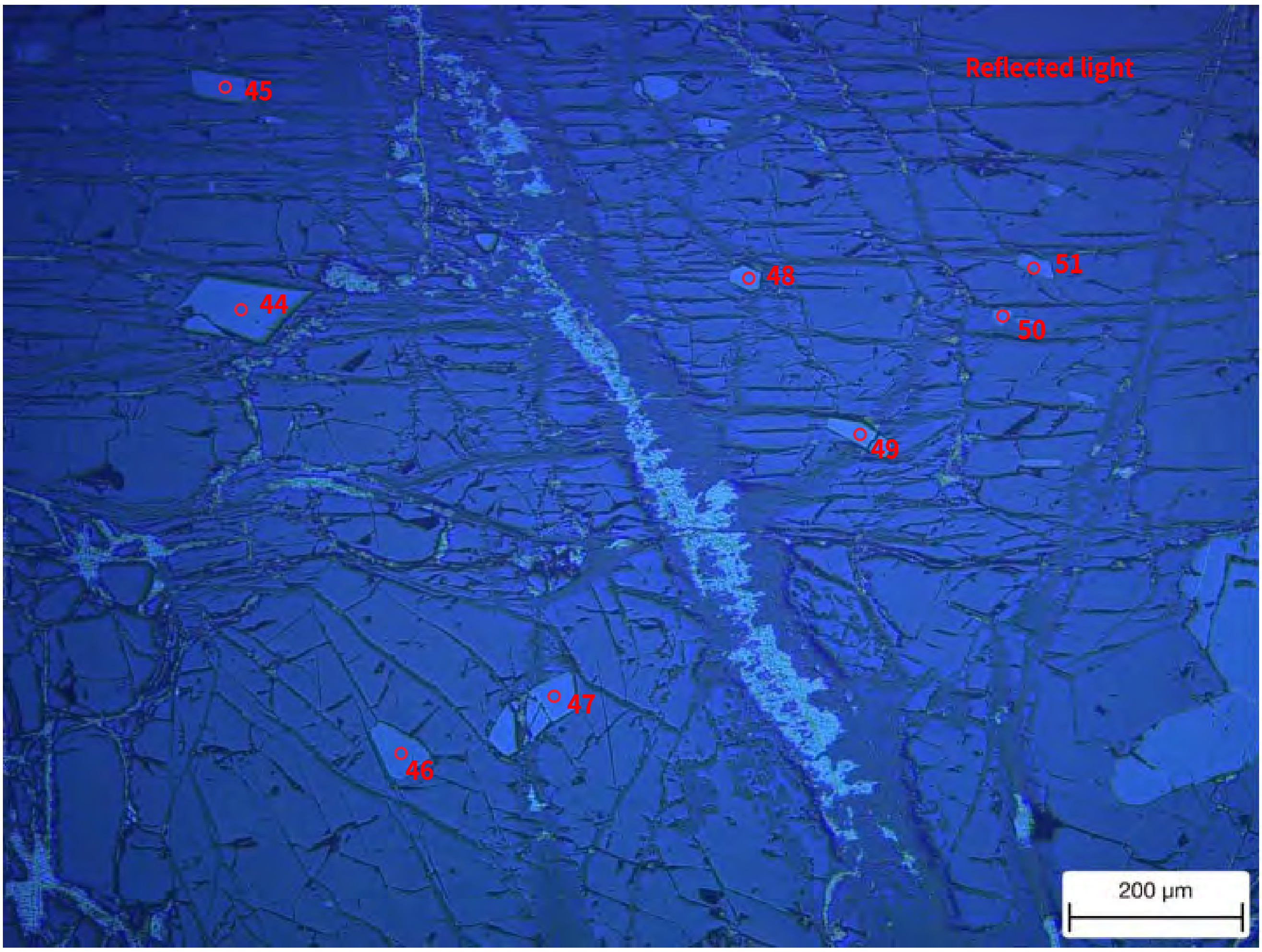
45
Reflected light
48
51
44
50
49
47
46
200 µm

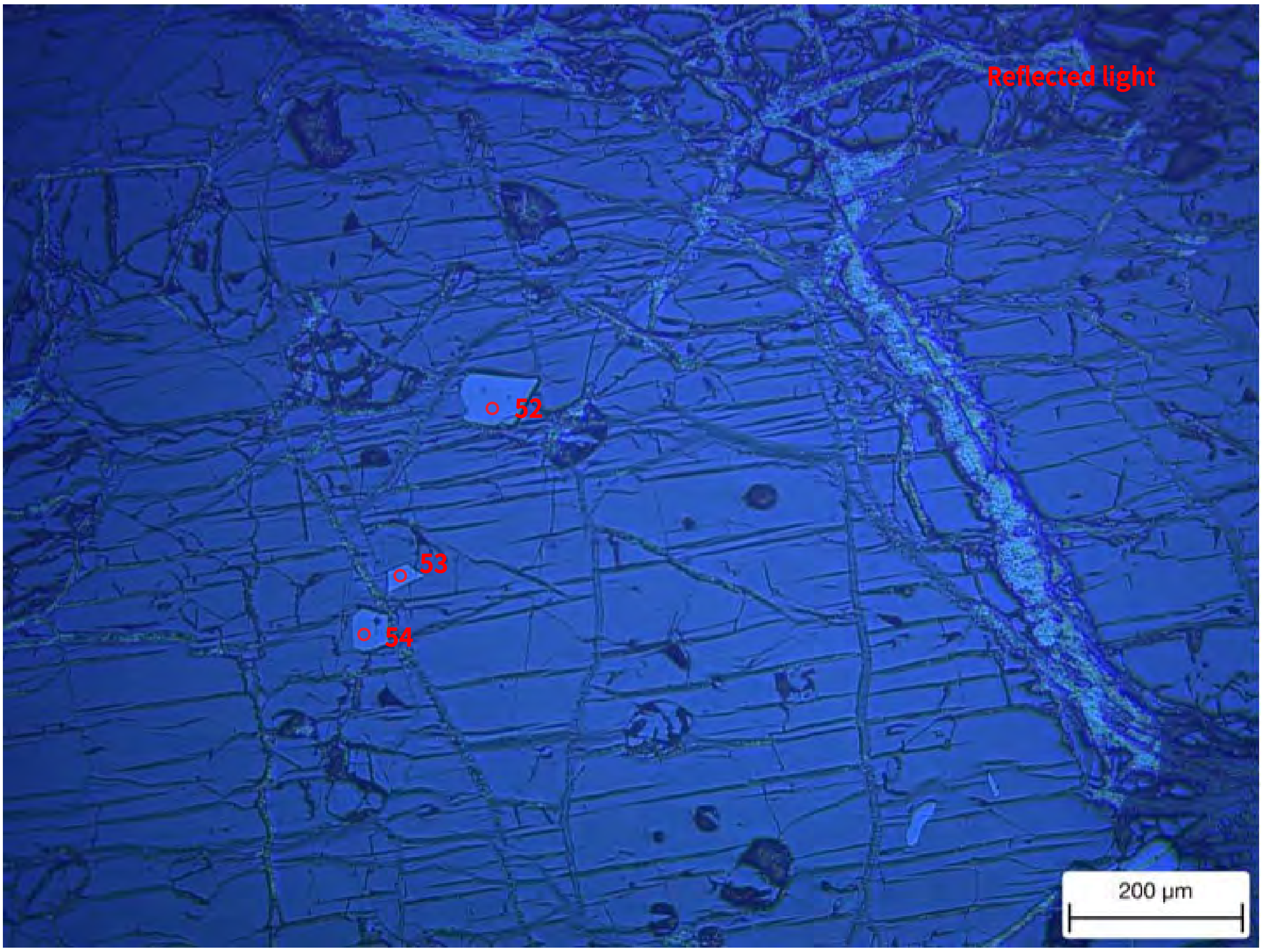
Reflected light
52
53
54
200 μm

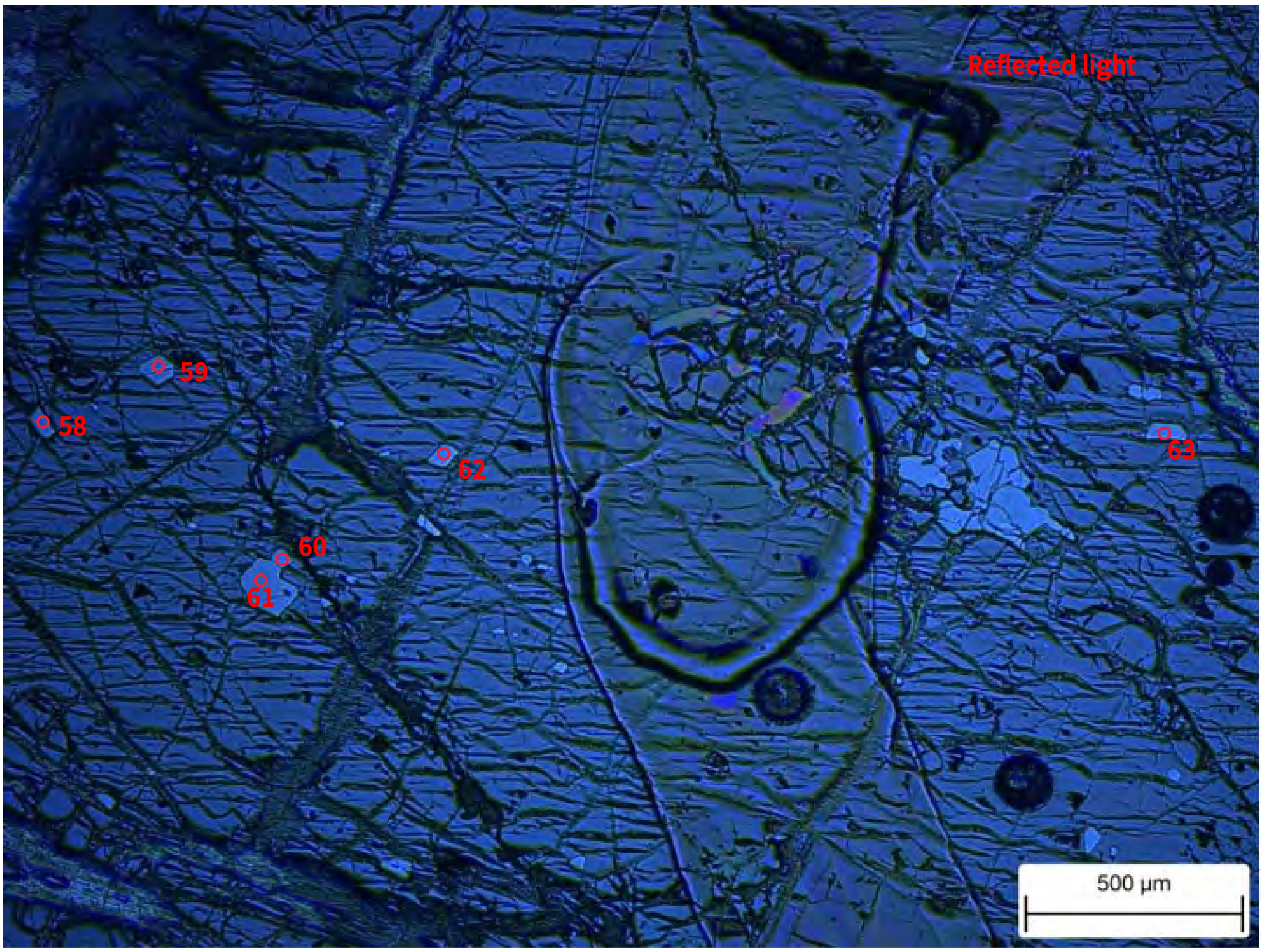
Reflected light
59
58
62
63
60
61
500 μm

Sample C17-59

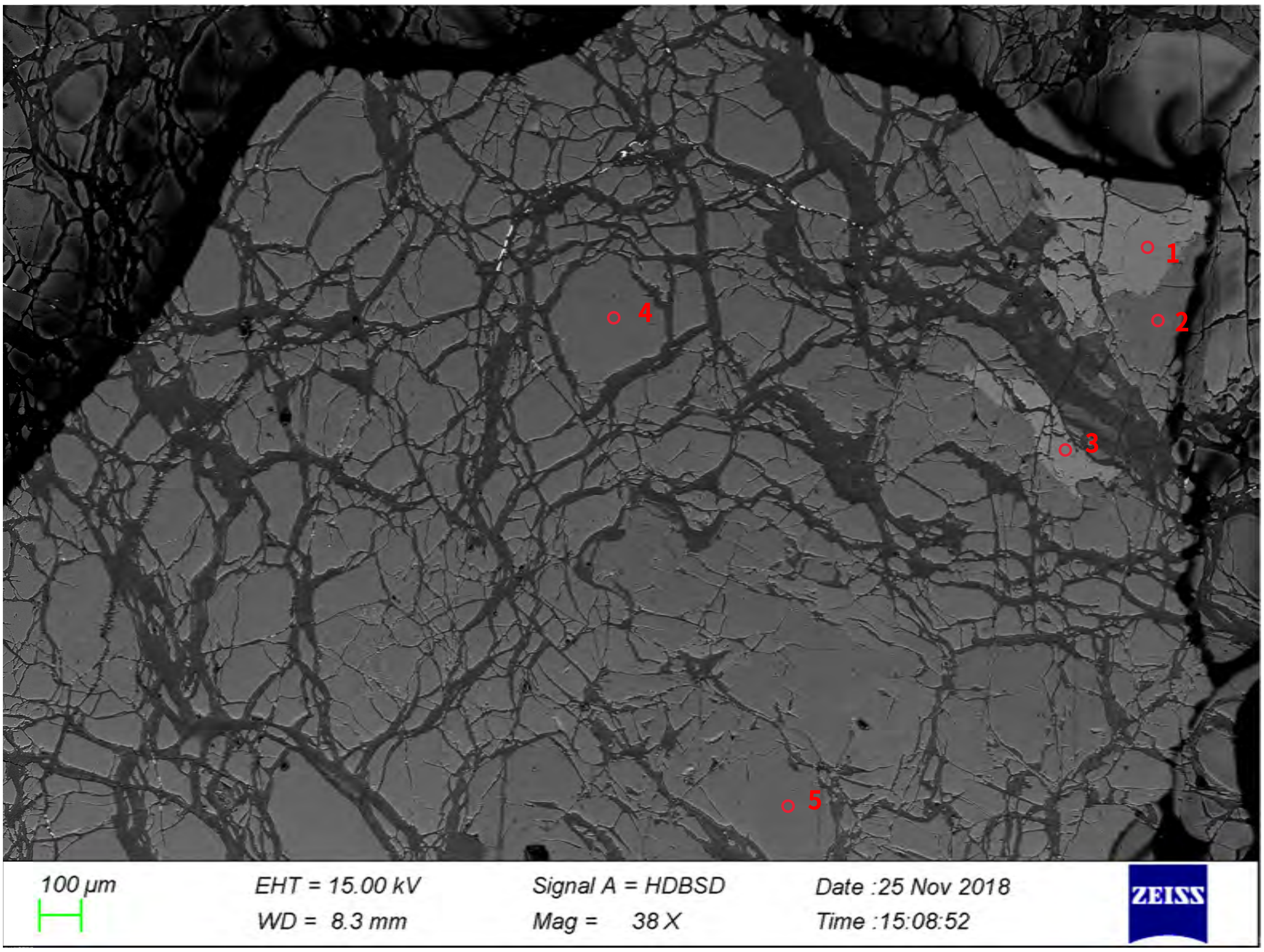

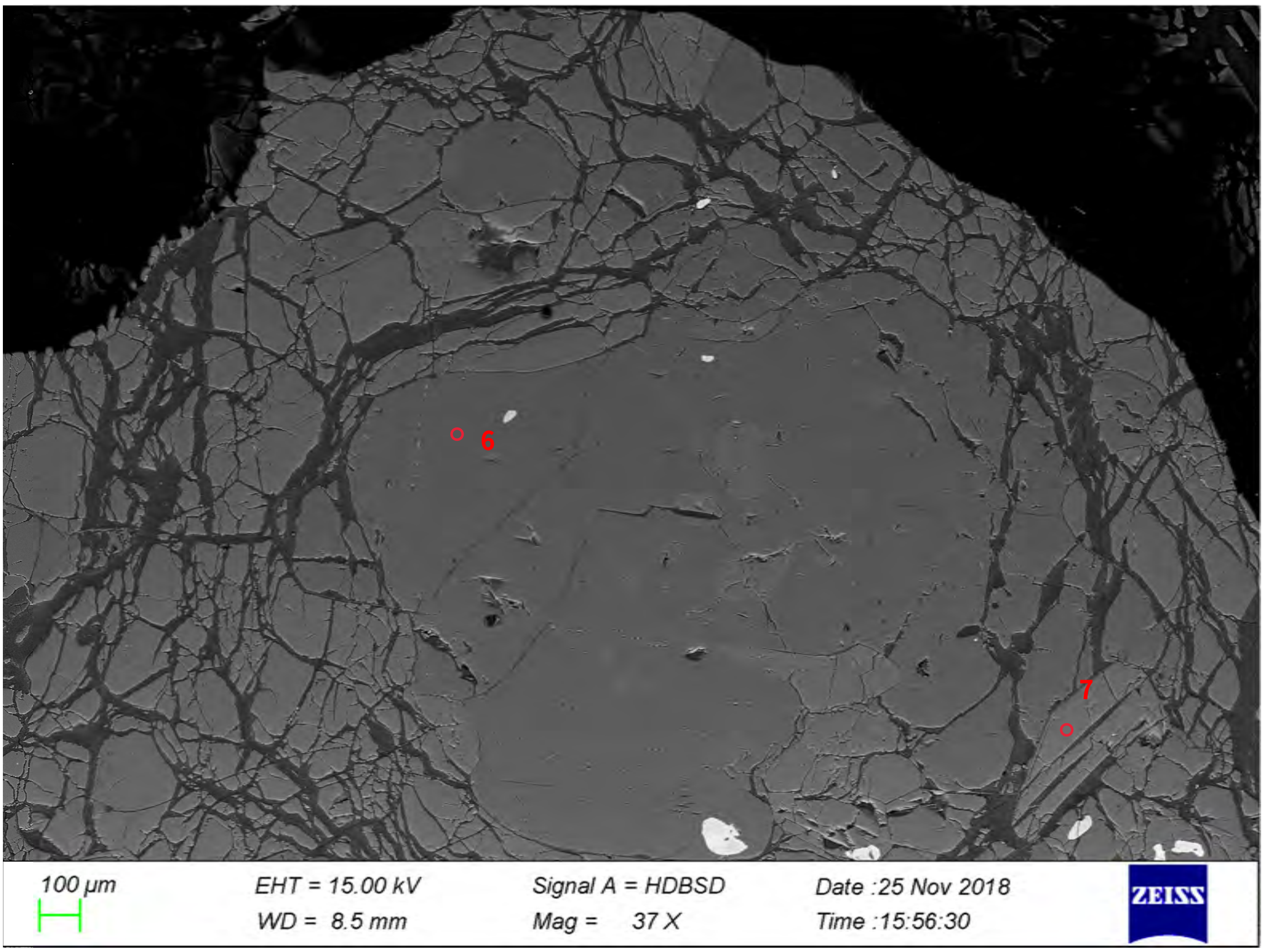

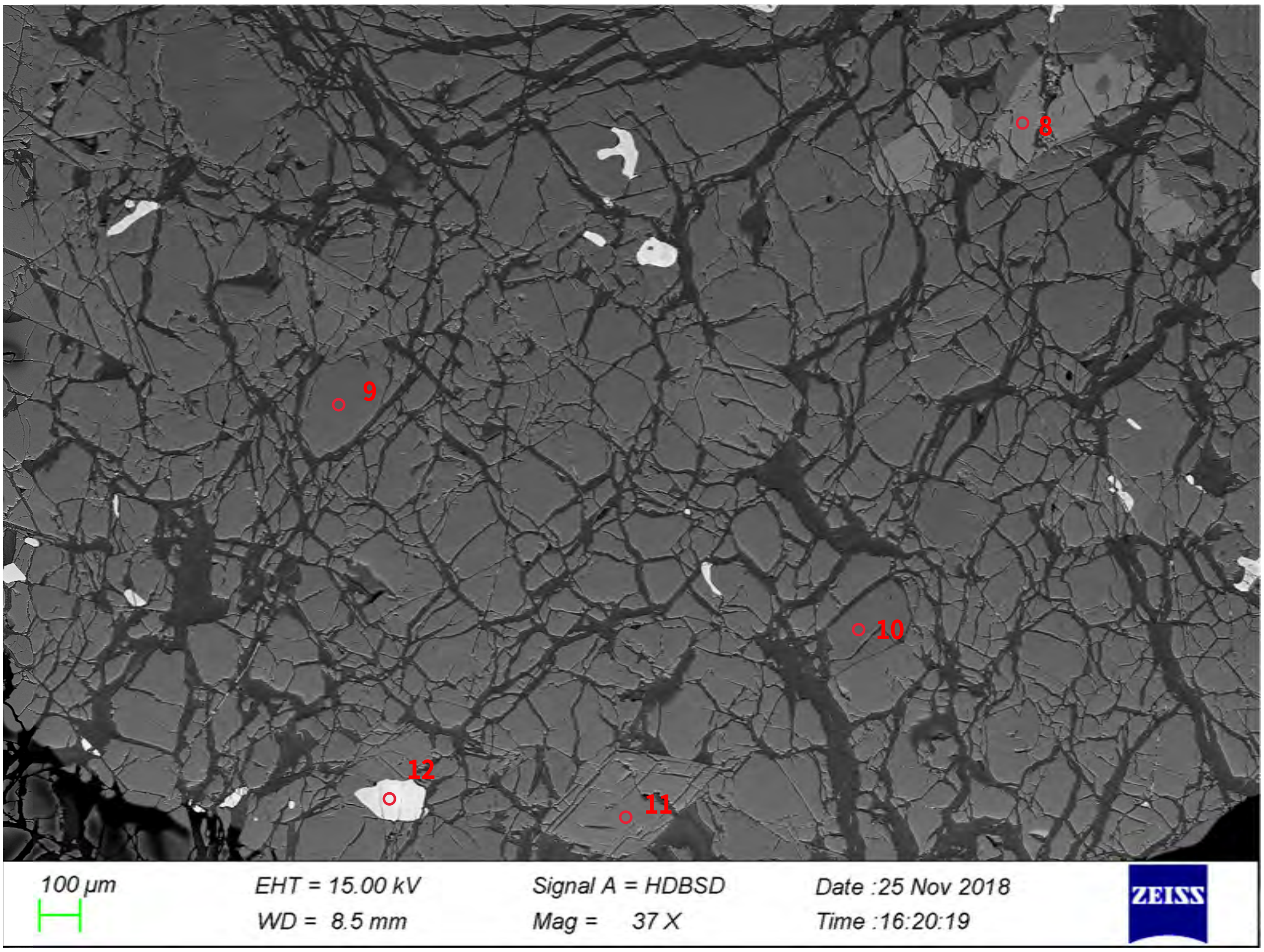
8
9
10
11
12
100 µm
EHT = 15.00 kV
WD = 8.5 mm
Signal A = HDBSD
Mag = 37 X
Date :25 Nov 2018
Time :16:20:19
ZEISS

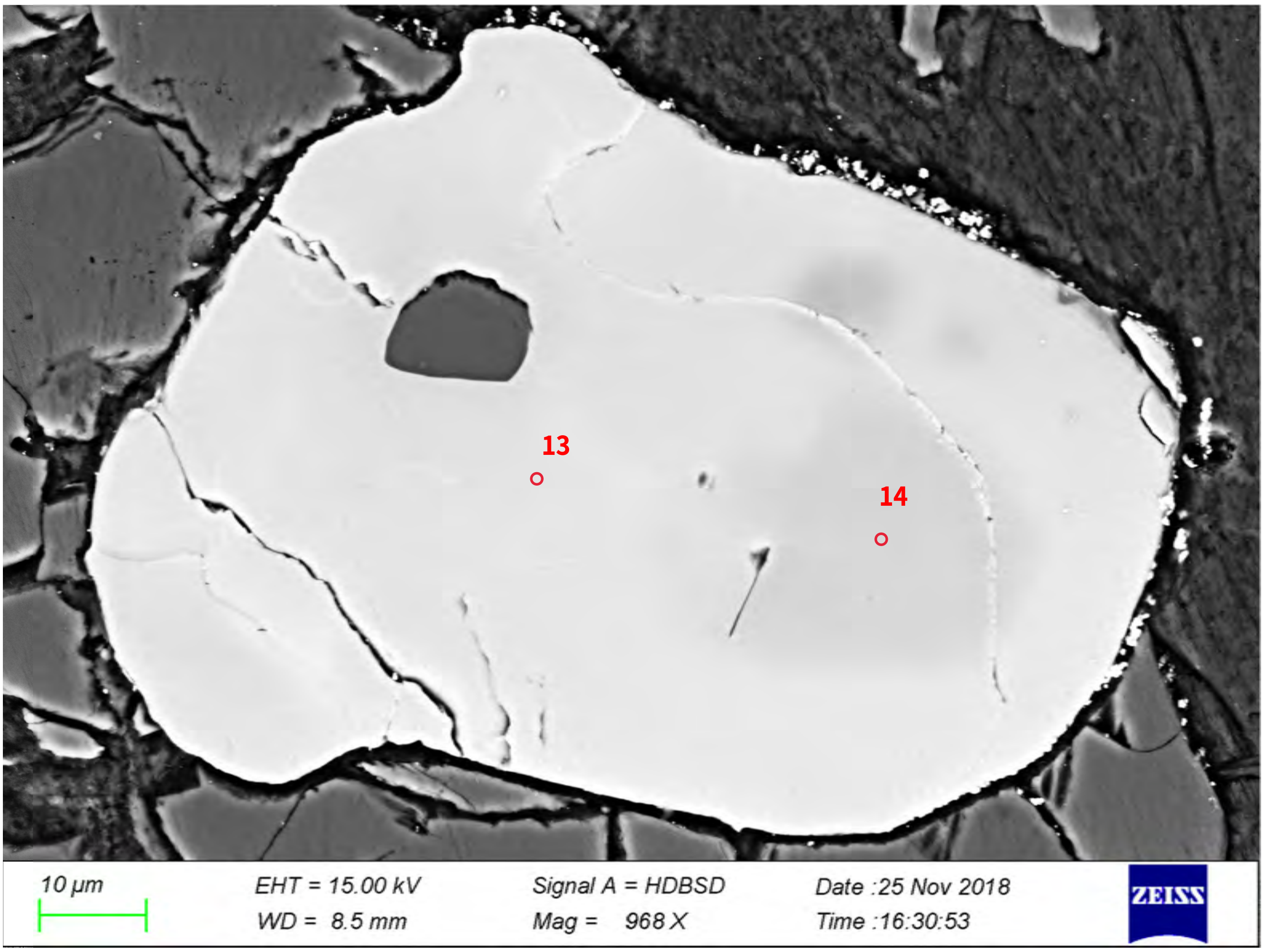
13
14
10 µm
EHT = 15.00 kV
WD = 8.5 mm
Signal A = HDBSD
Mag = 968 X
Date :25 Nov 2018
Time :16:30:53
ZEISS

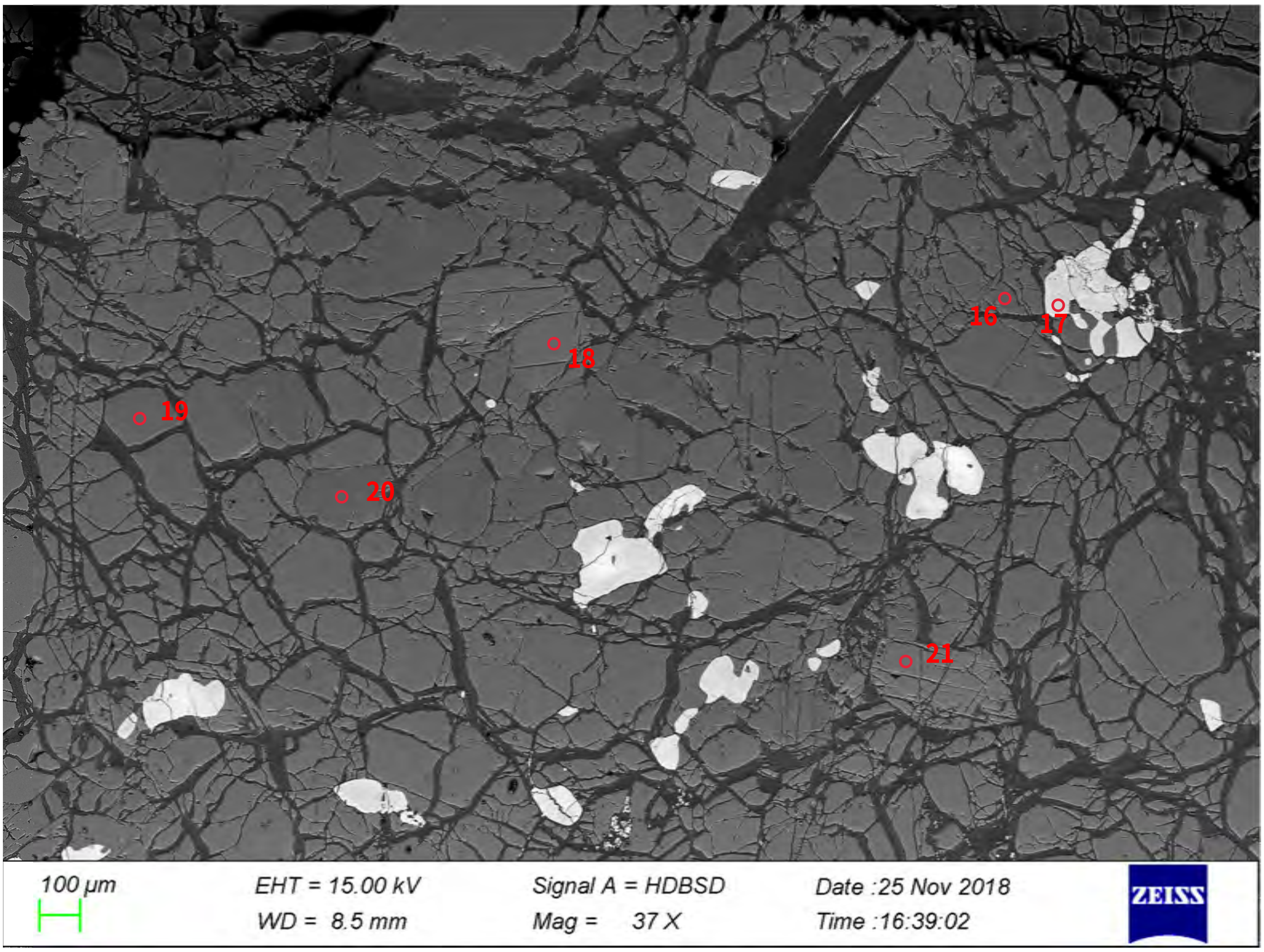
16
17
18
19
20
21
100 µm
EHT = 15.00 kV
WD = 8.5 mm
Signal A = HDBSD
Mag = 37 X
Date :25 Nov 2018
Time :16:39:02
ZEISS

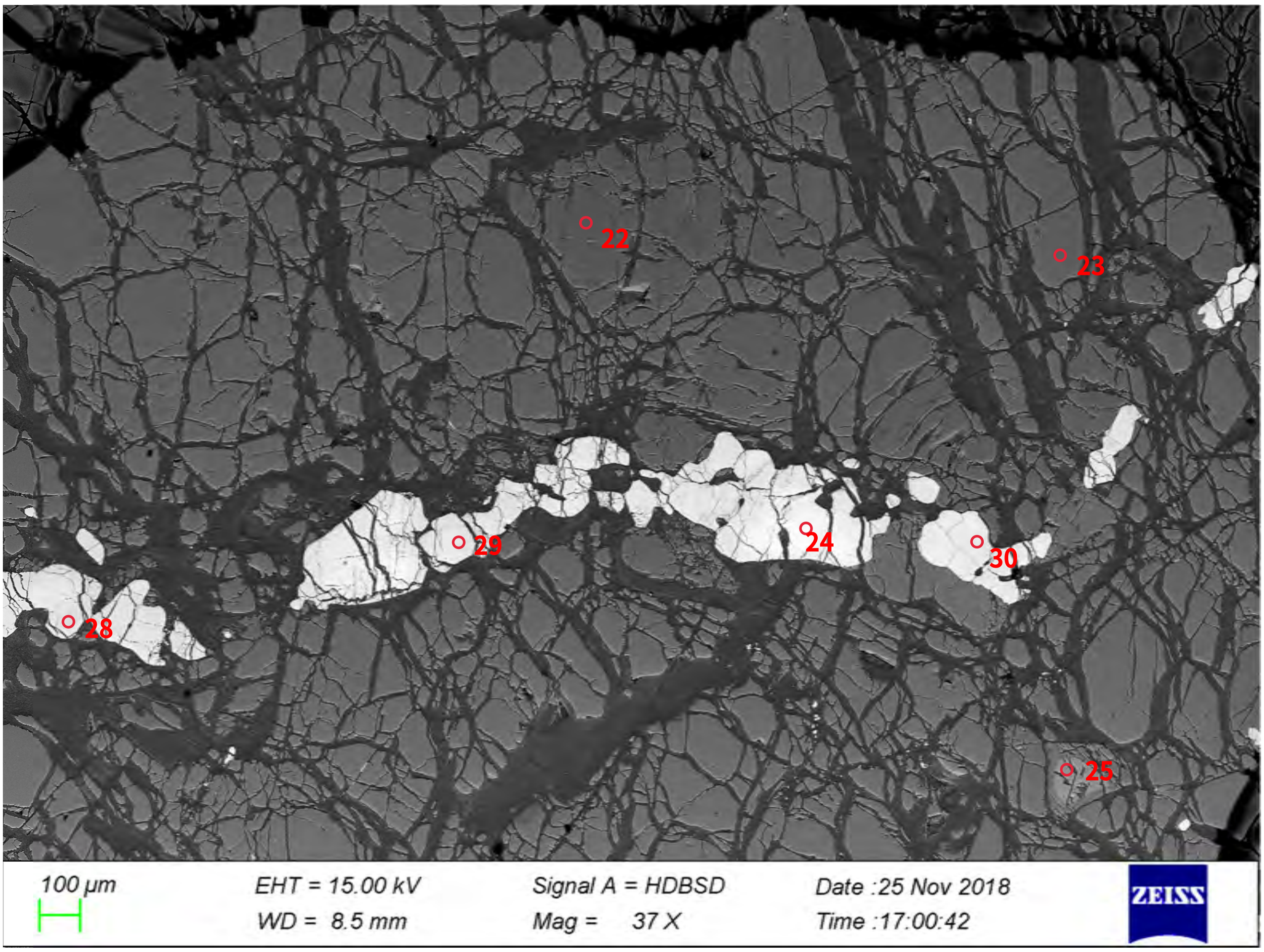
22
23
24
25
28
29
30
100 µm
EHT = 15.00 kV
WD = 8.5 mm
Signal A = HDBSD
Mag = 37 X
Date :25 Nov 2018
Time :17:00:42
ZEISS

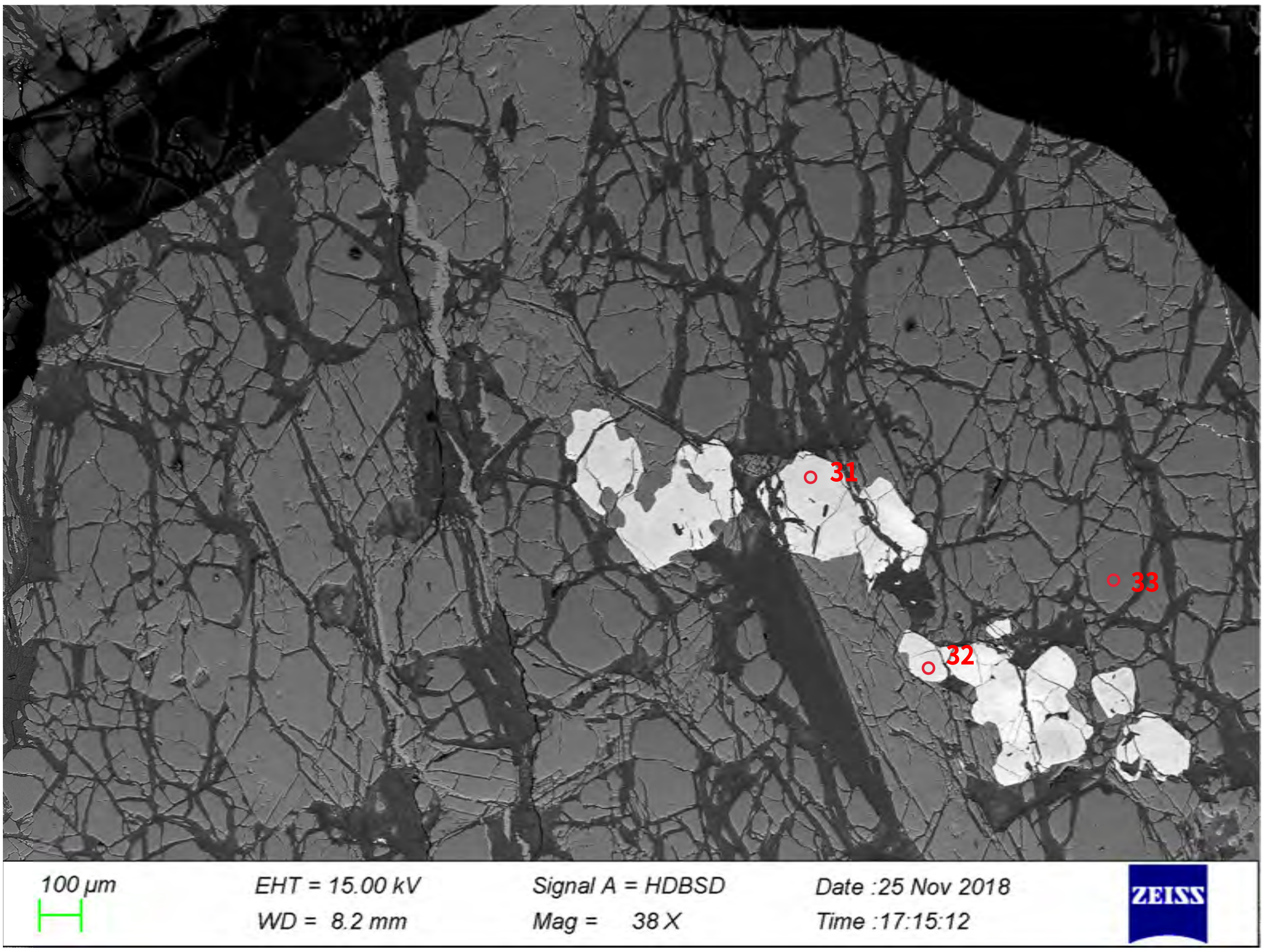
31
32
33
100 µm
EHT = 15.00 kV
WD = 8.2 mm
Signal A = HDBSD
Mag = 38 X
Date :25 Nov 2018
Time :17:15:12
ZEISS

Sample C17-62

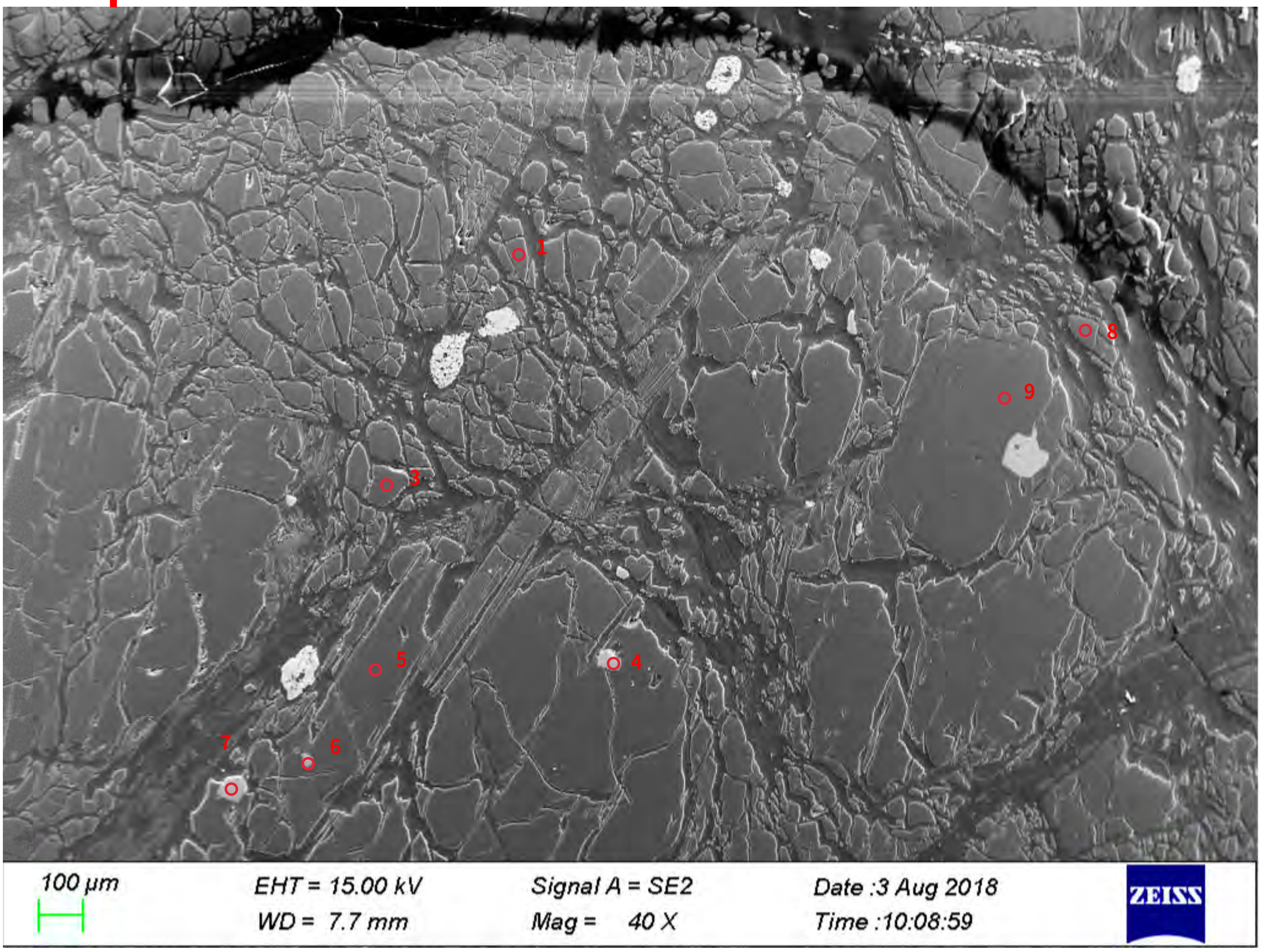

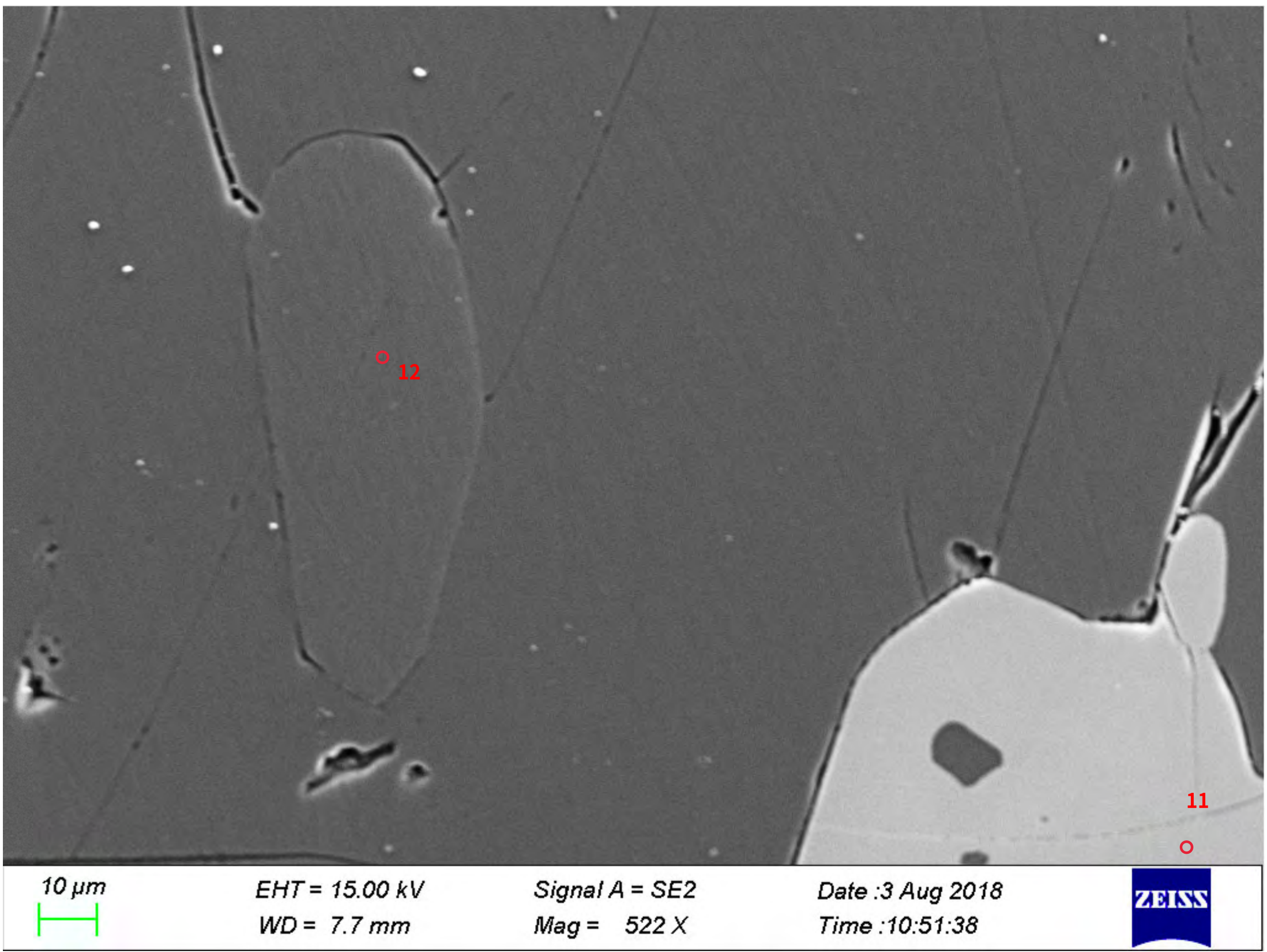

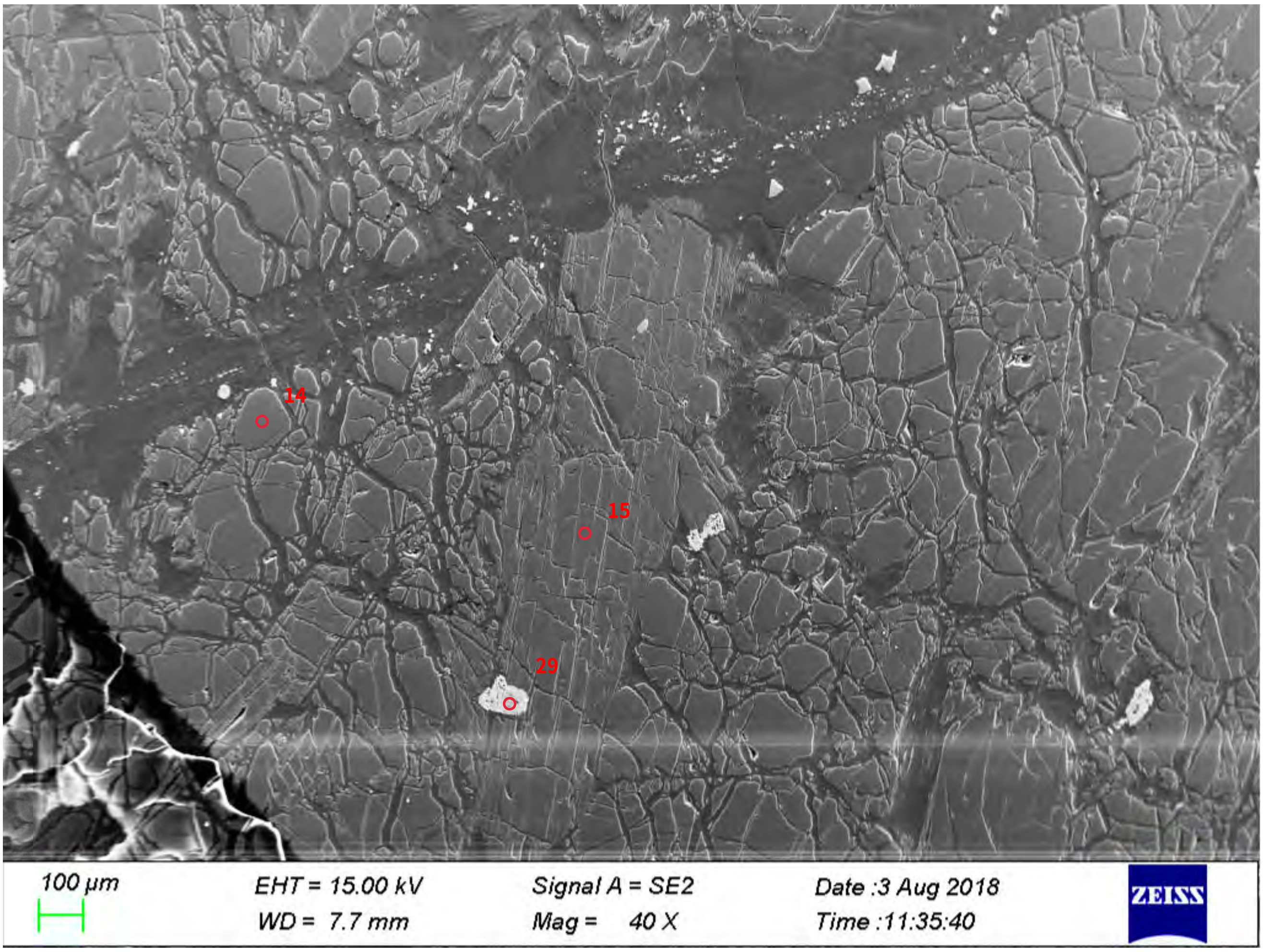
14
15
29
100 µm
EHT = 15.00 kV
WD = 7.7 mm
Signal A = SE2
Mag = 40 X
Date :3 Aug 2018
Time :11:35:40
ZEISS

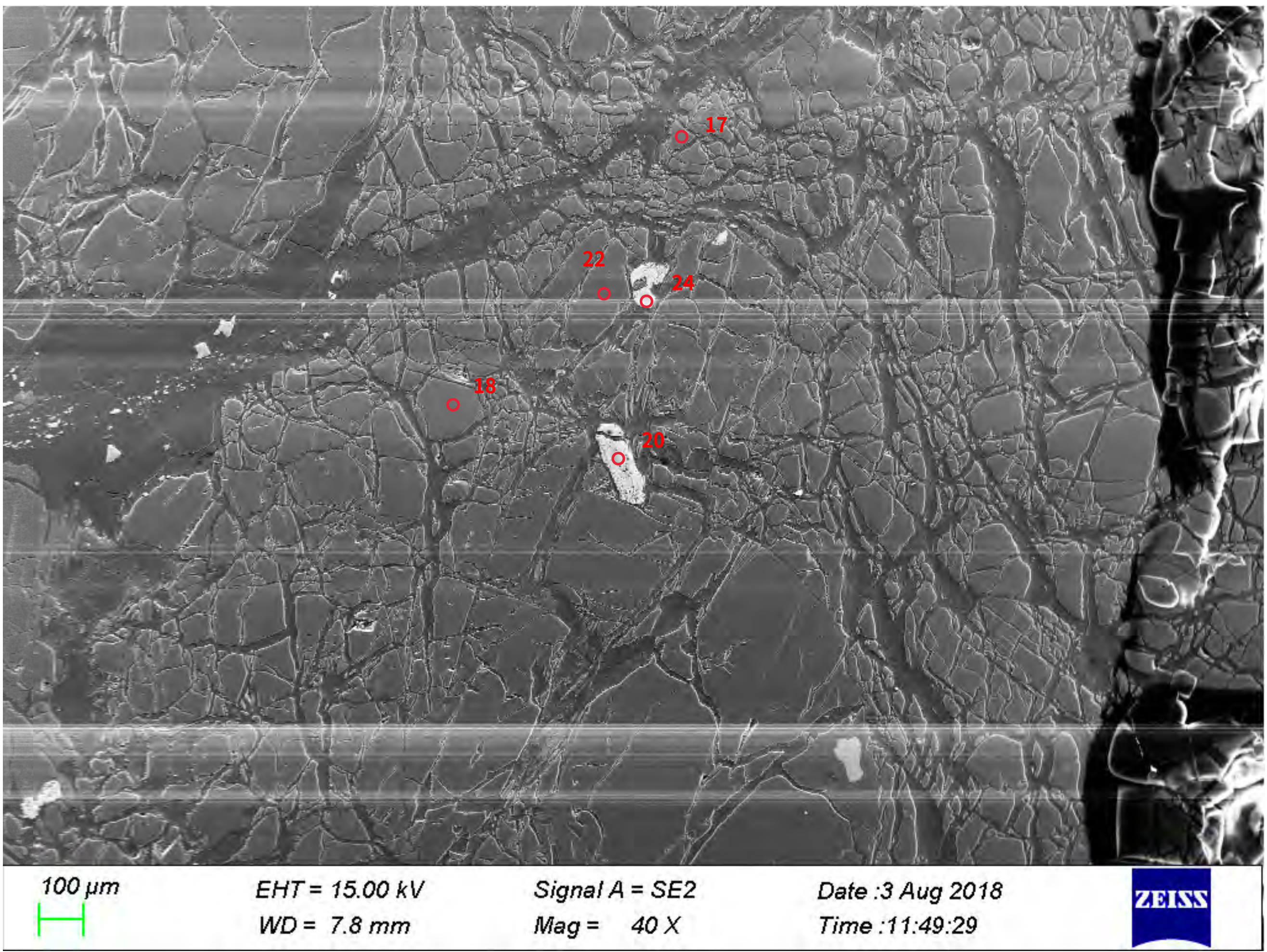
17
22
24
18
20
100 µm
EHT = 15.00 kV
WD = 7.8 mm
Signal A = SE2
Mag = 40 X
Date :3 Aug 2018
Time :11:49:29
ZEISS

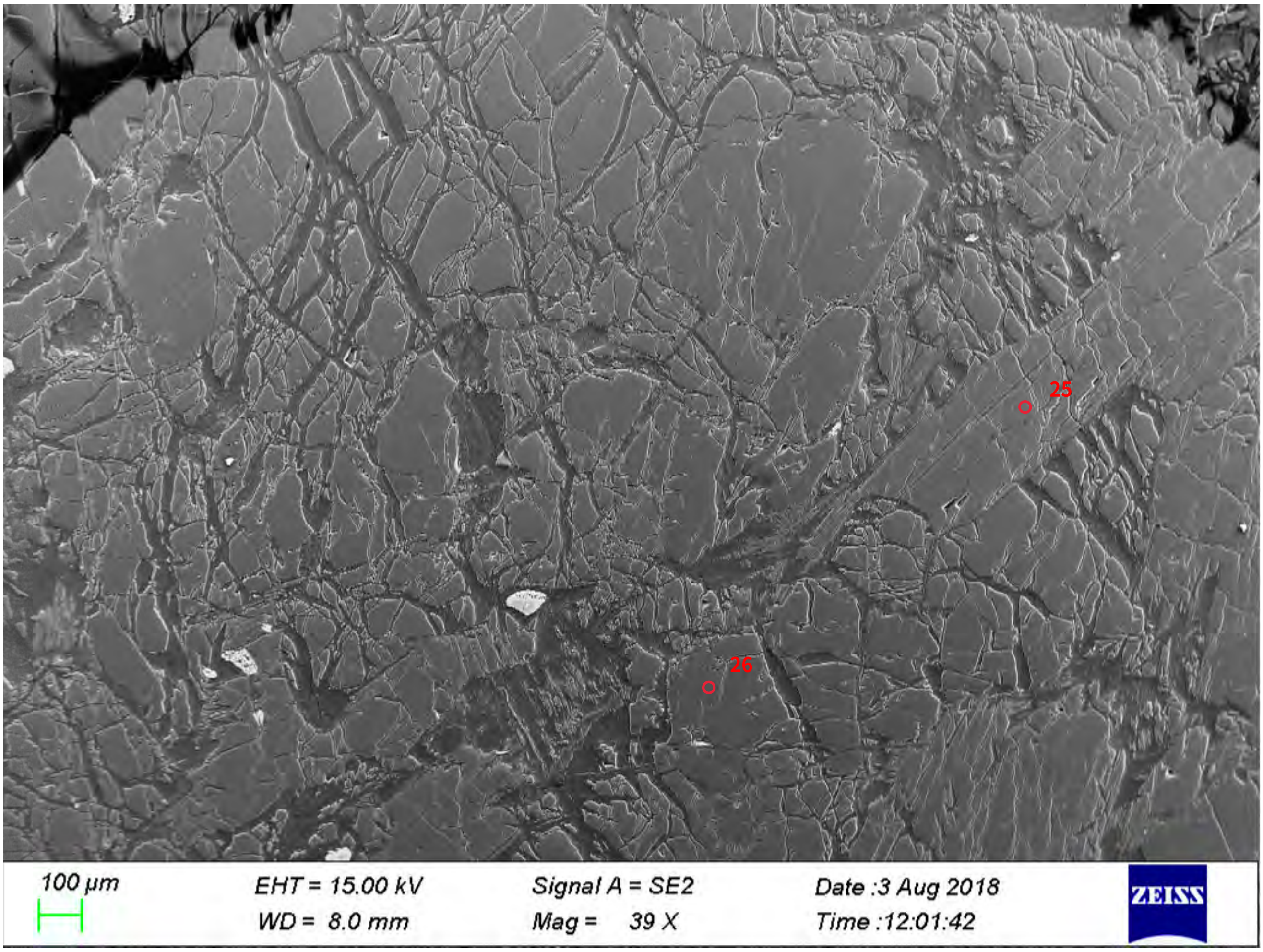
25
26
100 µm
EHT = 15.00 kV
WD = 8.0 mm
Signal A = SE2
Mag = 39 X
Date :3 Aug 2018
Time :12:01:42
ZEISS

Sample C17-63

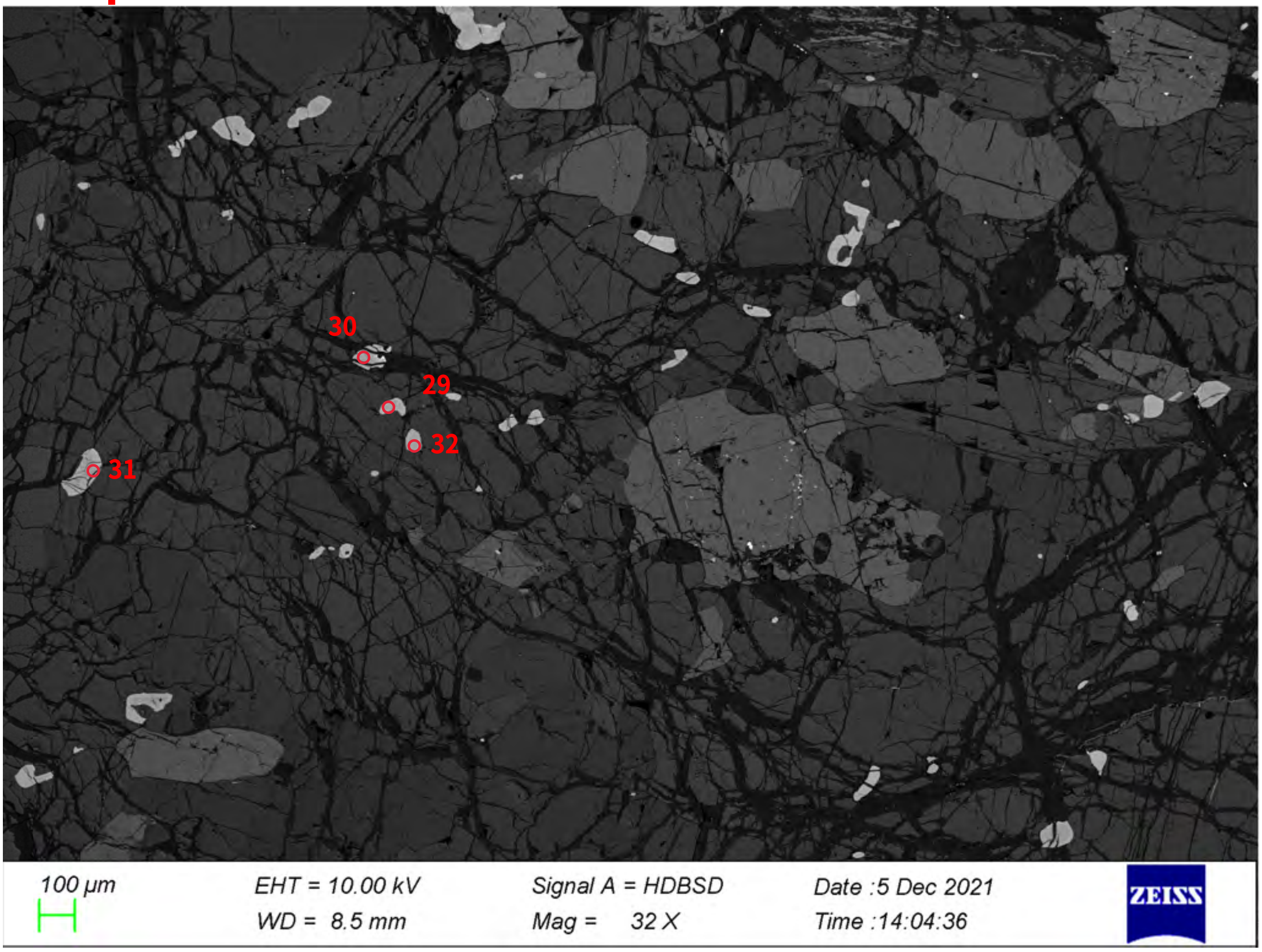

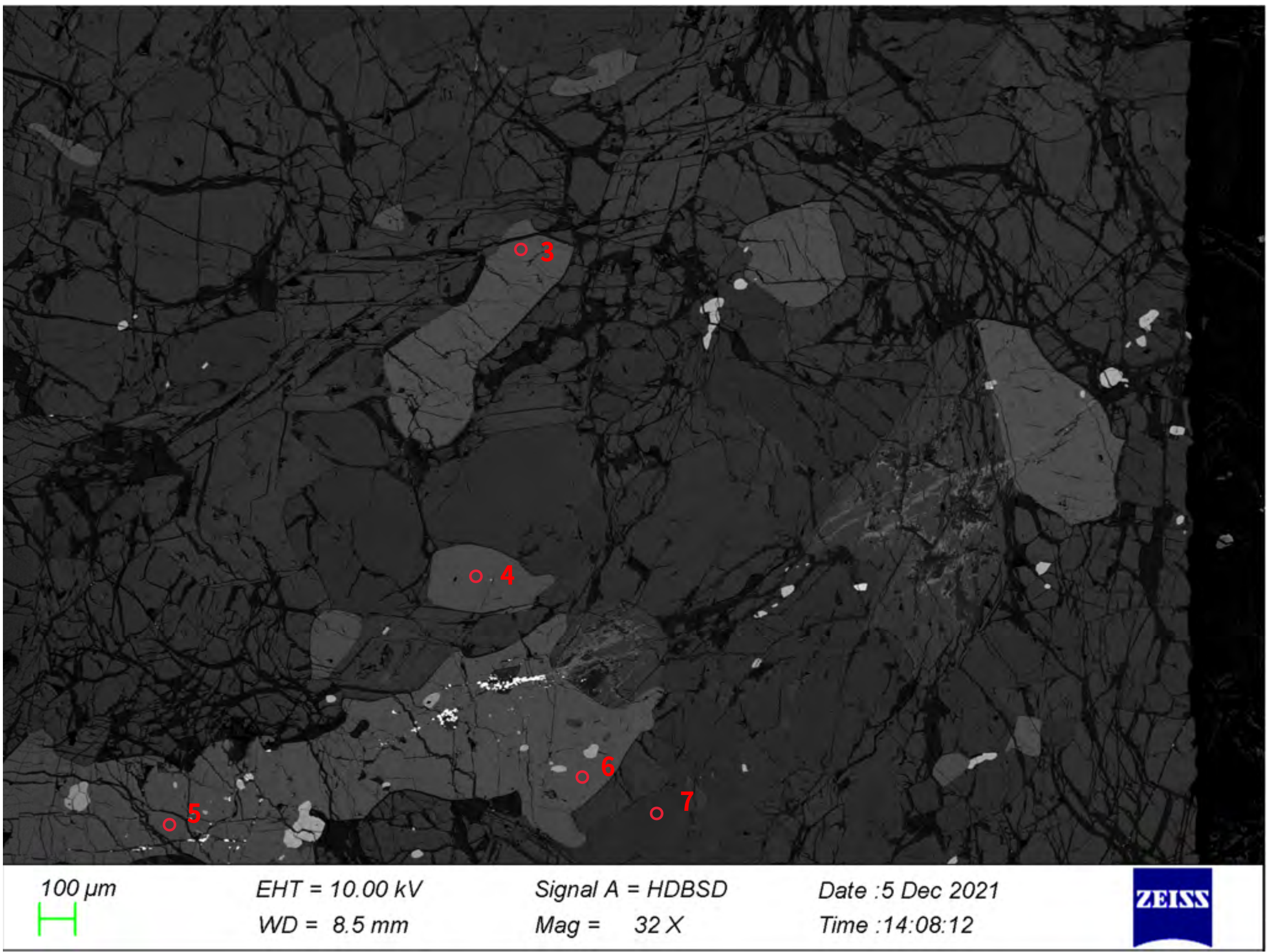

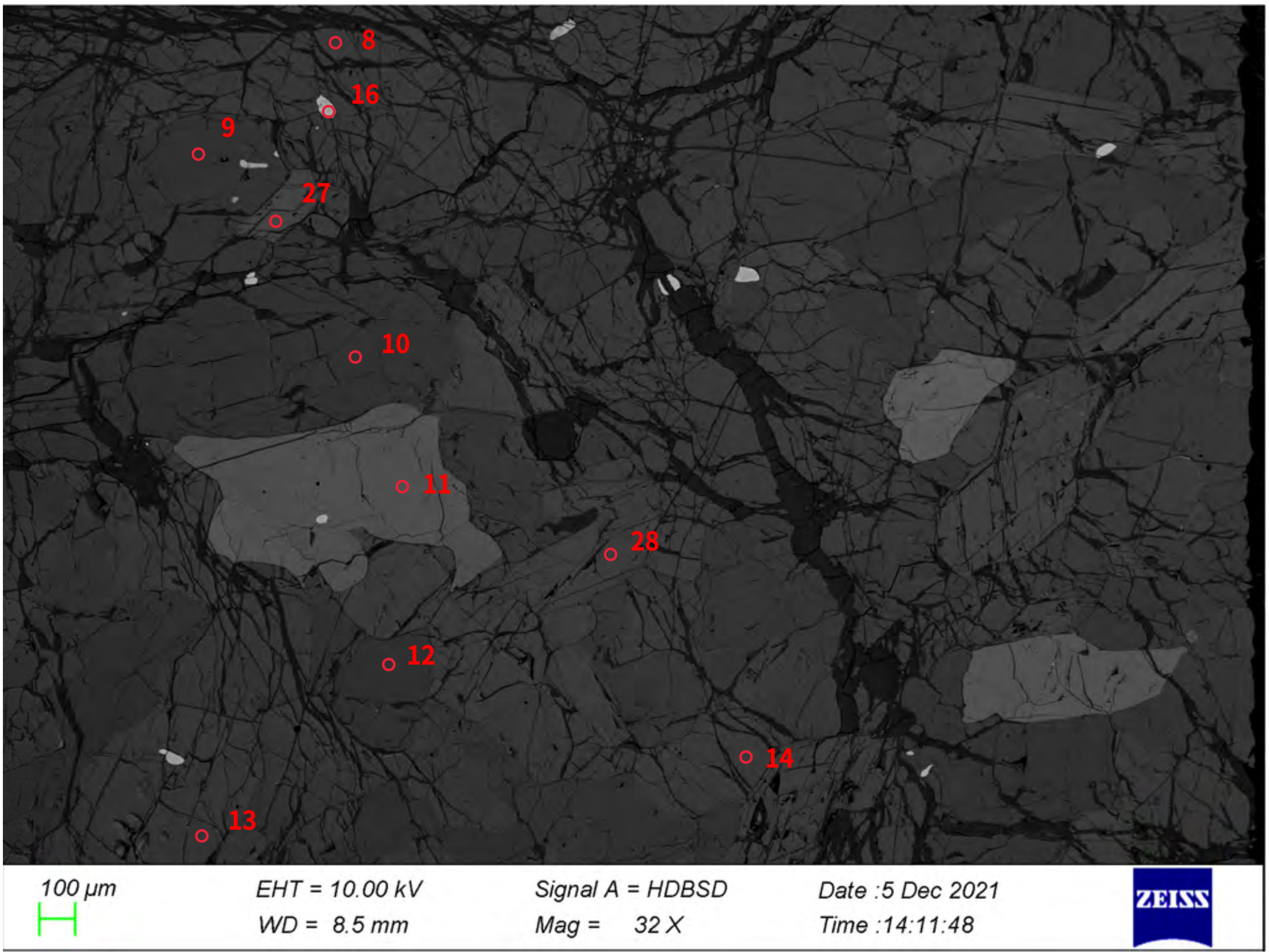
8
16
9
27
10
11
28
12
14
13
100 µm
EHT = 10.00 kV
WD = 8.5 mm
Signal A = HDBSD
Mag = 32 X
Date :5 Dec 2021
Time :14:11:48
ZEISS

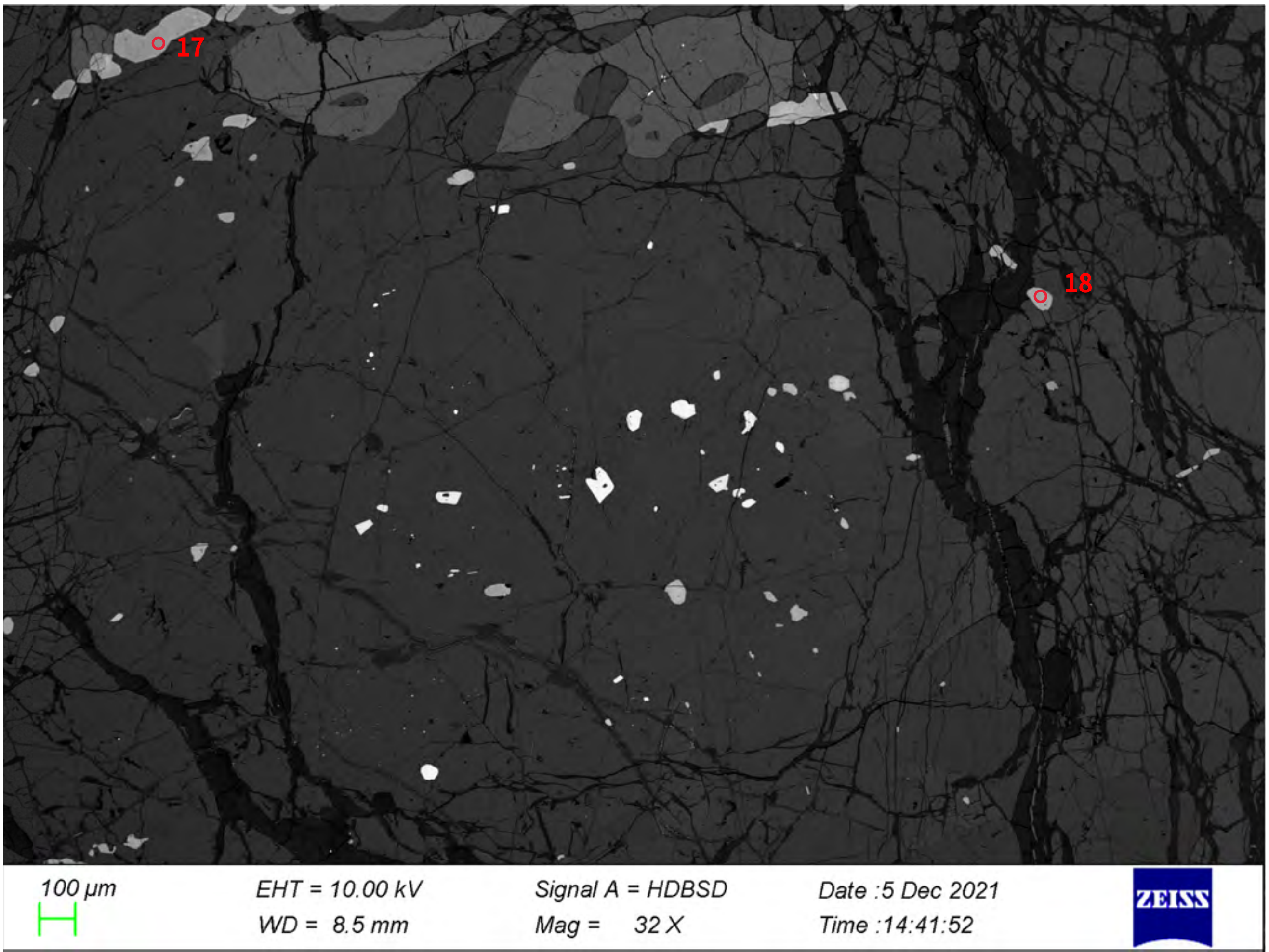
17
18
100 µm
EHT = 10.00 kV
WD = 8.5 mm
Signal A = HDBSD
Mag = 32 X
Date :5 Dec 2021
Time :14:41:52
ZEISS

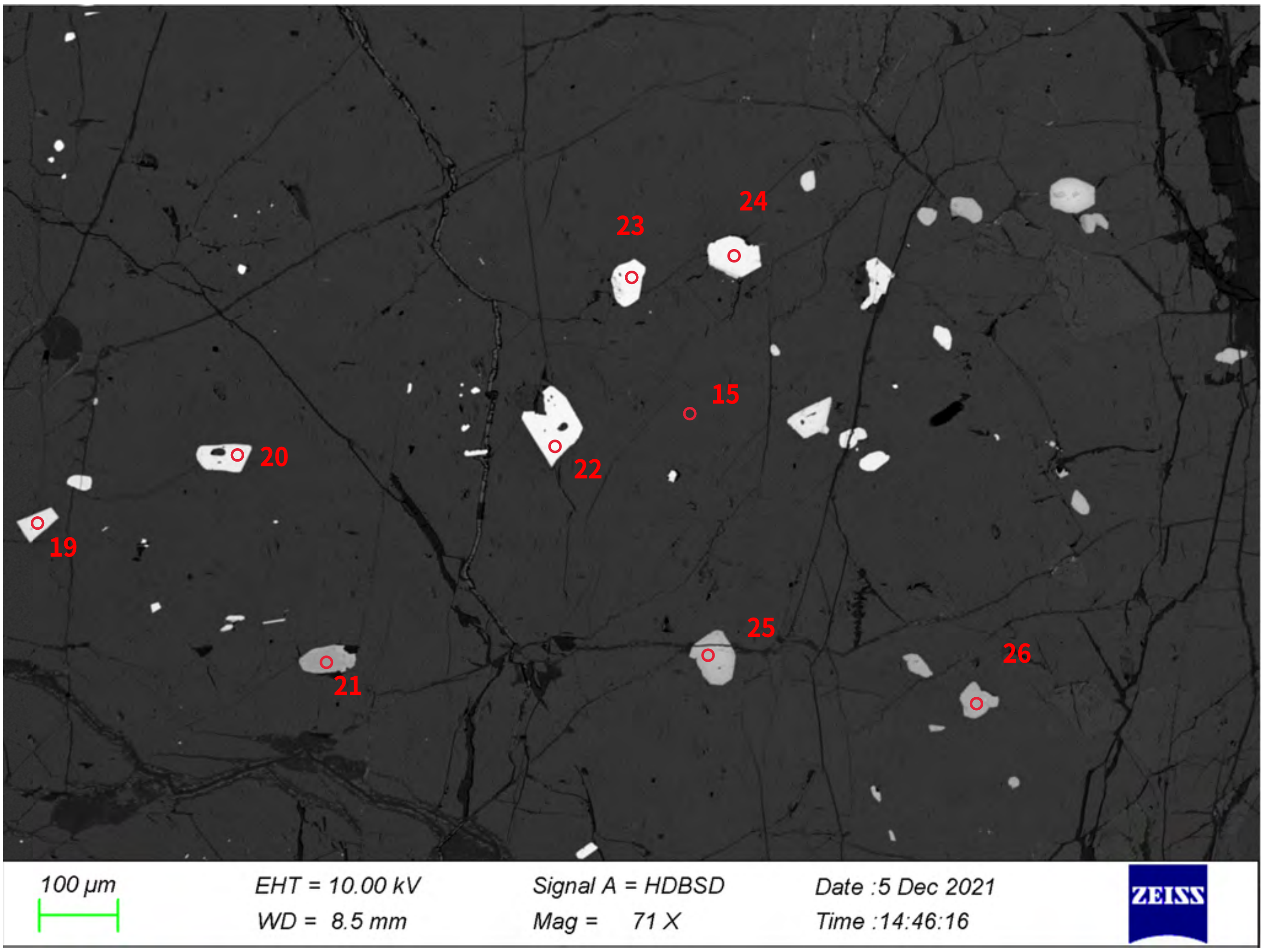

23
24
15
20
22
19
25
26
21
100 µm
EHT = 10.00 kV
WD = 8.5 mm
Signal A = HDBSD
Mag = 71 X
Date :5 Dec 2021
Time :14:46:16

Sample C17-64

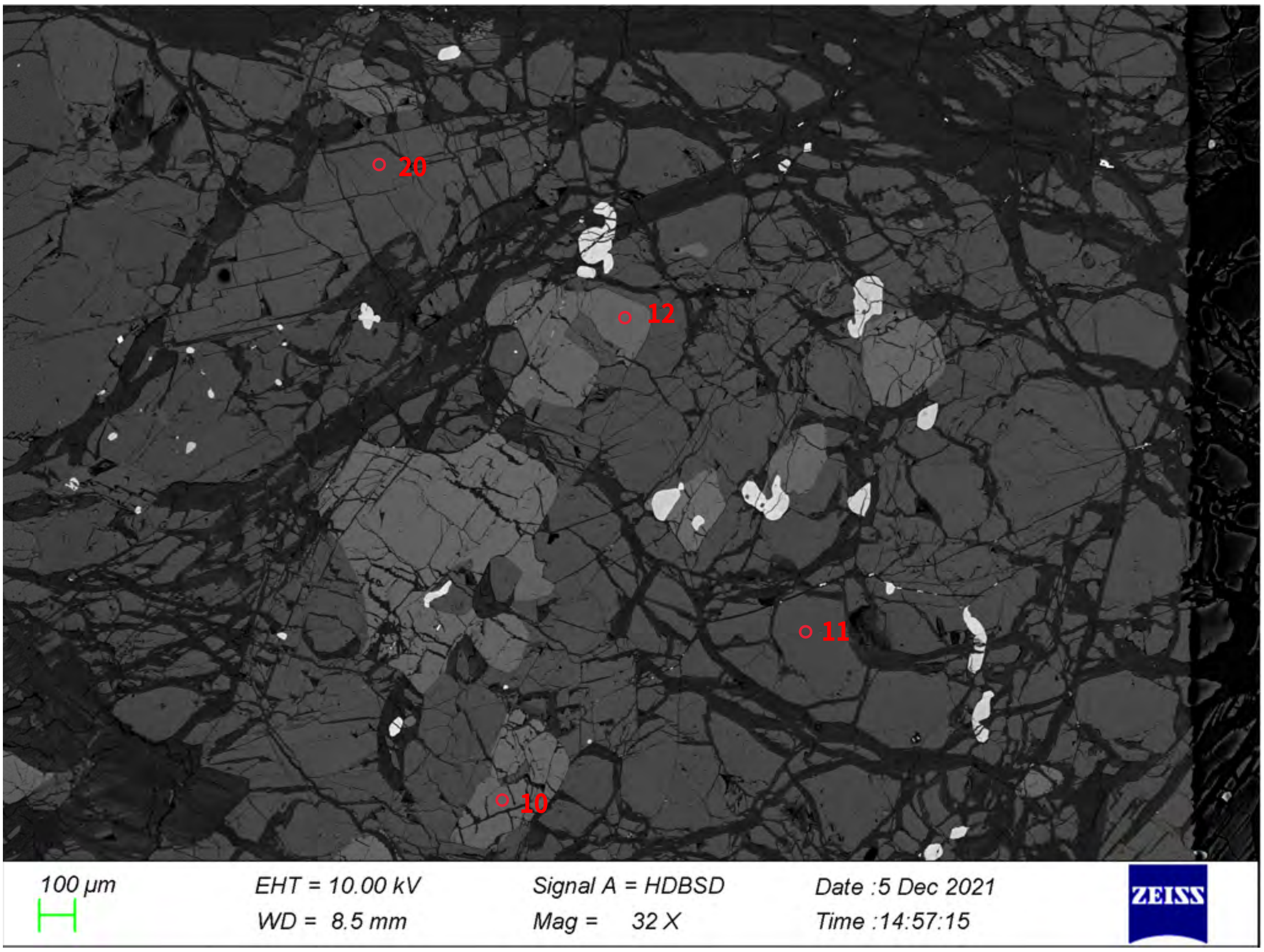

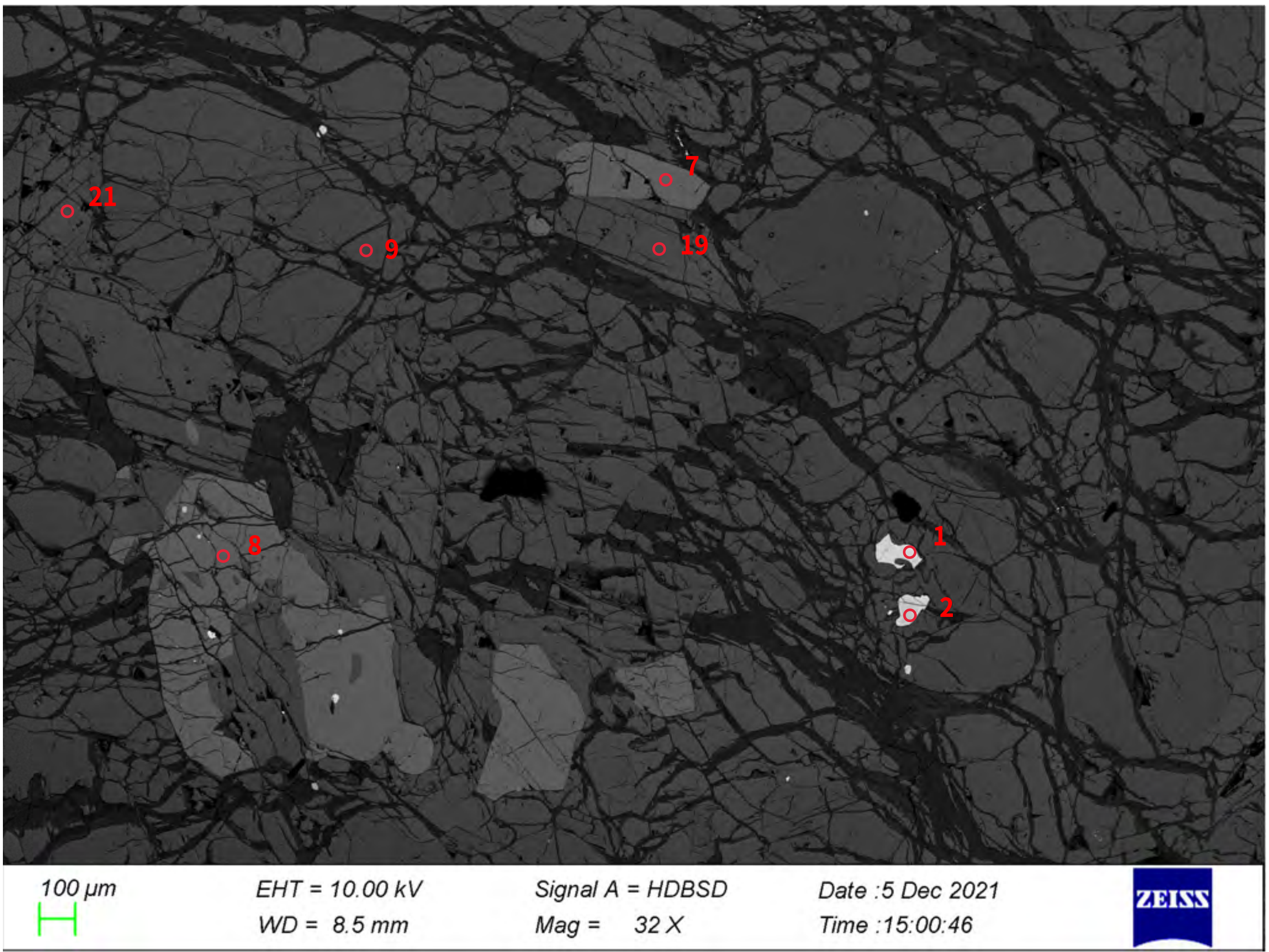

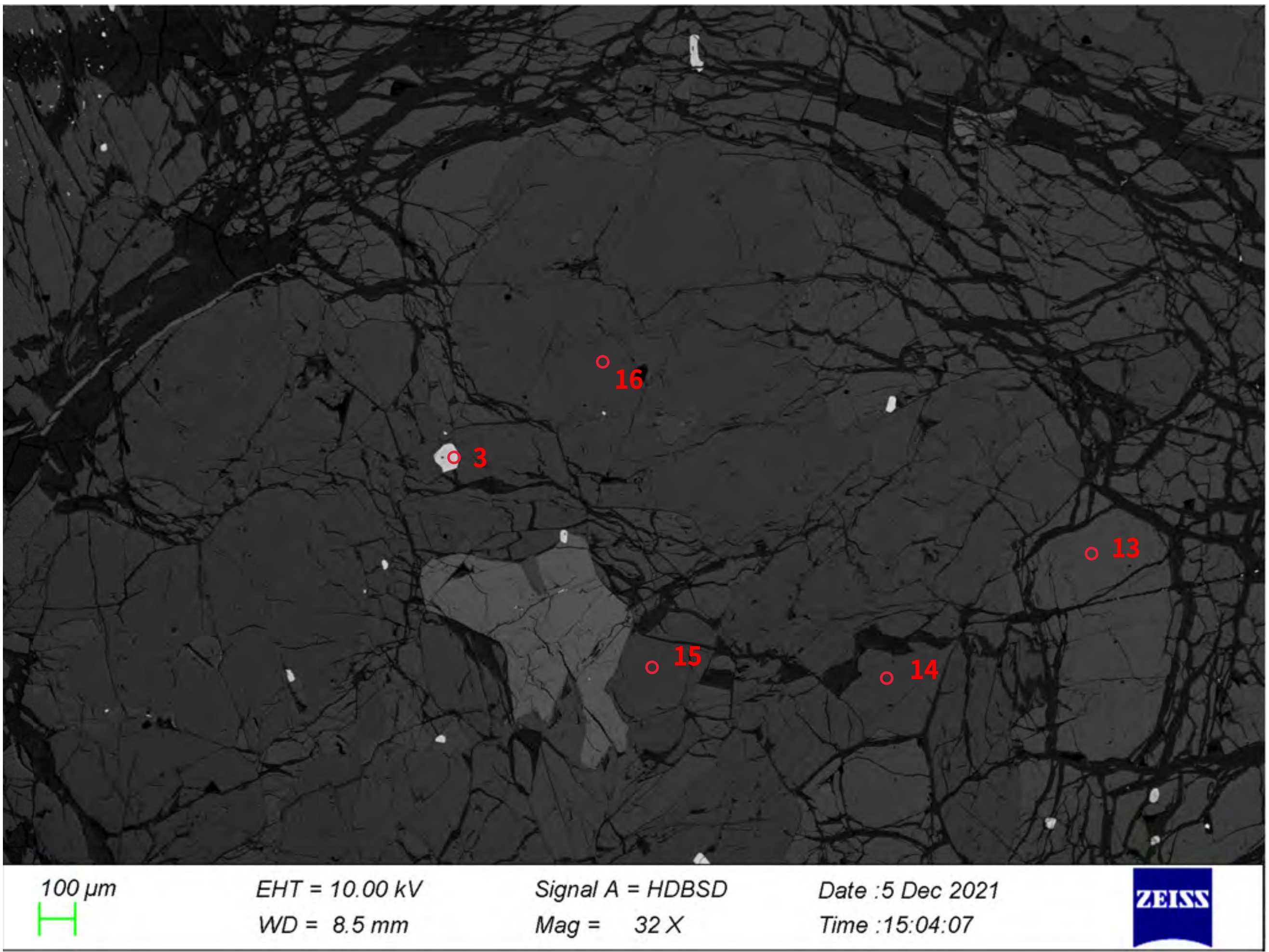
16
3
13
15
14
100 µm
EHT = 10.00 kV
WD = 8.5 mm
Signal A = HDBSD
Mag = 32 X
Date :5 Dec 2021
Time :15:04:07

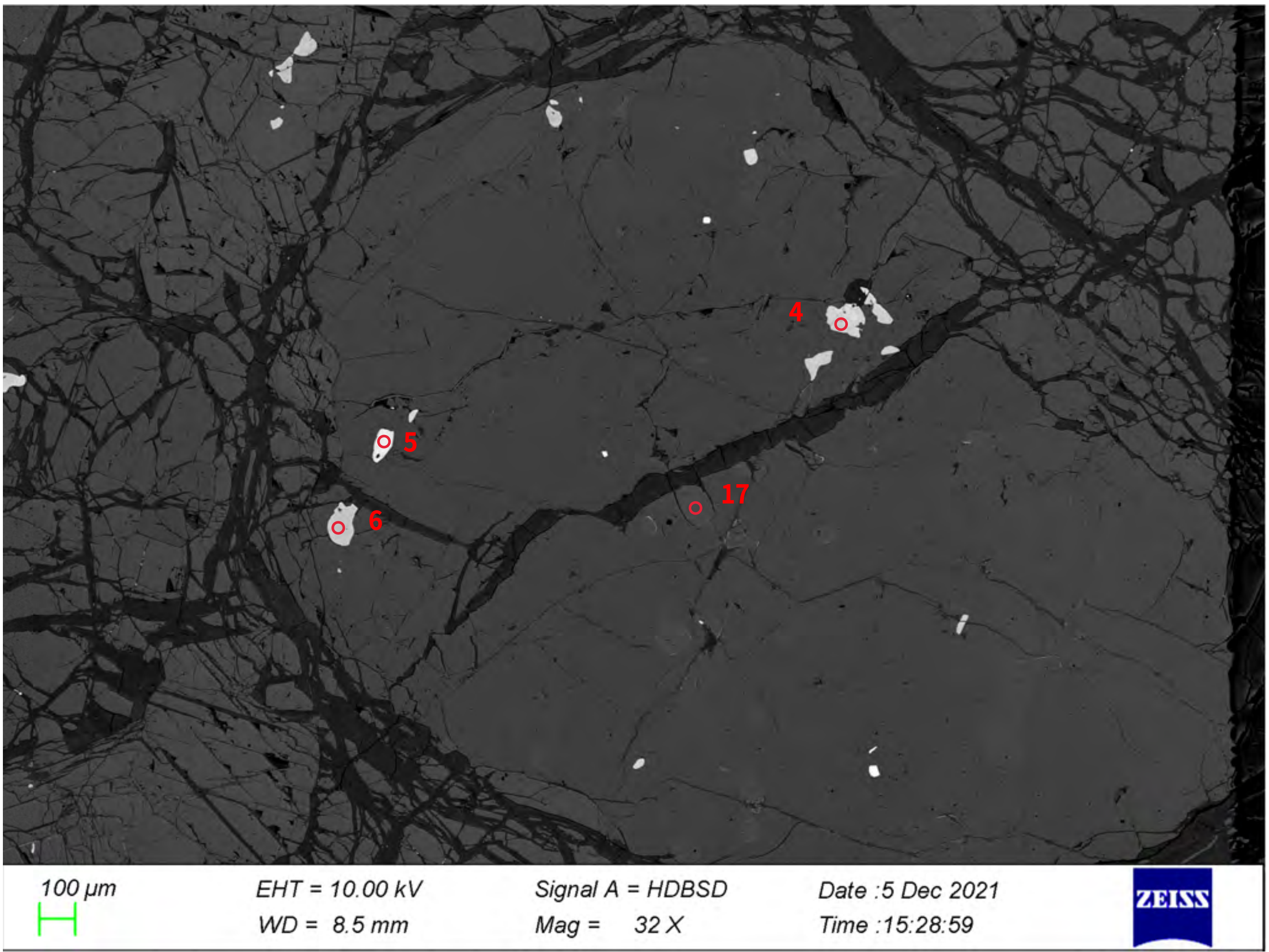
4
5
17
6
100 µm
EHT = 10.00 kV
WD = 8.5 mm
Signal A = HDBSD
Mag = 32 X
Date :5 Dec 2021
Time :15:28:59

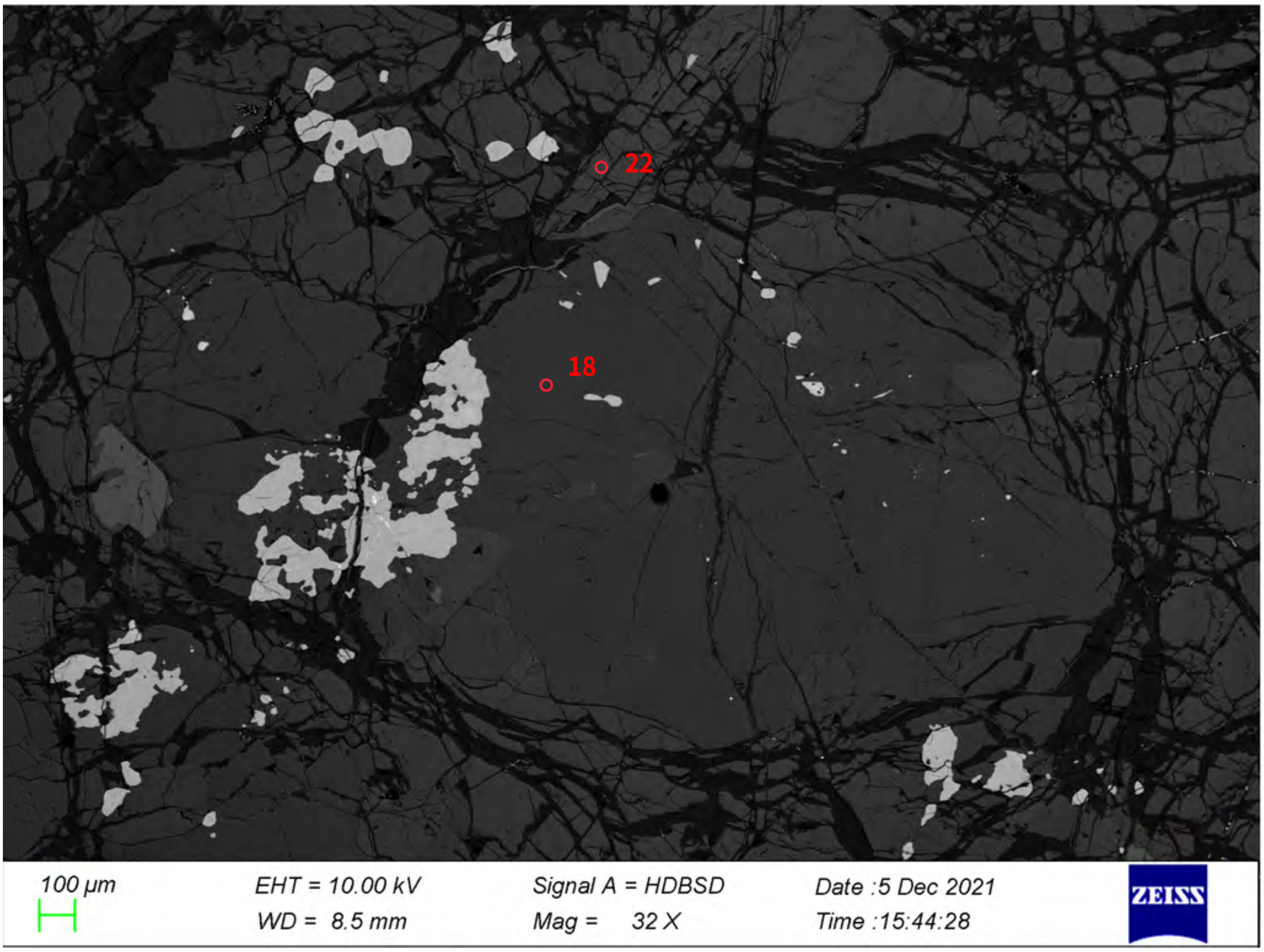
22
18
100 µm
EHT = 10.00 kV
WD = 8.5 mm
Signal A = HDBSD
Mag = 32 X
Date :5 Dec 2021
Time :15:44:28

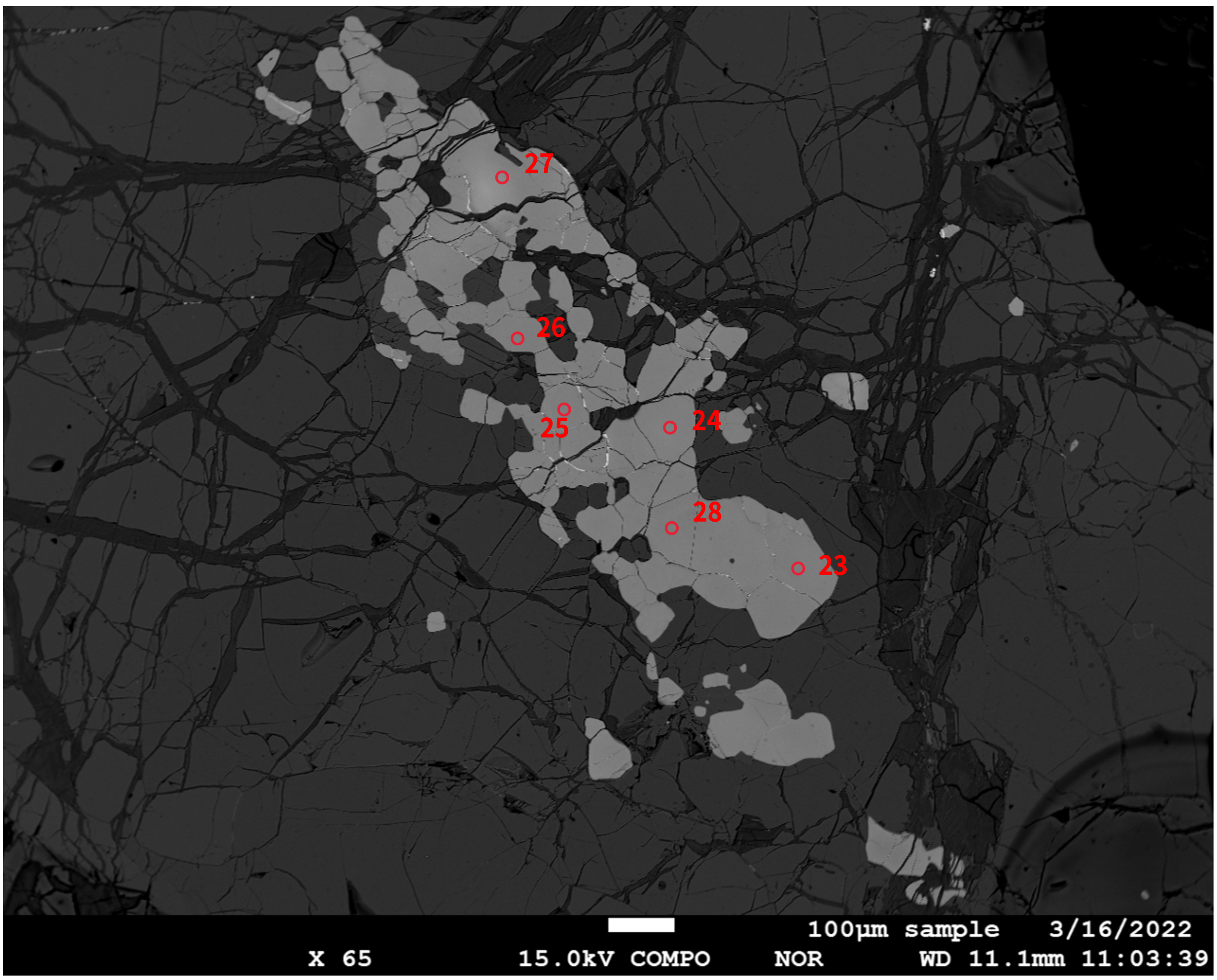
27
26
25
24
28
23
100µm sample 3/16/2022
X 65 15.0kV COMPO NOR WD 11.1mm 11:03:39

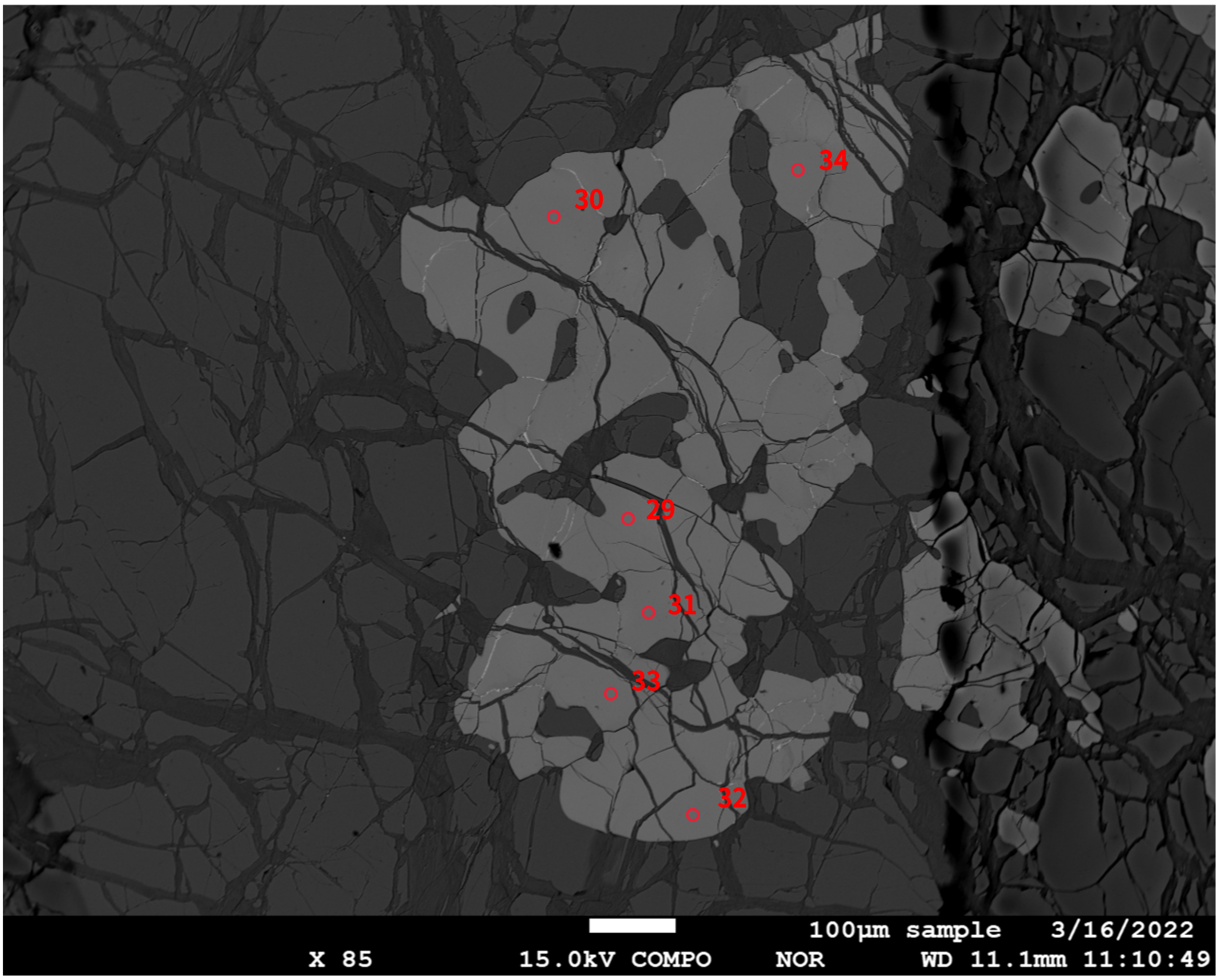
30
34
29
31
33
32
100µm sample 3/16/2022
X 85 15.0kV COMPO NOR WD 11.1mm 11:10:49

Sample C17-68

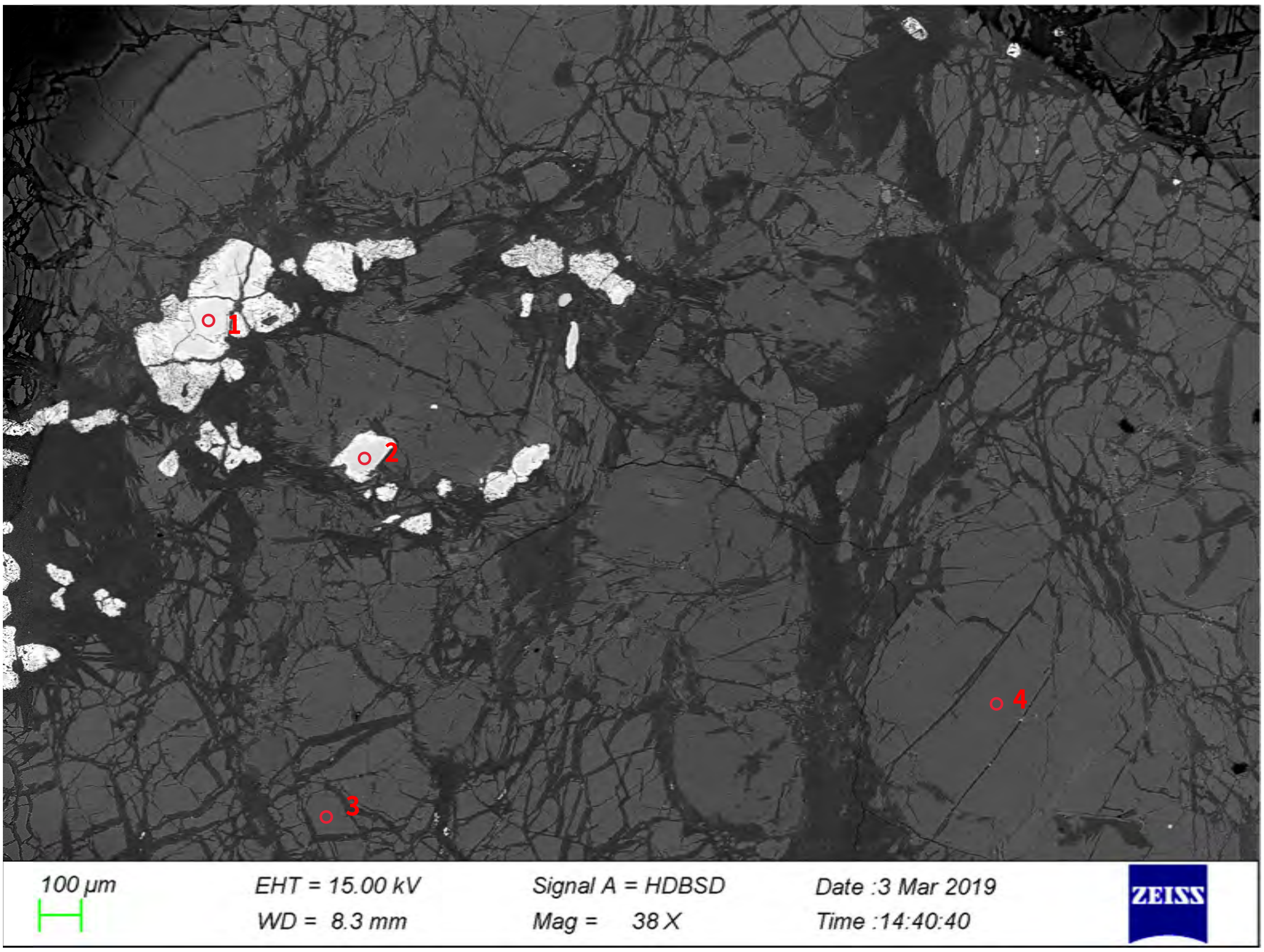

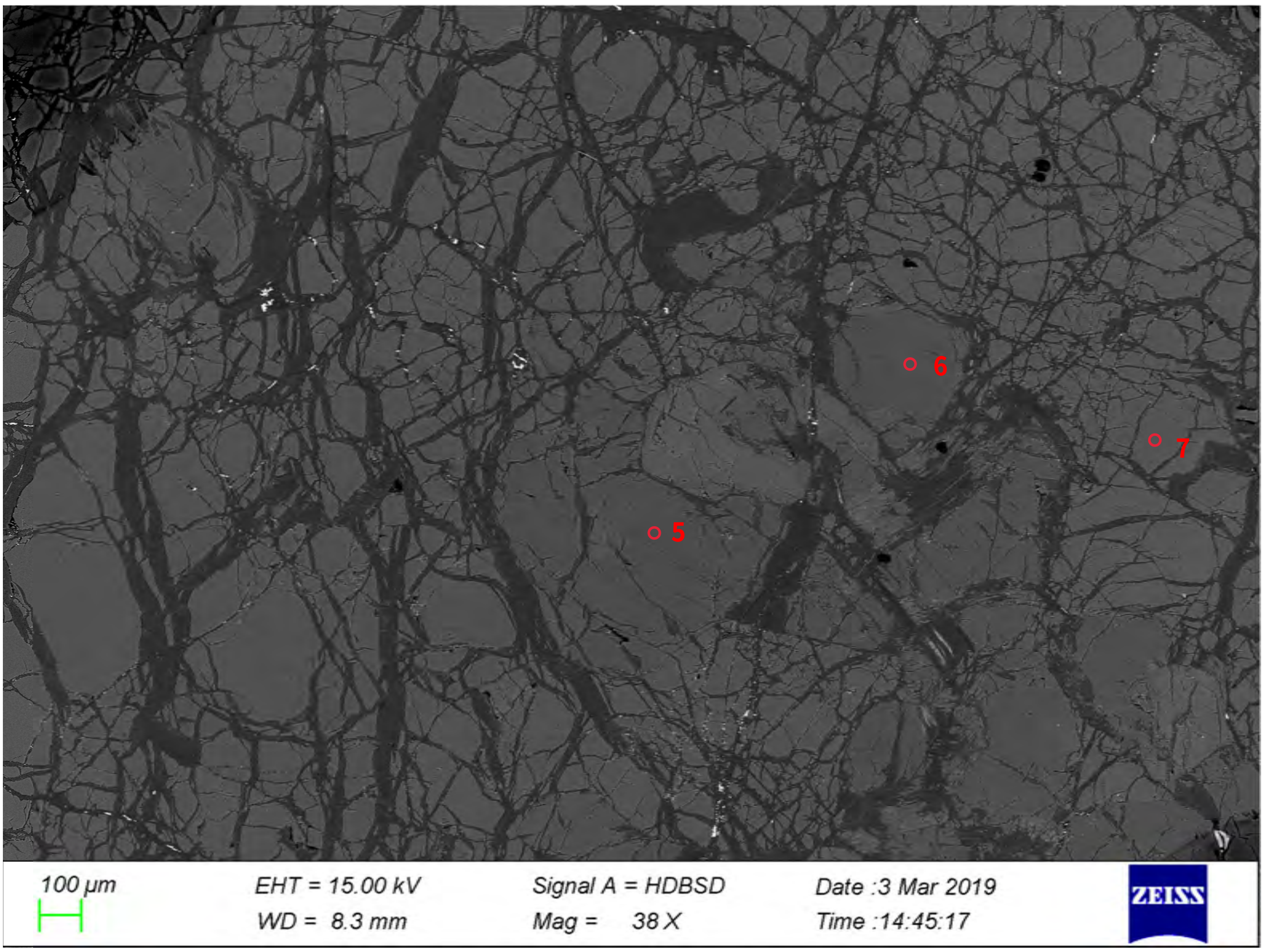

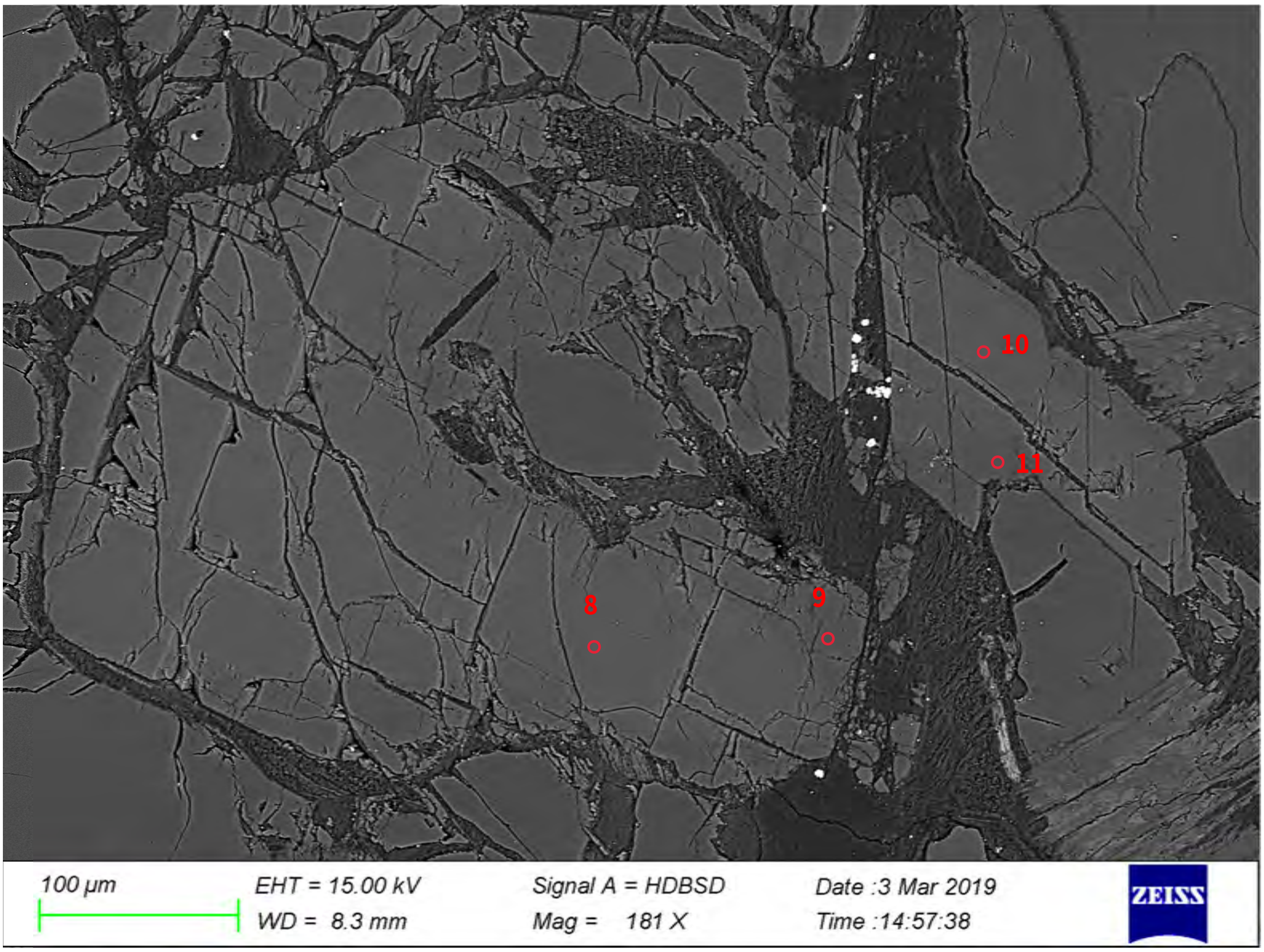
10
11
8
9
100 µm
EHT = 15.00 kV
WD = 8.3 mm
Signal A = HDBSD
Mag = 181 X
Date :3 Mar 2019
Time :14:57:38
ZEISS

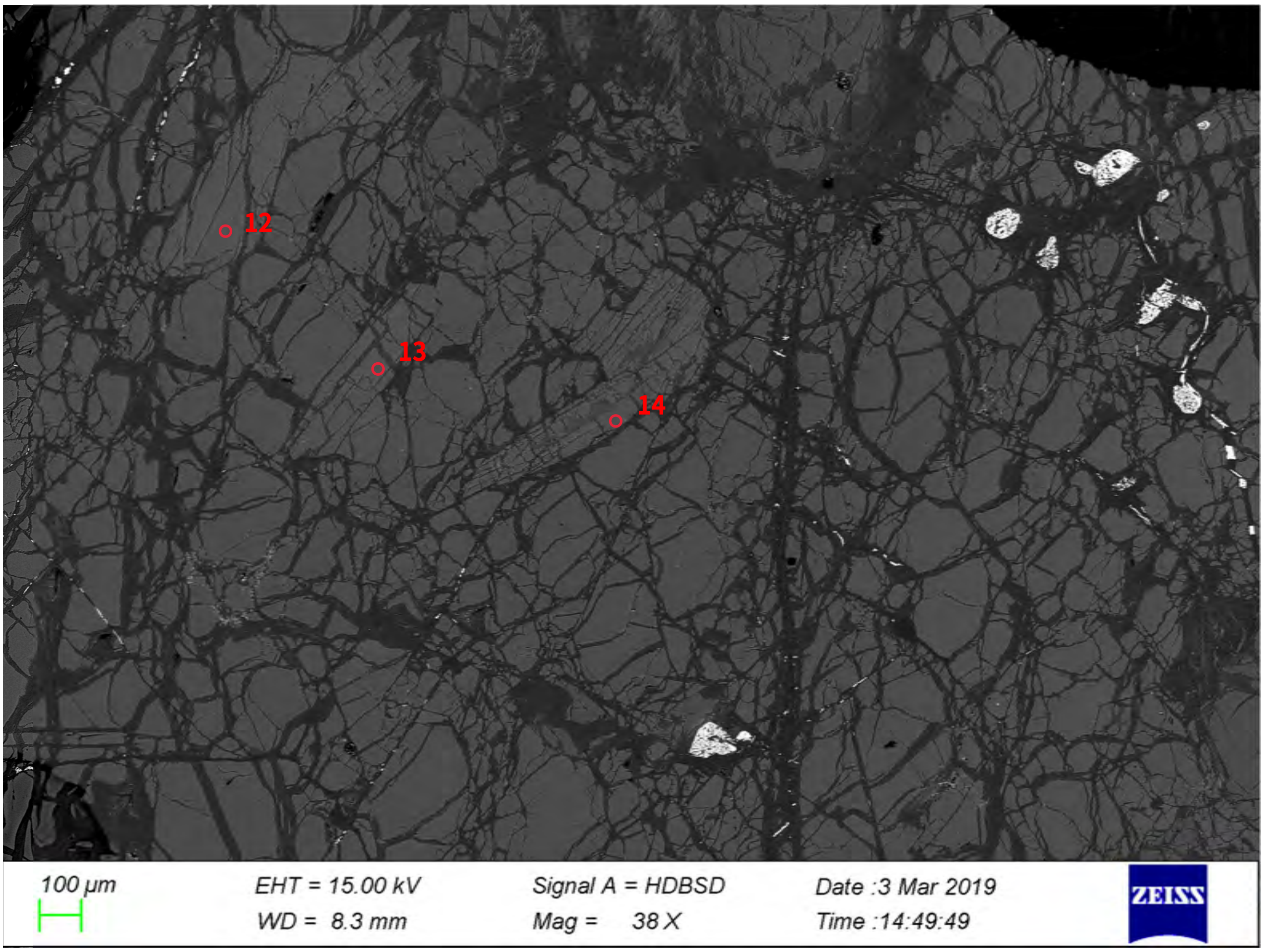
12
13
14
100 µm
EHT = 15.00 kV
WD = 8.3 mm
Signal A = HDBSD
Mag = 38 X
Date :3 Mar 2019
Time :14:49:49
ZEISS

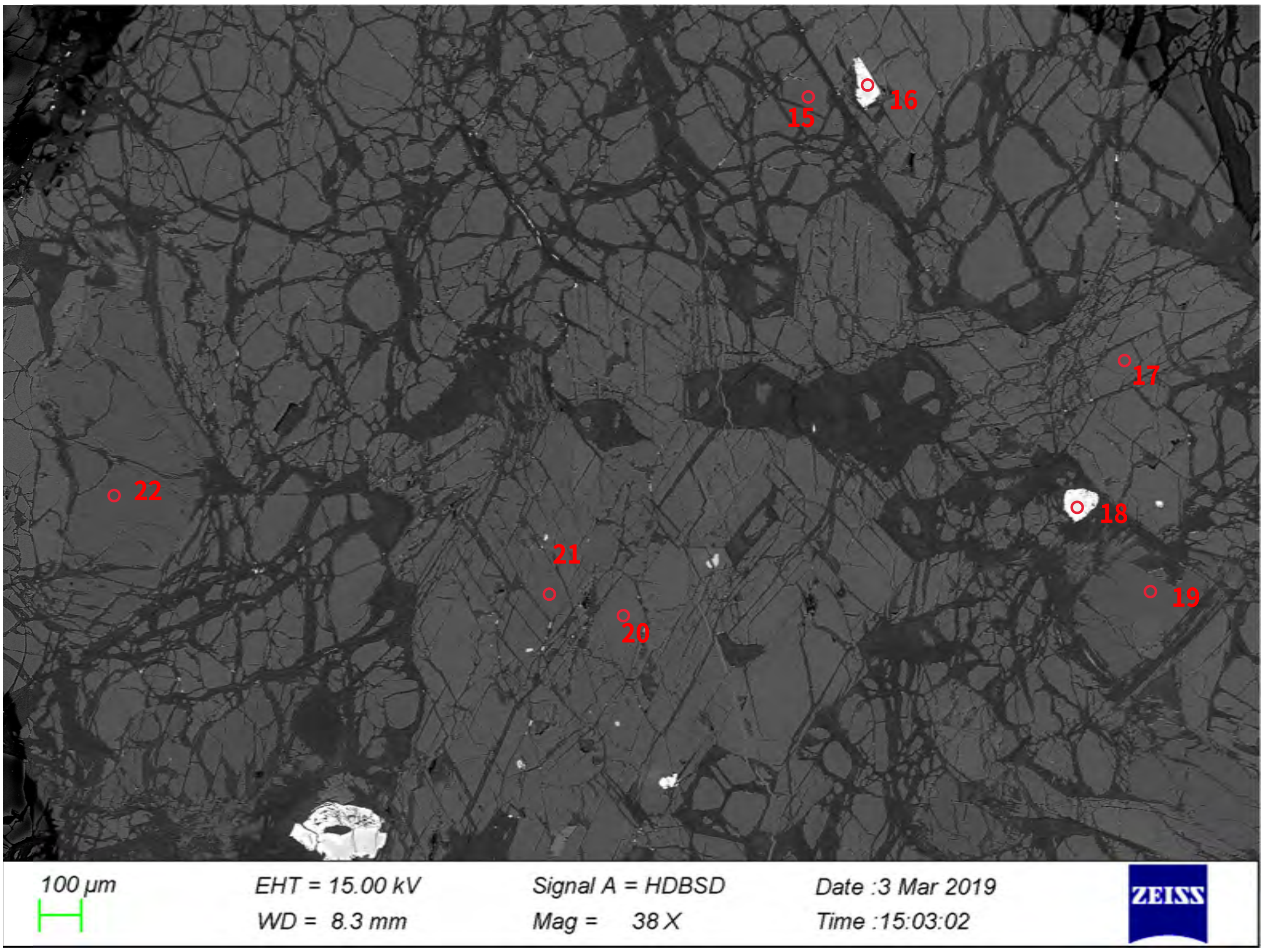
15
16
17
18
19
20
21
22
100 µm
EHT = 15.00 kV
WD = 8.3 mm
Signal A = HDBSD
Mag = 38 X
Date :3 Mar 2019
Time :15:03:02

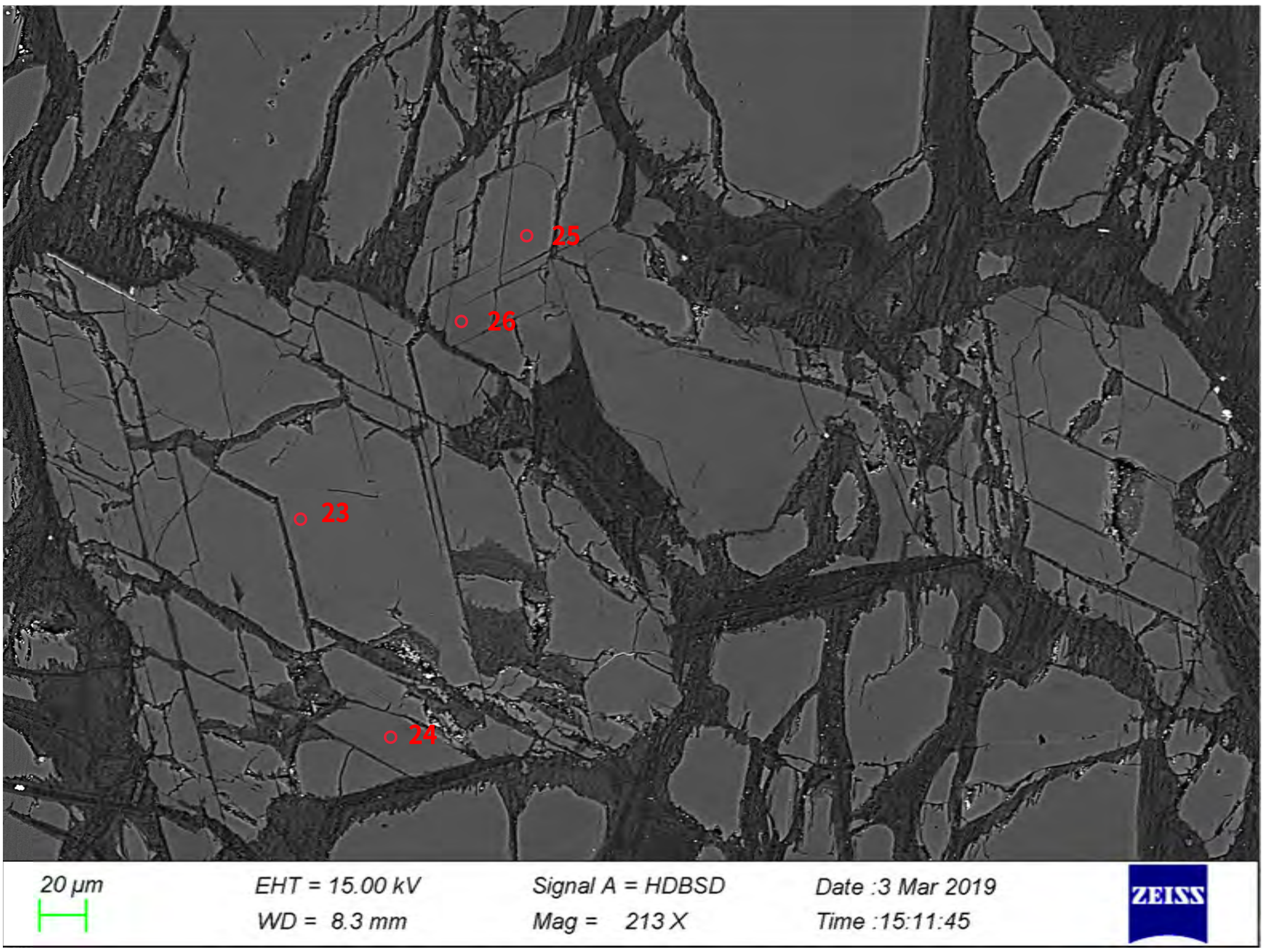
23
24
25
26
20 µm
EHT = 15.00 kV
WD = 8.3 mm
Signal A = HDBSD
Mag = 213 X
Date :3 Mar 2019
Time :15:11:45

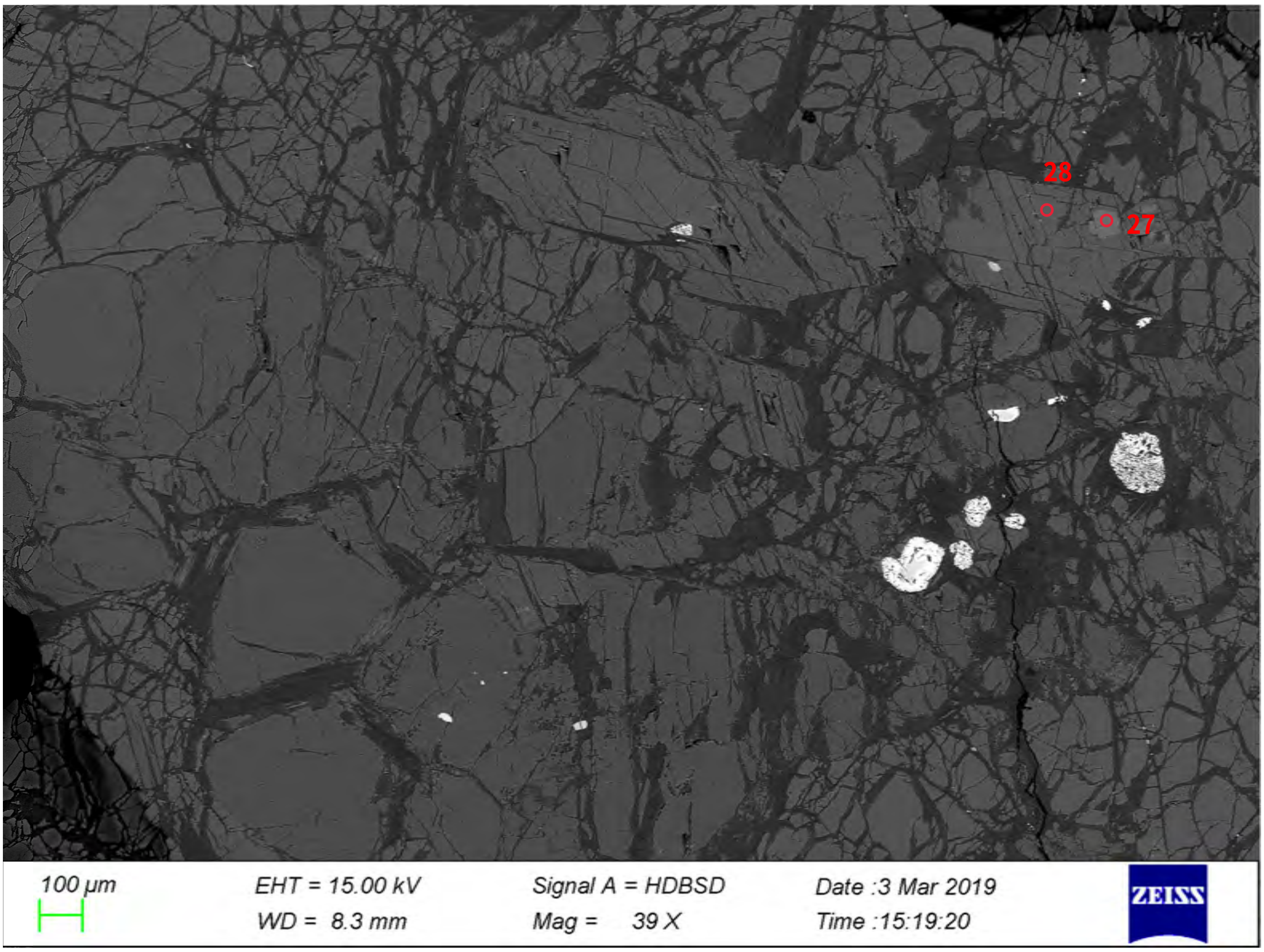
28
27
100 µm
EHT = 15.00 kV
WD = 8.3 mm
Signal A = HDBSD
Mag = 39 X
Date :3 Mar 2019
Time :15:19:20
ZEISS

Sample C17-72

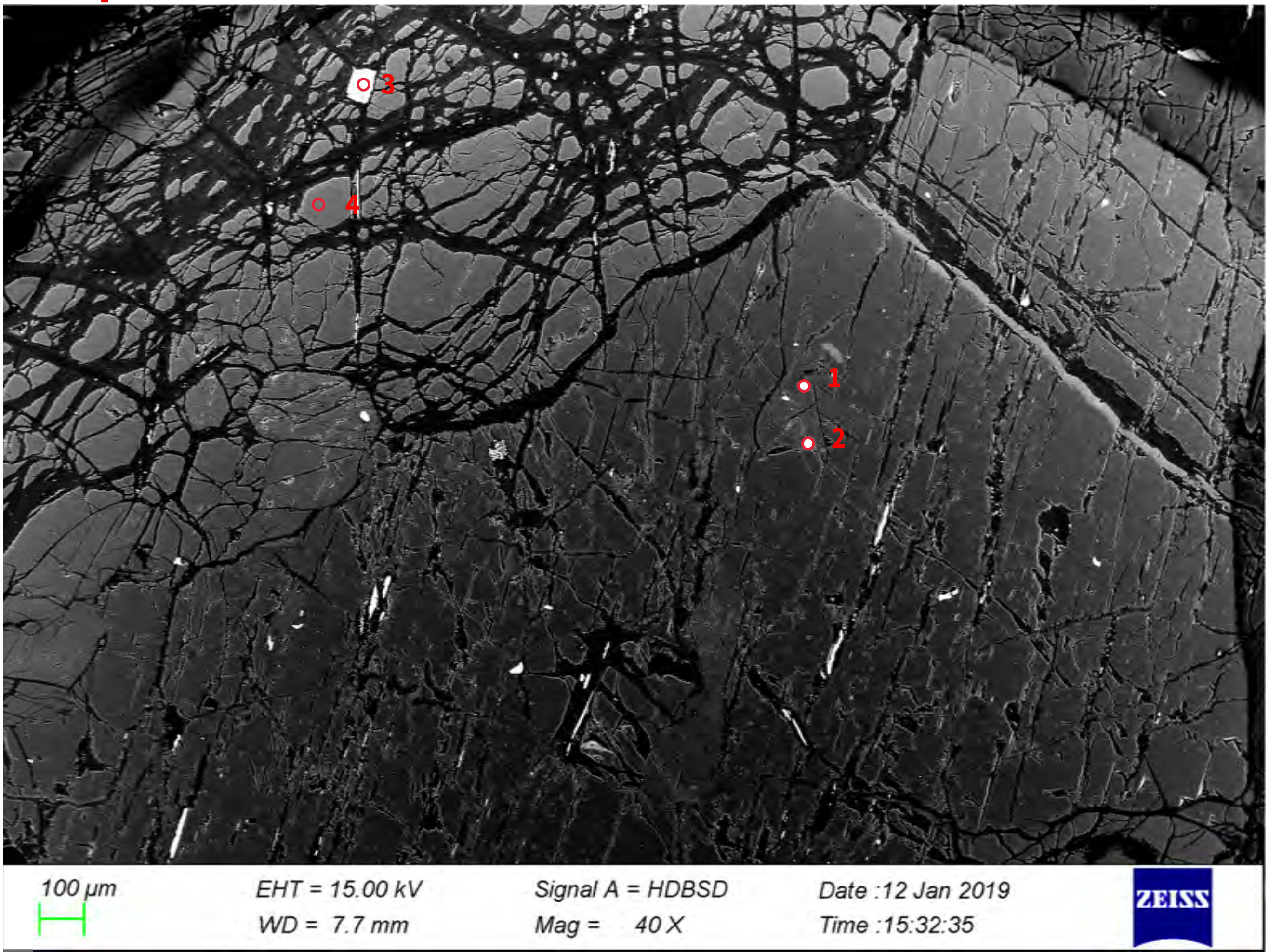

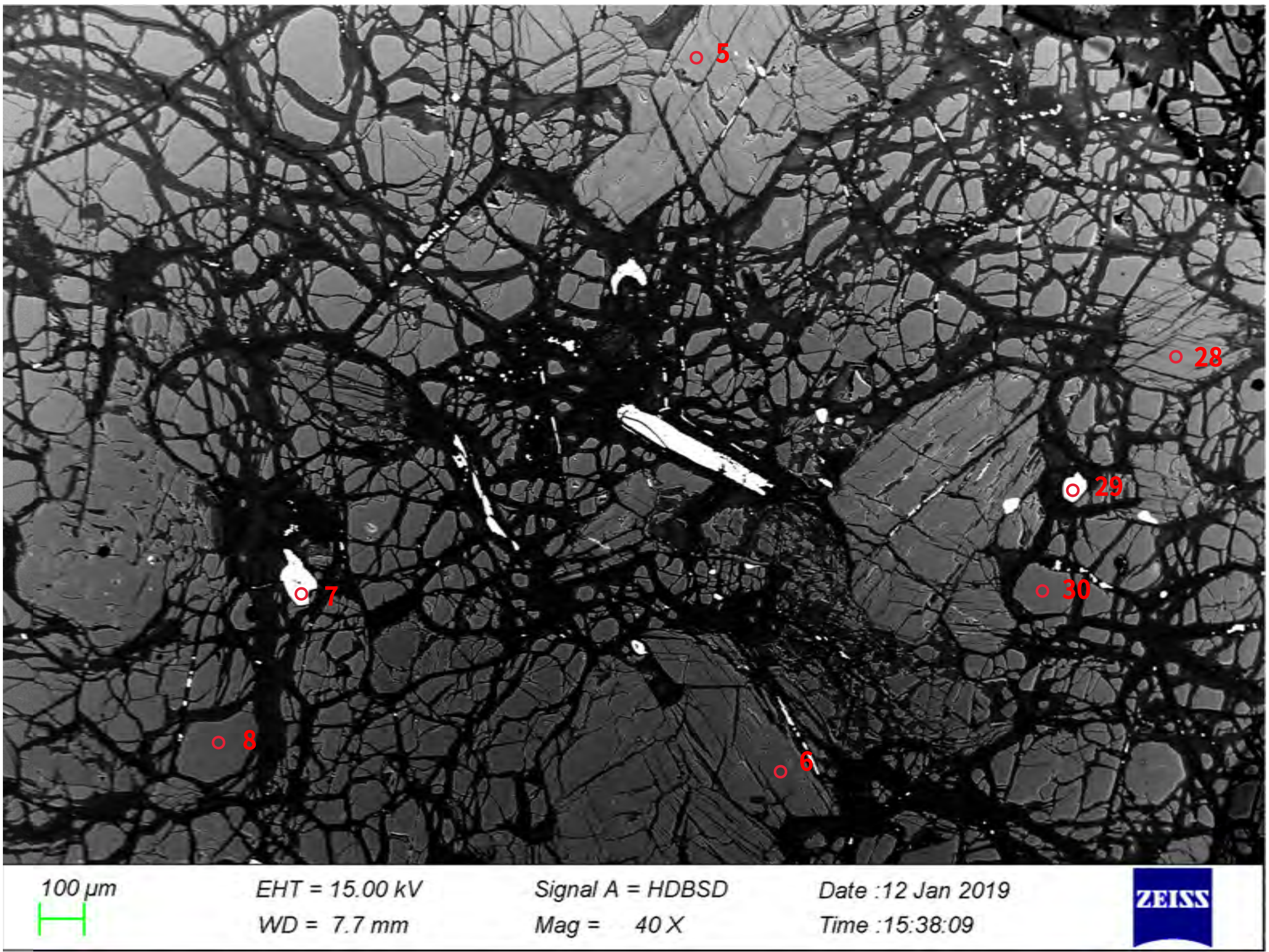

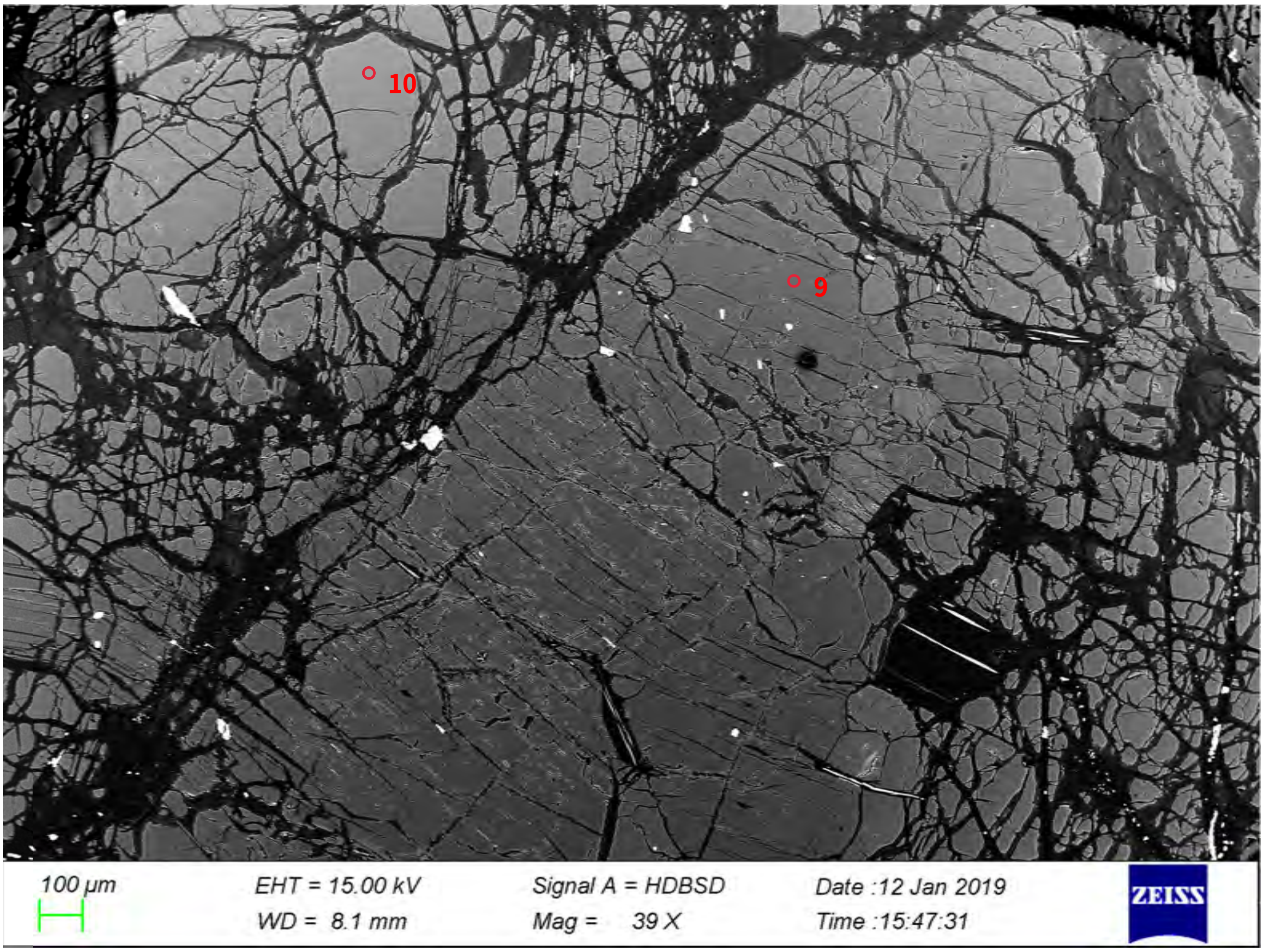
10
9
100 µm
EHT = 15.00 kV
WD = 8.1 mm
Signal A = HDBSD
Mag = 39 X
Date :12 Jan 2019
Time :15:47:31
ZEISS

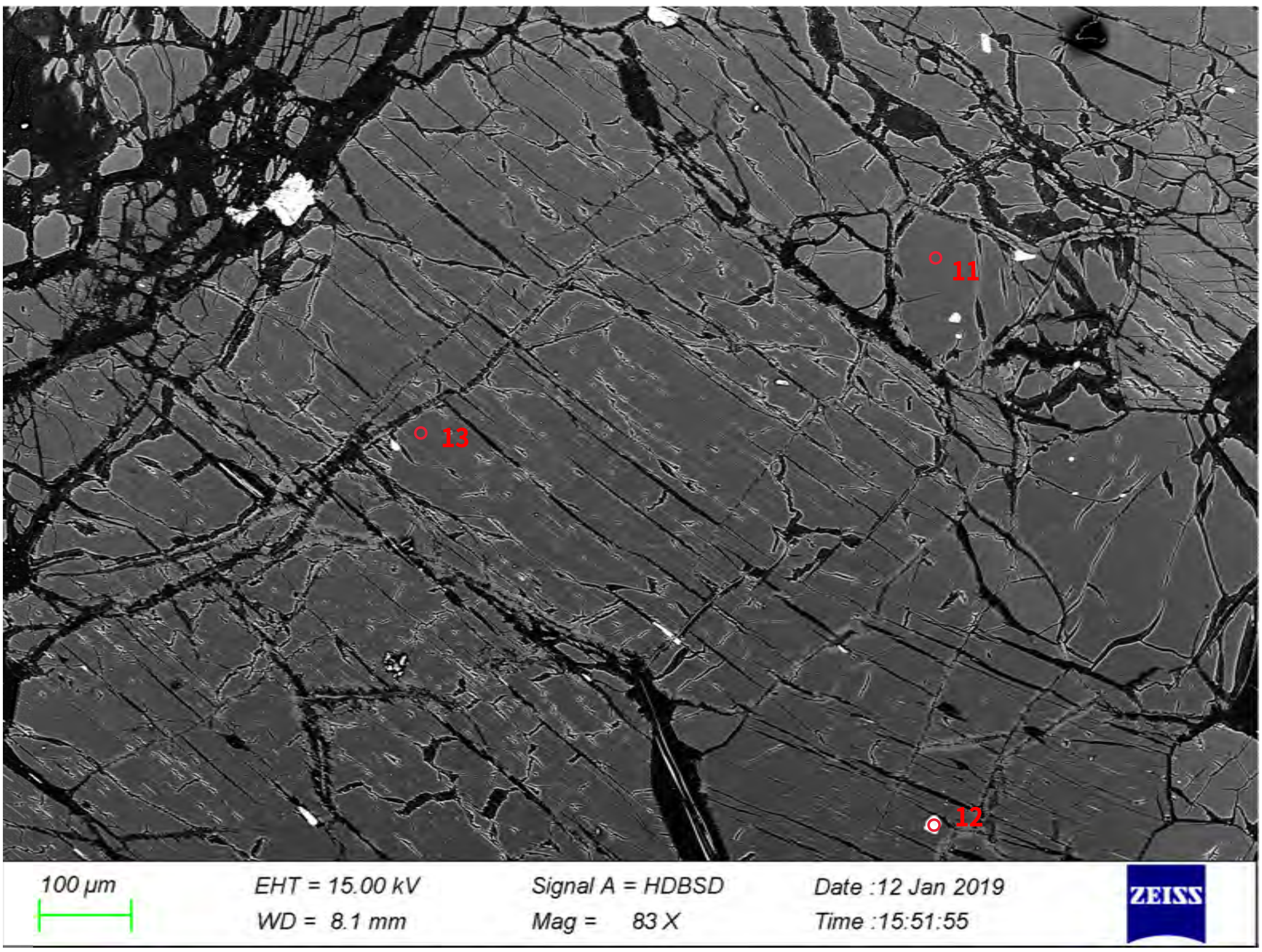
11
13
12
100 µm
EHT = 15.00 kV
WD = 8.1 mm
Signal A = HDBSD
Mag = 83 X
Date :12 Jan 2019
Time :15:51:55
ZEISS

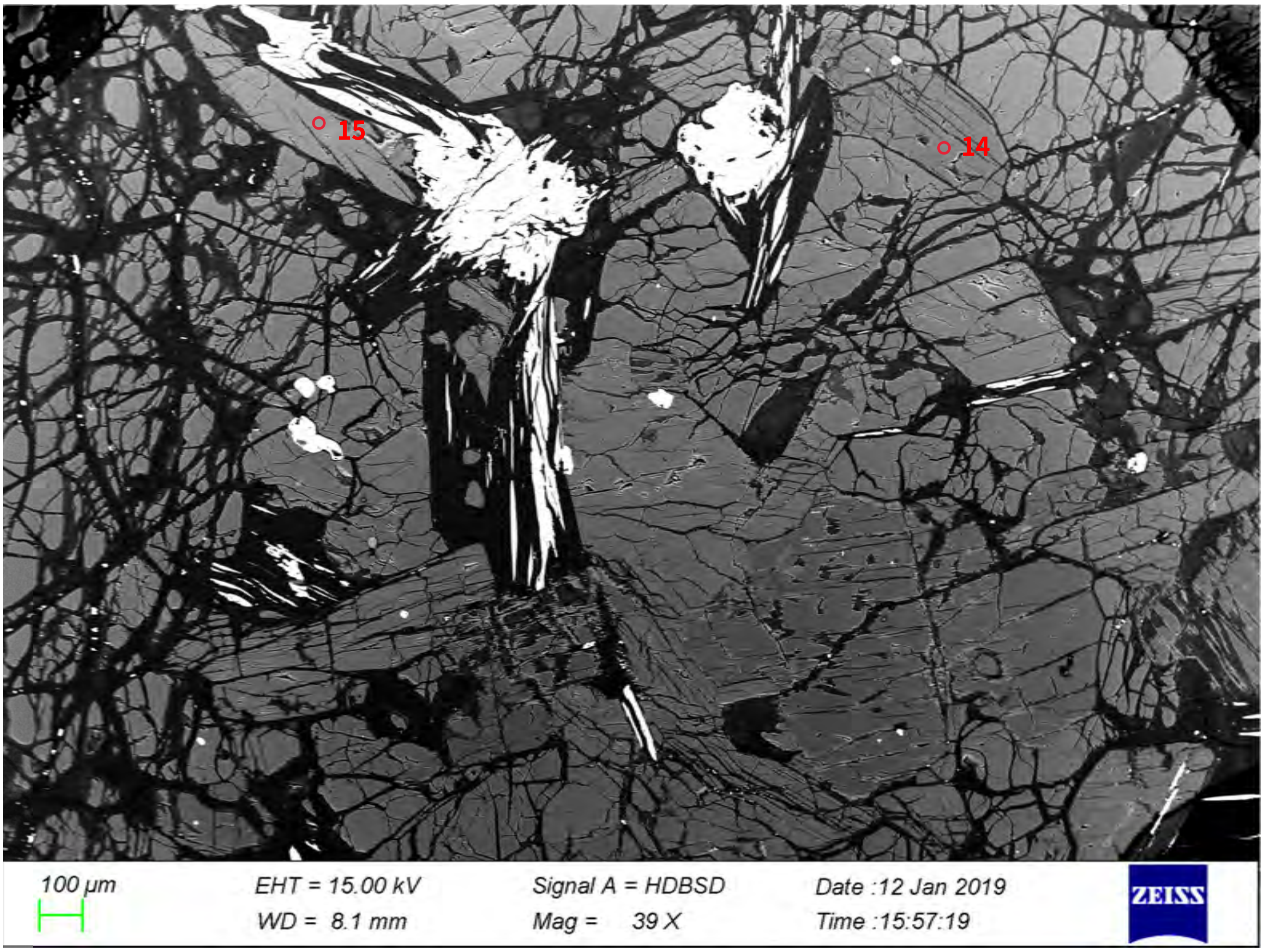
15
14
100 µm
EHT = 15.00 kV
WD = 8.1 mm
Signal A = HDBSD
Mag = 39 X
Date :12 Jan 2019
Time :15:57:19
ZEISS

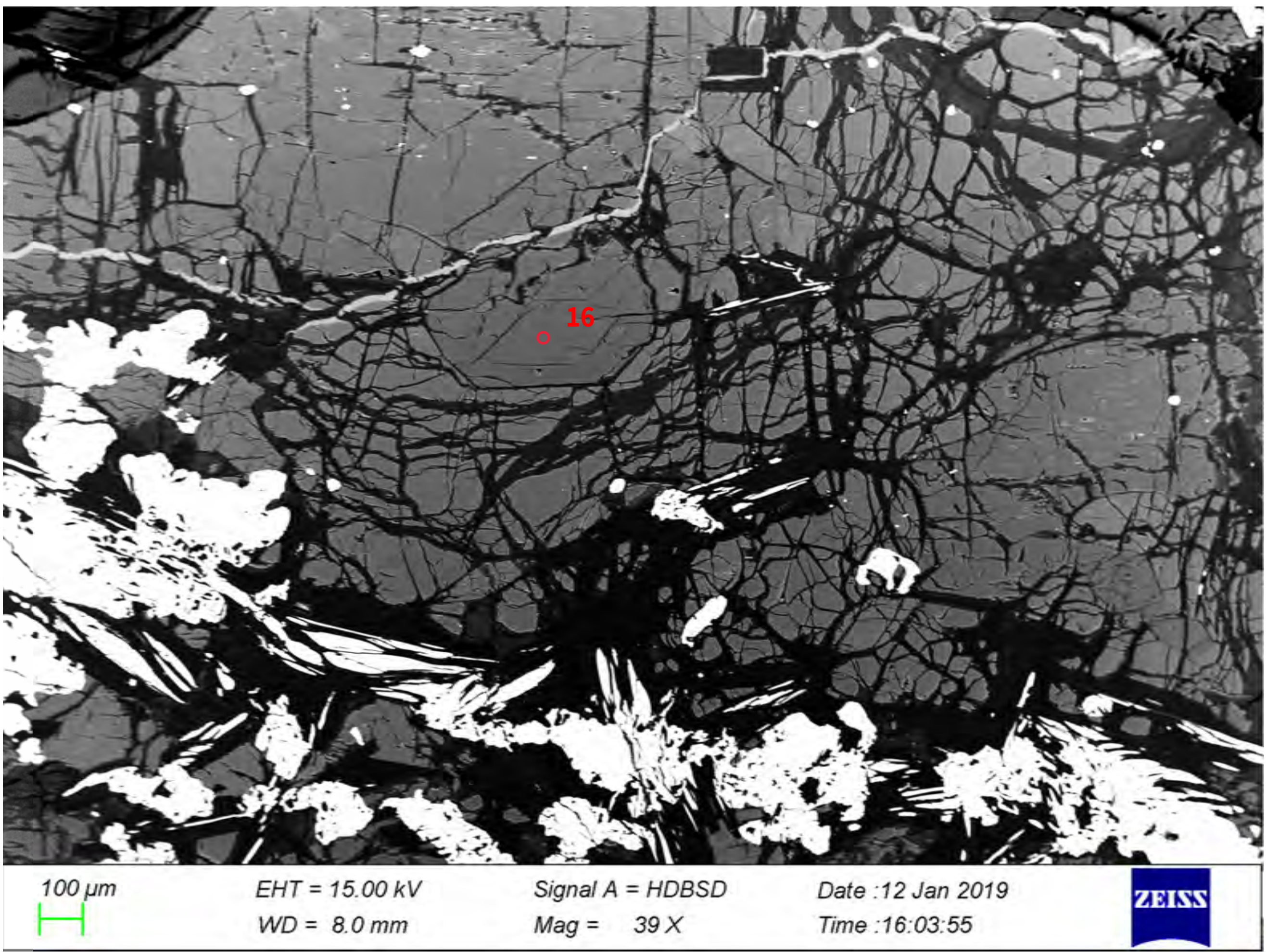
16
100 µm
EHT = 15.00 kV
WD = 8.0 mm
Signal A = HDBSD
Mag = 39 X
Date :12 Jan 2019
Time :16:03:55
ZEISS

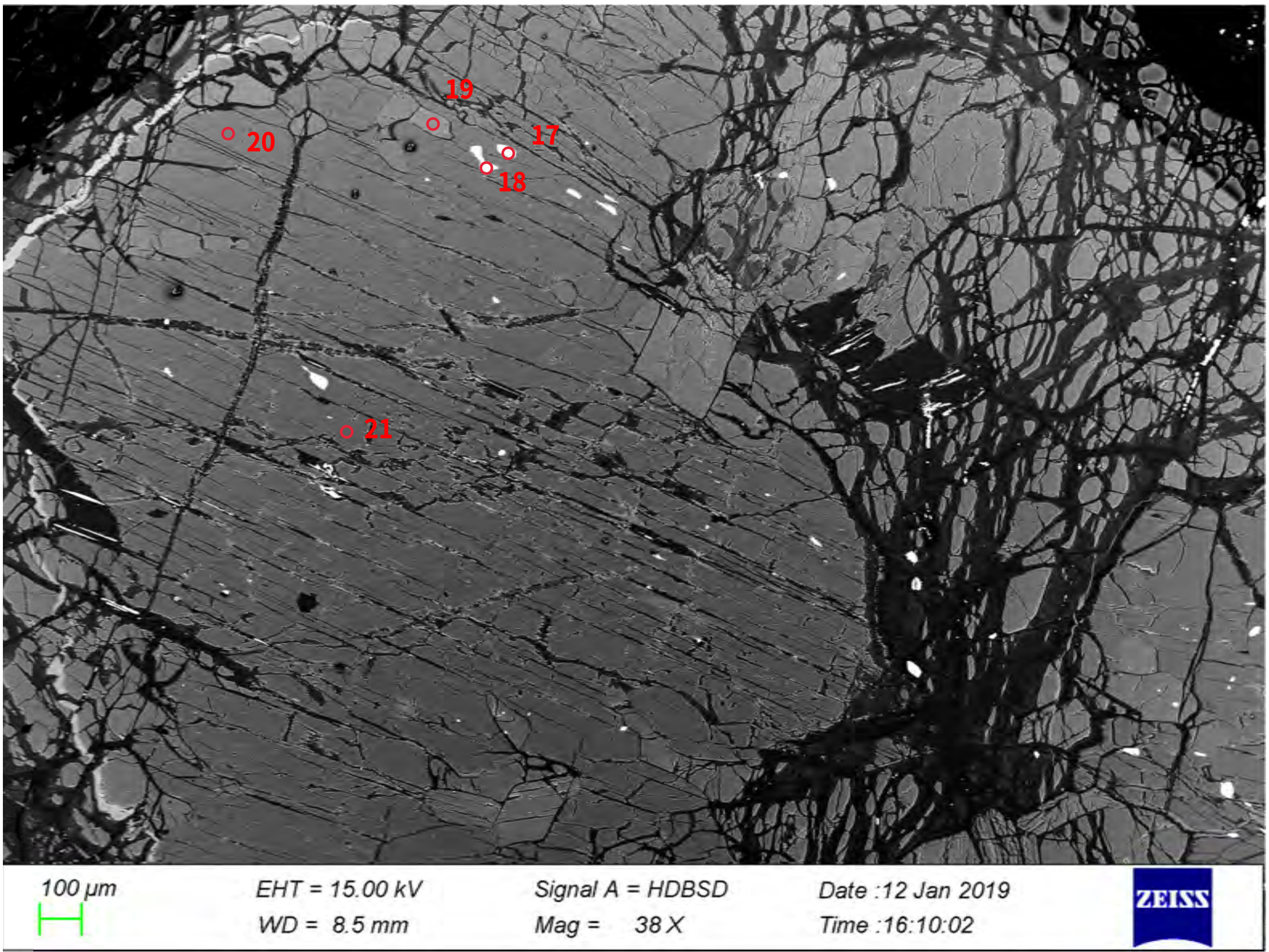
19
17
20
18
21
100 µm
EHT = 15.00 kV
WD = 8.5 mm
Signal A = HDBSD
Mag = 38 X
Date :12 Jan 2019
Time :16:10:02

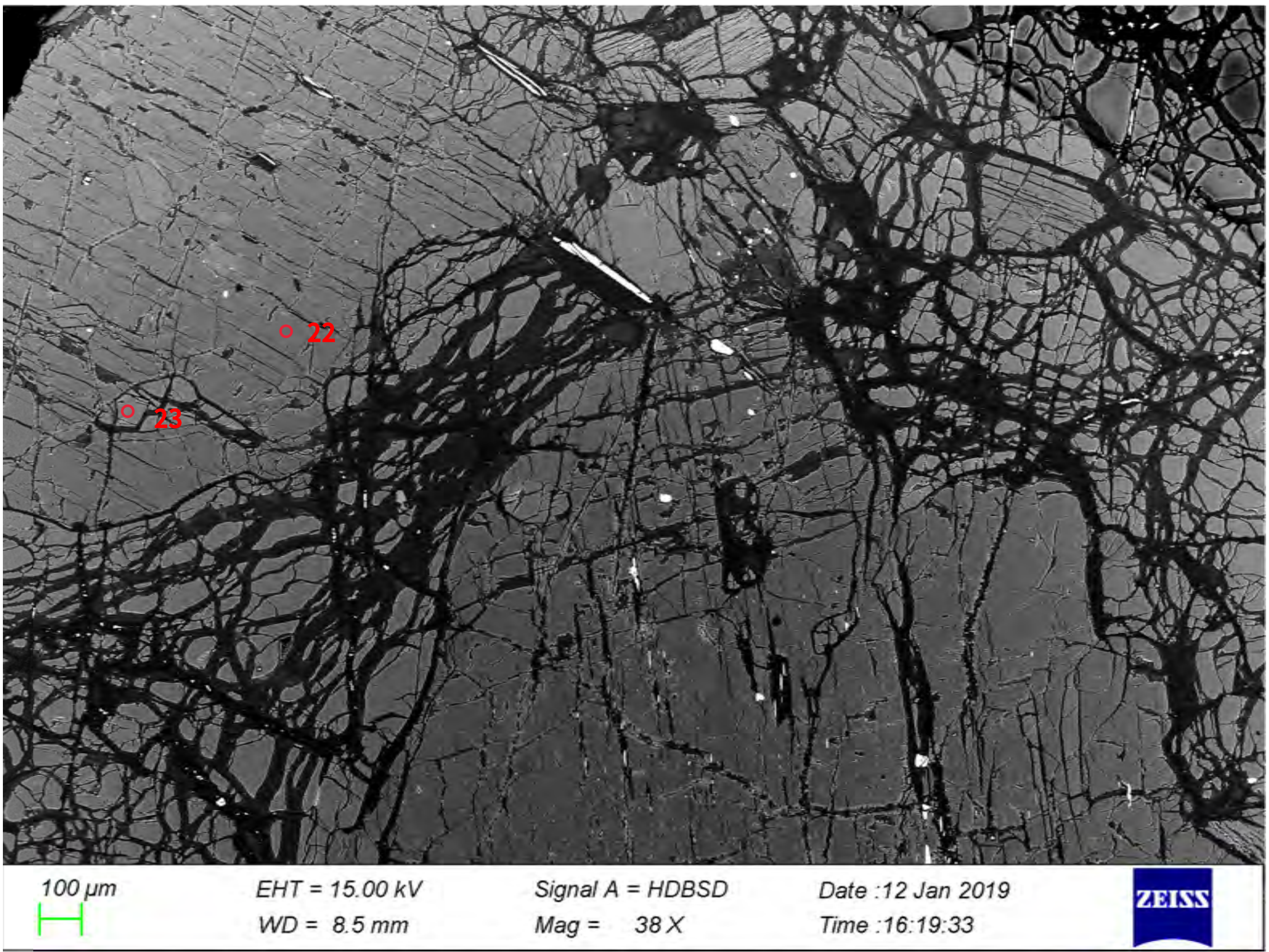
22
23
100 µm
EHT = 15.00 kV
WD = 8.5 mm
Signal A = HDBSD
Mag = 38 X
Date :12 Jan 2019
Time :16:19:33

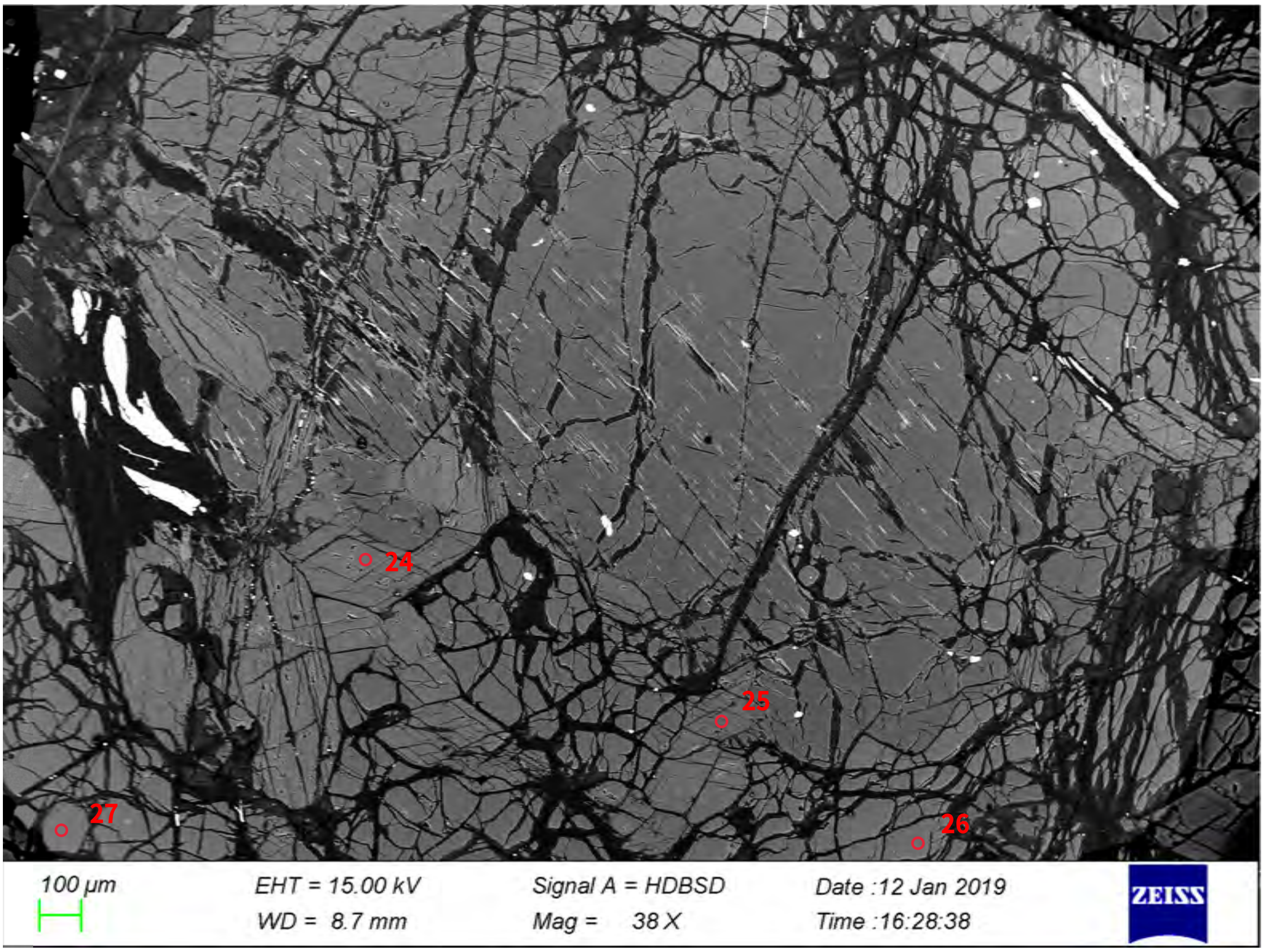
24
25
26
27
100 µm
EHT = 15.00 kV
WD = 8.7 mm
Signal A = HDBSD
Mag = 38 X
Date :12 Jan 2019
Time :16:28:38
ZEISS

Sample C19-52

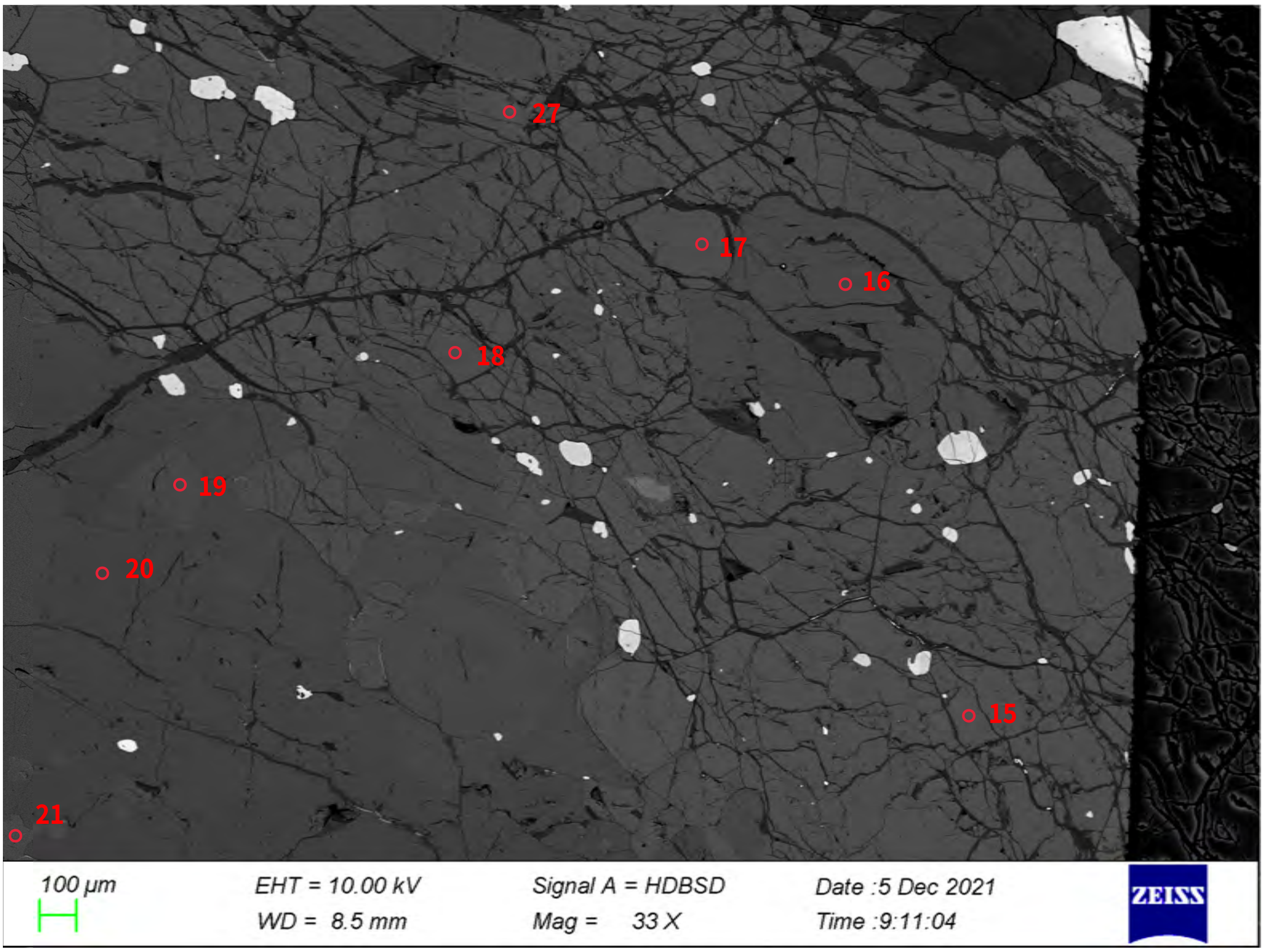

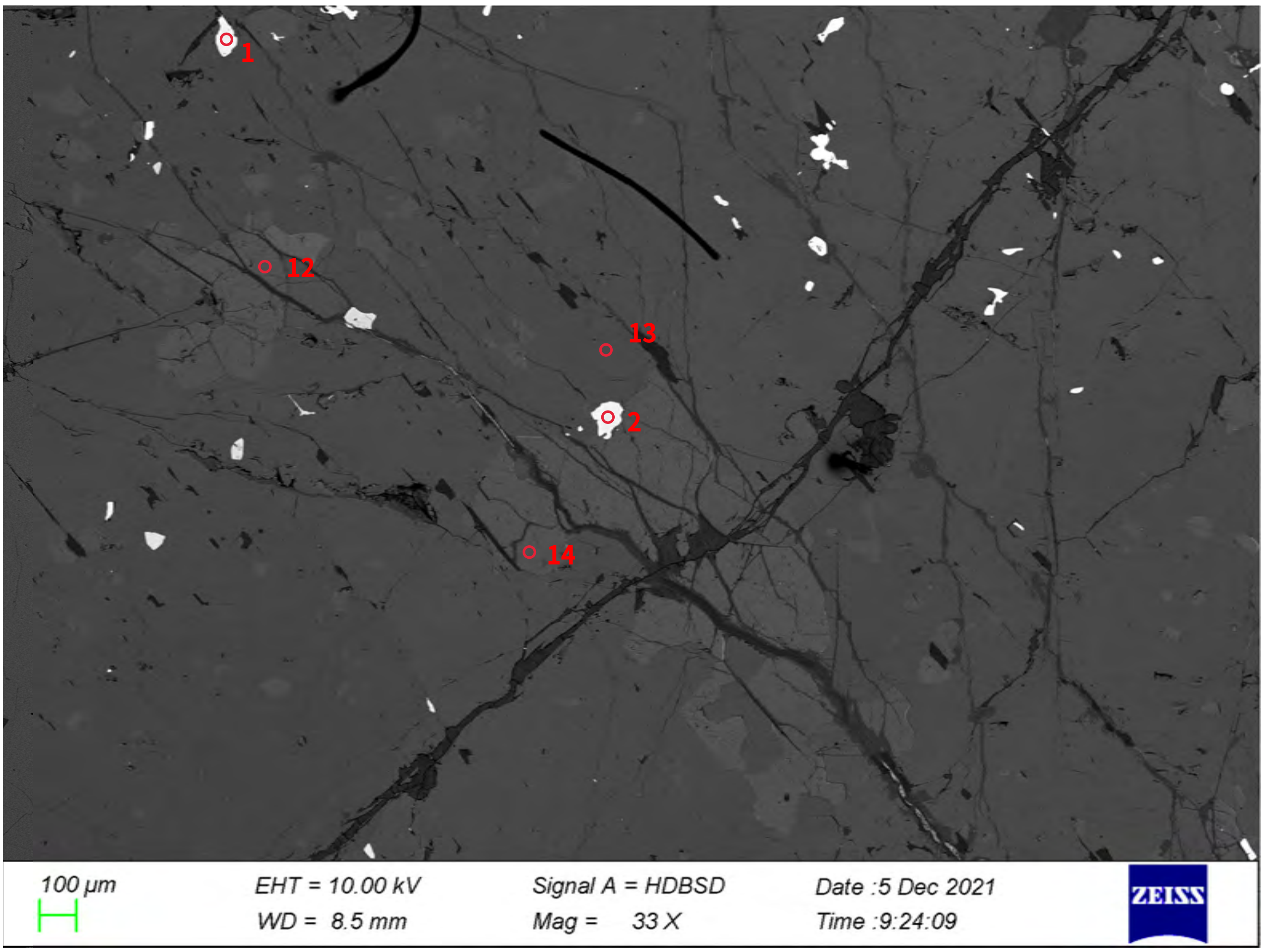

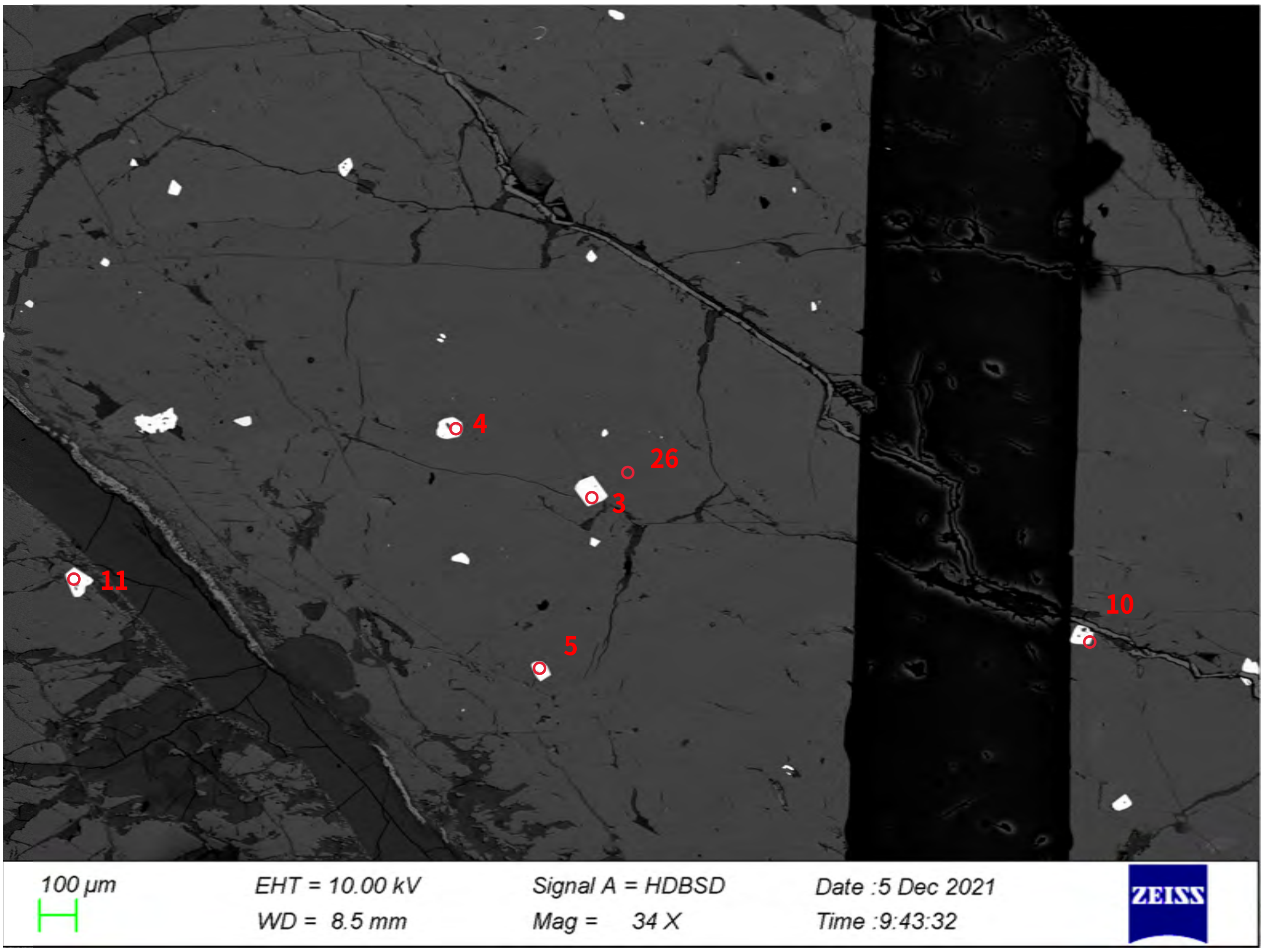
4
26
3
11
5
10
100 µm
EHT = 10.00 kV
WD = 8.5 mm
Signal A = HDBSD
Mag = 34 X
Date :5 Dec 2021
Time :9:43:32
ZEISS

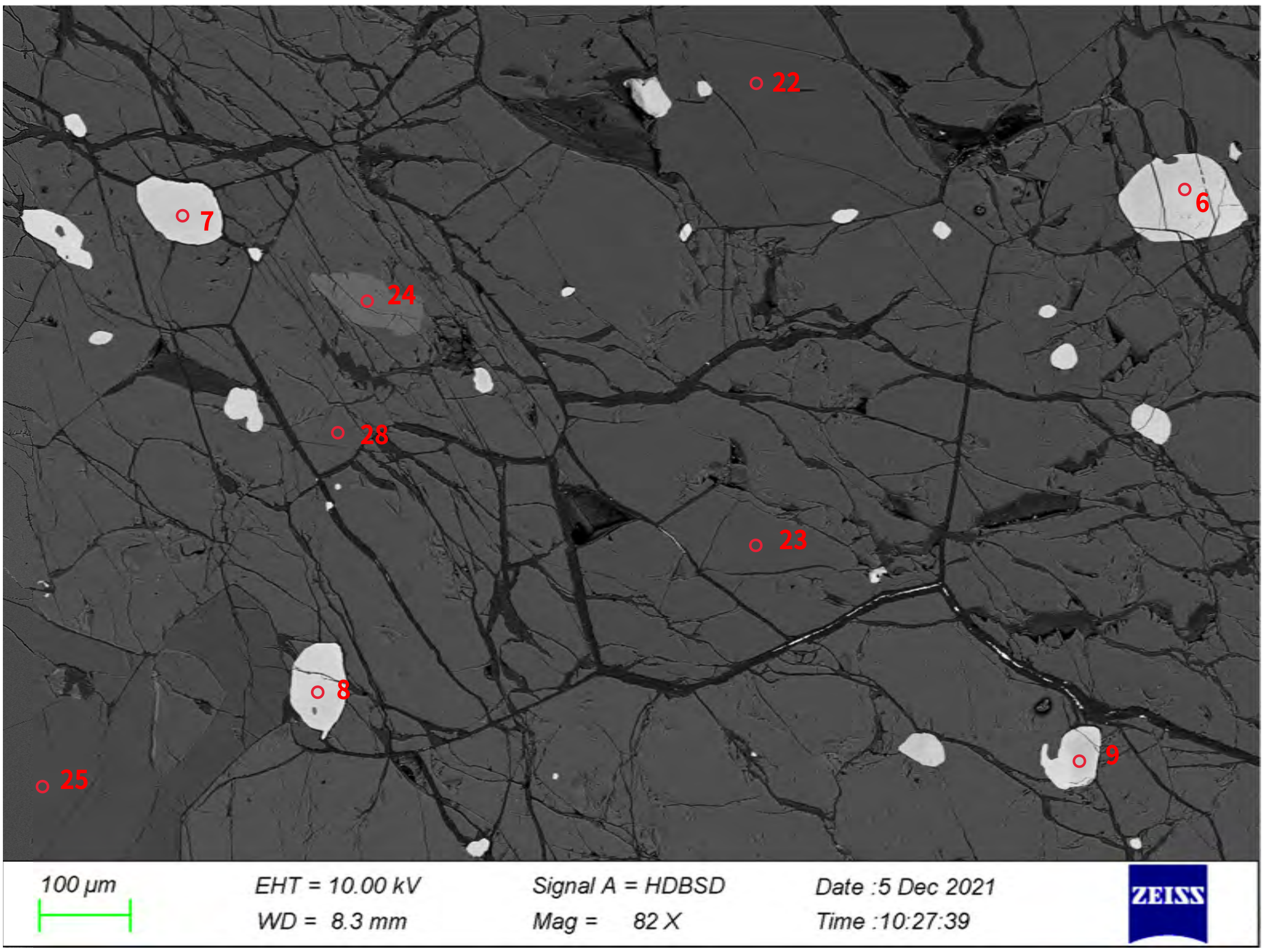
22
6
7
24
28
23
8
9
25
100 µm
EHT = 10.00 kV
WD = 8.3 mm
Signal A = HDBSD
Mag = 82 X
Date :5 Dec 2021
Time :10:27:39
ZEISS